



# 23<sup>rd</sup> International HISWA Symposium on Yacht Design and Yacht Construction

17 & 18 November 2014, Amsterdam, The Netherlands

## PROCEEDINGS



Organized by:

HISWA - National Association of Watersport Industries in The Netherlands  
The International Trade Show of Marine Equipment METS 2014  
Delft University of Technology



# 23<sup>rd</sup> International HISWA Symposium on “Yacht Design and Yacht Construction”

Amsterdam, 17 & 18 November 2014

## PROCEEDINGS

Edited by P.W. de Heer

### Organizing Committee

**Pepijn de Jong**  
**Michael Steenhoff**

Delft University of Technology  
HISWA Vereniging – The Dutch National Association  
of Watersport Industries  
Amsterdam RAI Convention Centre

**Irene Dros**

### Scientific Committee

**Bart Bouwhuis**  
**Prof. Hans Hopman**  
**Pepijn de Jong**  
**Bram Jongepier**  
**Geert Kapsenberg**  
**Thys Nikkels**  
**Michael Steenhoff**  
**Peter van Terwisga**

Vripack  
TU Delft  
TU Delft  
Feadship  
MARIN  
Dijkstra Naval Architects  
HISWA Vereniging  
Damen Shipyards

November 2014

Organized by HISWA - National Association of Watersport Industries in The Netherlands,  
The International Trade Show of Marine Equipment METS 2014  
Delft University of Technology

Photo cover: Royal Huisman

Delft University of Technology  
Section Ship Hydromechanics and Structures

**Printed by:**

**Sieca Repro B.V.**  
**Turbineweg 20**  
**Postbus 117**  
**2600 AC Delft**

**Phone: +31 (0)15 2561919**  
**Email: info@sieca.nl**

**KONINKLIJKE BIBLIOTHEEK, DEN HAAG**  
Depot van Nederlandse Publicaties  
Postbus 74  
2501 AJ Den Haag

23<sup>rd</sup> International Symposium on “Yacht Design and Yacht Construction”: Proceedings of the 23<sup>rd</sup> International Symposium on “Yacht Design and Yacht Construction”, Amsterdam, 17 & 18 November 2014 – Delft University of Technology, Section Ship Hydromechanics and Structures, The Netherlands.

**ISBN/EAN: 978-90-811322-3-7**

Subject headings: Yacht Design, Yacht Construction

## TABLE OF CONTENTS

Table of Contents .....	3
Symposium Program .....	5
Program Monday November 17, 2014.....	5
Program Tuesday November 18, 2014.....	6
Introduction .....	7
Symposium Papers .....	9



## SYMPOSIUM PROGRAM

### Program Monday November 17, 2014

**Moderator**        **Hans Hopman**

12.00 – 13.00        **Registration**

13.00 – 13.15        **Opening**

#### *Session 1*

13.15 – 13.55        **Will increasing regulations affect the demand for superyachts?**

C. van Hooren, *SYBAss*

13.55 – 14.35        **Dynamic positioning capabilities for superyachts**

J. Calver, J. Roy, *BMT Nigel Gee*

14.35 – 15.15        **A quantitative study on relative motions during tender boarding**

P. van Loon, *Feadship*

15.15 - 15.30        **Coffee break**

#### *Session 2*

15.30 - 16.10        **Parameters affecting the performance of the C-class wing sail**

M. Magherini, S.R. Turnock, I.M. Campbell, *University of Southampton*

16.10 - 16.50        **Dynamic measurement of pressures, sailshape and forces on a full scale spinnaker**

J. Deparday, P. Bot, F. Hauville, *Naval Academy Research Institute, France*

D. Motta, D. J. Le Pelley, R.G.J. Flay, *Yacht Research Unit, University of Auckland*

16.50 - 17.30        **Can a flapless hydrofoil provide a realistic alternative to a standard Moth foil with a flap?**

J.R. Mackenzie, *Australian Maritime College*

17.30 - 18.30        **Reception**

18.45                 **Dinner cruise**

## Program Tuesday November 18, 2014

**Moderator** Hans Hopman

09.30 - 09.30 **Opening day 2**

### *Session 3*

09.35 – 10.15 **The interaction between sailing yachts in fleet and match racing situations**  
P.J Richards, N. Aubin, D.J. Le Pelley, *Yacht Research Unit, University of Auckland*

10.15 – 10.55 **Comparison of downwind sailing performance predicted from wind tunnel tests with fullscale trials from America's Cup Class Yachts**  
I.M. Campbell, *Wolfson Unit MTIA*

10.55 – 11.10 **Coffee break**

### *Session 4*

11.10 – 11.50 **Experimental and numerical assessment of mega-yacht aerodynamic performances and characteristics**  
F. Fossati, P. Schito, F. Robustelli, *Politecnico di Milano*  
A. Cuoci, M. Derudi, *Politecnico di Milano*  
S. Dellepiane, *Azimut Benetti*

11.50 – 12.30 **Advanced propulsion trains for superyachts**  
S. Brealey, J. Roy, *BMT Nigel Gee*  
F. Hoppe, *Renk*

12.30 – 13.30 **Lunch break**

### *Session 5*

13.30 – 14.10 **Solving vibrational resonance on a large yacht using a Tuned Mass Demper**  
A.W. Vredeveldt, *TNO*

14.10 – 14.50 **Glass as a load bearing material in yacht structures**  
K.M. Jansen, *Feadship*

14.50 – 15.30 **Adhesion: lessons learned about adhesive bonding in ship structures**  
K. Custers, B.-J. Bekkers, *Damen Shipyards*

15.30 – 15.45 **Coffee break**

### *Session 6*

15.45 – 16.25 **Merits of flapping roll stabilizer fins**  
R. Dallinga, S. Rapuc, *MARIN*

16.25 – 17.05 **Design optimisation for small craft**  
A. Markov, A. Abma, *Vripack*

17.05 **Closing**

## INTRODUCTION

Before you lie the Proceedings of the 23<sup>rd</sup> International HISWA Symposium on Yacht Design and Yacht Construction to be held in Amsterdam on November 17<sup>th</sup> and 18<sup>th</sup> 2014. The 23<sup>rd</sup> edition marks a number of changes surrounding the oldest symposium in the area of yacht design and research. First and foremost, it is the first symposium without Lex Keuning in charge since the 13<sup>th</sup> edition of 1994. His substantial contribution to the symposium over the last decades was commemorated during the last symposium two years ago. Here I would like to congratulate Lex on the outstanding quality of the symposium during this period and to thank him for his many years of hard work and dedication he has put in to the HISWA Symposium. It is our challenge to continue this impressive track record.

Besides this change, there have been quite some changes in the scientific committee. The committee has been strengthened by the addition of a few members from both academia and the industry. This illustrates the nature of the HISWA Symposium: to form a bridge between the work that is carried out in the academic setting and the practitioners, the designers and builders of yachts and the industry surrounding them, and to encourage the active discussion between them.

Another change is the move of venue to the Elicium Centre of the RAI Congress Centre. It provides a more central location and modern environment at the heart of the RAI Congress Centre. It allows a closer link with the METS trade show that is organized at the same time. New is also the possibility to participate in the Breakfast Briefing on Tuesday morning of the METS trade show. To have a look at the METS trade show is highly recommended. An opportunity to do so is offered on Tuesday afternoon after the symposium closing.

What remains the same is that the Organizing Committee is again very content with the interesting program that has been put together by the Scientific Committee. The program covers yacht design and yacht construction in a very broad manner, with topics ranging from sail performance of America's Cup class sailing yachts to the innovative use of materials such glass and innovative bonding techniques in yacht construction. There are papers dealing with the design and onboard systems of super yachts just as well as papers dealing with the design of small craft. The key note will address recent changes in rules and regulations and their impact on the community of yacht designers and builders.

Also, we are again very pleased with the participation of such a large number of students. They of course will shape the future, also in the field of yacht design and research. The symposium is intended for the sharing of ideas on yacht design and yacht construction between the professionals but also with students. Not only during the paper presentations, but also in the numerous breaks and the symposium dinner that will be held during the now almost traditional dinner cruise through the Amsterdam canals.

Finally, I would like to express our gratitude to our sponsors, Damen Shipyards, Maritime Research Institute Netherlands, Royal Huisman Shipyards, and Feadship, without whom the aims of the symposium, i.e. offering a worthwhile and motivating gathering of interested people from the various branches, research institutes and schools active in this field, would not be possible at an affordable price.

Pepijn de Jong  
Chairman Organizing Committee  
Scientific Committee





## **SYMPOSIUM PAPERS**



## **Will increasing regulations affect the demand for superyachts?**

**Chris van Hooren, Superyacht Builders Association (SYBAss)**

### **1. SUMMARY**

After several years of reduced demand, the superyacht market is again showing signs of improvement. At the same time, there is considerably more regulatory oversight in terms of both tempo and volume. Some fear this may discourage potential superyacht owners from entering the business.

This paper introduces the International Maritime Organization (IMO) and identifies the regulations it specifies for superyachts. The increased degree of regulation is illustrated by a number of amendments to IMO instruments that have recently entered into force or will do so shortly.

Steady growth in the number of vessels seems to indicate that increased regulation does not, in fact, affect demand for superyachts. Knowledgeable owners appear to understand that regulatory oversight ensures their safety at sea, and guarantees that the environmental impact of their superyacht will meet all international standards.

Nevertheless, it is an understandable reaction to chafe at regulations as compliance with new rules calls for new approaches that require additional time and costs. Regulations are often less appropriate for superyachts due to their specific characteristics and type of operation (although this may also create opportunities for progressive shipyards). This calls for better industry representation at the level where regulations are made or amended.

### **2. THE INTERNATIONAL MARITIME ORGANIZATION (IMO)**

Seafaring has always been one of the world's most dangerous occupations. In response to major disasters, states moved towards internationalising the laws that regulate safety at sea and, increasingly, aim to prevent pollution from ships. This led to the creation of the International Maritime Organization (IMO) in 1948.

There is no doubt that IMO has come a very long way since its inception. Globalisation has transformed international trade, new powers have emerged in shipping, and the plethora of measures established by IMO has provided the bedrock on which a safer and cleaner industry can continue to develop and flourish. Moreover, IMO's work has demonstrated beyond doubt that international standards are the only effective way to regulate an industry as diverse and truly international as shipping.

IMO standards are now firmly embedded in the collective consciousness and practices of the shipping industry and continue to have a strong influence today. Indeed, the comprehensive body of IMO conventions (some fifty in total), supported by literally hundreds of codes, guidelines and recommendations, govern just about every facet of the industry – from the design, construction, equipment and operation of ships to the training of seafarers, and from the drawing board right to the scrapyards. The main IMO treaties have been ratified by states that are, collectively, responsible for more than 98 per cent of the world's fleet.

### **3. THE YACHT CODES**

With a few exemptions, superyachts operating in international waters have to comply with relevant IMO conventions. This includes, among others, the International Convention for the Safety of Life at Sea (SOLAS), the International Convention on Load Lines (ICLL), the International Convention for the Prevention of Pollution from Ships (MARPOL), the Collision

Regulations (ColReg) and the International Convention on Standards of Training, Certification and Watchkeeping for Seafarers (STCW). SOLAS, ICLL and MARPOL are of special interest for the design and construction of vessels.

It is widely recognised that it has become increasingly impractical to apply to pleasure yachts the standards and requirements established by the major IMO Conventions. These were developed and have evolved to deal with merchant cargo ships and passenger ships, not superyachts. And this is the issue which has been addressed in two Yacht Codes.

### **3.1 The Large Yacht Code**

For superyachts carrying 12 guests or less, the UK Maritime and Coastguard Agency (MCA) published the Large Yacht Code in 1997. This provided a 'code' approach for vessels which were unsuited to the application of conventional merchant shipping regulations. The Code was notified to the IMO as the provisions for the United Kingdom under the equivalence arrangements of the ICLL, SOLAS and the STCW (IMO Circular Letter No 2937).

Since its original publication, the Large Yacht Code has made a significant impression on a maritime sector which previously found it very difficult to embrace conventional regulation. Enjoying international recognition and support within individual countries, the code has become the de facto international standard for this type of yacht.

The Large Yacht Code was developed, and is being kept up to date, in close cooperation with an industry working group to ensure that it keeps up to date with developments in the industry and amendments in the related international conventions. The third edition of the Large Yacht Code – LY3 [1] was launched in 2012 and incorporates “substantial equivalent” solutions for the crew accommodation requirements of the Maritime Labour Convention (MLC) issued by the International Labour Organization. This third edition of the code entered into force on 20 August 2013, coinciding with the date of entry into force of the MLC.

### **3.2 The Passenger Yacht Code**

Similarly to the Large Yacht Code, the Passenger Yacht Code for Yachts Carrying 13 to 36 Passengers (PYC) was published in 2010 by the Red Ensign Group (for UK and UK overseas territories and crown dependencies). This Code was also notified to the IMO as the provisions for the United Kingdom under the equivalence arrangements of the ICLL, SOLAS and the STCW (IMO Circular Letter No 3171).

The Passenger Yacht Code was also developed, and is being kept up to date, in close cooperation with an industry working group. At this time the Code contains provisions for motoryachts only. However, a special working group has drafted provisions for sailing yachts to be included in a future edition of the code subject to the completion of additional research. The fourth edition of the Passenger Yacht Code, including references to the full crew accommodation requirements of the MLC, has been published in January 2014 [2]. Edition five is expected in early 2015.

## **4. SOME REGULATORY DEVELOPMENTS**

Amendments to existing IMO Conventions, as well as new IMO Conventions considered necessary for the safety of international shipping or protection of the environment, are developed by IMO's Marine Safety Committee (MSC) and Marine Environmental Protection Committee (MEPC), both supported by a number of subcommittees.

It is inevitable that developments of the conventions that underlie the Yacht Codes will be included in future editions of these codes, either in full or in the form of equivalent provisions. Some new conventions or amendments to existing conventions that may affect the design and build of superyachts are listed below.

### **4.1 International Ballast Water Management Convention**

While ballast water is essential for safe and efficient modern shipping operations, the multitude of marine species carried in ships' ballast water can pose serious ecological, economic and health problems. The International Convention for the

Control and Management of Ships' Ballast Water and Sediments (BWM) was adopted in 2004. Ratification is in progress and the BWM is expected to come into force soon for new and existing ships.

The BWM requires cumbersome de-ballasting procedures and the installation of a costly and space-demanding ballast water treatment system for vessels carrying ballast water. As superyachts do not carry cargo, de-ballasting can possibly be avoided with an innovative approach to trim, list and stability control (e.g. clever arrangement of tanks for consumables or a permanent in-board fresh water ballast system).

#### 4.2 Hong Kong Convention on the safe and sound recycling of ships

The Hong Kong Convention was adopted in 2009 to prevent, reduce or minimise the adverse effects of the recycling of vessels on human health and the environment. The ratification of the Hong Kong Convention is proceeding slowly and current indications suggest entry into force will not take place until 2016/2017.

Countries that have ratified this convention ensure that certain hazardous materials are not fitted on new ships while new builds are provided with an Inventory of Hazardous Materials (IHM) that must be kept up to date over the life of a vessel (e.g. after refits).

The creation of the IHM will be a significant administrative burden for shipyards as most hazardous materials are contained in the supplies of third parties. Requiring suppliers to provide the necessary certificates of conformity will be an onerous task [3] [4].

#### 4.3 Air pollution and energy efficiency

To reduce future emissions of CO<sub>2</sub> (a greenhouse gas), a new chapter has been added to MARPOL Annex VI making mandatory the Energy Efficiency Design Index (EEDI) for new ships over 400GT. The EEDI of a ship is the amount of CO<sub>2</sub> produced per transport work (tonnes-mile) under design conditions. The EEDI is based on design parameters, not operational parameters. The new Chapter 4 entered into force on 1 January 2013.

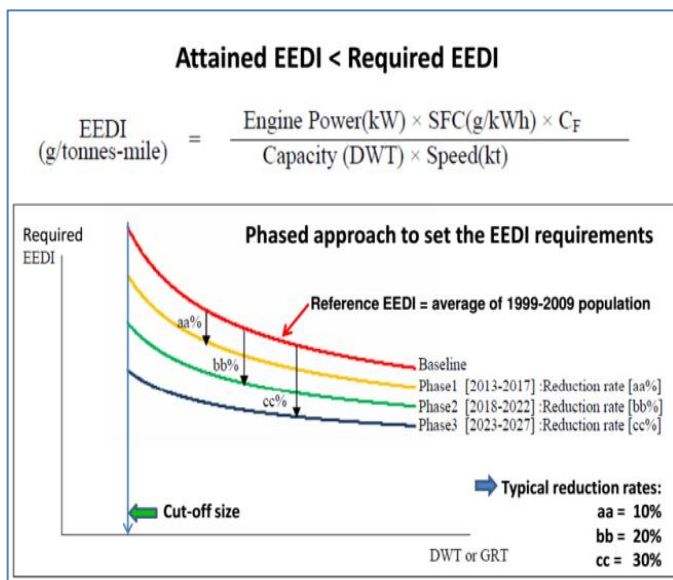


Figure 1: EEDI Requirements

For new ships, attained EEDI must be less than required EEDI. Required EEDI will decrease over time, relative to a reference EEDI representing the average of the 1999-2009 population of the type of ship under consideration (Figure 1).

The significant reduction in required EEDI over the next 15 years will, apart from lowering design speeds, be a driver for the development of innovative low-resistance hull forms and more efficient propulsion installations, as well as the use of lower carbon fuels.

At this time, no EEDI reference lines - and hence no required EEDI values - are defined for LY3 and PYC yachts. Nevertheless, according to Regulation 20 of Chapter 4, the attained EEDI value shall be calculated for each new ship over 400 GT whose type is defined in MARPOL Annex VI Regulation 2. This seems to include PYC Yachts as they are considered to be passenger ships.

At this time IMO has defined only one reference line for passenger ships (cruise vessels). SYBAss has established that this EEDI reference line is unsuitable for PYC Yachts (Figure 2) and has brought this to the attention of the relevant flag states.

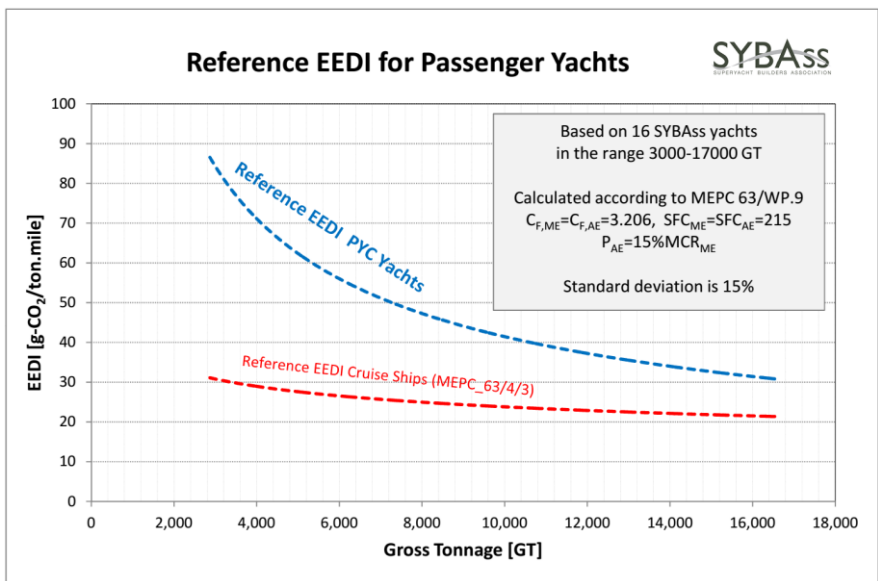


Figure 2: Reference EEDI for PYC Yachts and Cruise Ships

4.3 NOx emission limits

MARPOL Annex VI sets limits on NOx emissions from ship engines over 130 kW. The emission standards are commonly referred to as Tier I, II and III (Figure 3). Tier I and Tier II levels have already been mandatory for some time and could be achieved by in-engine measures.

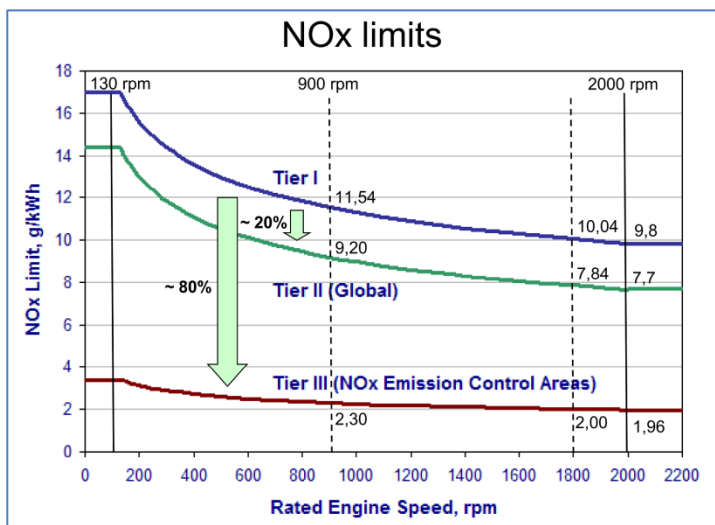


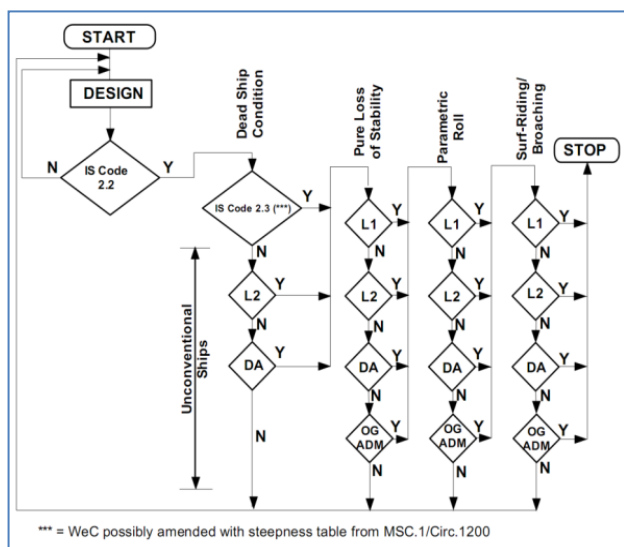
Figure 3: MARPOL Annex VI NOx limits (courtesy of MTU)

Tier III will apply only within NOx emission control areas (NECAs). Tier III will enter into force on 1 January 2016 for the NECAs already designated (North American and United States Caribbean waters). The entry into force for new NECAs will depend on when they are decided upon.

Given the present state of technology, only costly and space-demanding selective catalytic reduction installations appear to provide feasible solutions for meeting the very low Tier III NOx limits. To allow more time for innovations in this field, SYBAss and ICOMIA have obtained a five-year delay of entry into force of the Tier III NOx requirements for yachts of less than 500 GT. The related request and three underlying extensive studies are contained in [5].

4.4 Second-generation intact stability criteria

Significant changes in the design and operation of ships have occurred over recent decades. These changes, and their impact on the intact stability performance of ships, have motivated the development of so-called second-generation intact stability criteria by the IMO. Consolidation of various proposed criteria and the testing of various ship types is now in progress, with a target completion year of 2015. After adoption, the new criteria will be included in Part B (recommendations) of the Intact Stability Code 2008 (IS 2008) [6]. They will become mandatory once their performance has been proven to be satisfactory (Part A of IS 2008).



**Figure 4: Multi-tiered approach to intact stability**

Figure 4 illustrates the multi-tiered approach for the second generation intact stability criteria. In this process, the current criteria of the 2008 IS Code are applied for all ships covered under IMO instruments (this includes the Large Yacht and Passenger Yacht Codes).

In addition, each ship is also checked for vulnerability to pure loss of stability, parametric roll, surf-riding/broaching and excessive stability (the latter is not shown in Figure 4).

Vulnerability for each mode is first tested using simple but conservative criteria (L1). If a possible vulnerability is detected, then the more rigorous level 2 criteria (L2) are used, if necessary followed by direct stability assessment (DA). If the direct stability assessment shows an elevated level of risk, then ship-specific operational guidance (OG) will be developed.

The process is repeated for all four stability failure modes.

As an NGO participating in the work of IMO, SYBAss has determined that the original proposals of the level 1 criteria for pure loss of stability and parametric roll were unsuitable for superyachts because of their sleek lines. With the help of the Technical University of Trieste SYBAss has proposed more appropriate criteria which have been adopted [7].

The present level 1 criteria for pure loss of stability and parametric roll appear to be sufficiently simple and acceptable robust to be used by yard's naval architects during preliminary design stages, when it is still feasible to modify design parameters as necessary. Up to now very few superyachts were found vulnerable on level 1 [8], although vulnerability may be higher at light draught. Level 2 calculations are more sophisticated and require more detailed design information. Level 2 calculations, and certainly direct assessments, seem to be work for seakeeping specialists [9].

#### 4.5 The Polar Code

Ships operating in Arctic and Antarctic environments are exposed to a number of unique risks. Ice in the water can impose additional loads on the hull, propulsion system and appendages. Ice accretion or ice-related damages affect stability. Poor weather conditions and the relative lack of good charts, communication systems and other navigational aids pose challenges for mariners. The remoteness of the areas makes rescue or clean-up operations difficult and costly.

The IMO will shortly adopt the International Code for Ships Operating in Polar Waters (the Polar Code) intended to establish additional provisions for consideration beyond the existing requirements of the SOLAS and MARPOL Conventions. The more comprehensive Polar Code will replace the existing IMO Polar Guidelines and become mandatory under the new SOLAS Chapter XIV for new and existing ships.

The Polar Code will address operational and design issues. Recent studies have demonstrated that, depending on the applicable ice class, compliance with the Polar Code may affect the design of a superyacht considerably. This is especially the case with regards to structural strength, intact and damage stability, subdivision and tank arrangement, machinery and lifesaving appliances.

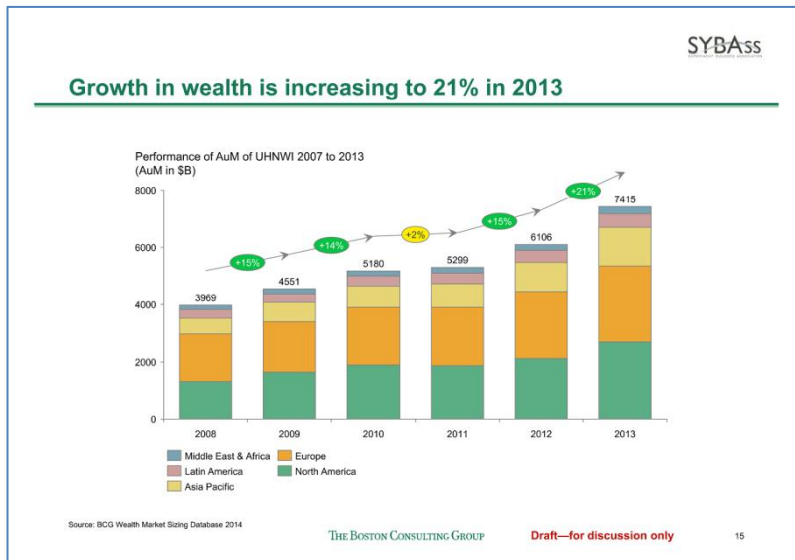
#### 4.6 PYC and sailing yachts

IMO instruments have no special provisions for sailing yachts. As mentioned, specific requirements for sailing vessels will be included in the Passenger Yacht Code in a way similar to that used in the Large Yacht Code. With additional research required, the anticipated date for this extension is 2016 [10].



**5. THE DEMAND FOR SUPERYACHTS**

Superyachts operating internationally are subject to the same or equivalent standards as merchant ships. Some people seem to fear that the surge in regulation is in danger of swamping the superyacht industry and may convince owners to cash out or not enter the business at all.



Potential new build demand can be estimated by looking at the growth in number of Ultra High Net Worth Individuals (UHNWI) and their propensity to buy superyachts.

In 2013, total Assets under Management (AuM) of UHNWI grew by 21 percent (Figure 5). The number of billionaires is at an all-time high and for most countries exceeds pre-crisis levels.

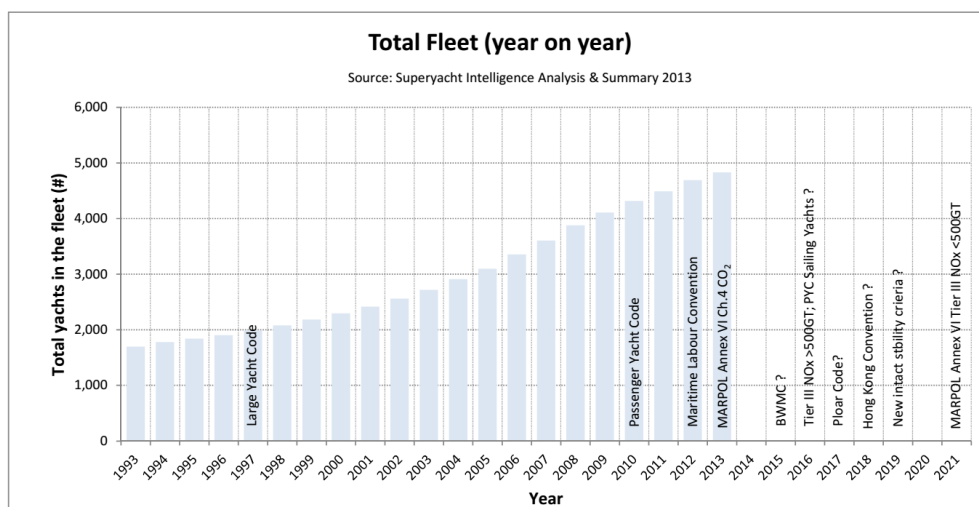
It can therefore be concluded that the potential demand for new builds shows a healthy growth.

But what about the propensity; is it adversely affected by increased legislation?

**Figure 5: Growth in Wealth in recent years**

Figure 6 shows the development of the superyacht fleet over the last 20 years [11]. (Expected) dates of entry into force of (new) regulation are indicated. It demonstrates a steady increase in the number of superyachts. This can be expected to continue over several years, irrespective of future demand being affected by the currently low propensity to buy superyachts among the fast growing group of UHNWIs from Asia (Figure 7). The only relative decline was between 2012 and 2014 – this was the result of lower order numbers in 2009 and 2010, when the impact of the global financial crisis first made itself felt.

From the above one may conclude that increased regulation has not affected the demand for superyachts.



**Figure 6: Timeline Superyacht Fleet and Regulations**

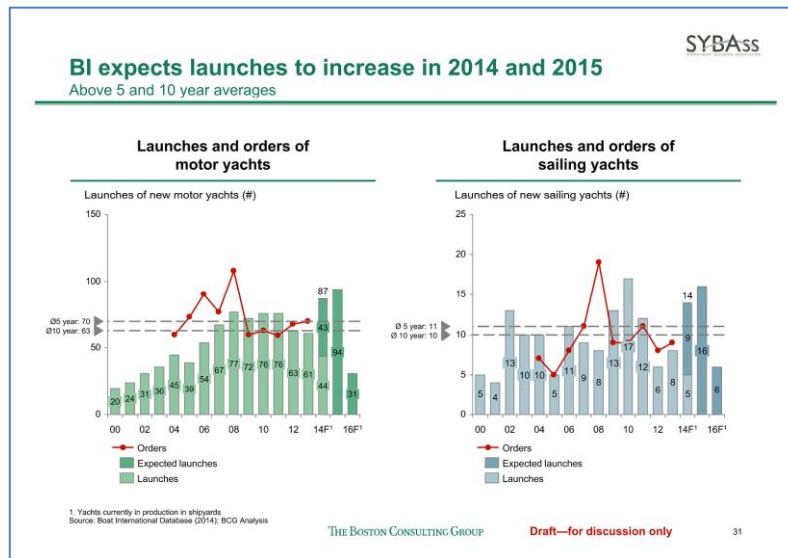


Figure 7: Launches and Orders

## 6. CONCLUSIONS

While regulatory oversight for internationally operating vessels has existed for many years, it has noticeably increased in tempo and volume over the last decades, and will continue to do so over the next decade. This is not surprising considering the world fleet has doubled over the last two decades [12], posing greater potential loss of life. At the same time, the number and average size of superyachts launched has increased every year, and they are manned by larger crews. Coupled with the ongoing effort to lower the environmental impact of the maritime industry and the movement towards strengthening seafarers' rights, this has led to a surge in regulation.

Given the steady growth of the number of superyachts, the increased legislation does not seem to have discouraged owners from ordering new superyachts in the past or in the coming years. Knowledgeable owners obviously understand that the regulatory oversight ensures improved safety for themselves, their guests and their crews, whilst the environmental impact of their superyachts meets the standards established by the international community. Owners lacking maritime knowledge should be spared regulatory horror stories, instead coming to see regulations as proof of a safe and sound investment [13].

Nevertheless, it is understandable that those who work in the yachting industry chafe at new regulations. International standards are set by the international community and there is not much our industry can do about them other than realising equivalent solutions that suit our ship type better. Compliance with new rules calls for an innovative approach involving extra time and cost, although it may also create opportunities for progressive shipyards [14]. The problem is that regulations are often drafted with large merchant vessels in mind, making them less appropriate for superyachts because of their different characteristics and type of operation. This can be avoided to some extent by active industry representation on the level where regulations are made or amended.

For this reason the REG flag states have created Industry Working Groups which meet annually to discuss possible improvements or desirable extensions of the mentioned Yacht Codes. Input to IMO committees and subcommittees can be achieved through relevant Non-Governmental Organisations (NGOs) with IMO observer status. Another possible route is through official national IMO delegations that often consult their industry stakeholders with regard to amendments or new conventions. It should, however, be noted that some disciplines in our industry could do a lot better when it comes to regulatory representation.

**REFERENCES**

- [1] UK Maritime and Coastguard Agency: "The Large Commercial Yacht Code", Third Edition, August 2012.
- [2] The Red Ensign Group: "A Code of Practice for Yachts carrying 13 to 36 Passengers", Fourth Edition, January 2014.
- [3] P.C. Kuipers et al: "Strategy for SYBAss members regarding recycling convention", ARN and SYBAss, November 2010.
- [4] Andrew Johansson: "A Safer Environment", The Superyacht Report Issue 154, June 2014.
- [5] ICOMIA and SYBAss: "Tier III NOx emission standards and their impact on the superyacht sector", MEPC\_65/4/8 and MEPC\_65/INF.15, May 2013.
- [6] International Maritime Organization: "International Code on Intact Stability, 2008", 2009 Edition.
- [7] SYBAss: "Level 1 assessment of parametric roll – direct calculation of GM variation in regular waves", SLF\_54/3/8 and SLF\_54/INF.13, November 2011.
- [8] C.M. van Hooren: "Second Generation Intact Stability Requirements for Superyachts", SWZ Maritime, Jaargang 133, 2012.
- [9] S. van Duyn en B. Scheeren: "Second Generation Intact Stability Criteria Level 2", SWZ Maritime, Jaargang 135, 2014.
- [10] Cayman Registry: "Report of the PYC Working Group on Sailing Vessels", August 2014.
- [11] Ellie Brade: "Superyacht Intelligence Analysis & Summary", The Superyacht Report, 2013.
- [12] International Maritime Organization: "International Shipping Facts and Figures", March 2012.
- [13] Paul Duncan: "Drowning in a sea of 'Yes'", The Superyacht Report Issue 153, May 2014.
- [14] Dirk de Jong: "Pleasure Yacht or Passenger Ship?", SWZ Maritime Issue 135, February 2014.

# DYNAMIC POSITIONING CAPABILITIES FOR SUPERYACHTS

J. Calver, Naval Architect, BMT Nigel Gee Ltd., UK

J. Roy, Yacht Design Director, BMT Nigel Gee Ltd., UK

## SUMMARY

Dynamic Positioning (DP) systems are a mature and well proven technology. The Superyacht industry has embraced DP as a concept and many large yachts now feature some level of station-keeping capability. However as DP is not widely understood beyond the basic principles, capabilities are frequently over specified and the resulting impact on the level of installed power is often severe or at odds with the propulsion system specified for the yacht.

This paper provides background to the principles of basic station-keeping, typical thruster arrangements, and how DP is used in practice. Various fundamental methods of controlling the degree of DP capability are discussed, along with the impact on the vessels' design of implementation. A case study is used to explore a range of power generation and propulsion systems each with specific attention to the impacts on the primary design variables for large yachts.

Suggested levels of station-keeping / DP capability suitable for application to large yachts are explored allowing a better informed system specification to be made.

## 1. INTRODUCTION

In 1961, the drill ship 'Eureka' was launched from Orange shipyard. Built and owned by Shell, she was designed to drill in waters up to 3600 feet deep, a feat made possible only by the inclusion of a pioneering onboard system; Eureka was the first true dynamically positioned vessel in the world.

Since 'Eureka' the field of Dynamic Positioning (DP) has exploded in terms of complexity, reliability and uptake. Whilst it was undeniably the offshore industry that pioneered and developed DP systems, it is now widely installed on cable and pipe laying vessels, survey ships, cruise ships and increasingly, yachts.

In 1997 Lurssen's 96m 'Limitless' became one of the first luxury motoryachts to be fitted with a full DP system, allowing a yacht to keep station without dropping anchor for the first time. It was several years before DP became a commonplace in yachts of 'Limitless's size, however as diesel-electric installations have become more commonplace in the yachting world the inclusion of a DP system in the vessel's specification has become more prevalent. Nowadays, it is a feature that is expected of most large yachts.

It is often difficult to determine exactly what level of station-keeping capability to specify for a vessel. Of course, from an operational standpoint every yacht captain would love to command a yacht capable of accurately and reliably holding station in a Force 8 wind with associated sea state and current, however the practical implications of this would significantly detriment the vessel's design. It is important therefore to specify an appropriate level of DP capability when commissioning a vessel, such that the operational profile may be fulfilled with minimal impact to the vessel's overall function as a piece of luxurious real estate.

## 2. PRINCIPLES OF DP

It is important to make the distinction between DP and station-keeping, as used in this paper. Dynamic Positioning refers to the process whereby a computer controls the various thrusters and propulsors installed on the vessel to result in the desired thrust vector, in response to a joystick input from the bridge. DP systems account for external forces acting upon the vessel, such as wind, waves and current. One common feature of a DP system is a station-keeping function. This is the vessel's capability to react to external loading to maintain a certain position and heading, and is a good indicator of the vessel's overall DP capability.

The essence of designing a DP system capable of adequate station-keeping can be summarised in the following sentence; the vessel must be able to produce a force and moment equal and opposite to the force and moment acting upon it by environmental factors.

In practice this means that the vessel must have a thruster configuration whereby forces and moments about the vertical axis

can be produced. Furthermore, the installed power plant must be capable of providing the required power to the thrusters.

At some point, the environmental factors will overcome the thrust offered by the vessel. At this point, the vessel will begin to drift or yaw, and the edge of the station-keeping envelope will have been reached.

DP capability analysis involves finding the maximum wind speed at each heading that a vessel is able to maintain position and heading. Successful station-keeping at a specific wind heading requires the vessel to be capable of adequately opposing the environmental forces and moments imposed on the vessel by wind, current and wave forces. Typical station-keeping analysis software calculates the wind force and moment at each heading for a specific vessel, and iteratively increases the wind speed until the maximum available thrust from the thruster configuration is reached. As a result, an operational envelope is developed, showing the vessel's maximum station-keeping capability at each wind heading.

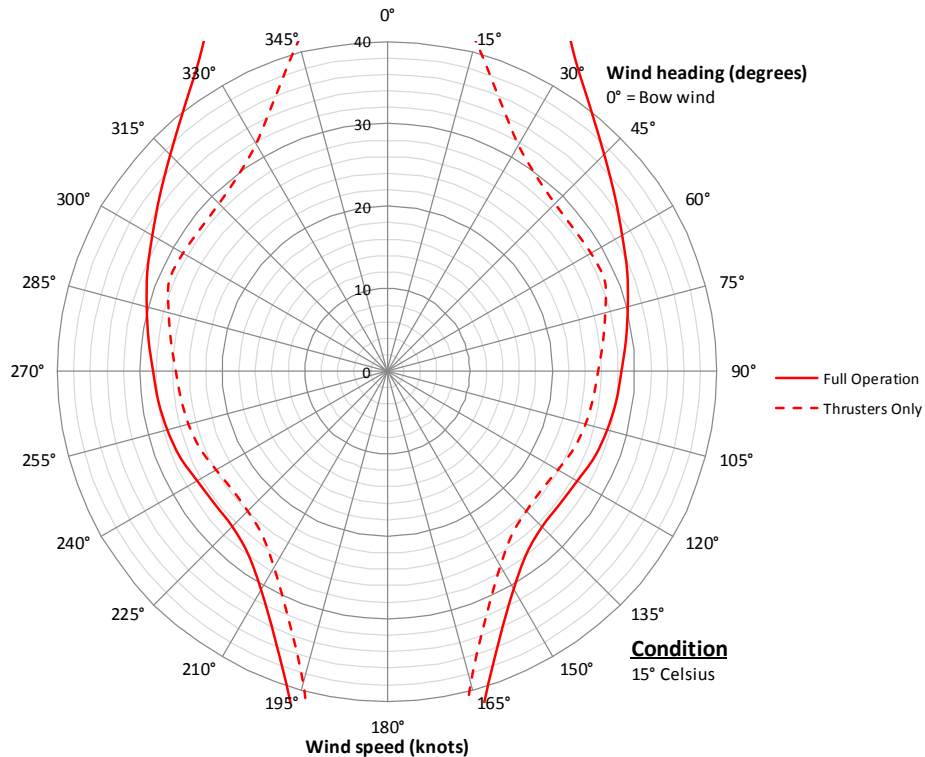


Figure 1 - Typical station-keeping capability analysis for a large motoryacht

Whilst a station-keeping plot shows the maximum wind speed the vessel is able to hold position and heading in, this also implies that if the wind speed being experienced is lower than the limiting value, then the vessel has adequate manoeuvring capacity. This is how station-keeping plots also define the capability of the DP system as a whole.

Within the type of analysis used in large yacht design it is often only wind loading that is considered. More advanced analysis including the hydrodynamic performance is needed to include loadings from wave forces and currents.

The early specification of required station-keeping capability by yacht clients typically does not consider the effects of wave or current loadings. It is an important aspect to understand as withstanding a 30 knot beam wind in sheltered harbour conditions requires a significantly different system specification to one designed to withstand 30 knots in open ocean conditions in a fully developed sea state.

### 3. TYPICAL THRUSTER ARRANGEMENTS ON LARGE YACHTS

The typical thruster arrangement for large yachts tend to follow a common configuration; twin CP screw propellers, with one or two fixed tunnel bow thrusters. Larger yachts may also have a stern thruster, commonly also fixed tunnel thrusters but occasionally retractable azimuthing units. Vessels fitted with fixed pitch main propellers (FPP) often use an azimuthing stern thruster, as the propellers are not usually part of the DP system (due to the low slow-speed torque characteristics of the main engines). Whilst azi-pods, which offer a greater degree of manoeuvrability, are becoming more common, the overwhelming majority of vessels follow the conventional arrangement.

This arrangement has remained unchanged for many years mainly because it makes use of space which has little practical use within the hull; bow thrusters are placed in the fore peak, immediately aft of the collision bulkhead, while stern thrusters are placed below the deck in the stern-rise section of the hull (and skeg). This arrangement is also well suited to provide the transverse forces and yawing moments required by a DP system.

The purpose of this paper is not to develop or evaluate new methods of providing manoeuvring thrust, but to analyse the power requirements of a yacht fitted with a 'standard' arrangement. However, it does seem that in modern yachts the naval architect is constrained in the arrangement that can be fitted, and that DP and manoeuvring is a rather secondary consideration. As will be shown, there is a practical limit to what the standard arrangement of thrusters can achieve in terms of DP capability.

#### **4. PRACTICAL USE OF DP SYSTEMS**

How DP systems are actually used in yachts is a somewhat subjective topic, with each captain using his system differently, depending on his experience with DP, the reliability and capability of the system.

One constant however is that using a DP command module to 'park' a vessel at sea without an anchor, and have it remain in a fixed position by using computers to automatically control the thrusters, is a very energy intensive operation, using a lot of fuel. It is also undesirable as with the vessel operating in this mode, there is little or no human element involved in the control over the thrusters and when they operate. Consequently it is difficult to conduct tender operations or swimming activities around the vessel when it is operating in such a mode. This functionality only really comes in useful when the water is very deep, as occurs close to shore around several Mediterranean islands, or when dropping anchor would not otherwise be a feasible option.

A more common use of the system is when used in conjunction with an anchor to keep the vessel headed into any incoming swell in order to reduce motions. This provides the security of having weighed anchor, with the additional comfort of maintaining an optimum or desired heading.

In practice DP systems provide an enhanced manoeuvring capability, with a computer controlling the thrusters to achieve the motion vector requested by the captain via joystick control. When used in ports and harbours, and manoeuvring in tight spaces, this feature is highly effective.

#### **5. DRIVERS OF DP CAPABILITY**

Increasing the DP capability of a vessel may be achieved in four distinct ways;

- Increasing the longitudinal or transverse separation between thrusters
- Increasing the range of thrust vectors achievable by a thruster
- Increasing the power available to a thruster
- Decreasing the environmental loading on the vessel (i.e. reduce the windage area, streamline the superstructure, or optimise the below waterline hull form for seakeeping capability).

As the latter option has a dramatic effect on the overall design of the vessel, it is omitted from this study – it is therefore assumed that the superstructure and wind profile of the vessel remain unchanged. In reality if extreme DP capability were desired, the designer should work to streamline the above waterline hull and superstructure to minimise the wind forces acting upon it. The impact on vessel design investigated here is strictly with respect to vessel arrangement and machinery options.

The impact of each method of increasing station-keeping capacity is studied in the following chapter.

#### **6. METHODS OF INCREASING DP CAPABILITY**

##### **6.1 Increasing Thruster Separation**

When there is a lateral separation in the centre of drag of the above waterline area and the below waterline area, the yacht will experience a yawing moment. In order to maintain heading, the vessel must be able to produce an equal and opposite moment to counter the environmental loading. On a yacht, this is most efficiently provided by either a pair of bow and stern

thrusters (longitudinal separation), or by twin screw propellers (separated transversely). Consequently, any increase in separation of these thrusters, either longitudinally or transversely will increase the moment-producing capacity of the thrusters, and therefore potentially an increase in DP capability, with no increase in required power.

The impact of increasing thruster separation on a yacht's design are generally unfavourable. The position of the vessel's main shaftline is determined primarily by rudder positioning, propeller separation and the practical constraints of the engine room layout. Whilst it would be marginally beneficial to station-keeping to increase the distance between the propellers, it is difficult to justify potentially jeopardising the performance of the propeller to marginally increase DP performance.

A more realistic method of increasing capability may be to increase longitudinal separation of the bow and stern thrusters. However traditional tunnel thrusters have a minimum tunnel length (function of diameter) which limits the extent to which the thruster can be moved forward.

Stern thruster positioning is also largely determined by spatial constraints – moving the stern thruster as far aft as possible is advantageous, but not if this means having to extend the skeg such that its proportions become extreme.

## 6.2 Increasing Vector Range

In a DP system, the vector angles that a thruster can achieve are very important. They increase the versatility of the thruster, and the capability of the entire vessel to produce a force and moment combination that will counter the environmental force.

Increasing the range of vectors that a single thruster can achieve can take many forms. The vector range of a screw-propeller may be increased by adding a rudder directly behind it, increasing the turning range of an existing rudder or using high-lift rudders. A water-jet may be improved by increasing its turning range. Instead of a tunnel thruster, an azimuthing thruster could be fitted. Anything that increases the range of angles at which the thruster can produce thrust, will inevitably increase the DP performance of the vessel.

Typical de facto large yacht systems are configured with twin FPP or CPP propellers married with fixed funnel thrusters fore and aft. In some cases the use of azimuthing stern thrusters are used. Such a systems are limited in their capability to produce a full spectrum of effective thrust. However in the greater majority of cases such configurations are more than sufficient. Where a higher level of station-keeping is required, or full DP capability, then there is a strong case of the adoption of a fully azimuth propulsion system.

## 6.3 Increasing Thrust Capacity

In reality the most common method of improving DP performance of a de facto yacht arrangement is to increase the power developed by the thrusters. By increasing the amount of thrust available, both translational and rotational manoeuvring capabilities are enhanced.

The impact of increasing power delivery of the thrusters is seen across many facets of the vessel;

*Hydrodynamic;* More powerful thrusters are invariably physically larger. For tunnel thrusters, this results in enlarged cut-outs at the bow, impacting the streamlines around the hull, and causing an increase in drag.

*Arrangement;* Larger units take up more space within the vessel. Bow thrusters may be located in a compartment beneath a chain locker or deck, limiting the vertical space for a tunnel thruster, whilst stern thrusters are typically tucked away beneath the tender bay deck. This is often a fairly large space within the vessel which has no practical use other than as a technical space, however sufficient vertical space must exist between the deck and the keel to allow for the unit. As bow thruster units get larger they need to be positioned further aft, due to the minimum tunnel length being a function of the diameter. This either has an impact on the vessel's arrangement, or drives a move towards using two smaller units, which again takes up more space, and causes more drag. Where thrusters are electrically driven, supporting electrical equipment volumes (such as frequency drives) will also increase in size to handle a higher power, as will cooling and ventilation requirements.

*Mechanical;* Thruster sizing is often a significant factor driving the size of the installed electrical generating machinery. It is commonly seen that whilst a vessel may meet its' operational hotel load using one or two generators, to supply the peak manoeuvring electrical load three or four generators are required. Thruster sizing will also impact the selection of main switchboard sizing, along with electrical distribution systems from the generators to the thrusters.

*Noise & Vibration;* It might be expected that larger bow and stern thruster units result in more noise and vibrations. However, the largest source of N&V emanating from thrusters is not from the machinery itself, but rather from the pressure pulses and potential cavitation caused by uneven pressure distributions over the propeller. Whilst resiliently mounted tunnels are used to attenuate this vibration, the dominant noise source is structure-borne vibrations. As pressure pulses can

occur on both large and small units it is not necessarily true that larger units create more noise, and a well-designed tunnel inlet can significantly reduce the vibrations experienced.

There comes a point that the improvements in system performance are not proportional to the increase in power level and the impacts outlined above become nonsensical or overly constraining to the design. It is at this point that the adoption of a fully azimuthing propulsion system should be considered.

## 7. SPECIFIED PERFORMANCE

It is important to consider the level of performance written into the specification carefully. The majority of build specifications call for a station-keeping capability at a certain wind speed in beam seas.

There are several reasons for this, most commonly that it is often assumed that the most onerous condition for station-keeping is a beam wind; This is not normally the case, particularly when a stern thruster is fitted (as is shown below).

The intent of the station-keeping specification is often to ensure the vessel has adequate manoeuvrability in port, rather than a true requirement of at-sea station-keeping. Consequently, one of the most onerous manoeuvres undertaken would be to move away from a berth in a beam wind; if the wind were quartering, the required thruster load could be reduced by swinging the bow or stern into the wind prior to moving off.

Additionally, a beam-wind thruster calculation can be done relatively simply and easily, using an Excel sheet and various assumptions. At the preliminary stages of design this is important, when some of the factors affecting DP system performance may be unknown.

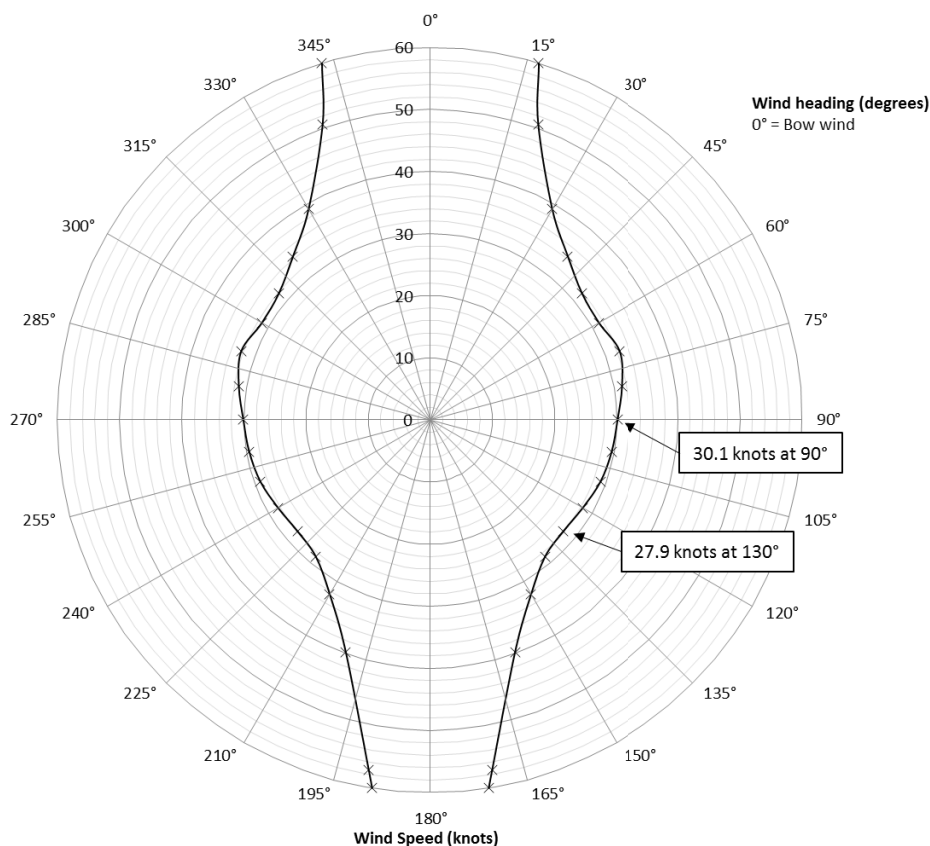


Figure 2 – Limiting wind speed in a beam-wind is not necessarily the lowest limiting wind speed of the vessel

There can however be a significant difference between the beam-wind station-keeping performance of a vessel, and the minimum wind magnitude at any angle. Consider Figure 2, where the vessel is shown to be capable of holding station in 30.1 knots of beam wind, however at a wind heading of 130°, (stern quartering), the maximum wind speed is 27.9 knots. The most onerous wind direction for a ‘standard arrangement’ yacht is normally seen to be a stern-quartering angle, as the rudders behind the main propellers are unable to vector the propellers thrust when operating in reverse, and also due to the reduced thrust achieved by a propeller operating in reverse.



Considering the points above, for the application of yachts, a beam-wind station-keeping specification is the most appropriate in the majority of circumstances. However if the specification is intended to ensure a minimum degree of at-sea station-keeping capability in any wind direction, then more focus should be given to the most onerous wind direction, in conjunction with wave and current loading criteria.

## 8. CASE STUDY

In order to quantifiably evaluate the impact on vessel design of an increasingly onerous DP capability, and to determine which of the various methods of increasing DP performance discussed above yields the most fruit, two case studies are presented.

As discussed in Section 6, the most realistic method of improving DP capability is to increase the amount of power and hence thrust available to the thrusters. It is considered that allowing the DP requirement to influence main engine selection is nonsensical. Therefore, the extra power will be allocated to the bow and stern thrusters only.

The study aims to relate the power requirement of the thrusters to the level of station-keeping performance. The impact on the yacht of this increased power requirement will then be studied, from an electrical and spatial perspective.

The basis vessel chosen for the study is representative of the size vessel typically seen with DP capability by BMT Nigel Gee Ltd., and has been chosen as a 'standard' form of motor-yacht.

### 8.1 Basis Vessel

The vessel studied is a 112m LOA motoryacht, which represents the larger end of the yachting fleet.

Briefly, it features a typical arrangement comprising twin screw propellers (diesel-mechanical CPP drive), an electrically driven bow tunnel-thruster, and an electrically driven stern azimuthing thruster.

#### *Principle Particulars*

- LOA: 112m
- LWL: 101.2m
- BOA: 16.2m
- Profile Area: 1200m<sup>2</sup>
- Profile longitudinal centroid: 4.5m forwards of amidships
- Frontal Area: 260m<sup>2</sup>

#### *Thrusters*

- 1 x bow tunnel-thruster, developing a maximum 70kN of thrust, at 480kW. Due to electrical losses, 526 ekW is required from the generators.
- 1 x stern azi-thruster (360°), developing 66kN at 385kW. Electrically driven, this draws 421ekW from the generators.
- Twin-screw propellers with rudders, developing 335kN forwards (235kN in reverse).

#### *Machinery*

- 2 x CPP propellers, with a maximum 3300kW shaft power on each shaft.
- 4 x MTU 12V2000M41A, producing a total of 2026ekW.

### 8.2 DPCalc Program

BMT have internally developed software (DPCalc, v.1.3) which predicts the station-keeping capability of a vessel, based on specific principle parameters, environmental conditions and thruster arrangements. Currently the program is capable of considering wind loads only, but development plans include the addition of current loading. It should be noted that DPCalc offers a static analysis of station-keeping capability. No consideration is given to wind gusts or yacht motions, which may negatively impact the station-keeping performance of the vessel.

The software uses inputs of the vessel such as lateral above-waterline projected area, frontal above-waterline area, and LOA alongside empirically derived values of drag coefficients (taken from literature) to predict the wind loading on the vessel.

The position, orientation and maximum thrust of the various propulsors on the vessel (bow & stern thrusters and main propellers) are then used in a quadratic solver to find the most efficient combination of thrust allocation (based on

minimising overall thrust magnitude) that will counter the external forces, reducing the overall force and moments acting on the vessel to zero. In an iterative process, the program cycles through each wind heading, incrementally increasing wind speed at each heading until the quadratic solver fails to find a solution, indicating that vessel can no longer hold station.

It is important to note that the results calculated by DPCalc are highly dependent on the wind drag coefficients used to calculate the longitudinal, transverse and yawing moments induced by wind. Ideally these coefficients will be collected via wind tunnel tests for each specific yacht – indeed for yachts with DP fitted, wind tunnel tests typically form a part of the model test schedule. However at a preliminary design stage, coefficients specific to the design being developed are not available and coefficients from basis vessels must be used.

For the basis vessel used here wind coefficient data is available, and so has been used for this specific yacht.

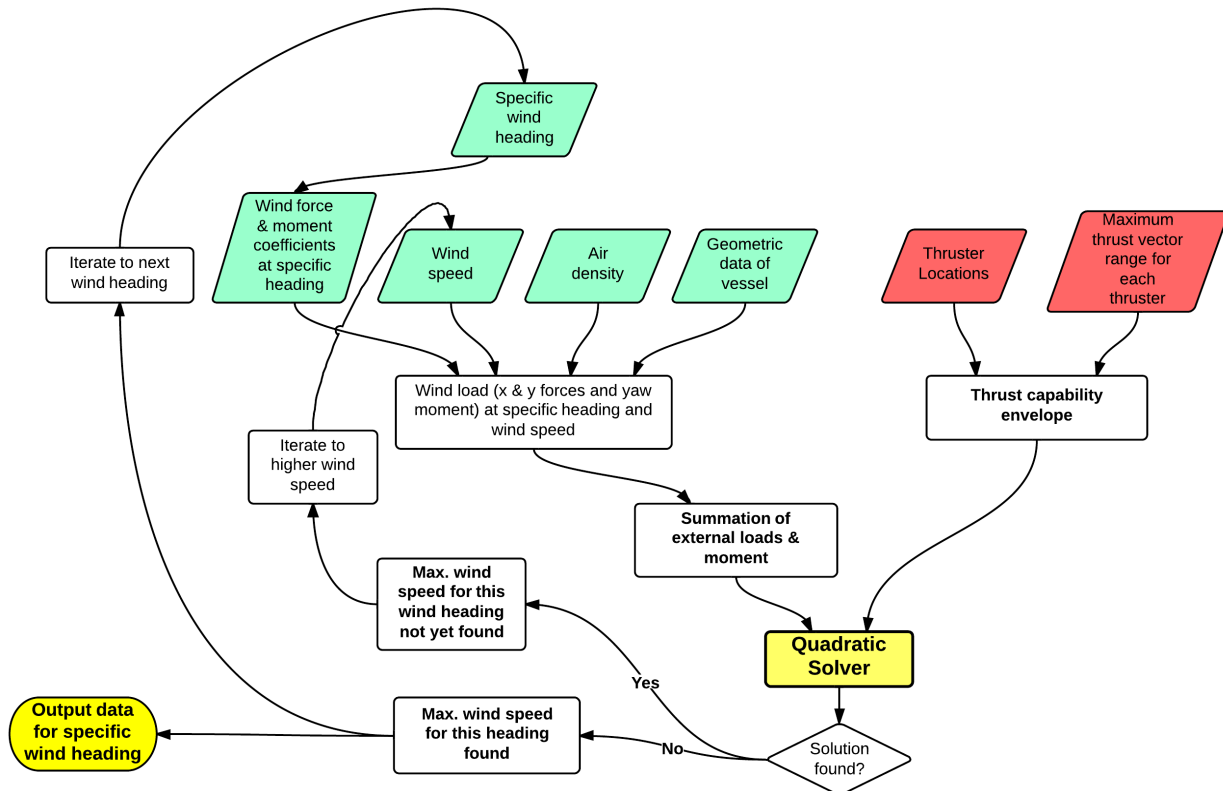


Figure 3 - Calculation method of DPCalc v1.3

### 8.3 Power Requirements

The basis vessel was configured in DPCalc as it is currently designed. The power to the thrusters was then increased at the same rate (such that the ratio of bow thruster power to stern thruster power remained constant). As previously discussed, the thrust developed by the main propellers remains constant.

DPCalc works by equating forces, however to be useable in design force (i.e. thrust) needs to be related to power. In the absence of specific manufacturers' data, thrust has been related to power according to IMCA M.140 guidelines (145N/kW for tunnel thrusters, 171N/kW for azimuthing thrusters and propellers, 120N/kW for propellers running in reverse).

In each case, the capability of the vessel with the thrusters at 10%, 50%, 150%, 200% and 300% of the original designed power has been found.

Figure 4 shows the polar capability plot of the vessel as the size of the thrusters are increased.

By plotting the lowest limiting wind speed at any angle against the power consumed by the thrusters (Figure 5), it can be shown that the relationship is non-linear, with the required power increasing at a greater rate than the limiting wind speed. This would be expected, as wind loading force increases proportionally to the square of the wind speed.

It can be seen however that the disparity between the lowest limiting wind speed (typically seen at 130° for this vessel) and the beam-wind limiting wind speed increases proportionally through the power range.

By using fixed electrical efficiencies to calculate the load on the generators of the thrusters, and a fixed hotel load of 1010ekW, the total required electrical load can be plotted.

It can be seen for the basis vessel that the installed thrusters and generators are predicted to provide a minimum limiting wind speed capacity of approximately 30.4 knots.

By increasing the rated power of the thruster units by 50%, and increasing the installed electrical generating capacity by the equivalent of an extra generator, this speed can be increased to around 35.8 knots. Similarly, by reducing the thruster sizes by 50% the capacity will drop by 6.6 knots, to 23.8 knots.

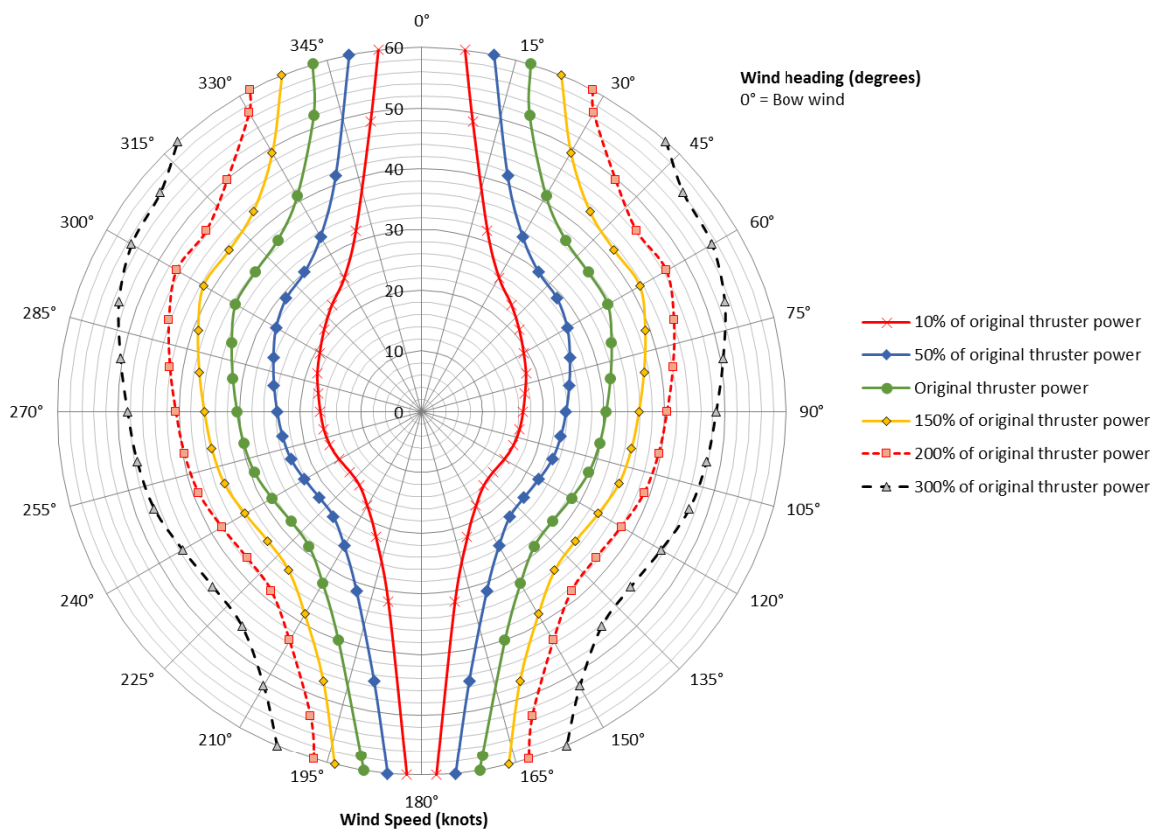


Figure 4 – Station-keeping capability polar plot at a range of bow and stern thruster powers

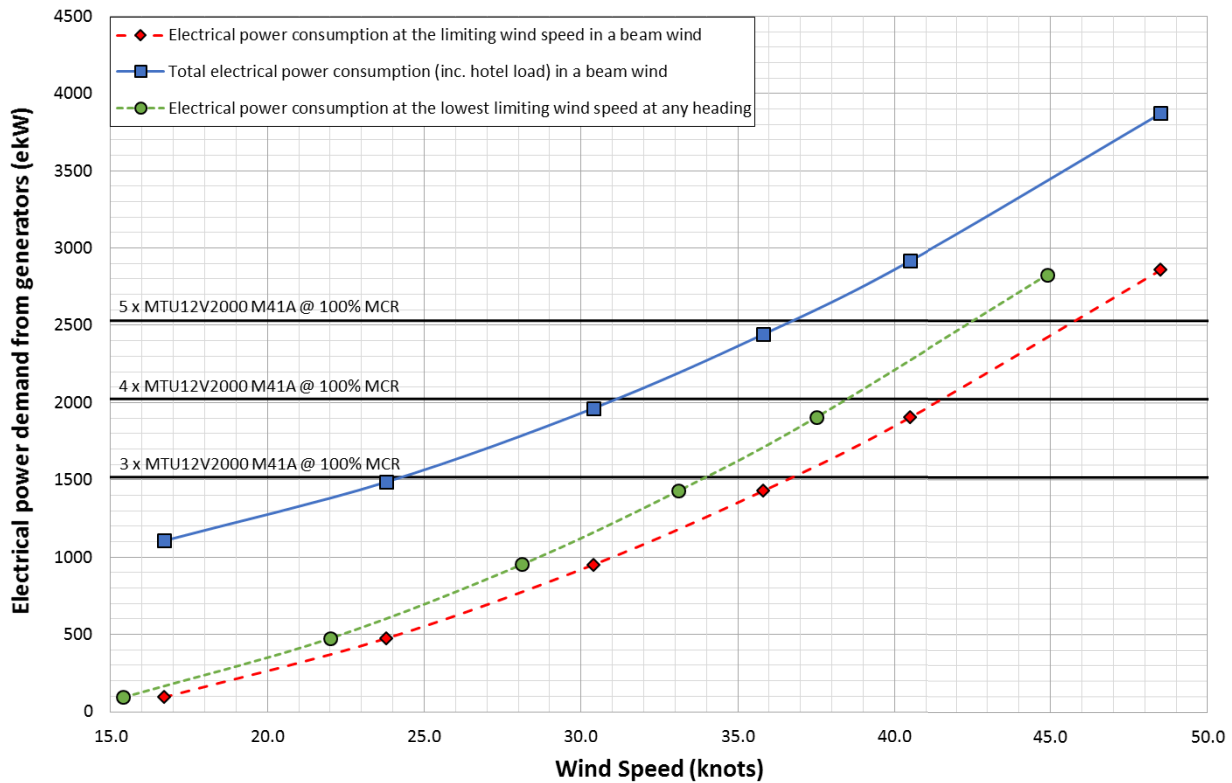


Figure 5 – Limiting wind speed plotted against electrical power consumed

### 8.4 Impact of Power Delivery

This vessel has electrically driven thrusters, and so the impact on the vessel of the DP capability chosen is both mechanical and spatial in nature.

Beam wind specified	Total thruster power required	Bow thruster power	Stern thruster power	Total required Electrical Installation	Total electrical installation capacity minus maximum hotel load	%age of genset installation that is only required for thrusters
<i>knots</i>	<i>bkW</i>	<i>bkW</i>	<i>bkW</i>	<i>ekW</i>	<i>ekW</i>	-
25	506	260	245	1565	365	23%
30	840	432	408	1932	732	38%
35	1236	636	600	2365	1165	49%
40	1690	870	820	2863	1663	58%
45	2208	1137	1072	3431	2231	65%

Table 1 – Power requirements of the vessel to hold station at various beam wind speeds

As the amount of electrical power installed is usually driven by the sizing of the thrusters, the DP capability specified has a significant impact on the number and size of generators installed.

The higher the DP specification, the more electrical machinery the vessel carries purely for DP operations. The maximum anticipated hotel load for this vessel is around 1200ekW. Whilst some level of redundancy in the system is required, (also allowing for hours swapping on the generators), it can be reasonably assumed that the majority of the remaining installed capacity is installed for thruster operations only.

Table 1 shows that for a specification which calls for station-keeping capability in a beam wind of 35 knots, nearly 50% of the installed electrical power is required solely to satisfy this specification criteria.

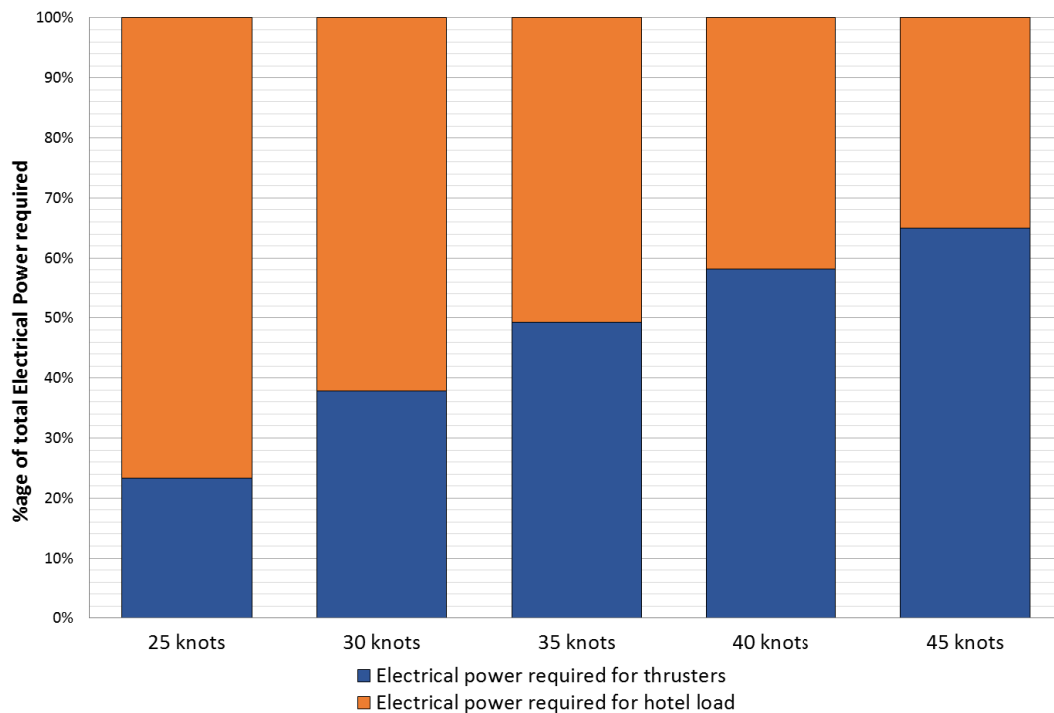


Figure 6 – Percentage of electrical power required for each application

The bow thruster motor on this vessel is mounted horizontally, with the electric motor running along the vessel’s centreline, aft of the thruster tunnel. The bow thruster room has been designed such that there is very little space between the electric motor and the watertight bulkhead – this is a common arrangement on a yacht where space, particularly on the tank deck, is at a premium.

Any increase in the size of the thruster tunnel or drive unit would therefore require a bulkhead rearrangement, increasing the length of the thruster room by one or more frames. Similarly, if the size of the bow thruster becomes prohibitive, it may be necessary to move to a pair of bow thrusters, requiring even more space. In this situation it may be beneficial to use rim-drive thrusters (a thruster where the motor is integrated into the tunnel, thereby reducing the space required in the bow thruster compartment).

In addition to the increase in size of the unit, if the thrusters are electrically driven (as they are in this vessel) the frequency converters will get larger. The bow and stern thruster frequency converters in this case are combined with the shore power converter (a common arrangement), located roughly amidships on the tank deck. It takes up a considerable amount of technical space, and weighs nearly 7 tonnes. As the size of the converter is approximately proportional to its’ rated power, if the thruster power was to double the size and weight of the converter could also be expected to double. This would in turn increase the size and weight of the circuit breakers in the main switchboard, and the cabling weights to the thrusters. Larger frequency converters require a larger cooling circuit, with more wild heat to dissipate.

It becomes clear that by simply increasing the power of the thrusters has many knock-on effects downstream, affecting multiple systems.

## 9. FURTHER WORK

A useful extension of this study would be to collate a list of typical yacht anchorages and ports around the world visited by large yachts, with typical durations of stay and visitation frequency.

By combining this with appropriately selected spatial and temporal resolutions of wind speed data in these locations, the operational envelope of manoeuvrability may be evaluated against the vessel’s capability, effectively giving an operability index for the vessel tailored to its’ realistic operating conditions.

There are many areas in which the authors envisage the DP analysis software being developed. Principally, a restructuring of the software to ease further development, modularising elements of the calculation, would be very beneficial. This will then allow individual components to be upgraded, for example, increasing the accuracy of the side force developed by a

rudder in a propellers slipstream by using actuator disc theory, or improving the estimation of wind loadings by employing more accurate correlation techniques to estimate the wind drag coefficients.

There are also a multitude of features that could be added, including the modelling of current and wave loading, and the ability to evaluate a vessel's ability to hold specific heading against loadings when anchored by the bow.

Naval architects and yacht designers are invariably not experienced seafarers and opportunities to spend any significant amount of time on the vessels that they design are sparse. Whilst attempts were made during the writing of this paper to engage the skippers of several large yachts, a very limited response was received. It is always important to obtain feedback from seafarers on how systems are used in practice; what works, what is useful, and importantly, what is not. By further engaging the seagoing community, areas of associated research and study are likely to become apparent.

## 10. CONCLUSIONS

The basic principles of Dynamic Positioning have been introduced, providing a brief insight into how station-keeping capability prediction software operates. Typical arrangements of thrusters within a yacht have been discussed, with the merits of this layout presented. It should be noted that whilst this is a 'standard' yacht layout, it should by no means be considered the only way to achieve manoeuvring capability.

Various methods of increasing DP capability are discussed, with the feasibility and impact on design of each evaluated. It is considered that the option with the least drastic effect on the vessel's design is to increase the power and thrust available to each thruster. If the power consumption to meet the specified criteria becomes large enough that the power installation required is unfeasible, then a move towards a podded propulsion system should be considered.

Yachts are rarely used in a true station-keeping mode of operation. Station-keeping specification criterion are therefore mainly used as a method of specifying an in-harbour manoeuvring capability for the vessel. Consequently, a beam-wind based criteria is considered suitable for use in this specification, despite the fact that a beam-wind is rarely the most onerous wind heading for station-keeping.

For the basis yacht studied, it is seen that to achieve any significant increase in DP capability requires a large increase in thruster sizing and consequently installed electrical power generating machinery. At a beam-wind station-keeping capability above 35 knots, over half of the electrical power installed is installed purely for DP operations.

The level of DP specification should clearly be a carefully considered parameter, with the practical value of a more capable system being evaluated against the various design compromises outlined in this paper.

## 11. REFERENCES

Holvik, J. (Kongsberg Simrad Inc), "Basics of Dynamic Positioning", *Dynamic Positioning Conference*, Houston, 1998

The International Marine Contractors Association, "Specification for DP Capability Plots", *IMCA M.140 Rev. 1*, June 2000

## 12. AUTHORS' BIOGRAPHIES

**James Calver** is a Naval Architect at BMT Nigel Gee Ltd. Having previously worked on the structural design of various commercial vessels, he is now involved in the naval architecture of yacht design projects, ranging from concept design to detail design.

**James Roy** is the Yacht Design Director at BMT Nigel Gee Ltd. He is responsible for development of the company's yacht design activities and managing conceptual, preliminary and detail design work as well as consultancy services.

The authors would like to thank Captain Bill Zinser and Captain AJ Anderson for their valuable contributions to the content of this paper.

# A QUANTATIVE STUDY ON RELATIVE MOTIONS DURING TENDER BOARDING

Ir. P.T. van Loon, Feadship, The Netherlands

## SUMMARY

Feadships are more often equipped with large beach lounges. While at anchor, owners and guests board and leave the yacht by tender at this beach lounge. Tender boarding is often already limited at a low swell. The ease of tender boarding is much dependant on the relative motions between tender and yacht. Especially the vertical relative motions hinder and impede a safe and comfortable transfer for the passengers. Studying the vertical relative motions can be used for evaluating tender boarding.

To research the relative motions the geometry and behavior of yachts are modeled and diffraction calculations are executed. Through these calculations the vertical relative motions of the tender are deduces. During this study, the surrounding conditions, the yacht's heading, and the boarding locations around the yacht are varied.

Studying the relative motions leads to an understanding of issues that occur during tender boarding. Through the execution of analysis, an optimal boarding location and yachts heading for tender boarding are deduced.

## 1. INTRODUCTION

Feadships are more often equipped with large beach lounges. These lounge areas with large open platforms close to the waterline form the ideal location for tender boarding. While at anchor, owners and guests board and leave the yacht by tender at this beach lounge. An example of tender boarding via a beach club is illustrated by figure 1.

However, while passengers transfer between tender and yacht at sea, both tender and yacht are moving due to excitation forces. These excitation forces are caused by the surroundings, i.e. wind, waves and current. In practice, tender boarding is often already limited at low swell. This leads for instance to cases in which the surroundings can be seemingly calm but still tender boarding is unable. The ease of tender boarding is much dependent on the relative motions between tender and yacht. According to crew, horizontal relative motions can be controlled by crew by applying fenders and mooring lines, where vertical relative motions cannot that simply be controlled. In practice, especially the vertical relative motions hinder and impede a safe and comfortable transfer for the passengers. Practical cases occur in which the tender vertically moves over one meter, while no alternative means of boarding the yacht are available. As part of a larger study into the design of beach lounges and tender garages at Feadship, these relative vertical motions which trouble tender boarding have been studied. By quantifying the relative vertical motions, data could be attained which can be used to benefit tender boarding and the operational profile of the yacht overall.



Figure 1: Tender boarding from a platform

## 2. AIM AND SETUP STUDY

The sub-study into relative vertical motions aims to evaluate the performances of the design concepts from the overall design study. These designs have a number of functionalities, of which one is to facilitate a transfer between tender and yacht. In order to evaluate the concepts' performances in meeting their required functionalities, the parameters influencing the performances and the comparison are to be known. From the overall design study, the sub-study into relative vertical motions and their influence on tender boarding will be discussed in this paper.

To study the relative vertical motions, the following framework is to be set up; first the dimension of the studied yacht and tender are determined. Secondly, the relevant surrounding conditions, in which tender boarding takes place, are considered. Thirdly, the yacht's orientation to these conditions, i.e. the yacht's heading, is considered. Lastly, relevant locations around the yacht where relative vertical motions are studied are determined. When these background questions are answered, the relevant cases for which the vertical relative motions are to be mapped are known. To later on evaluate the attained results, directives to tender boarding are considered on beforehand as well.

Next step is to determine the relative motions. Both the yacht and tender and their motions are to be modelled. Their motions combined lead to the relative motions. To correctly model the yacht and its motions, the tender motions and the surroundings (and their influence on each other), software to perform diffraction calculations at the Delft University of Technology is used.

By combining the input from the relevant cases and the results obtained by use of the diffraction program, the relative motions are computed. When the relative motions are determined for relevant cases, they can be evaluated and compared. From this data conclusions are drawn which specifically aim to evaluate and benefit tender boarding.

Following up the study mentioned above, the relative vertical motions have been studied during a recent series of model tests at Marin. The results attained during this second study will be used to verify the drawn conclusions from the original study.

### 3. STATING RELEVANT CASES

Several steps are taken in order to attain all input before the relative motions could be determined. These steps focus on setting up the framework for determining relative motions, which yields the input for the later calculations.

#### 3.1 Choice of a benchmark yacht and tender

In the overall design study a benchmark yacht and tender are chosen for setting up design concepts. The choice for this yacht and tender is dependent on their dimensions. A benchmark yacht of minimum dimensions for applicability of design concepts is chosen. This same yacht has been chosen as benchmark yacht for the study into relative vertical motions. The yacht's main dimensions are listed in table 1.

Loa	62.00 m	7.50 m
Boa	11.10 m	2.50 m
Draft	3.25 m	0.60 m
Freeboard	2.30 m	0.60 m

Table 1: Dimensions benchmark yacht and tender

The dimensions of the benchmark tender follow from the choice for the benchmark yacht. Tender dimensions are chosen for a tender which yachts of about 60 meters are equipped. An analysis of dimensions of the 60 last built Feadships and their tenders results in the dimensions of the benchmark tender as listed in table 1.

The conclusions which result from this study will also be checked to hold true for a larger yacht. The performed calculations for the benchmark yacht will also be performed for a larger yacht, which is a scaled up model of the benchmark yacht.

#### 3.2 Environmental conditions

The yacht is anchored at sea when tender boarding takes places. The most common locations for yachts to anchor are their most common sailing areas, generally the West Mediterranean Sea and the Caribbean Seas. An analysis of these areas will show which wave conditions (combinations of zero crossing periods and significant wave heights) are most common and thus relevant conditions to consider in this research. The scatter diagrams<sup>[1]</sup> showing which wave conditions occur and are most common in the West Mediterranean and Caribbean Seas are depicted in figure 2.

In practice, wind and wave conditions set limitations to the use of the tender and to the beach lounge. Generally when conditions are far too rough or unpleasant the tender and beach lounge will not be used. For instance, in seas with a significant wave height of 3 meters or higher the tender is no longer used. A similar criterion holds for wind (5 Bft. or higher). For this reason, as indicated with the fat lines and dots in figure 2, only wave conditions below these criteria are of interest. Per area the wave conditions with the highest occurrence are of most importance.

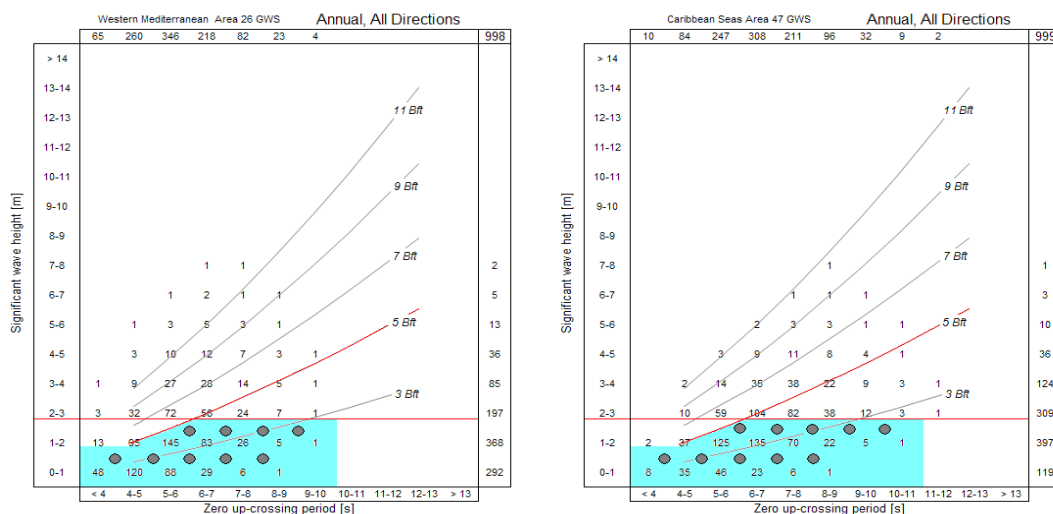


Figure 2: Selection of relevant conditions from wave scatter plots



With the wave periods known, a simplification can be made to the motions of the tender; the length of the tender is small relative to the occurring wave lengths, this means that the tender is expected to follow the wave profile and doesn't pitch or roll much. The following relation (which is derived from the 'Dispersion Relationship for deep water' [2]) is used;

$$\lambda = 1.56 \cdot T_0^2 \quad (1)$$

With the shortest zero crossing period being 4 seconds, the shortest wave length is about 25 meters. This is 3.3 times the length of the tender. The vertical motions of the tender can thus sufficiently accurate be modelled by the vertical motions of the water surface, i.e. the wave elevation.

For the calculations wave spectra will be used to model irregular seas. Yachts anchor locations are not in open seas but in coastal waters. The JONSWAP Wave Spectrum is a spectral formulation for fetch-limited (or coastal) wind generated seas. For this reason JONSWAP Wave Spectra will be used to model the wave conditions.

Besides waves, also wind and current influence the motions of tender and yacht. However, these aren't expected to influence the vertical relative motions and are therefore not further considered in this study. The influence of incidental waves, for example from passing vessels, is also not considered in this study. For tender boarding these incidental waves aren't expected to play an important role, since these waves are easily detectable by crew members and in practice crew assists guests while boarding by alerting them which moment is suitable to board and which isn't. Hereby, a possibly negative impact of incidental waves on relative motions can simply be averted.

### 3.3 Yacht's heading

When the yacht is anchored, at zero speed, the surroundings determine the heading of the yacht to the direction of the incoming waves. The yacht's heading (relative to incoming waves) is of interest since it influences the height of relative waves next to the yacht. Wind, waves and current don't necessarily come from the same direction. For instance, currents tend to follow coastlines when a current nears them. Waves and wind however, can come from another direction as such currents. Generally the yacht weathervanes around its anchor between head waves (-180 degrees) and beam seas (-90 degrees).

Which heading occurs the most is not of interest since the heading can (and in practice will be) influenced by the yachts propulsion system. This way the heading which is most favourable for tender boarding can be kept for a while. In practice crew uses the propulsion system to create some leeway on the side of the yacht since they experience this to make tender boarding easier. The effect of leeway on the relative motions will be investigated. For this reason a heading of -150 degrees will be investigated. Generally the yacht shows the most roll response at a heading of -120 degrees. This heading is also investigated.

To make this study executable a number of headings will be chosen between head waves and beam seas which will be investigated. These headings are head seas (-180 degrees), -150 degrees, -120 degrees and beam seas (-90 degrees).

### 3.4 Measuring locations

The relative wave elevation will be determined at a set number of locations around the yacht. In the overall design study, for the considered designs not only tender boarding, but several functionalities were considered, which led to a total of thirteen set locations around the yacht for determining relative wave elevations, which are depicted by figure 3. Not all of those

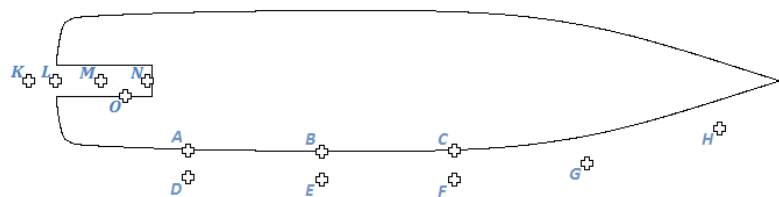


Figure 3: Modelled locations around the hull

locations are of interest when tender boarding is considered on its own. For instance locations G and H were considered since the functionality of tender launching was also considered, which for certain yachts occurs at these locations. For tender boarding, the locations representing actual location where the tender will lie during tender boarding are relevant. The relevant locations from figure 3 are locations D, E, F, K and M. Locations D, E and F represent tender locations next to a side platform, location K represents a tender location next to an aft platform and location M represents a tender location in a stern dock.

### 3.5 Setting a directive

So far, the framework of relevant cases has been set up by determining relevant yacht and tender dimensions, surrounding conditions, yacht's heading and locations for modelling relative wave elevations. In the introduction of the paper it was stated that crew in practice can sufficiently control the tender's horizontal relative motions, and from analysing the relevant wave

lengths and the length of the tender it is stated that pitch and roll of the tender are not relevant either. This leads to only the heave motion of the tender being of interest. To practically evaluate later on obtained vertical relative tender motions it is desired to set a directive to whether these motions are acceptable or not. This directive is as follows; for the amplitude of the vertical relative tender motions, an acceptable distance of over one staircase step is allowable. A maximum staircase step is 200 mm. However when boarding a tender, a passenger is assisted by supports and crew, which makes for a larger step being acceptable. In this case, it is considered that a maximum step of 250 mm up or down can be expected to be safely made.

#### 4. DIFFRACTION CALCULATIONS

With the setup of the study considered, the necessary modelling and calculations can be performed to determine relative motions. By use of diffraction calculations performed with software Ansys AQWA the RMS-values of the vertical relative motions of the water surface will be determined. Figure 4 illustrates the different steps in the performed calculations.

The geometry and orientation of the benchmark yacht are modelled in AQWA Workbench and the yacht's behaviour in seaway can be modelled. An anchored yacht shows three relevant degrees of freedom in its motions; heave, pitch and roll. Especially the roll-response of the yacht needs attention in this modelling phase, due to the addition to the roll damping by zero-speed fin stabilizers.

In AQWA GS RAO's for the relative wave heights are determined at the relevant locations around the yacht's waterline. When all RAO's are collected, this data is combined with the wave data to compute the spectra of the relative vertical wave heights. From these spectra the RMS-values are determined, which are used to determine the significant wave height.

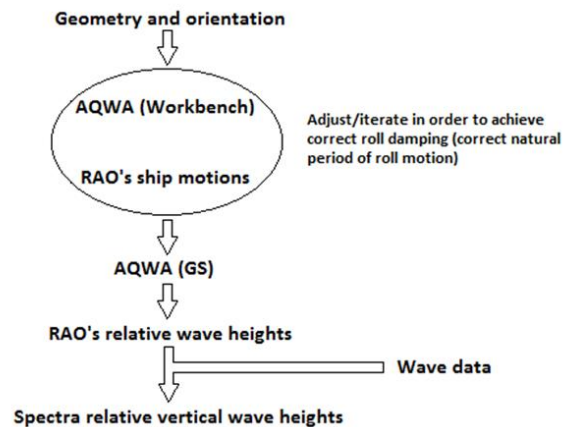


Figure 4: Steps taken in diffraction calculations

#### 4.1 Modelling

The benchmark yacht is modelled with its hydrostatical properties, which are checked to reports from earlier performed model tests of the benchmark yacht. To correctly model the roll damping a check is performed to earlier performed model tests as well.

The separate additions to the total roll damping could not be modelled in the software. Ansys AQWA doesn't take viscous or Eddy damping into account. The passive stabilizers, and thus their addition to the roll damping, couldn't be modelled either. The final and most important addition, of the zero speed fin stabilizers, which give the roll damping a strong non-linear character (as depicted in figure 5), couldn't be modelled either. The total roll damping is modelled in the software by inputting a single value to represent the total equivalent linear damping. The non-linear character of the roll damping and the limited possibilities to correctly model this damping limits the cases which could be investigated; the planned complete operational analysis (all combinations of heading, surrounding conditions and measuring locations) could not be performed. The cases which could be investigated follow from the Marin report of the earlier performed model tests, by which the single value for the equivalent linear damping could be determined. The iteration process in figure 4 stands for the process to adjust the roll damping until the roll RAO of the model corresponded to the roll RAO of the model tested at Marin.

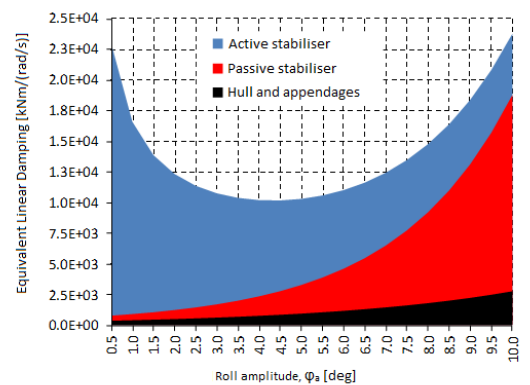


Figure 5: Characteristic of total roll damping

The wave spectra in the Marin tests in combination with the heading of the tests (-90 degrees) are cases for which the relative wave elevations can be modelled. Furthermore, all cases when the yacht's heading is in head seas (-180 degrees) are modelled as well, since the yacht does not roll at this heading. The headings -150 and -120 degrees are also of interest. These orientations could not be investigated if the roll damping is not correctly modelled. These orientations will be investigated, based on the following assumptions; the RAO's of the models roll motion are investigated for all four relevant headings, which is depicted in figure 6. It shows that for heading -150 degrees less roll response occurs than for heading -90 degrees at the same wave

frequencies. Less roll response equals lower roll amplitude. Since the stabilizer fins deliver the same amount of work at lower roll amplitude (fin forces are independent of the roll response), in reality more equivalent linear damping is provided by the fins in heading -150 degrees than for -90 degrees (this can be seen in the characteristic of the roll damping illustrated in figure 5). However, in the model in AQWA the same amount of roll damping will be modelled for -150 degrees as for -90 degrees. Too few damping is thus modelled for -150 degrees in AQWA. The roll motion for -150 degrees is thus insufficiently damped, which results in too much roll response. The roll can be said to be damped 'too conservative' for -150 degrees. It is expected that the too high roll response results in higher relative motions. This 'conservative' modelling makes that the results for relative motions are too large for heading -150 degrees. On its turn, this makes that the results of calculations will be 'on the safe side'; heading -150 degrees is modelled with the same amount of damping as for -90 degrees. Comparing the RAO's of the models roll motion shows for heading -120 degrees more roll response than for heading -90 degrees at the same wave frequencies. Clearly, not all wave conditions can be investigated for heading -120 degrees. Only the same wave conditions as for -90 degrees will be investigated for heading -120 degrees, since these are conditions which lie around the peak of the roll spectrum and the peaks of the roll RAO's of -90 and -120 degrees lie fairly close to each other, but it is to be kept in mind that the roll is too much damped and the 'real' results are expected to be higher.

Overall, the complete operational analysis is not performed during this study, as it would only add value to the study if it could be performed correctly. The following analysis is performed; the conditions of the Marin tests for headings -90 and -120 degrees and all wave conditions for headings -150 and -180 degrees are modelled.

## 4.2 Data acquisition

When all modelling is performed, the RAO's for the three relevant ship motions of the yacht are calculated for the wave frequency range of 0 to 2 rad/s. These RAO's are added to the model, which is inputted inputted from Ansys Workbench into Ansys AQWA GS. This part of the software is used to calculate the RAO's of the relative wave elevations at the relevant locations.

Besides the incoming wave, also the diffracted and radiated wave from the yacht and the RAO motion of the yacht are taken into account. Figure 7 shows the separate components for a wave with a period of 1 rad/s and the yacht on heading -150 degrees. The top image shows the incident wave, which amplitude is everywhere around the yacht the same. The second image depicts the diffracted wave, which shows the wave coming from the top right in the figure and building up along the portside and reflecting of the yachts stern. The third image shows the radiated waves propagating in longitudinal and sideways direction from the bow and stern (combined pitch and roll motion). The bottom image depicts the RAO motion. It takes the heave, pitch and roll motions of the yacht into account. A plane is drawn at two meters above and parallel to the still waterline. When the yacht starts to heave, pitch and roll this plane stays fixed in its pivoting point. The wave heights are then denoted relative to this plane, and thus relative to the yacht.

When all four images are combined, at any given location the RAO-value of the relative vertical wave height is given for the selected combination of wave frequency and heading. The frequencies and heading are chosen and the relative

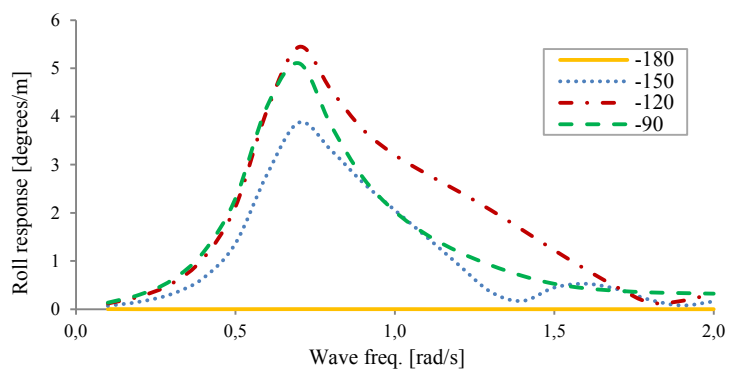


Figure 6: RAO's of the model's roll motion per heading

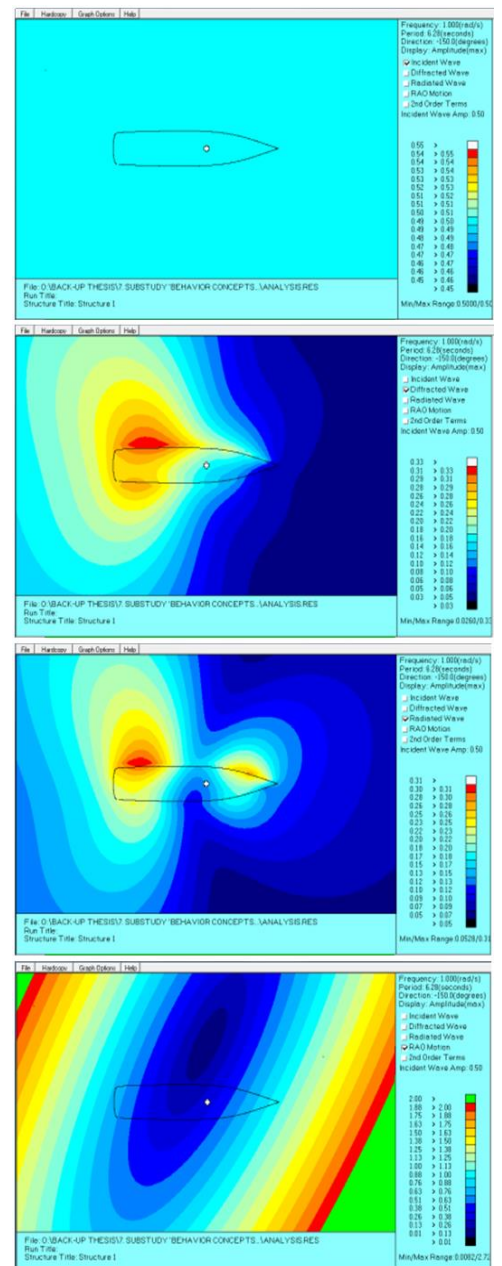


Figure 7: Components in relative wave height

wave elevation is determined. The output is a single value. This value is the relative wave amplitude. The incident wave is set to have a wave amplitude of 1 meter to obtain the preferred RAO-value (in meter relative wave height per meter incident wave height).

Ansys AQWA shows results one by one per frequency (from 0.1 to 2.0 rad/s in steps of 0.1 rad/s) for regular waves. These values are combined to complete a single RAO. In total 5 locations are considered with per location 4 headings and 20 frequencies. These 400 single RAO-values are combined into 20 RAO's.

### 4.3 Data processing

With the RAO's of the relative wave heights known, the following calculations are made: the motion spectrum of the relative wave heights is determined by combining a wave spectrum with the RAO of the relative wave. As illustrated in figure 8, the wave spectrum (input spectrum) is multiplied with the square of the RAO (response function<sup>2</sup>). This results in the motion spectrum of the relative vertical motion (output spectrum). This spectrum is set up per location, per heading, per wave condition.

The area under the spectrum is denoted as  $m_0$ . The square root of  $m_0$  is the Root Mean Square (RMS) or standard deviation ( $\sigma$ ). This value can be used to determine the significant wave height of the relative waves. The standard deviation is the statistical average used to rate the wave heights. The relationship of the RMS to a normal (or Gaussian) distributed signal is illustrated in figure 9. The wave elevation and as a consequence the wave frequent ship motions follow typically such a Gaussian distribution. However roll motions with active roll stabilisation may not exactly follow a Gaussian distribution. The rather nonlinear and impulsive character of the dampening forces as excited by the 'kick' of the stabilisers are the cause of this different behaviour. In this case, the validity of this Gaussian distribution is considered to hold up.

The significant wave height,  $H_{1/3}$ , of the relative wave are calculated by the following formulas<sup>[3]</sup>,

$$RMS = \sqrt{m_0} = \sigma \quad (2)$$

$$H_{1/3} = 4 \cdot \sigma \quad (3)$$

The tender moves both up and down, thus the wave height is to be used. The directive that is set dictates that the step onto or from the tender is not to be higher than 250 mm thus the tender can move either 250 mm up or 250 mm down. The relative wave height, expressing the vertical motion of the tender, is not to exceed 500 mm. As it shows in figure 9,  $4 \cdot m_0$  (from  $-2 \cdot m_0$  to  $+2 \cdot m_0$ ) holds 95.4 % of all samples. This means that if the significant wave height doesn't exceed 500 mm, then it is known for a fact that 95.4 % of all occurring waves don't have a height over 500 mm. Statements involving the significant wave height thus have a 95.4 % certainty of holding up.

Performing all calculations results in a large number of RMS-values, which are to be used to calculate significant wave amplitudes, check directives to hold up, and to be drawn conclusions from.

## 5. CONCLUDING FROM THE DATA

With all data gathered, the vertical relative motions around the yacht are compared. At first, an optimal location for tender boarding is considered. Next, the set directive is evaluated. These evaluations are then checked to hold up for the scaled up model. Finally, the results from the recent series of model tests at Marin, as mentioned in the setup of this study, are consulted to verify the drawn conclusions from the original study.

### 5.1 Optimal location for tender boarding

The suitable locations for tender boarding, which were earlier stated as measuring locations for the relative wave heights, can be compared to draw qualitatively conclusions concerning tender boarding in relation to vertical relative motions. To do so, the

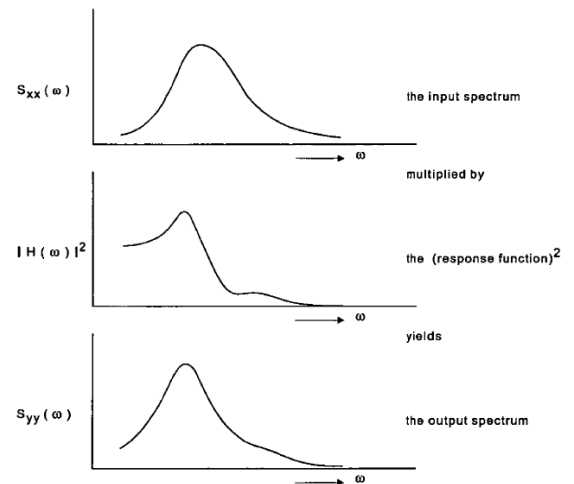


Figure 8: Spectra and RAO calculation

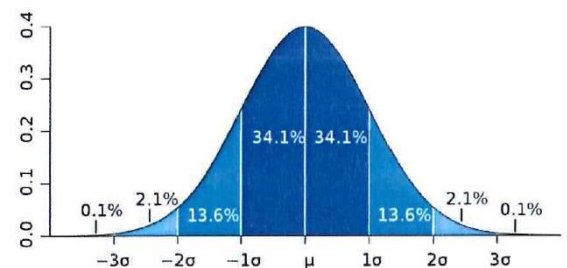


Figure 9: Relationship RMS to Gaussian signal

RMS values of the relative vertical motions spectrum are compared. Table 2 lists these RMS values for the relevant locations in the relevant conditions. Overall the following can be stated, the lower the RMS value, the more favourable a location is for tender boarding. When comparing the locations, the location with the lowest RMS values is favoured.

From the data in table 2, it can be seen that from the locations on the side of the yacht, locations D,E and F, the location closest to the stern of the yacht, location D, is in most combinations of heading and surrounding conditions favourable. Furthermore, the stern platform, which is according to crew on board most yachts currently used for tender boarding and illustrated by location K, is in most cases less favourable than location D. From all locations which lie around the yacht, Location D is expected to be the most favourable location for tender embarkation because the RMS of the relative vertical wave height is the smallest.

Location M represents a location in a bottomless stern dock, which was a concept in the overall design study. It can be seen that this location is favourable over all other locations for all heading other than 180 degrees. At 180 degrees, location D remains favourable.

### 5.2 Evaluating the directive

As described in chapter 3, the following directive has been set to the relative motions of the tender during tender boarding; the significant wave height of the relative vertical motions is not to be higher than 500 mm. This directive can be checked for all modelled combinations of location, surrounding conditions and heading, to draw quantitative conclusions concerning tender boarding in relation to vertical relative motions. Table 3 shows the significant wave height for the relevant locations and surrounding conditions.

From table 3 it can be seen that the directive is not met (cell highlighted) for a most combinations of location and surrounding conditions. This confirms the problems which are experienced during tender boarding, which was to be expected as this underlies the aim of the overall design study. The headings cannot be compared to each other with certainty from these results, since the roll damping couldn't be sufficiently modelled. It is however clear that for location D in head seas the directive is always met.

### 5.3 Scaled up model

As earlier mentioned, the same modelling and calculations have been performed with a scaled up version of the model (to be approximately 90 meters in length) to evaluate if the results are valid for larger yachts as well.

Just as for the original model location D is the best location on the yacht's side for tender boarding. Just as for the original model, the roll damping of the scaled up model was problematic to model. For this reason, the results for headings 150, 120 and 90 for the scaled up model are overestimated.

The directive is just as for the original model in most cases not met. However, just as for the original model, it seems that location D in head seas is the preferred location for tender boarding, as the directive is there met in most surrounding conditions.

### 5.4 Validating results with Marin test results

As earlier mentioned, similar modelling and calculations as in this study have been performed more recent model testing at Marin. In this test program, vertical relative wave heights have been modelled and measured around a

Heading [deg.]	Hs [m]	T0 [s]	RMS relative wave height				
			D [m]	E [m]	F [m]	K [m]	M [m]
180	1,0	4,0	0,12	0,19	0,21	0,22	0,11
	1,0	5,0	0,08	0,15	0,16	0,30	0,14
	1,0	6,0	0,06	0,12	0,12	0,26	0,12
	1,0	7,0	0,05	0,09	0,10	0,22	0,10
	1,0	8,0	0,04	0,07	0,08	0,18	0,08
	2,0	6,0	0,13	0,23	0,25	0,52	0,25
	2,0	7,0	0,10	0,18	0,19	0,43	0,20
	2,0	8,0	0,07	0,15	0,15	0,35	0,17
	2,0	9,0	0,06	0,12	0,13	0,29	0,14
	2,0	10,0	0,05	0,10	0,10	0,24	0,12

150	1,0	4,0	0,12	0,10	0,16	0,27	0,12
	1,0	5,0	0,15	0,13	0,15	0,28	0,13
	1,0	6,0	0,16	0,16	0,16	0,24	0,11
	1,0	7,0	0,16	0,17	0,18	0,19	0,09
	1,0	8,0	0,13	0,15	0,15	0,16	0,07
	2,0	6,0	0,32	0,31	0,32	0,48	0,21
	2,0	7,0	0,32	0,35	0,36	0,38	0,17
	2,0	8,0	0,25	0,29	0,31	0,31	0,14
	2,0	9,0	0,20	0,24	0,25	0,25	0,12
	2,0	10,0	0,17	0,20	0,21	0,21	0,10

120	0,9	7,1	0,19	0,20	0,21	0,10	0,05
	1,8	7,1	0,41	0,44	0,46	0,20	0,09

90	0,9	7,1	0,17	0,17	0,18	0,02	0,05
	1,8	7,1	0,21	0,21	0,21	0,02	0,05

Table 2: RMS values vertical relative motions

Heading [deg.]	Hs [m]	T0 [s]	Significant relative wave height				
			D [m]	E [m]	F [m]	K [m]	M [m]
180	1,0	4,0	0,49	0,74	0,85	0,89	0,43
	1,0	5,0	0,34	0,59	0,65	1,19	0,54
	1,0	6,0	0,25	0,47	0,50	1,05	0,49
	1,0	7,0	0,19	0,37	0,39	0,86	0,41
	1,0	8,0	0,15	0,29	0,31	0,70	0,33
	2,0	6,0	0,50	0,93	1,00	2,10	0,98
	2,0	7,0	0,38	0,73	0,78	1,72	0,82
	2,0	8,0	0,30	0,58	0,62	1,41	0,66
	2,0	9,0	0,24	0,48	0,50	1,16	0,55
	2,0	10,0	0,20	0,40	0,41	0,98	0,47

150	1,0	4,0	0,47	0,42	0,66	1,08	0,49
	1,0	5,0	0,58	0,53	0,59	1,14	0,50
	1,0	6,0	0,63	0,63	0,65	0,95	0,43
	1,0	7,0	0,63	0,69	0,72	0,77	0,35
	1,0	8,0	0,51	0,58	0,61	0,62	0,28
	2,0	6,0	1,26	1,26	1,30	1,91	0,86
	2,0	7,0	1,27	1,39	1,44	1,53	0,70
	2,0	8,0	1,02	1,17	1,23	1,24	0,57
	2,0	9,0	0,82	0,94	0,99	1,02	0,46
	2,0	10,0	0,69	0,80	0,84	0,86	0,40

120	0,9	7,1	0,75	0,80	0,85	0,40	0,19
	1,8	7,1	1,62	1,75	1,85	0,78	0,38

90	0,9	7,1	0,69	0,69	0,70	0,07	0,20
	1,8	7,1	0,83	0,84	0,84	0,08	0,22

Table 3: Significant wave heights around model

yacht of approximately 90 meters in length. The vertical relative wave heights were both measured during model tests and they were modelled in a diffraction program in which the roll damping was correctly modelled, after it had been determined by model testing. This enabled not only to validate the conclusions drawn from the earlier performed study in Ansys AQWA, but also to perform the complete operational analysis (for all relevant wave conditions and headings). The findings from this verification are listed below;

- When vertical relative motions are concerned, a location on the side of the yacht close to the yacht's stern is the optimal location for tender boarding.
- The set directive for the significant wave height is also in the Marin testing often not met. It is most of the times met at the location on the yacht's side close to the stern in a heading of -180 or -150 degrees. Also is it always met at a location aft of the yacht in a heading of -90 degrees.

A new conclusion that can be drawn from the Marin test results follows from the comparison of the headings. With the roll damping correctly modelled, the headings can be compared to each other as well (which was unable in the original study). Whereas crew experienced a bit of leeway being beneficial to tender boarding, the results from the Marin tests however show that creating leeway is not always beneficial. Only in surrounding conditions with relatively short waves (zero crossing period of 4 or 5 seconds, which do not most often occur according to the scatter plots in figure 2) the vertical relative wave heights at 150 degrees are (only slightly) lower than for 180 degrees. For most conditions, a heading of 180 degrees is preferred over 150 degrees.

## 6. CONCLUDING FROM THE STUDY

Practice shows that boarding a tender at sea from a yacht is troubled by relative motions. This study aimed to evaluate these relative motions and their influence on tender boarding. From a series of software modelling and model tests a number of conclusions from the viewpoint of relative motions are drawn concerning tender boarding at sea.

First of all this study clearly shows that in the multiple cases, while the surrounding conditions are perceived as seemingly calm by the owner, guests and crew on board of the yacht, tender boarding can very much be troubled by the relative vertical motions. In many cases the tender moves relative to the yacht over a height which is larger than can comfortably be overcome by owner and guests.

The optimal location for tender boarding at sea is, contradictory to a currently mostly used platform at the stern of the yacht, a platform on the side of the yacht close to the yacht's stern. The platform on the yacht's stern would be a suitable location for tender boarding, if the yacht is kept at a heading in beam seas. In practice crew uses the yacht's propulsion installation to create some leeway on the yacht side, but it is unpractical to position the yacht in beam seas solely for the purpose of tender boarding, especially if tender boarding can also take place comfortably on the earlier optimal location with (or even without) far simpler heading control.

During this study, when considering the tenders relative motions, no evidence was found that supports the crew's opinion that creating some leeway on the yacht's side is beneficiary to tender boarding. In fact, all software modelling and model tests show that a heading of -180 degrees (head seas) is preferred over a heading of -150 degrees (with some leeway). The fact that crew however do prefer leeway over head seas could be explained by a possibly higher probability of water overrunning a side platform or water coming into the beach club in head seas. Or by the fact that slamming of waves under a platform has a higher occurrence at one heading over the other. Or it could be explained by not the height of the relative motion but by the speed and/or acceleration of the relative motions. Finally, the simple fact that leeway might feel more comfortable as no wind might be felt could lead to the crew's opinion. These possible explanations are currently being studied in the continuation of the study into relative motions during tender boarding at headship.

## REFERENCES

- [1] "Global Wave Statistics, area 26 West Mediterranean" and "Global Wave Statistics, area 47 Caribbean Seas"
- [2] Journée, J.M.J and Massie, W.W., Lecture Notes "Ofshore hydromechanics" (2001)
- [3] Ir. R.P. Dallinga, Article "*Seakeeping of Motor Yachts*" (2002)

# PARAMETERS AFFECTING THE PERFORMANCE OF THE C-CLASS WINGSAIL

**M. Magherini**, Ship Science, University of Southampton, UK

**S. R. Turnock**, Ship Science, University of Southampton, UK

**I. M. Campbell**, Wolfson Unit Marine Technology and Industrial Aerodynamics, University of Southampton. UK

## SUMMARY

Wing sails offer a different design challenge to those of more conventional soft sail rigs. This study was undertaken in order to assess which parameters influence wingsail performance of C-Class catamarans, and to what extent, the results from the wind tunnel can be applied in the design developments of future wingsails. A combined wing sail and C- Class catamaran was tested in the low-speed section of the 7' x 5' wind tunnel at the University of Southampton. Testing assessed the appropriate settings for the movable element of the multiple-element wing sail as well as heeling angle, trampoline porosity, spanwise camber distribution and gap at the foot of the wingsail. Both upwind and downwind conditions were considered through measurement of driving force, heeling force, heeling and yawl moments. The results demonstrate that low heel angles improve overall performance and that the gap underneath the wingsail foot adversely affects the generation of lift by the sail. An airfoil shaped trampoline is suggested in order to benefit both a reduced gap and a better control over the heel. For heavy wind condition, negative twist at the tip of the wingsail allows higher boat speeds.

## NOMENCLATURE

$\alpha$	Angle of attack of wingsail [deg]
AC	America's Cup
AoA	Angle of Attack
AR	Aspect Ratio
$\beta_A$	Apparent wind angle [deg]
$\beta_T$	True wind angle [deg]
$\nu$	Kinematic viscosity of air [m <sup>2</sup> /s]
$\phi$	Heel angle [deg]
CB	Centre of buoyancy
$C_D$	Drag coefficient [-]
$C_{DI}$	Induced drag coefficient [-]
CEh	Centre of effort height [m]
CE	Centre of effort
CFD	Computational Fluid Dynamics
CG	Centre of gravity
$C_L$	Lift coefficient [-]
CLR	Centre of lateral resistance
$D_F$	Driving force [N]
DWL	Design water line
G	Acceleration due to gravity [9,81 m/s <sup>2</sup> ]
$H_F$	Heeling force [N]
$H_M$	Heeling moment [Nm]
L	Length [m]
$L_{WL}$	Length water line [m]
L/B	Length to breadth ratio [-]
L/D	Lift to drag ratio [-]
q	Dynamic pressure [Pa]
Re	Reynolds number [-]
$R_H$	Total hull resistance [N]
$R_M$	Righting moment [Nm]
TWA	True Wind Angle
TWS	True Wind Speed
$V_A$	Apparent wind speed [knots]

$V_S$	Boat speed [knots]
$V_T$	True wind speed [knots]
VMG	Velocity Made Good
VPP	Velocity Prediction Programme
$Y_M$	Yaw moment [Nm]

## 1. INTRODUCTION

The C-Class catamarans are a sailing class competing in the Little America's Cup (LAC), an international match racing event with the winner of the eliminations series competing in the final race with the defender of the cup. From a research perspective the most interesting element characterizing a C-Class catamaran is their sail propulsion system: a symmetrical rigid wingsail that allows the catamarans to reach velocities 50% higher than the true wind velocity in upwind sailing, and more than double downwind.

The interest in the class, after several years of relative obscurity, has rapidly grown again in recent times due to the new format of the America's Cup: the trophy was competed for in the AC72, 22m long catamarans powered by 40m high wingsails. In order to allow teams to develop experience of wingsails, the AC45 (L=13,45m) has been designed as an essential step toward the AC72.

It is worth noting that there is revived interest in wind assisted ship propulsion [1] [2]. Alternative types of sail assistance devices were compared and it was concluded that kites were particularly attractive. However, the operational issues associated with their safe operation may favour fixed structures which with suitable control for optimum drive force generation can provide potential energy savings. The technologies developed originally as part of the LAC may aid the future design of such systems.

The aim of the study is to consider how various design parameters influence the performance of a scaled C-Class catamaran wind tunnel model and thus examine possible design options for future catamarans powered by wingsails.

## 2. SOFT SAILS VS WINGSAILS

As the sail area of a C-Class catamaran is fixed, from a designer point of view the key factor is to maximize the power achievable from the 300 square feet (27.87m<sup>2</sup>) of wing sail area allowed across a range of possible wind speeds. Figure 1 shows a typical C class catamaran in the upwind sailing condition.

A wingsail has some features in common with aircraft wing design with its use of multiple elements such as flaps and slots. As a result of this it can develop higher lift coefficients than conventional sail rigs [3]. The use of stiff components will increase the predictability of the achieved sail shape under given wind conditions, although it can be argued that a fixed geometry reduces the ability of the sailor to more precisely tune their sail for given wind conditions. High-lift devices typically use either slots or flaps to modify the flow regime around the sail section: the slot channelling flow from the high pressure to the low pressure side of the sail and the flap altering the effective camber.

The multi-element wingsail adopted in C-Class combines the slot and a shaped rear flap. The flow through the slot ensures the flow over the leading edge of the flap remains attached as well as generating higher sideforce. The effects are:

- increase in maximum achievable  $C_L$ ,
- delay in stall angle,
- benefits in performance in terms of better boundary layer control, and
- increased control of the camber in order to adjust the angle of attach (AoA) at different mast's heights for the local apparent wind angle ( $\beta_A$ ).

In order to generate the maximum achievable  $C_L$ , the entire sail should be uniformly loaded to obtain the semi-elliptic load distribution: soft sails' tip tends to be overloaded whereas the bottom can never be fully loaded. The physical reason for such behaviour is the nature of the wind driving a yacht: a twisted flow. As a consequence, the top is stalling before the bottom of the sail preventing the achievement of high average lift coefficients. Differentially, the control system of a wingsail allows twisting the sections at different heights, in order to offer always the optimum  $\alpha$  to the twisted  $\beta_A$ .





Figure 1 C-Class catamaran flying windward hull

### 3. C-CLASS WINGSAIL DESIGN CONDITION

The WinDesign [4] Velocity Prediction Program (VPP) was used to estimate the general sailing parameters related to boat speed  $V_S$ , apparent wind speed  $V_A$ , and apparent wind angle  $\beta_A$ , for a range of wind speeds of a C Class catamaran. Due to the lack of specific  $C_L$  and  $C_D$  values for a wingsail, for starting the design process using the VPP it has been assumed that a wingsail typically generates twice the lift coefficient of a normal soft sail [5] and hence the sail area was doubled in the input for the VPP:

$$C_{L \text{ wingsail}} \cong 2C_{L \text{ soft sail}} = \frac{L_{\text{soft sail}}}{\rho V^2 A_{\text{soft sail}}}. \quad (1)$$

The demihull of a typical C-Class “*Team Invictus*” is used for the hydrodynamic modelling. Catamarans assume two equilibrium states: flying and non-flying condition. The VPP is operating in three different “configurations”: the boundaries between these set up are defined by the user, defining:

1. the break angle = heel angle at which the windward hull is clear of the water,
2. the fly-angle = mean heel angle at which the catamaran will sail while flying the weather hull.

The maximum heel angle considered for the predictions is the fly-angle at which the crew is at their maximum righting moment. For a C-Class catamaran, a crew of 180kg in total and a fly-angle of 10 degrees were considered to be realistic. The multidimensional Newton-Raphson iterative method is used by the solution algorithm to generate the results shown as a velocity polar diagram in Figure 2. The angles plotted in the diagrams are true wind angles [degrees]; the polar curves represent estimated boat speeds [knots] at different true wind speeds. In addition to that, the dots in the polar diagram specify best VMG headings at given  $V_T$  for upwind and downwind sailing.

Table 1 Best  $\beta_A$ ,  $\beta_T$  and VMG for Invictus VPP

$V_T$ [knots]	$\beta_A$ [deg]		$\beta_T$ [deg]		VMG [knots]	
	Up	Dw	Up	Dw	Up	Dw
4	18,6	51,7	46,2	127,3	3,81	2,9
6	18,8	49	47	126,1	5,69	4,43
8	18,7	40,1	43,7	124,3	7,19	6,71
10	19,5	37,7	42,4	125,1	8,18	9,04
12	-	40	-	128,6	8,93	11,19
14	21,4	43,9	42,2	132,1	9,57	13,03
16	22,2	47,7	42,2	134,8	10,13	14,67
20	23,7	54,7	42,2	138,5	11,08	17,63

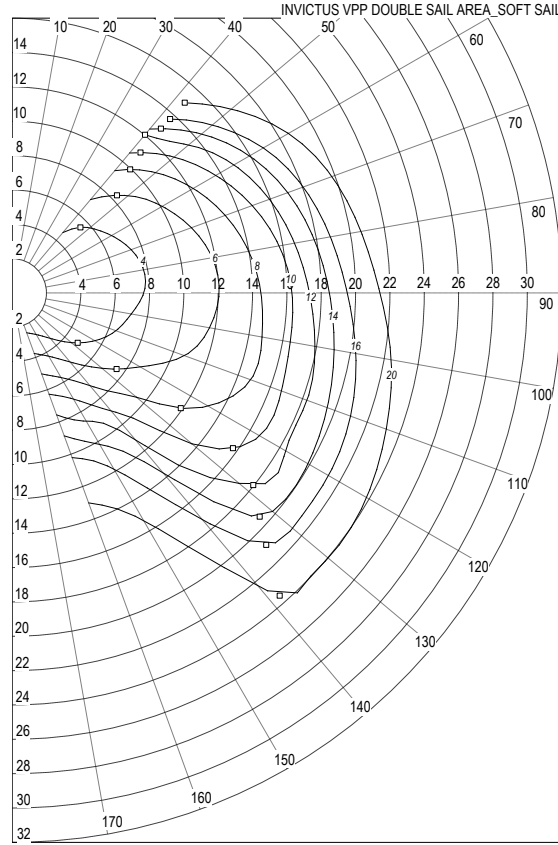


Figure 2 *Invictus VPP using double soft sail area*

The global range of  $\beta_A$  (Table 1) at which the wingsail will operate is estimated by the VPP to be between 20 and 60 degrees from the  $\beta_T$ . In other words, C-Class catamarans are able to sail so fast that they can keep the apparent wind always to the front. Interestingly, for downwind sailing condition both  $\beta_A$  and  $\beta_T$  presents a non-monotonic behaviour with increasing  $V_T$ : for values higher than  $V_T=10\text{kn}$ , both angles start increasing. This result is also confirmed by proven technique used to sail downwind a C-Class catamaran [3].

### 3.1 Upwind requirements

The upwind requirement for a sailing yacht is that the ratio  $D_F/H_M$  is maximised. Driving force and heeling forces are given respectively as:

$$D_F = L \sin \beta_A - D \cos \beta_A, \quad (2)$$

$$H_F = (L \cos \beta_A + D \sin \beta_A) \cos \phi, \quad (3)$$

The heeling moment of a catamaran is:

$$H_M = H_F a, \quad (4)$$

where  $a$  is the distance between the CLR and the CE of the sailplan. In a steady sailing condition, the heeling moment generated by the sailplan has to be balanced by the righting moment produced by the hull and its crew:

$$H_M = R_{M \text{ cat}} = W_{\text{CAT}} l_1 \cos \Phi + W_{\text{CREW}} l_2 \cos \Phi; \quad (5)$$

where,  $W_{\text{CAT}}$  and  $l_1 \cos(\phi)$  are respectively the weight of the catamaran and the distance between CB and CG in which the total weight is applied. Identical meaning has  $W_{\text{CREW}}$  and  $l_2 \cos(\phi)$ , for the crew's weight. Last equation relates  $\phi$  with the  $H_M$ : being a cosine function, an increase in the heel angle will decrease the righting moment.

Therefore, the maximum righting moment is achieved when the heel angle is at a minimum. A decrease in drag will cause a decrease in the  $H_F$  and an increase in the  $D_F$ . Lift and drag for a sail of area  $A$  are defined as:

$$L = \frac{1}{2} \rho A V_A^2 C_L; \quad (6)$$

$$D = \frac{1}{2} \rho A V_A^2 C_D. \quad (7)$$

The drag coefficient is defined as:

$$C_D = C_{D0} + C_{DI}, \quad (8)$$

where,  $C_{D0}$  is the form drag due to the skin friction and turbulence of the air following over the sail and its supporting structure with its associated flow separations;  $C_{DI}$ , the induced drag, is a function of the vertical distribution of aerodynamic loading and it is defined:

$$C_{DI} = \frac{C_L^2}{\pi A R}. \quad (9)$$

Recent studies [6] implemented an additional pressure drag coefficient due to separation, likely to occur in high lift situation. Nevertheless, this study employs the classical potential flow model (eq. 8). The induced drag is the largest drag component. For reducing  $C_{DI}$ , a high aspect ratio airfoil is required; nevertheless, a tall rig will have a higher vertical centre of effort CEh increasing the heeling moment and ending in penalizing the  $D_F$ . To reduce the CEh, a negative lift distribution can be used at the tip of the wingsail which has been proved to obtain the best  $D_F/H_M$  for strong winds condition [7].

### 3.2 Downwind requirements

High speed sailing catamaran never sail straight downwind in order to achieve the maximum  $V_{MG}$ , for the following reason:

- when  $V_S$  is increasing (accelerating), consequently  $V_A$  will inevitably decrease (course in the direction of the wind),
- since  $D_F = f(V_A^2)$  and  $R_H = f(V_S^3)$ , it becomes difficult to obtain any significant gains in sailing straight to the wind.

C-Class catamarans tack downwind jibing through approximately 90 degrees jibe to jibe (so called technique “iceboating” after the similar technique used when sailing on ice) [3]. At these angles and with the speeds these catamarans can reach, the  $V_A$  is moved well forward of the beam and they manage to fly a hull while close reaching in the accelerated  $V_A$ . The higher  $V_S$  is, the higher  $V_A$  becomes, and the more power is obtained. Sail drag is of secondary importance, whereas the lift force generating the thrust in the direction of the course is of prime importance. Therefore, the downwind requirement is to design a wingsail than can generate a  $C_{L,MAX}$  over the entire span of the wing. A high level of camber is requested in order to adjust the wing’s AoA to the twisted flow acting on it; with flap angle of about 30-35 degrees, wingsails can produce their best performances.

## 4. WIND TUNNEL TESTING

In order to assess the complex interaction of the differential twisting of a wingsail with its trampoline, a scaled model (Table 2) was tested in the large cross-section straight flow low speed section of the University of Southampton 7’x5’ closed return wind tunnel.

### 4.1 Wind tunnel model-design

The model’s requirements considered crucial were:

- possibility of changing the heeling angle in the tests,
- possibility of controlling the AoA of the wingsail,
- possibility of changing type of trampoline.

Due to time constraints, a wingsail designed in a previous research project was used [8]; therefore, the model also required being able to accommodate the wingsail previously tested. The scaling procedure started from the area of the model wingsail of GDP 34:

$$A_{wingsail} = 0.72 \text{ m}^2.$$

The area of a C-Class wingsail is:

$$A_{wingsail \text{ C-Class}} = 27.87 \text{ m}^2.$$

Therefore, the scaling factor is:

$$\lambda = \sqrt{\frac{A_{wingsail \text{ C-Class}}}{A_{wingsail}}} = 6.22. \quad (10)$$

Next, all the dimensions of the full scale catamaran has been scaled according to  $\lambda$ :

Table 2 *Main wind tunnel model dimensions*

Parameters	Full Scale	Model Scale
Sail Area [m2]	27.87	0.72
LOA [m]	7.62	1.225
Beam [m]	4.267	0.686

The catamaran structure is composed of aluminium box sections of 31x31x3mm (Figure 3). The demihulls are connected together by two aluminium cylinders with a diameter of 30mm and 3mm of thickness bolted to the square bars. To enable model testing at different heeling angle, a semi-circular aluminium bar is designed to be connected to the dynamometer fittings with holes at every 5 degrees of heel. The axis of rotation of the whole model is the one given by the rotation of the bow fitting around the aluminium bar connected in the forward fitting of the dynamometer.

To represent the windage resistance, demihulls made by foam scaled from *Invictus* hull are designed to cover entirely the aluminium structural bars, in order to provide a realistic aerodynamic shape (Figure 4).

A benefit of this model design is its flexibility, it can be reused for different types of boat by redesigning the foam shape covering the aluminium bars. The beams can be removed or changed in dimensions either to test monohulls or catamarans with different width.

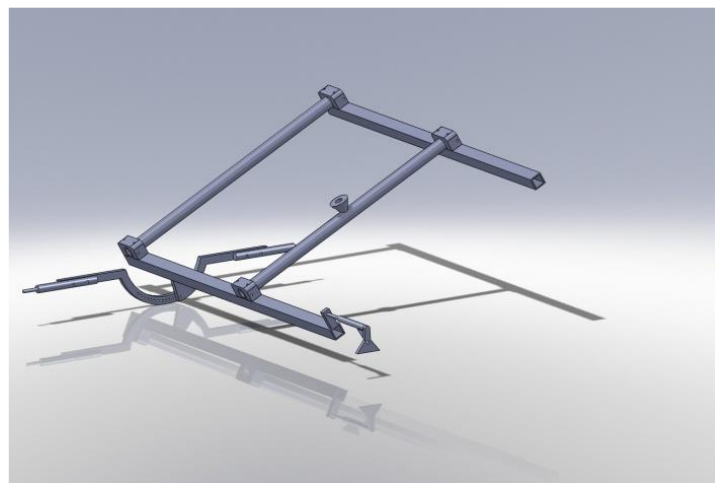


Figure 3 *Wind tunnel model internal structure*

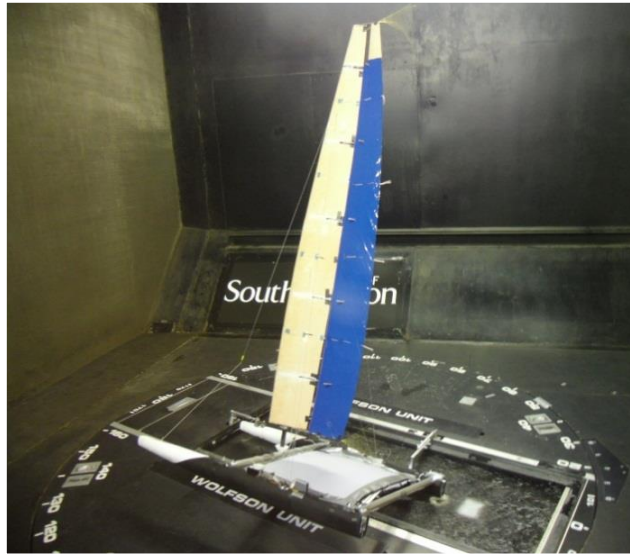


Figure 4 *Wind tunnel model during tests. Flow is left to right*

#### 4.2 Methodology of testing.

During the tests, the angle of attack of the fore element was controlled with an electrical winch (Figure 5), whereas the second element was manually fixed at a certain angle relatively to the first. In other words, the “global” angle of attack of the wingsail was controlled. For upwind sailing, a flap angle of 10 degrees (angle between the longitudinal axis of the wingsail’s fore element and the flap) was estimated to be realistic. For the downwind case, a flap angle of 20 degrees was adopted as constant cambered configurations. For the twisted configurations, the first step was to set the wing at a constant flap angle (respectively 10 or 20 degrees for upwind/downwind  $\beta_{AS}$ ). This ensured a correct opening of the slot gap between the two elements. For achieving twist on the flap element, a hinge and track system was adopted [8]: shrink wrapping was used around wooden sections of the element to cover the wing.



Figure 5 *Wind tunnel model control system*

For the sealed gap configuration tested, the mast was shortened by about 100mm at the base, and a plastic sheet was applied to seal the wing foot with the solid platform (Figure 18); nevertheless, same wing area has been considered for  $C_L$  and  $C_D$  calculation.

The following testing procedure for the different configurations was adopted:

- Setup of the model: the turntable was fixed at a certain  $\beta_A$ , the model was fixed at given heel angle, the camber distribution was adjusted,
- Dynamometer re-zeroed (function of the acquisition software): due to the drift in the experimental instruments after long runs, the zero has to be reset. The strain gauges are measuring an unsteady signal; therefore, the data are sampled for a period of 10 seconds and then the mean force block values are recorded. In order to recreate the oscillation of the measurements, before re-zeroing a small “kick” was given to the model [9],
- Wind ON: constant dynamic pressure mode operated by the wind tunnel technician,
- Wingsail trimming: due to the friction applied by the lateral shrouds, the wind pressure was not powerful enough to completely sheet out the wing; hence, the wing was left at zero angle of attack and started to be pulled from the zero lift condition; with such a method it was possible to record more data points,
- Data acquisition: using Lasso software, each set of sailing points ( $D_F$ ,  $H_F$ ,  $H_M$ ,  $Y_M$ ) were acquired for different trims. In order to obtain a complete distribution of points in the  $C_D/C_L^2$  plot, the wingsail was trimmed in order to acquire at least eight data points for each run before stall is reached,
- Wind OFF: the technician was shutting off the tunnel’s fan when the set of data for a particular run was completed (i.e. 8 data points acquired, maximum driving force achieved and stall appeared by looking at the tell tales),
- End zero value: measured forces with the wind completely stopped were acquired in order to apply the end zero corrections (discussed in the next chapter); the same “kick procedure” explained for re-zeroing the dynamometer was employed.

For completing a run, the average time requested is of about 20 minutes. Longer run times should be avoided due to the increase in the internal temperature of tunnel which affects the measurements [10] [11] [12].

Tests without wing for the different configurations have been conducted separately to acquire windage data: these values were subtracted from the recorded data with sails allowing analysis of forces due to sail alone.

### 4.3 Wind tunnel corrections

From the acquisition software Lasso the values for driving force, heeling force and consequently heeling moment and yawing moment were acquired. These raw values need to be corrected. Firstly, the end zero correction was employed, using the formula (for instance, for the driving force):

$$D_F = D_{F\text{ raw}} - D_{F\text{ end}} \frac{1 + \text{RUN\#} - \text{START RUN\#}}{\text{FINISH RUN\#} - \text{START RUN\#}} \quad (11)$$

This correction is due to the drift in the dynamometer load cells during a set of runs proved by the presence of residual stresses after every run even after the wind in the tunnel is off. Secondly, the forces need to be transformed from the boat axis (set at zero leeway angle on the balance) to tunnel axis. The  $\beta_A$  for the heeled condition can be estimated as follows [13]:

$$\beta_{A\text{ heeled case}} = \tan^{-1}(\tan \beta_{A\text{ upright}} \cos \phi) \quad (12)$$

Reversing the above equation and (2) (3) lift and drag coefficients are then calculated as (6) (7) by the forces normalized by the sail area and the dynamic pressure: this procedure is simplifying the analysis because the algorithms adopted by the VPP are working with coefficients in the plane normal to the mast.

Wall boundary and wake blockage corrections were employed [9]:

$$C_{D\text{ corrected}} = C_D + \frac{\delta A_W C_L^2}{c} \quad (13)$$

$$\beta_{corrected} = \beta + \frac{\delta A_W C_L}{c}. \quad (14)$$

$\delta$  is the downwash correction for the specific wind tunnel ( $=0.09$ ),  $A_W$  is the wingsail area, and  $C$  is the tunnel cross section area ( $=14,6m$ ). The same correction routine presented above has been adopted for the “wing only” case (without windage), the only difference consisted in subtracting the windage values (for  $D_F$ ,  $H_F$ ,  $H_M$ ,  $Y_M$ ) from the totals before transforming the forces to tunnel axis.

#### 4.4 Experimental uncertainty

In order to obtain the same characteristics in terms of flow pattern between full scale and model scale, the Reynolds number has to be the same:

$$Re_{full\ scale} = \frac{vL}{\nu} = Re_{model\ scale}, \quad (15)$$

$\nu$  is function of the temperature of the air; therefore it will change as the tunnel temperature increases (for instance, after a long run). For this reason, the tests were conducted at constant dynamic pressure mode. Knowing that  $q$  is:

$$q = \frac{1}{2} \rho_{air} V_A^2; \quad (16)$$

the analysis with lift and drag coefficients can be conducted without issues about air temperature changes. Nevertheless, with the wind speeds used for sailing yachts tests, the same  $Re$  as the full scale case can never be achieved. Screens are fitted to improve flow uniformity which however remains uneven [14]. The screens also create fine scale turbulence in the airflow increasing the effective  $Re$ .

Four different dynamic heads at different wind speeds have been tested measuring the forces generated at  $\beta_A=0deg$ . The result shows a dependency of the measured forces with  $Re$ : on the x axis, the  $Re$  is calculated using the maximum chord length of the model; on the y axis, the driving force ( $C_x$ ) and heeling force ( $C_y$ ) coefficients are obtained by normalizing the forces by the wingsail area and  $q$ . The runs were conducted in a short time and an average temperature of  $31^0$  Celsius.

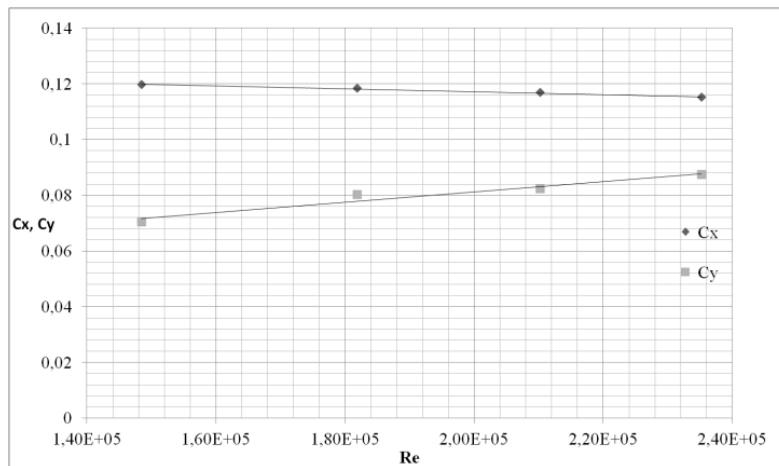


Figure 6 Reynolds number dependency study for driving and heeling forces

Due to the variety of configurations tested, the main issue encountered was the control of the slot gap between the two elements while the wingsail was cambered. Moreover, due to the curved trailing edge of the second element, a change in the camber results in an increase in the slot gap. After several attempts, a solution for fixing the flap angle was found: depending by which particular twist was requested, little aluminium bars were applied along the span fixing the hinges relatively to the first element. Consequently, templates made out of cardboard were taken for each

different setting at different section heights, in order to control any amount of variation in the camber distribution during a run. The templates guaranteed the possibility of repeating a particular camber distribution after any number of runs with different configurations.

## 5. RESULTS AND DISCUSSION

### 5.1 Effect of heel

Tests were conducted for 3 different heel angles: 10, 20, 30 degrees. In Figure 7,  $D_F$  versus  $H_M$  ratio is reported in the upwind case for the net configuration.

The optimum heel angle was found to be at  $\phi=10$  degrees driving forces achieved at same heeling moments are always higher at 10 degrees than for the higher angles. The reason for that is mainly due to the reduction in the  $\beta_A$  with heel (eq. 12): being a cosine function, with an increase in heel ( $\phi$ ), the  $\beta_A$  in the heeled condition decreases, reducing the driving force generated by the wingsail.

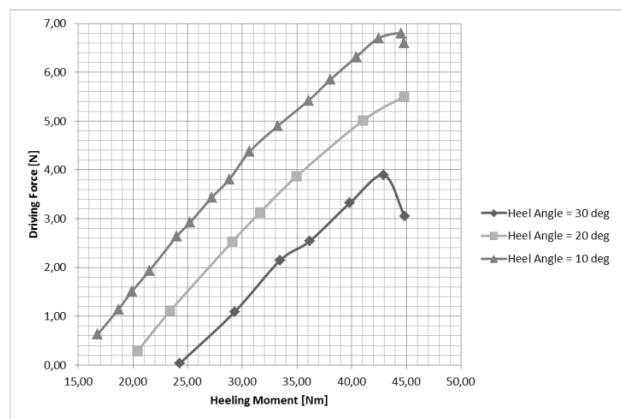


Figure 7  $\beta_A=20deg$ , net platform, with windage

Since both  $C_{DI}$  and  $C_{DO}$  vary with the square of the lift, it is informative to plot  $C_D$  vs.  $C_L^2$  (Figure 8).

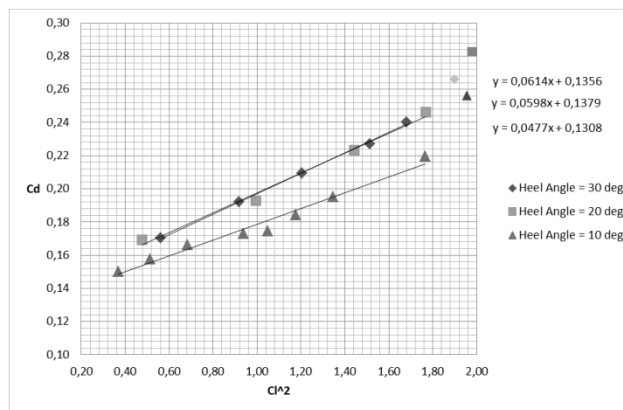


Figure 8  $\beta_A=20deg$ , no trampoline, with windage

The behaviour of a sailplan can be analysed by four features derived from  $C_D$  vs.  $C_L^2$ :

- $C_{DI}$  is the slope of the straight line through data,
- $C_{D0}$  is the intercept of the straight line with the zero lift axis,
- $C_L$  max,
- $C_L$  value above which separation starts.



The base drag is lower for  $\phi=10\text{deg}$  ( $C_{D0}=0.131$ ). It increases with higher heeling ( $C_{D0}=0.137$  at  $\phi=20\text{deg}$ ): that is due to the smaller projected area of the bare hull in the direction of the wind. After subtracting the windage values, the base drags at different heel are similar, giving consistency in the results [12].

The induce drag increases with the heel angle ( $C_{D1}=0.048$  at  $\phi=10\text{deg}$ , to a value of 0.061 at  $\phi=30\text{deg}$ ): the increased gap underneath the wing foot due to heel is influencing the induced drag of the wingsail.

Tests conducted with a  $\beta_A=25\text{deg}$  demonstrated that the negative effect of heeling on the  $D_F/H_M$  ratio is less sensible. In other words, during a downwind leg in which the maximum thrust requirement will not be limited by the  $H_M$ , heeling at more than 10 degrees will not affect negatively the performance as during an upwind leg.

### 5.2 Effect of trampoline porosity

Three different configurations were tested for the upwind case: a solid platform made by an MDF panel, a net trampoline made out of fabric with a 2 mm net spacing, and finally a configuration with neither net nor platform. A comparison is made, for a consistent  $\beta_A$  of 20 deg, the influence of these root geometries on the wing sail drive force with windage for  $\phi=30\text{deg}$  (Figure 9) and the optimum  $\phi=10\text{deg}$  (Figure 10). Figure 11 presents their effect on induced drag and Figure 12 removes the effect of windage on drive force.

At the optimum heel angle  $\phi=10\text{deg}$ , the trampoline without net is the best performer. At  $\phi=30\text{deg}$  (Figure 9), the solid trampoline generates higher  $D_F$  than the “no-net” platform. Moreover, the platform’s differences in driving forces are more marked for the higher heel angle.

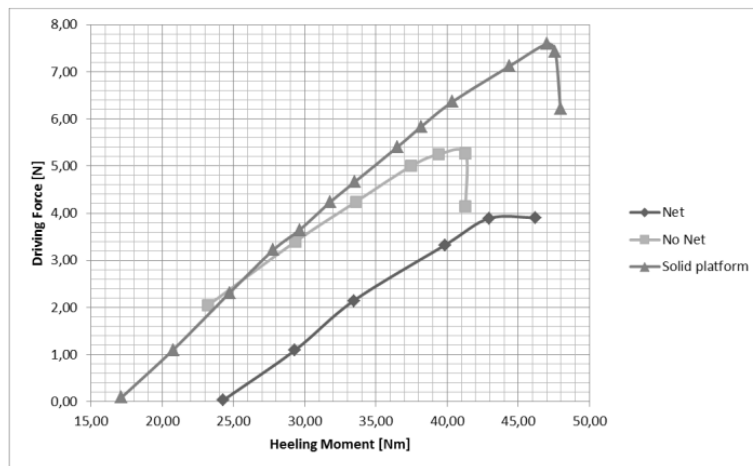


Figure 9  $AWA=20\text{deg}$ ,  $\phi=30\text{deg}$ , with windage

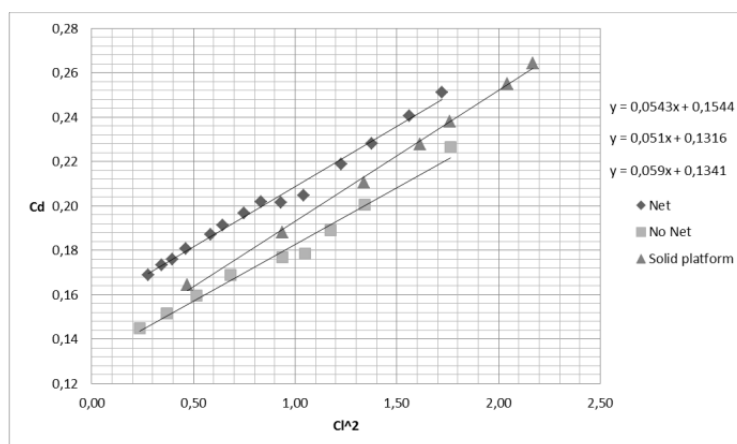


Figure 10  $AWA=20\text{deg}$ ,  $\phi=10\text{deg}$ , with windage

From the  $C_D/C_L^2$  plots a better understanding of what is presented above it is achieved. At  $\phi=10\text{deg}$  (Figure 10), the induced drag of the “no-net” trampoline is smaller ( $C_{DI}=0.051$ ); it is higher for the solid platform ( $C_{DI}=0.059$ ) and the net configuration ( $C_{DI}=0.054$ ). The small angle of heel allows the wingsail to operate close to the wind tunnel floor; therefore, the effect of the solid platform is not resulting in any advantage in terms of reducing the gap underneath the wingsail foot. Instead, the solid platform is disturbing the incoming flow at the lower sections of the wing.

The base drag of the “no-net” trampoline is smaller than the other configurations for every heel angle: this trend is more marked at  $\phi=30\text{deg}$  (Figure 11) at which angle the ‘no-net’ base drag is  $C_{D0}=0.13$ , whereas for the solid platform it is  $C_{D0}=0.16$ . The net platform is generating the highest base drag ( $C_{D0}=0.204$ ). For all heel angles, the net platform is the worst performer: the fabric net deforms like a sail between the demihulls generating parasitic drag without enhancing the lift of the sail.

Interestingly, at  $\phi=30\text{deg}$ , the solid platform is presenting the smaller  $C_{DI}$  ( $=0.043$ ) compared with the other platforms. This result demonstrates that the solid platform is generating an effective shield effect on the wing foot decreasing the gap underneath it.

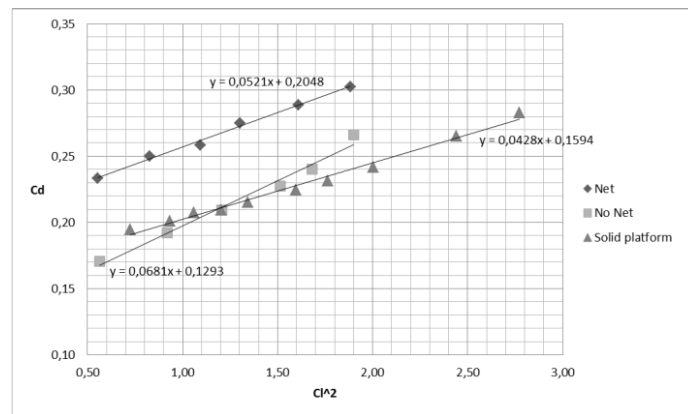


Figure 11  $AWA=20\text{deg}$ ,  $\phi=30\text{deg}$ , with windage

Moreover, by plotting the  $D_F$  vs.  $H_M$  ratio without windage at 30 degrees of heel, another consideration about the solid platform emerges: the catamaran without net is the best option (Figure 12). That implies that the solid platform for high heeling angle is acting as a longitudinal airfoil capable of generating a certain amount of lift and consequently driving force.

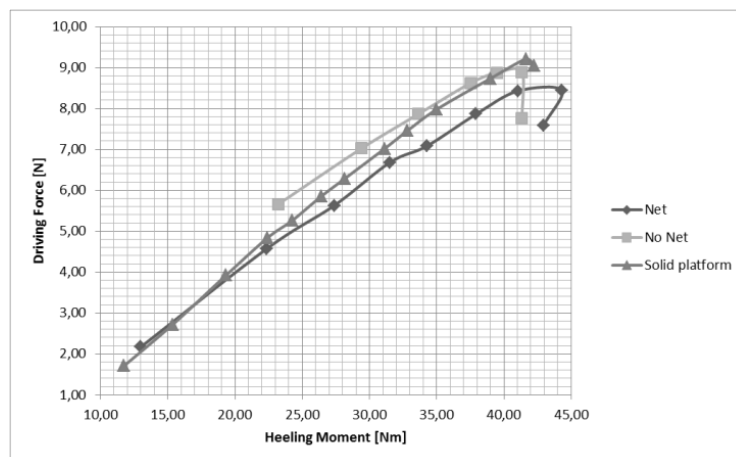


Figure 12  $AWA=20\text{deg}$ ,  $\phi=30\text{deg}$ , without windage

### 5.3 Effect of camber distribution

Different twist profiles have been tested simulating upwind and downwind requirements. The results have been compared with the “constant cambered” configurations: 10 and 20 degrees respectively for upwind and downwind sailing condition. Only the solid platform at  $\phi=10\text{deg}$  has been used for this batch of tests. The wingsail constantly cambered at 20 degrees performed better than the other twisted configurations due to the untwisted flow of the wind tunnel; therefore, results will not be discussed in this paper. However, it is worth noting what influences the sail performance is the relative twist to the on-set wind which is captured in this work.

Table 3 shows the flap angle of two significant twist profiles at different heights: the flap angle is intended as the angle between the longitudinal axis of the aft element (cambered at 10 degrees relatively to the fore one) and the twist imposed with the hinge and track system (Figure 13).

Table 3 *Twisted profile settings*

SECTIONS	TWIST A [deg]	TWIST B [deg]
<i>tip</i>	-10	0
<i>middle</i>	-5	0
	0	5
	5	10
<i>root</i>	10	15



Figure 13 *Twisted configuration A*

By analysing the results, the following statements can be made. At small values of  $H_M$ , the  $D_F$  vs.  $H_M$  ratio is higher for both twisted configurations “A” and “B” compared with the constant flap angle at 10 degrees.

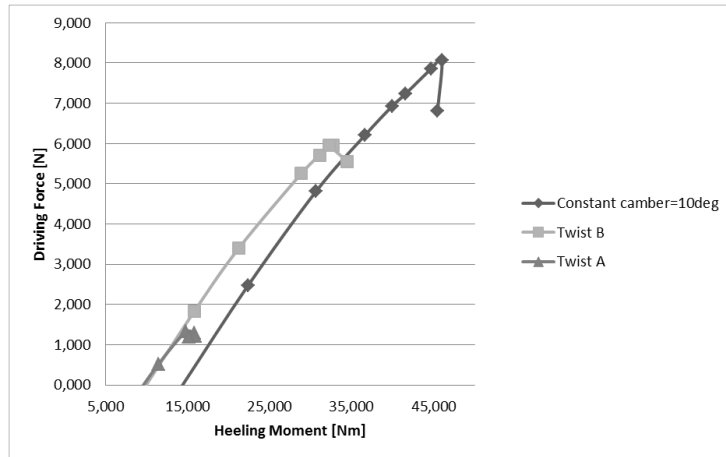


Figure 14  $AWA=20deg$ ,  $\phi=10deg$ , with windage

Twist “A” and “B” were tested in order to depower the tip of the wing (particularly in “A” in which a negative spanwise lift distribution at the tip is attempted). The beneficial effect of depowering the top of a sail is in the reduction of the CEh which results in decreased heeling moments. The maximum  $D_F$  achieved by the “constant cambered” wingsail is higher; nevertheless, wind tunnel tests are conducted at same wind speed for both constant and twisted configurations. If the wind speed is increased, the limitation of the maximum righting moment will set a fixed value of heeling moment before capsizing: in such a condition, the twisted configurations will be faster with higher  $D_F$  at given  $H_M$ . In other words, even though the constant cambered wing is able to produce higher maximum  $D_F$  overall, in heavy winds the wingsail will need to be depowered more than a twisted configuration for reaching the equilibrium  $R_M = H_M$ , resulting in lower driving force. In order to translate this finding to a real sailing situation, a VPP analysis is given in Section 5. The amount of lift and consequently driving force lost by depowering the tip of the wing (no tip vortex observed during the tests) is compensated by the decrease in CEh.

Figure 15 shows the CEh variations as function of heeling force coefficients for the 3 different configurations: on the x-axis,  $C_y$  is normalized by the wing area; on the y-axis, the CEh is plotted as percentage of the wingsail’s height above the waterline.

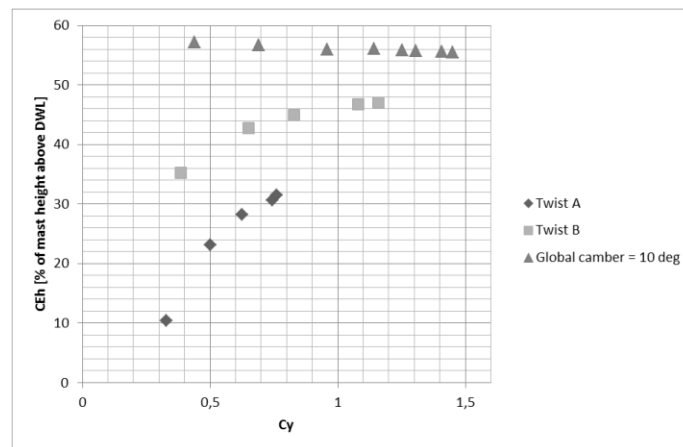


Figure 15  $CEh/C_y$  at  $AWA=20deg$ ,  $\phi=10deg$ , with windage

#### 5.4 Effect of gap at wingsail foot

The effect of gap on wingsail performance was investigated using the solid platform as shown in figure 16. The sealed configuration is considered to be beneficial for the upwind requirement of optimizing the efficiency of the rig.

The maximum driving forces achieved by sealed and with gap configurations are similar ( $D_F=8N$ ); comparing the results at fixed  $H_M$ , the “sealed gap” is the best performer because it generates higher  $D_F$ . The CEh in the sealed case is lower because the rig span was reduced.

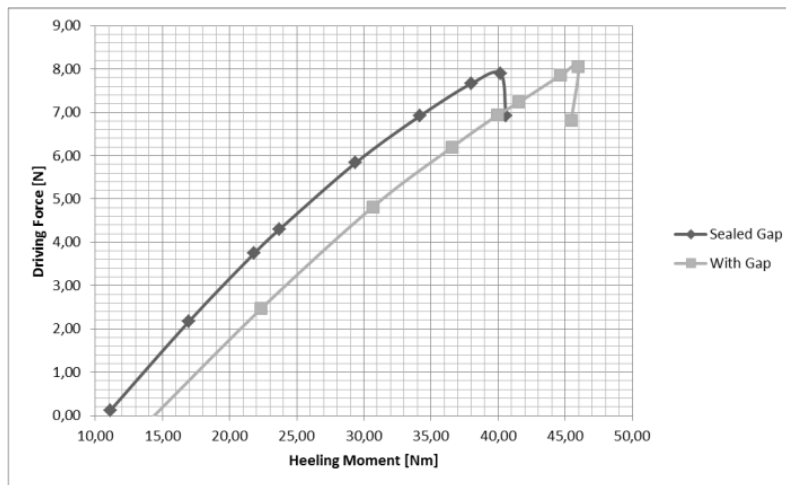


Figure 16  $AWA=20deg$ ,  $\phi=10deg$ , with windage

In Figure.17, the induced drag tested in the sealed configuration is higher ( $C_{DI}=0.065$ ) than the wing with the gap ( $C_{DI}=0.057$ ). In contrast with the classic lifting line theory, where an elliptical spanwise lift distribution and a sealed gap represents the best windward performances [7], the wind tunnel tests demonstrate that some practical implications have also to be taken into account (sealing platform shape has to be studied in combination with wingsail foot).

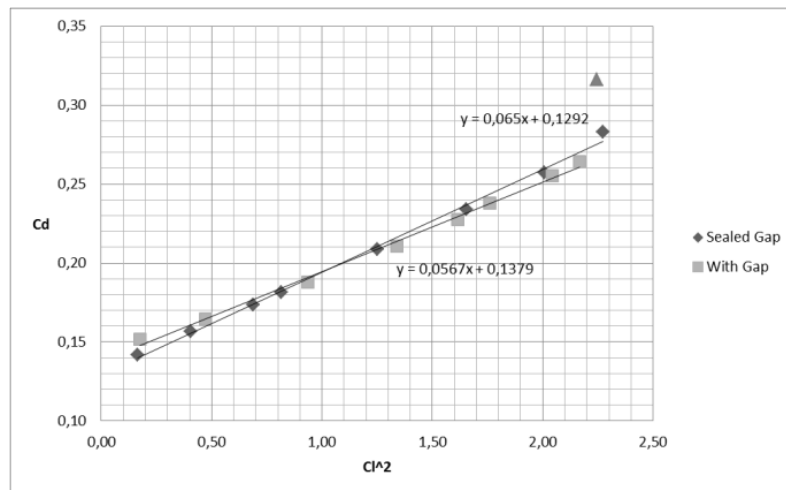


Figure 17  $AWA=20deg$ ,  $\phi=10deg$ , with windage

The disturbed flow generated by the solid platform affects the performance of the wingsail’s lower sections causing early separation as observed by the tell tales during the tests in Figure 18.

Moreover, the “sealed gap” wingsail presents a smaller base drag ( $C_{D0}=0.13$ ), probably due to the shorter rig: the lower part of the wing is covered by the windward demihull resulting in less total windage drag.

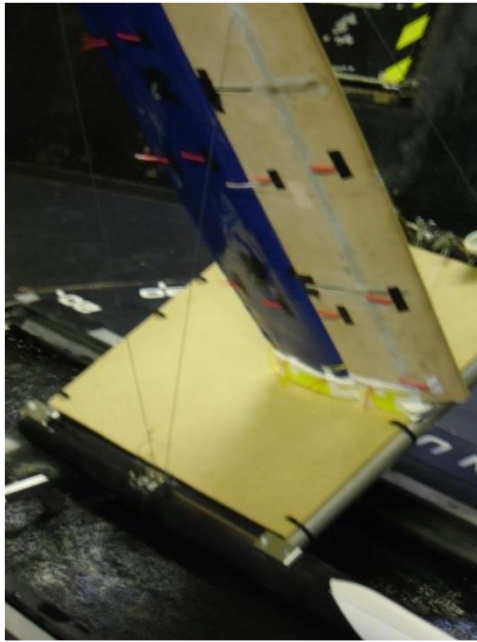


Figure 18 *Wingsail foot depowered in sealed configuration*

## 6. VPP WITH EXPERIMENTAL RESULTS

### 6.1 Scherer VPP

A VPP based on results from wind tunnel tests requires four values as a function of the  $\beta_{AS}$ :  $C_{LMAX}$  ( $Clx$ ),  $C_D$  ( $Cdt$ ),  $CEh$  ( $Zce$ ), and effective span ( $Span\ Eff$ ).

The  $C_L/\alpha$  plot from Scherer [5] shows that the wingsail is stalling at an AoA above 30-35 degrees. Nevertheless, wingsails can rotate on their base relative to the boat frame of reference, changing the overall angle of attack. The only limitation to this rotation is the position of the lateral shrouds. Therefore, the  $\beta_{AS}$  at which the stall starts to occur does not coincide with the maximum AoA before stall. The apparent wind angle can be increased by easing the wingsail. In other words, by sheeting out the wingsail, the angle of attack is kept at the optimum value even if the  $\beta_{AS}$  is increasing until the wingsail hit the lateral shrouds. An increase of 30 degrees ( $\beta_A=60$  degrees) is estimated to be reasonable. In the following table, the results for the double slotted wingsail from Scherer are tabulated. The internal values of  $Zce$  and  $Span\ Eff$ . used by the VPP for the initial run have been adopted. In reality, both centre of effort and effective heights will be different for the wingsail: the assumption is made in absence of this data from Scherer. As explained above, between 30 and 60 degrees,  $C_L$  and  $C_D$  are kept approximately constant because the wing will be eased in order to prevent stall. Windage components, which are associated with internal “shape function” in the VPP, are resolved into aerodynamic drag forces in boat system.

Table 4 *Scherer VPP experimental data*

$\beta_A$	$Clx$	$Cdt$	$Zce$	$Span\ Eff$
5	1	0.1	0.4866	1
20	2.1	0.38	0.4866	1
25	2.3	0.42	0.4866	1
30	2.4	0.42	0.4866	1
40	2.45	0.43	0.4866	1
60	2.35	0.5	0.4866	1
80	<u>1.6</u>	<u>1</u>	0.4866	1
120	<u>0.8</u>	<u>2</u>	0.4866	1
180	<u>0</u>	<u>2.4</u>	0.4866	1

The VPP fits a polynomial curve across the data points as presented in Figure 19: the solution algorithm starts to use the values of  $C_{LMAX}$ ; once the sail is generating too high heel force (i.e.  $H_M > R_M$ ), a smaller  $C_L$  of the polynomial fitting is used until the boat reach a steady state sailing condition (i.e.  $H_M = R_M$ ).

In order to do that, the VPP needs values in the range of  $\beta_A = 0-180$ deg: the underlined values of Table 4 are considered reasonable values to cover the range of  $\beta_{AS}$  requested for the interpolation.

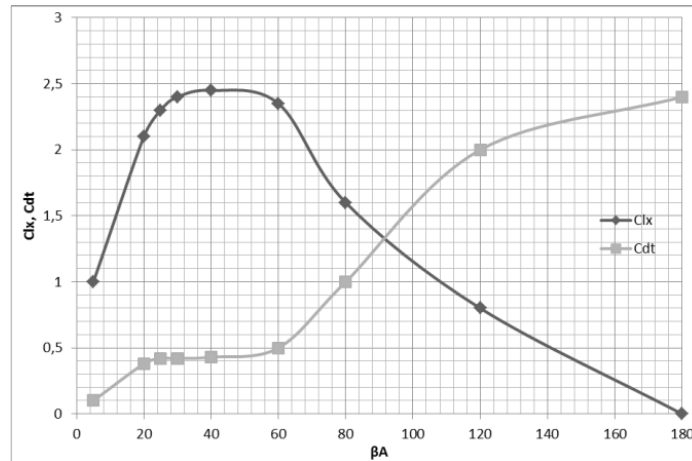


Figure 19 Scherer VPP polynomial fit

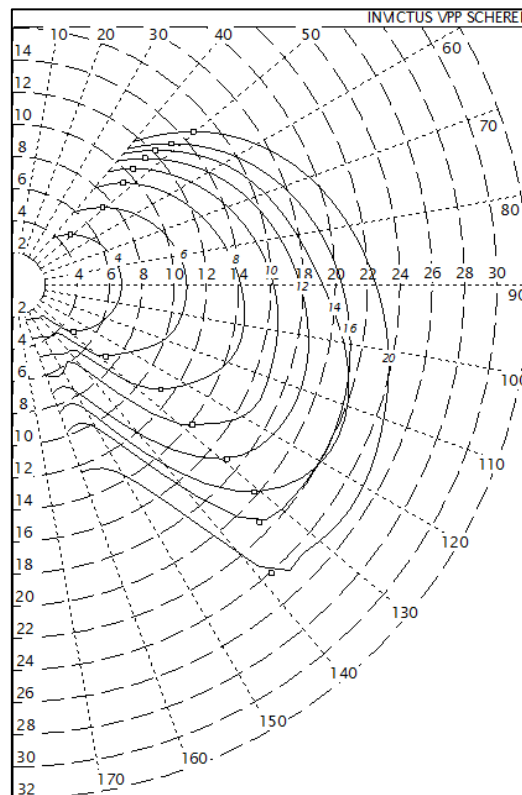


Figure 20 Scherer VPP

Comparing “Scherer VPP” (Figure 20) with the initial VPP setup (Figure 2), the former identifies faster performance for heavy winds (above 12 knots) when sailing off the wind. Considering that same values of flotation, CEh and Eff. Span. heights have been used, the reason for this behaviour is that the wingsail maximum  $C_L$  is maintained constant for higher  $\beta_{AS}$  as was explained previously. For the double sail area VPP, above  $\beta_A=25\text{deg}$ , the sail starts to generate less lift whereas the drag keeps increasing. The mast, which is effectively the leading edge of the main, for higher  $\beta_{AS}$  produces more turbulence on the leeward side of the sail decreasing the lift generated [15].

## 6.2 Wind tunnel VPP

The results from the wind tunnel indicate that the wingsail used for the tests [8] does not achieve the high lift expected for a wing with a slotted flap. This is due to a poor manufactory over the slot opening between the elements. It was therefore necessary to “manipulate” the results in a sensible way in order to compare the velocity predictions with Scherer VPP.

Two different VPPs were run from the experimental results of the present research: a VPP with the wing at constant camber of 10-20 (respectively for upwind and for downwind) and the twisted configuration “B” in order to predict which value of  $V_T$  marks the trade-off in performances between the constant cambered wingsail and the wing depowered at the tip.

For the constant cambered wing VPP, the following assumption was made: the  $C_{LMAX}$  found by Scherer was used to calculate the values of  $C_D$  by knowing the equation of the  $C_D/C_L^2$  straight line from the tunnel experiments.

With values of  $C_L$  and  $C_D$  “scaled up” while maintaining the same  $C_{DI}$  and  $C_{DO}$  for the  $\beta_{AS}$  of 20, 25, and 30 degrees, the assumption used for “Scherer VPP” (retarding the stall value of additional 30 degrees) is repeated. For the remaining  $\beta_{AS}$  the same typical values” for Scherer VPP are employed. The centre of effort heights and the effective span are the ones obtained in the tests. The following table represents the experimental data used in the VPP:

Table 5 *Experimental data for wind tunnel VPP*

$\beta_A$	Clx	Cdt	Zce	Span Eff
5	1	0.100	0.61	0.93
20	2.1	0.396	0.54	0.93
25	2.3	0.499	0.53	0.89
30	2.4	0.540	0.51	0.88
40	2.45	0.540	0.51	0.88
60	2.35	0.580	0.51	0.88
80	<u>1.6</u>	<u>1.000</u>	0.51	0.88
120	<u>0.8</u>	<u>2.000</u>	0.51	0.88
180	<u>0</u>	<u>2.400</u>	0.51	0.88

The VPP results are presented in Figure 21 as a polar diagram. The overall predictions are not affected because the  $\beta_{AS}$  that result in best VMG downwind are all below  $\beta_A=60\text{deg}$ . Comparing the results with the “Scherer VPP the two different VPP configurations reach similar boat speeds  $V_S$ .

It is considered that the “Scherer VPP” results are faster than the “constant cambered” wingsail for the following reasons. Firstly, the former CEh, taken from the internal VPP values for a soft sail with same dimensions, is lower than the latter case; in terms of performances this results in the possibility of using a bigger percentage of the maximum thrust achievable without the need of flattening or twisting the wingsail. This is confirmed by comparing the tables of best flattening function for the optimum VMG of the two VPPs. Flattening functions are used in order to reduce the  $H_M$  or sideforce by reducing Clx.



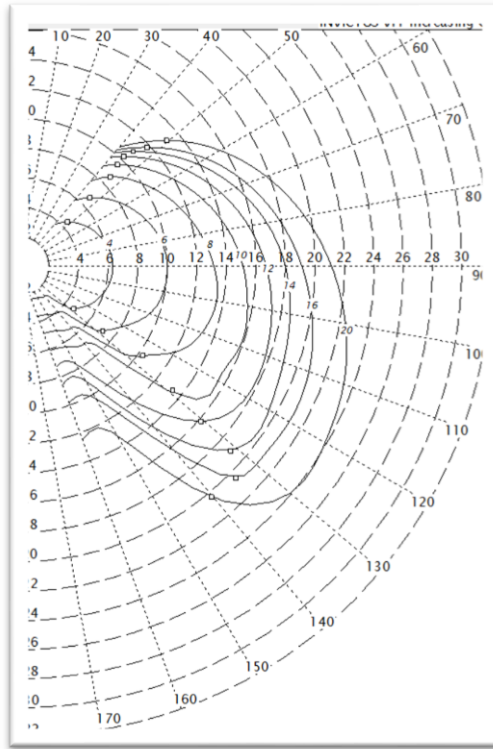


Figure 21 *Wind tunnel VPP*

Table 6 Upwind best flattening for "wind tunnel VPP" and "Scherer VPP"

$V_T$ [knots]	Constant camber	Scherer
4	1	1
6	0,993	1
8	0,877	0,936
10	0,667	0,718
12	0,535	0,577
14	0,442	0,486
16	0,374	0,413
20	0,293	0,327

“Scherer VPP” flattening function is higher for every wind speed: the  $C_{LMAX}$  is exploited better than the VPP using the tunnel data. Secondly, the induced drag measured in the tests is higher than the Scherer’s wingsail, resulting in higher total drag generated by the wing which clarifies the reason for the bigger differences in  $V_S$  in the upwind case.

For the twisted configuration “B”, a different VPP has been set: the values of  $C_{LMAX}$ ,  $C_D$  using the equation of the straight line of  $C_D/C_L^2$  are used. CEh and effective span have been calculated in the experimental tests.

The experimental values used in the VPP’s run are:

Table 7 Experimental data used for "Twist B" VPP

$\beta_A$	Clx	Cdt	Zce	Span Eff
5	1	0.10	0.61	0.88
20	2.1	0.43	0.46	0.88
25	2.3	0.52	0.46	0.82
30	2.4	0.58	0.43	0.85
40	2.45	0.58	0.43	0.85
60	2.35	0.61	0.43	0.85
80	<u>1.6</u>	<u>1.00</u>	0.43	0.85
120	<u>0.8</u>	<u>2.00</u>	0.43	0.85
180	<u>0</u>	<u>2.40</u>	0.43	0.85

By estimating the race course of the LAC 2013 [3], it is possible to define at which  $V_T$  the constant cambered wing has to be adjusted into the twisted configuration "B" to achieve better performances.

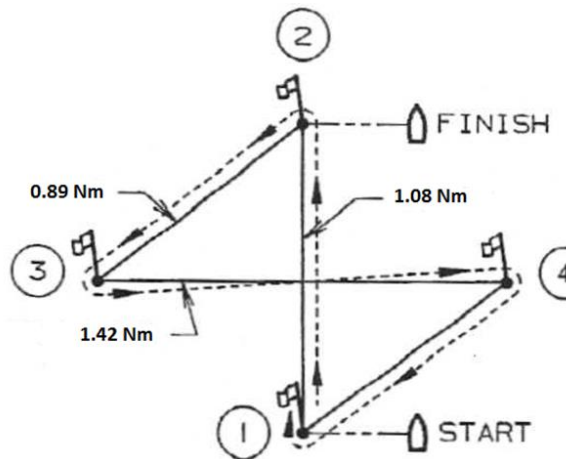


Figure 22: Sample Race track LAC 2013

The "constant cambered wingsail" and the twisted configuration "B" were sailed by the VPP along the new course of the LAC; the times in decimal minutes requested to finish the race for different  $V_T$  are reported in Table 8.

Table 8 Minutes to complete one lap for "Constant Cambered" and "Twist B" wingsail

VT [knots]	Constant camber [min of race]	Twist B [min of race]
4	137.3	142,0
6	88.6	91,7
8	66.6	67,9
10	55.2	54,7
12	44.9	44,6
14	41.1	39,0
20	35.7	32,4

From  $V_T=10$ knots (medium wind speed) the twisted configuration starts to prevail against the constant cambered wingsail. Moreover, as the breeze increases, the advantage around the track of the twisted configuration is higher.

## 7. CONCLUSIONS

The flexible catamaran rig with adjustable twist wingsail proved a viable method of answering specific design questions relevant to wing sail based high performance yachts. Specific conclusions are as follows

- (i) The heel angle reduces the performances of the catamaran, the optimum heel angle was found to be the flying angle (10 degrees) at which the windward demihull just sails clear of the water. Nevertheless, experiments have shown that downwind sailing is not affected by the heel angle to such a great extent as upwind.
- (ii) The upwind experiments showed a decreased induced drag for lower heel angles. The gap underneath the wingsail influencing performance. The importance of the gap is more marked in the tests conducted at 30 degrees of heel: the trampoline with the solid platform resulted in smaller induced drag. In other words, by using a solid trampoline to maintain constant the gap underneath the wing foot, the performances at high heel angle increases.
- (iii) The platform without the net was demonstrated to be the best option in terms of maximising drive force generated. The reason for this is the reduced drag of the trampoline. It is author's opinion that having a solid trampoline, able to generate a certain amount of lift in the direction of water, will produce righting moment useful in strong winds conditions. By adjusting the camber of the trampoline for light winds, lift can be generated to fly the windward hull. Nevertheless, the possibility of using a solid trampoline designed with an airfoil shape can be investigated in future research.
- (iv) As found in the experiments and confirmed in the VPP analysis, a negative spanwise lift distribution at the tip of the wing is beneficial for upwind strong wind conditions.
- (v) Sealing the gap underneath the wing foot did not improve the performances mainly due to the disturbed flow towards the wingsail's lower sections generated by the flying demihull. A visualization of the flow in wind tunnel (or CFD simulations) could have been beneficial to the understanding of the interaction and it should be motivation for future work in this area.

## 8. ACKNOWLEDGEMENTS

The Authors wish to thank The Royal Institution of Naval Architects for their willingness to allow publication and presentation of this research at the 23<sup>rd</sup> HISWA Symposium. This study was initially published in the RINA International Journal of Small Craft Technology (IJSCT) Part B2 2014.

## REFERENCES

1. Wellicome J. F., Some Comments on the Relative Merits of Various Wind Propulsion Devices. *Journal of Wind Engineering and Industrial Aerodynamics*, 20(1985) 11-142, Amsterdam.
2. Traut, T. et al, Propulsive power contribution of a kite and a Flettner rotor on selected shipping routes. *Applied Energy* 113, pp362-372, 2014
3. MacLane D.T., The Cogito project: design and development of an International C-Class Catamaran and her successful challenge to regain the Little America's Cup. The 13th Chesapeake Sailing Yacht Symposium, Annapolis, 2000.
4. Cloughton, A. Wellicome, J., Sheno, A., *Sailing Yacht Design: Theory*. Henry Ling Ltd, Dorset, 2006.
5. Scherer, J. Otto, *Aerodynamics of high performance wing sails*, SNAME CSYS, Annapolis, 1974.
6. Viola, I.M., et al, Upwind sail aerodynamics: A Rans numerical investigation validated with wind tunnel pressure measurements. *International Journal of Heat and Fluid Flow* (2012).
7. Wood, C.J., Tan, S. H., Towards an optimum yacht sail. *Journal of Fluid Mechanics*, vol. 85, part 3, pp. 459-477, 1978.
8. Andrews, T. et al, *Multihull America's Cup. Group Design Project*: University of Southampton, Southampton, 2011.
9. YET Lecture Notes, MSc in "Yacht and Small Craft": University of Southampton, 2011.
10. Campbell, I.M.C., Optimization of a sailing rig using wind tunnel data. SNAME 13th Chesapeake Sailing Yacht Symposium, Annapolis, 1997.
11. Campbell, I.M.C., The performances of off-wind sails obtained from wind tunnel tests. R.I.N.A. International Conference on modern Yacht, London, 1998.
12. Campbell, I.M.C., Cloughton A.R., Wind tunnel testing of sailing yacht rigs. 13th HISVA symposium, Amsterdam, 1994.
13. Jackson, P.S., Modelling the aerodynamics of upwind sails. *Journal of Wind Engineering and Industrial Aerodynamics* 63, 1996.
14. Campbell, I.M.C., A comparison of downwind sail coefficients from tests in different wind tunnels. *Innov'Sail*, Lorient, 2013.
15. Gentry, A., Studies of Mast Section Aerodynamics. In: *Proceedings of the 7th AIAA Symposium on the Aero/Hydrodynamics of Sailing*, Long Beach, California, 1976.

# DYNAMIC MEASUREMENTS OF PRESSURES, SAIL SHAPE AND FORCES ON A FULL-SCALE SPINNAKER

**J. Deparday**, Naval Academy Research Institute, France

**P. Bot**, Naval Academy Research Institute, France

**F. Hauville**, Naval Academy Research Institute, France

**D. Motta**, Yacht Research Unit, University of Auckland, New Zealand

**D.J. Le Pelley**, Yacht Research Unit, University of Auckland, New Zealand

**R.G.J. Flay**, Yacht Research Unit, University of Auckland, New Zealand

## SUMMARY

This work presents a full-scale experimental study on a sailing yacht in downwind conditions with simultaneous time-resolved measurements of pressures, sail shape and loads. Those on-water experiments on a J/80 class yacht permit the dynamic behaviour of the fluid structure system made of a light cloth sail and highly curved flow to be investigated. Aerodynamic forces on the asymmetric spinnaker were determined from pressure distribution and shape measurements and also from strain gauges located on the corners of the sail. Both time-averaged and instantaneous data are analysed.

The time-averaged pressures and forces were studied according to the apparent wind angle. The pressure distribution and thus the loads tend to decrease when the apparent wind angle is increased. The standard deviation of pressures was largest near the luff, decreasing downstream. Simultaneous time series recordings of the pressure distributions, flapping sail shapes, and forces in the sheets show a strong correlation. Flapping of spinnaker creates pressure peaks at the leading edge, increasing the aerodynamic forces dynamically by 50 to 70%. These results will also give reliable benchmark data to validate unsteady fluid structure interaction predictions from numerical simulations of downwind sails.

## NOMENCLATURE

AWA	Apparent Wind Angle
AWS	Apparent Wind Speed
Cf	Force coefficient $Cf = \frac{F}{\frac{1}{2}\rho S(AWS)^2}$
$\Delta Cp$	Difference of pressure coefficient $\Delta Cp = \frac{P_{leeward} - P_{windward}}{\frac{1}{2}\rho(AWS)^2}$
FEPV	Force Evaluation via Pressures and VSPARS
$\rho$	Density of air $\rho = 1.25 \text{ kg/m}^3$
S	Surface of the spinnaker $S = 63.1 \text{ m}^2$
TWS	True Wind Speed
VSPARS	Visual Sail Position And Rig Shape

## 1. INTRODUCTION

To improve sail design and investigate sail aerodynamics, wind tunnel testing (Viola & Flay (2009); Le Pelley & Richards (2011); Renzsch & Graf (2013); Campbell (2014)) and numerical simulations -with more and more Fluid-Structure Interaction models- (Viola et al. (2014); Renzsch & Graf (2010); Chapin et al. (2011); Ranzenbach et al. (2013); Trimarchi et al. (2013)) are largely used. However those methods are not perfect (Wright et al. (2009)) and full-scale testing is required for comparison and validation (Viola & Flay (2011)) since they permit to determine yacht performance in real sailing conditions.

Aerodynamic loads can be assessed in a variety of ways through on-water experiments. Sail boat dynamometers (Herman (1989); Hochkirch & Brandt (1999); Masuyama (2014); Fossati et al. (2013)) have helped to improve performance prediction. Measuring loads on the rigging lines and sails (Augier et al. (2012)) has contributed to a better comprehension on wind/rig/sail interaction. Measuring pressure distribution and flying shape of a full-scale sail (Viola & Flay (2010); Le Pelley et al. (2012); Lozej et al. (2012); Motta et al. (2014)) has permitted useful insights into sail aerodynamics.

However the steady approach has been mainly used on those experiments since most of wind tunnel tests and numerical models output time-averaged data. Some dynamic investigations have been carried out for upwind measurements at full-scale (Augier et al. (2012)), in wind tunnel (Fossati & Muggiasca (2012a)) and numerically (Fossati & Muggiasca (2012b); Augier et al. (2013); Augier et al. (2014)). For downwind conditions, the dynamic behaviour is mainly investigated by numerical models (Lombardi et al. (2012); Durand et al. (2013)) using Fluid-Structure Interaction models. The flying shape of the spinnaker is highly dependent on the dynamic trimming and the instability of the flow. It is complicated to reproduce

those conditions in a wind tunnel. This is why full-scale testing in downwind condition has been carried out in the perspective of a better comprehension of sail dynamics.

This paper reports on research on sail aerodynamics for downwind condition using full-scale experiments, created thanks to a collaboration between the Yacht Research Unit, University of Auckland, New Zealand and the Naval Academy Research Institute, France. The aim of this first experiment was to develop reliable and accurate methods for acquiring simultaneously aerodynamic loads, pressures and sail shape as well as trying to better understand the dynamic regime of a spinnaker. Those experiments were carried out in the bay of Brest, France on an instrumented J/80 class yacht.

## 2. EXPERIMENTAL SETUP

Figure 1 shows the arrangement of the sensors on the J/80 class sailing yacht. They measure various boat data (speed, boat motion, position, heading ...) as well as the wind data thanks to an ultrasonic 3D anemometer. Loads in the rigging and sails, the pressure and the flying shape of the spinnaker are also recorded. All sensors are linked to an inboard computer and communicate at their own frequency. Each sample is stored in a buffer at its own sampling rate thanks to a real-time acquisition software, RTMaps developed by Intempora. A resampling was applied during the post processing to obtain synchronous data for easier analysis. This setup is a further development of the experimental system presented in Augier et al. (2012). Load, pressure and flying shape measurements as well as the procedure applied are more detailed below.

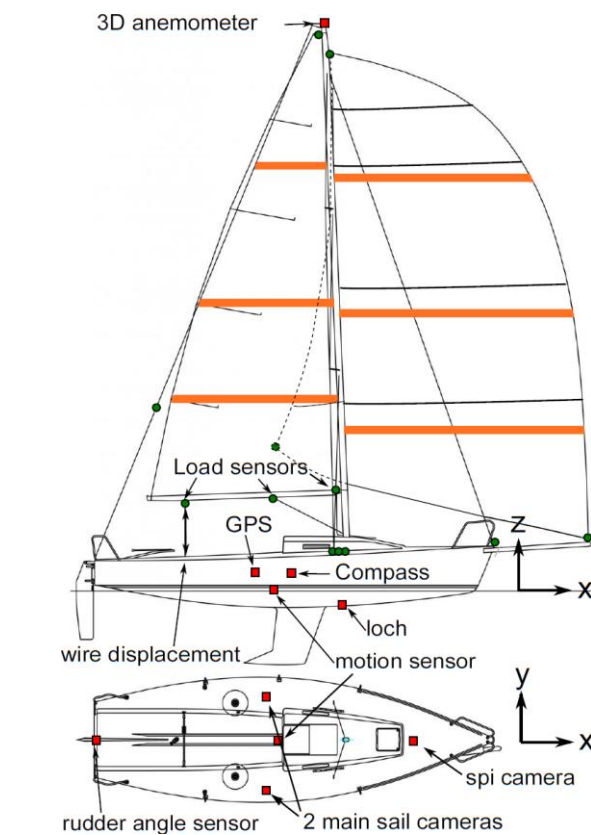


Figure 1 General Arrangement of system apparatus on J/80

### 2.1 Loads

The corner points of the spinnaker (head, tack, and clew) are fitted with instrumented shackles. The sensors communicate wirelessly to the acquisition system. The clew sensor is connected via a wire running along the foot to a small light box located near the tack point of the spinnaker. This box contains two strain gauge amplifiers, one for the tack sensor and one for the clew. A microcontroller receives and transmits instantaneously data to the receiver inside the boat via a wireless and low consumption ZigBee network. Another box is located at the head position for the head instrumented shackle. The sampling frequency of all those load sensors is 25Hz. The error of measurement is less than 2% of the measurement range of 5000N.

### 2.2 Pressures on spinnaker

Differential pressures between the pressure and suction sides are recorded at different points along curves of the spinnaker. Ultra-low range differential pressure sensors (Honeywell SXCL04DC) are stuck on the sail cloth on one side and face a 2mm-diameter hole to acquire the pressure difference. On the other side, a light sail cloth patch punctured as well is applied to smooth the surface of the custom built pressure system made at the Yacht Research Unit, at the University of Auckland.

Pressures are recorded along 4 horizontal stripes at different heights (see Figure 2). At 1/4, 1/2 and 3/4 of the spinnaker height, there are 12 transducers per horizontal stripe. The 4<sup>th</sup> stripe at 7/8<sup>th</sup> of the sail height has 8 transducers. There is a higher concentration of pressure taps near the leading edge, to be able to record leading edge suction peaks and similar features (see Figure 2). The pressure sensors have a sampling frequency of approximately 40Hz and the resolution and range of the sensors fit the criteria for sailing applications. The pressure acquisition system is described in more details in Motta et al. (2014).

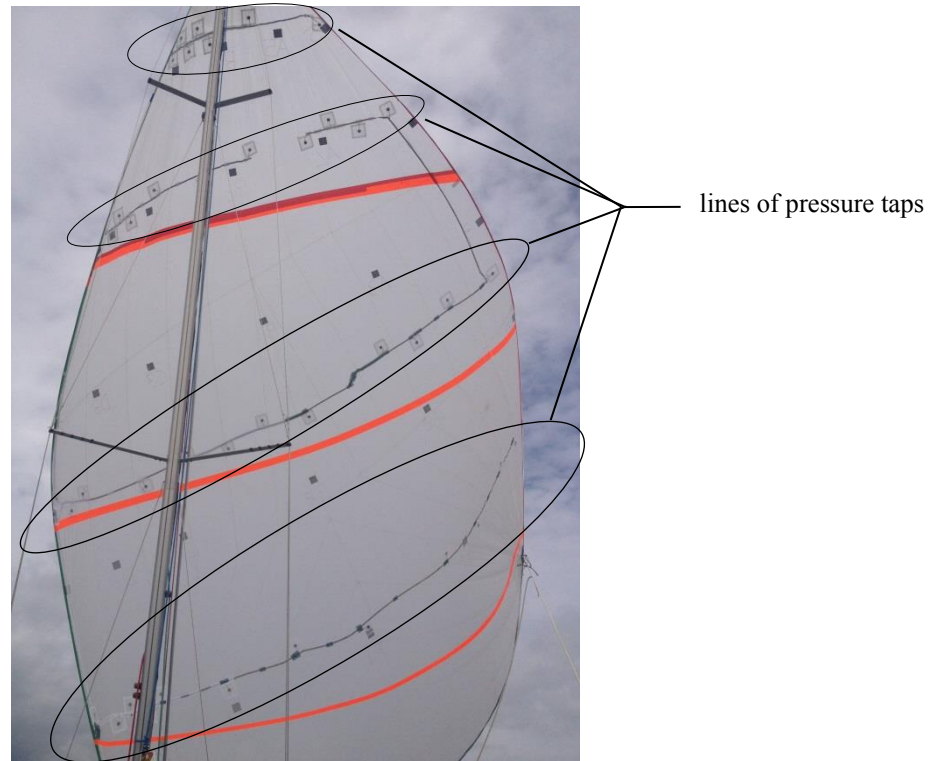


Figure 2 Picture of the spinnaker hoisted without the mainsail with VSPARS stripes in orange and lines of pressure taps

### 2.3 Flying shape

Three waterproof outdoor purpose GoPro Hero 2 cameras are mounted on the deck. Two are used for the mainsail, and one for the spinnaker. The video cameras have a frame rate of 25Hz, a good resolution (1280x960), and a wide field of view with an angle of 150°.

A sail analyser software VSPARS (Visual Sail Position And Rig Shape) is used during post-process to acquire the flying shape of the spinnaker. Three visualization stripes in orange are required at 20%, 40% and 70% of the sail height (see Figure 1 and Figure 2). The VSPARS system was developed in the Yacht Research Unit at the University of Auckland by Le Pelley and Modral (Le Pelley & Modral (2008)). The system is able to dynamically track the stripes, calculate the stripe coordinates in 3D space thanks to the known position of the camera and its distortion.

### 2.4 Force Evaluation via Pressures and VSPARS (FEPV)

The FEPV system uses the output files from VSPARS and the pressure system to obtain the aerodynamic forces and moments. From VSPARS, the 3D position of the stripes and the known tack and head positions permit to recreate the whole surface of the spinnaker. Unfortunately the foot shape cannot be captured by the camera as it is out of the camera field of view. Spline curves joining the leech points and the luff points are created and extended up to the known tack, head and clew positions. An optimisation process scales the foot in both longitudinal and transverse directions to match the calculated length. The sail surface is then interpolated by a fine quadrilateral mesh.

The pressure measurement system gives discrete pressure values. From the pressure tap positions taken as reference points, an interpolation scheme based on the Radial Basis Function interpolates the pressures to the centre of each geometrical cell of the mesh. Forces are computed by integrating the pressures on each cell area and directed with their normal direction. The system is more described in Motta et al. (2014).

### 2.5 Procedure

Sea trials were performed in the bay of Brest, offshore Ecole Navale. Those measurements are separated in two periods "1" and "2" corresponding to experiments carried out in the morning and in the afternoon. During both periods, the weather conditions were stable:

- average true wind speed: 6 m/s (12kts)
- gust: 8m/s (16kts)
- wind direction: 270° (westerly wind). Stable. Flat water.

The spinnaker was adjusted to be at the optimum trim. The trimmer did not fix the spinnaker sheet and could smoothly adjust to be on the verge of luffing at the leading edge. The Apparent Wind Angle (AWA) was kept constant as much as possible.

### 3. RESULTS

#### 3.1 Time-average results

At downwind courses, the environment is unsteady and dynamic: massively separated flow, flexible and soft sail, waves, helming, etc. Thus only time periods of 20 seconds were chosen where the standard deviation of the AWA was below 5° and of the Apparent Wind Speed (AWS) below 1kt (0.5m/s). In Figure 3, time series are shown during 40 seconds for the AWA and the load measured at the head of the spinnaker. When the standard deviations are below the thresholds, the 20s "stable" period is between the two vertical lines. To choose a "stable" period, only criteria on the input like the wind have been used. Loads are seen as an output and thus can fluctuate much more as shown in Figure 3. The average loads and pressure distribution are compared according to the AWA. A large range of AWA has been met in a rather constant TWS: from 5.8m/s to 7.1m/s thus between 11.2kts to 13.8kts.

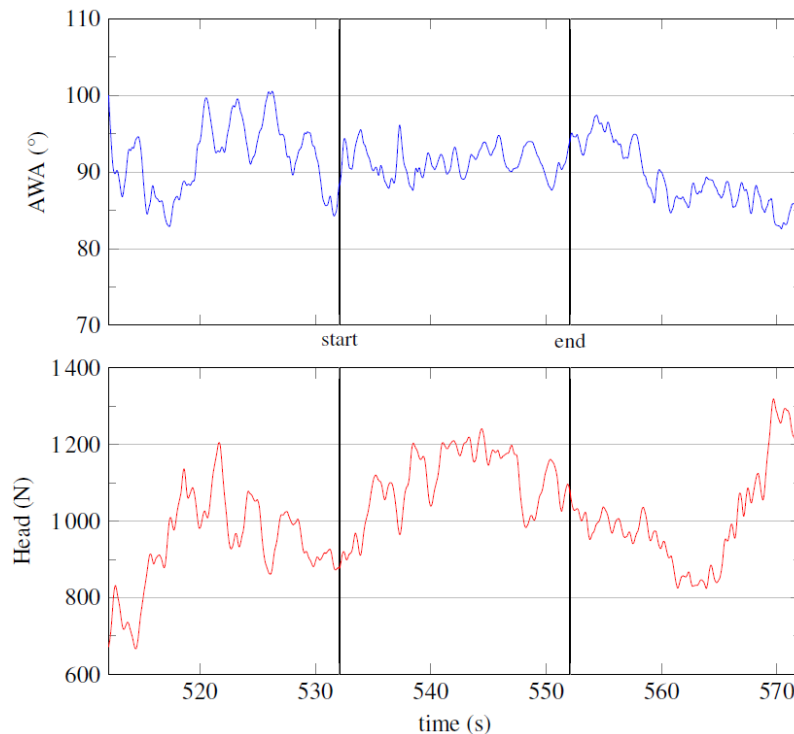


Figure 3 Evolution of AWA and the load measured on the head of the spinnaker during 40s of a run. 20s “stable” run detected between the two vertical lines

#### 3.1 (a) Spinnaker Loads

According to Figure 4, for the 3 corners the loads decrease when the AWA is increased. The highest load is found at the head of the sail. The tack load is in the same order of magnitude (around 1000N at 70° to 300N at 140°). Clew point is almost half loaded for tight angle till 90° whereas it has the same order of magnitude for AWA larger than 120°. The FEPV system calculates the total aerodynamic force produced by the spinnaker. From AWA 70-80° to AWA 120-150°, the aerodynamic force is divided by 3. Above 120°, it stays rather constant. The smaller loads at higher AWA are mainly due to the reduced AWS when running downwind.

To compare without the influence of the AWS, Figure 4 also shows the load coefficients. Head and tack force coefficients are rather constant according to the AWA and seem to slightly decrease for AWA larger than 110°. Whereas the clew force coefficient slightly increases in concordance with the smaller decrease rate of its load. The total aerodynamic force coefficient calculated by FEPV seems to slightly decrease when AWA is bigger than 110°.



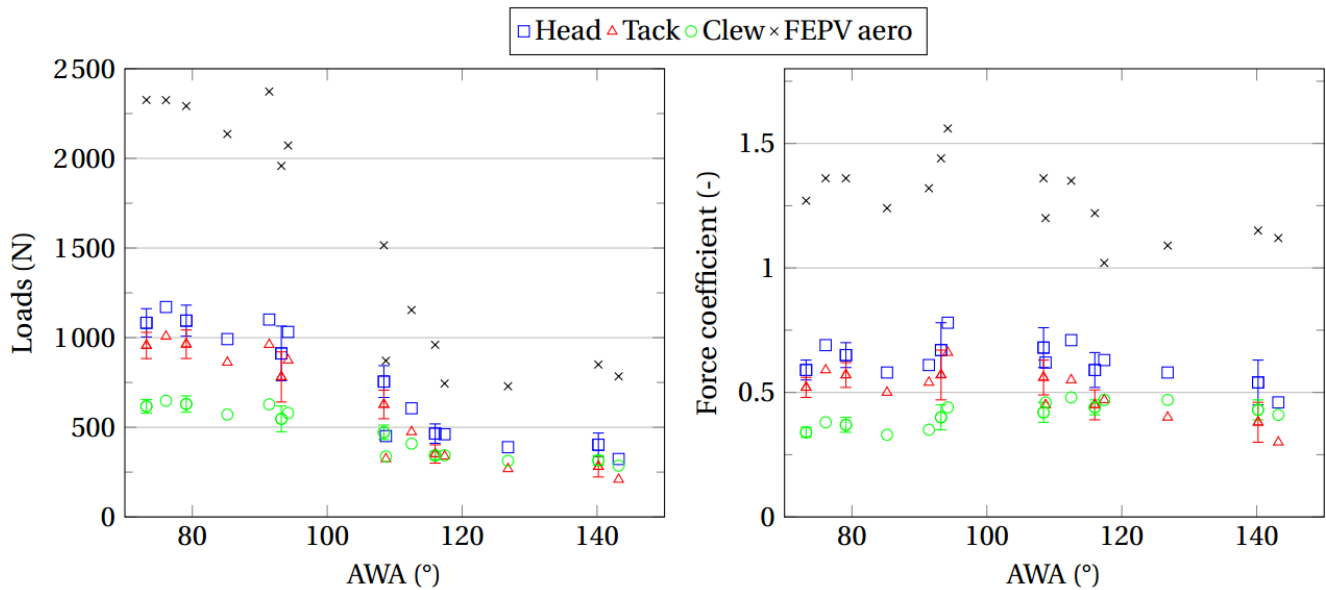


Figure 4 Loads on corners of the spinnaker.  
Error bars indicate the standard deviation obtained during one 20s “stable” run

### 3.1 (b) Pressures

Pressure measurements performed correctly even though in the afternoon the first stripe at 1/4<sup>th</sup> height of the sail did not record any measurements. However, we can compare the three stripes 1/2, 3/4 and 7/8 for most of the measurements.

Results are reported in Figure 5 for both tacks and for two periods of the day (in the morning and afternoon). In all figures, the pressure difference is leeward minus windward, thus giving negative values. The pressure coefficient plots have the negative direction upwards as commonly used. The suction is generally higher over the entire surface for lower AWA. At 3/4 and 1/2 stripes, the pressure distribution has similar behaviour. The leading edge suction peak is sometimes wide enough to be seen by the first pressure tap of the stripe. Then a pressure recovery is present at around 10 to 20% of the curve followed by a higher suction due to the sail curvature. Towards the trailing edge, the suction decreases. At 7/8<sup>th</sup> stripe, the pressure distribution is flatter and decreases along the curve. It is probably due to the more detached flow at the top of the spinnaker.

For tight AWA up to 120°, the trends of the pressure along the curve are similar for close AWA even for both tacks and at two periods of the day. It demonstrates a good repeatability. However for larger AWA the pressure distribution along the curve is more scattered. At higher AWA, it is more likely the air flow around the spinnaker is detached. Furthermore, due to lower AWS, the flying sail is less stretched and more curved. The entire sail shape is less stable, and therefore increasing the risk of collapsing and instabilities.

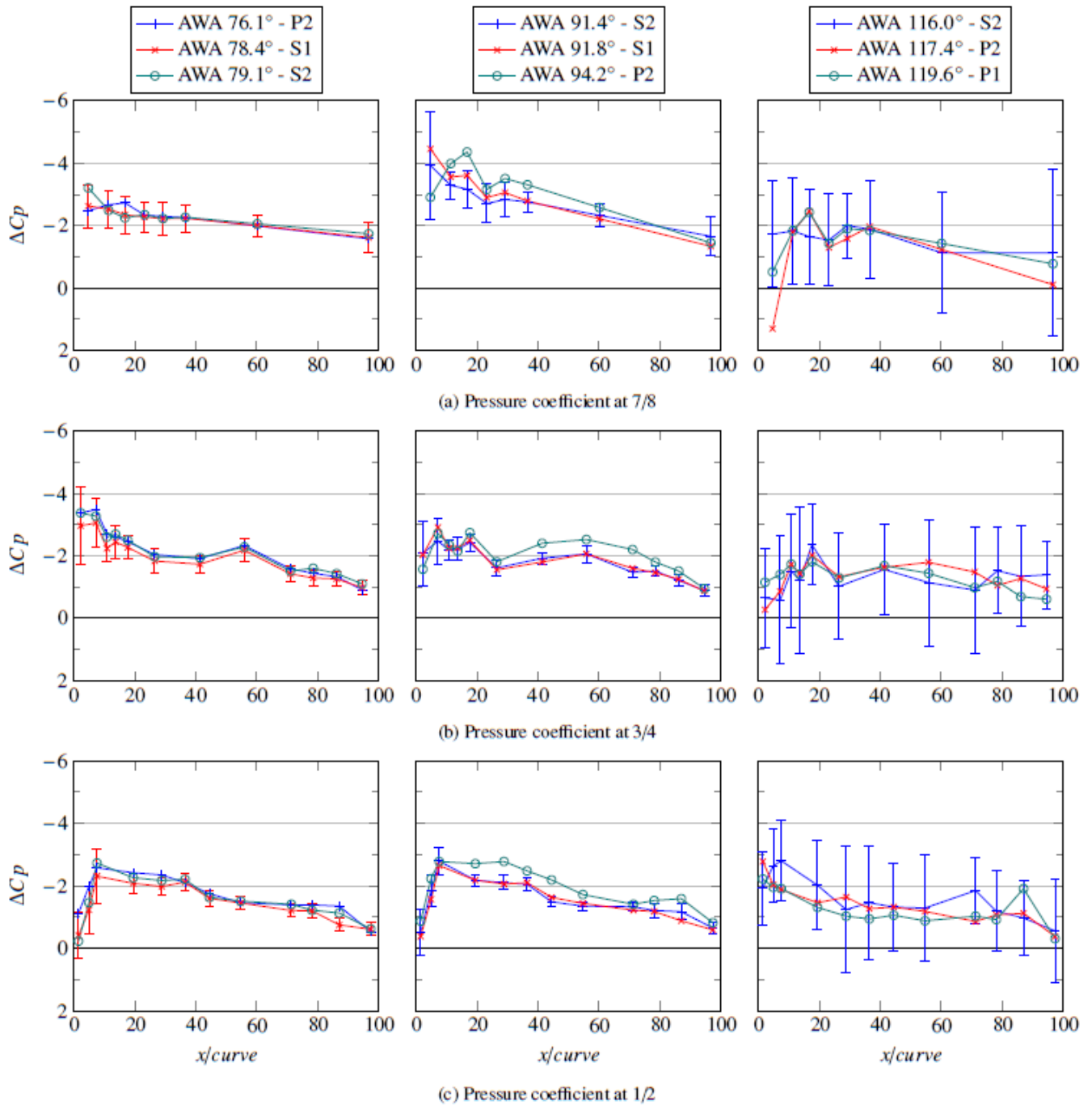


Figure 5 Differential pressure coefficients at different heights of the spinnaker along curve for different AWA.

P: Port tack, S: Starboard tack, 1: Set 1 (morning), 2: Set 2 (afternoon).

Error bars indicate the standard deviation during the 20s “stable” recording

### 3.1 (c) Standard deviations

Even during the “stable” runs where AWA and AWS are almost constant, pressure loads and flying shape fluctuate because of the unsteady nature of the “wind/spinnaker” system. This section presents the standard deviations of measured quantities to analyse the fluctuation amplitudes.

In Figure 4, standard deviations of loads are around 8% of the averages at the head and tack of the spinnaker for an AWA around 70-90°. Standard deviations for an AWA between 100° and 140° are around 11 to 20% of the average loads. The aerodynamic forces are highly dependent on the flying shape and thus the trimming. For greater AWA, as seen in Section 3.1 (b), the flying shape is less stable, resulting in larger variations of aerodynamic loads.

In Figure 5, for AWA between  $70^\circ$  and  $110^\circ$ , the standard deviation is rather small around 0.2, except at the leading edge where it is around 0.8 and can exceed 1. This higher standard deviation reveals the high suction peak and the flapping of the luff. For AWA bigger than  $110^\circ$ , the standard deviation of the pressure is much higher, of the same order of magnitude than the mean value of  $\Delta C_p$ .

Despite good repeatability of mean pressures and loads, the standard deviations highlight instabilities. At low AWA, at its optimum trim, the flying shape is very sensitive to the Angle of Attack. At high AWA, the flow around the spinnaker is massively separated and the shape is more unstable. The dynamic behaviour of the spinnaker for low AWA ( $78^\circ$ ) is more investigated in the next section.

### 3.2 Time-resolved results

For this section, we will only focus on a few seconds of a 20 second run where  $\overline{AWA} = 77.8^\circ$  and  $std(AWA) = 4.7 < 5^\circ$ . This run was chosen even if the mainsail was not hoisted, because the spinnaker was slightly flapping, the AWA was stable and the trimming of the spinnaker was fixed.

Flapping of spinnaker, high peaks of suction at leading edge, and extremum in forces are strongly correlated to each other as revealed in Figure 6.

Figure 6 describes space-time diagram of  $\Delta C_p(x, t)$  (Figure 6 (a) and (b)) and time series of  $\Delta C_p(t)$  close to the leading edge, at about 2% of the curve length (Figure 6 (c)) and force coefficients of corner loads (Figure 6 (d)). Positive pressure difference appears when the spinnaker is curling. Just before the spinnaker starts folding, the minimum of loads and suction are spotted. During the curling of the spinnaker, low suction area starts from the leading edge, evolves up to 15-20% of the curve, and then this area is reduced from the centre to the leading edge. During this diminution, high suction area replaces the low suction zone. So it occurs from 20% of the curve and reaches the leading edge at the end of the curling of the spinnaker. At that moment loads are also at their maxima.

For better explanation, we focus on 4 different instants, described in Table 1, of a flapping starting at 67.5s and ending at about 69s.

Minimum of suction and loads appear at *instant A*. Spinnaker loads are about 25% less than the average load recorded during this 20 second. At that moment, low suction areas are detected from 40% of the curve length up to the trailing edge, and also at the leading edge if the luff is folded like at the 3/4 stripe. The spinnaker starts luffing as snapshot a) of Figure 7 demonstrates. During a flapping, the minimum of suction does not appear when the spinnaker folds the most but before when the flying shape is almost full. As noticed just before instant "A", there is a loss of suction on the whole curve, thus sail cloth is less loaded. It might be the cause of the flapping since the spinnaker is less stretched.

*Instant B and C* are "intermediate" moments during flapping. For both heights, the low suction area increases from the leading edge up to about 15% of the curve length correlated with the increase of folded luff area. The maximum of luffing occurs and then the unfolding starts. The low suction area decreases from the inner part of the curve towards the leading edge. This low suction area is replaced by a very high suction zone which develops from 20% of the curve length to the leading edge. Nevertheless, this sequence does not occur at the same time for both heights. At instant B, the 3/4 stripe recovers and the low suction area is reduced while at the 1/2 stripe, low suction area is increased and the spinnaker starts luffing. At instant C, the latter stripe is still curling whereas the 3/4 has recovered its full shape (see snapshot b) and c) of Figure 7. The curling wave on the luff propagates downwards, as well as the recovery to full shape.

Figure 8 highlights also the change from a low suction area to a high suction region. The recovery of a curling to a full flying shape (instant C) produces high suction just behind the folded part of the sail. It also increases the suction from 20% up to the trailing edge. Despite the curling, high suction produced behind the folded area compensates and permits to increase the loads at the three corners of the spinnaker.

Maximum of loads and suction occur at *instant D*. The high suction area has reached the leading edge and produces also a peak of loads of about 35% higher than the average loads. As shown in Figure 8,  $|\Delta C_p|$  is much higher (about 1.5 more) than the average pressure distribution from 0 to 40% of the curve length and still slightly higher (about 0.5) up to 80 90% of the curve length. The maxima of suction at 1/2 and 3/4 heights occur exactly at the same time. The duration of this high suction peak is quite short compared to the period of curling especially at 1/2 height (1.5s of flapping compared to 0.5s of high pressure difference).

This short but strong increase of suction might be due to the fast recovery of the flying shape. The quick deceleration of the luff creates a "whiplash" giving a consequent added mass of air. It can also be related to a local increase of the flow speed amplifying locally  $\Delta C_p$ .

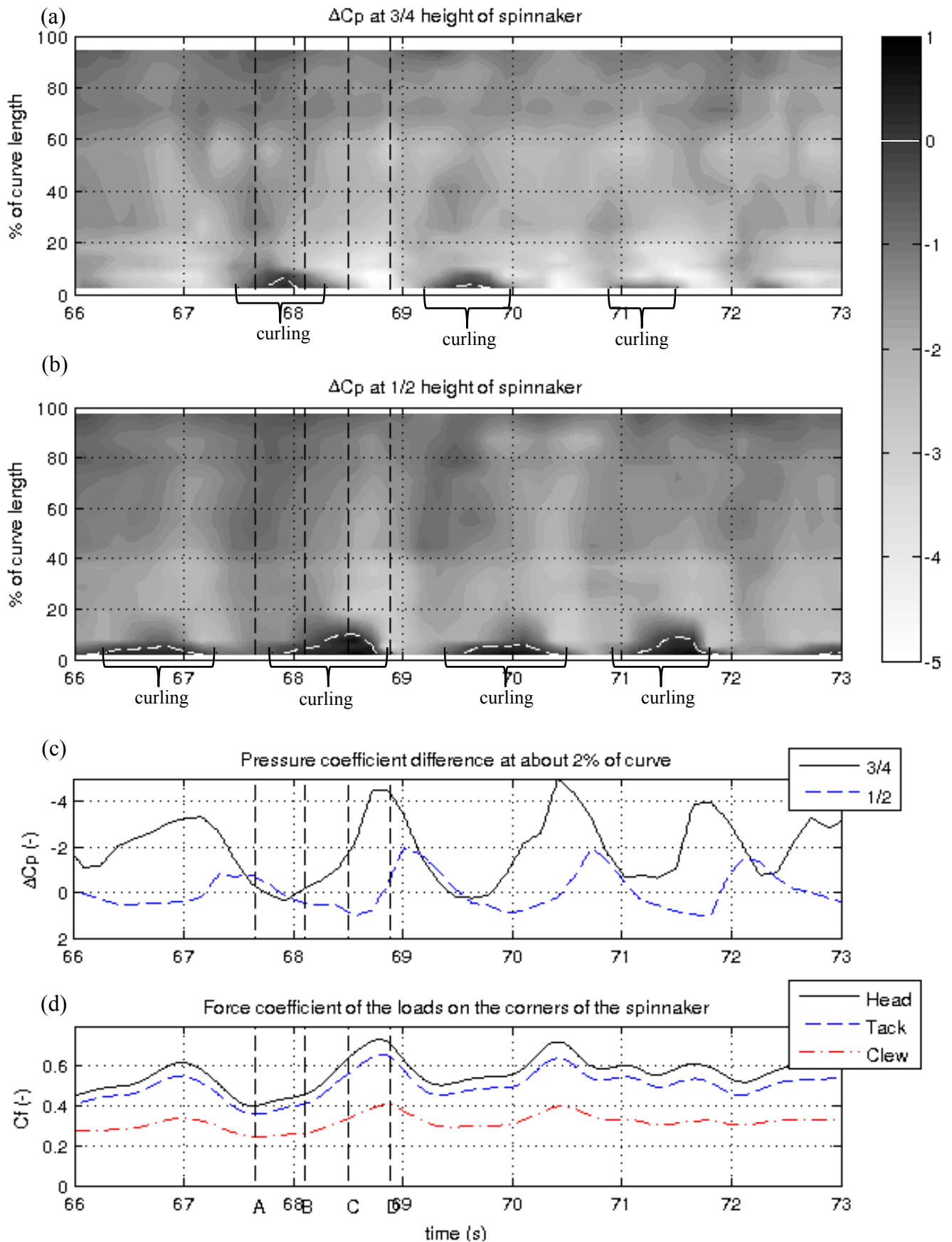
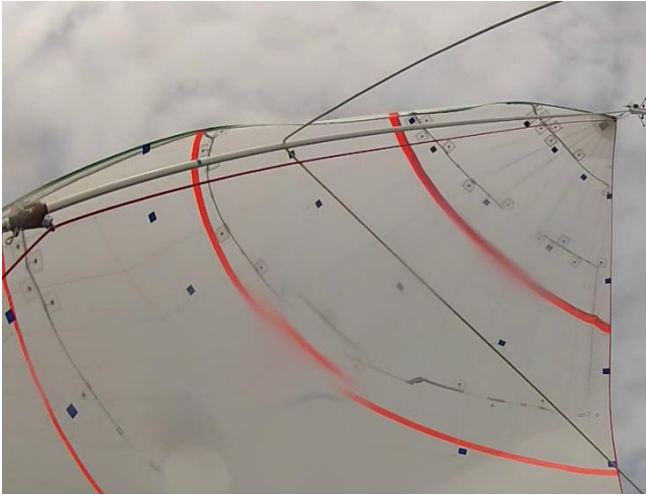


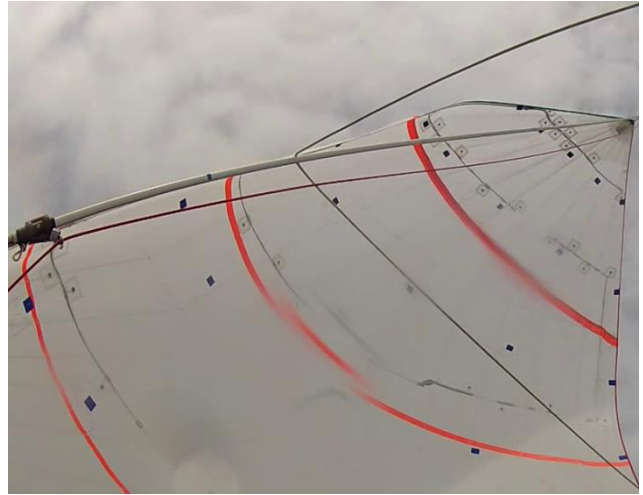
Figure 6 Evolution in time of the pressure distributions and loads on spinnaker  
 Space-time diagrams of  $\Delta C_p(x, t)$  at 3/4 height (a), at 1/2 height (b); time series of  $\Delta C_p(t)$  at  $x/c=0.2$  on both 3/4 and 1/2 height (c); time series of force coefficient of loads measured on the sail corners (d)

Table 1 Meaning of instants A, B, C and D

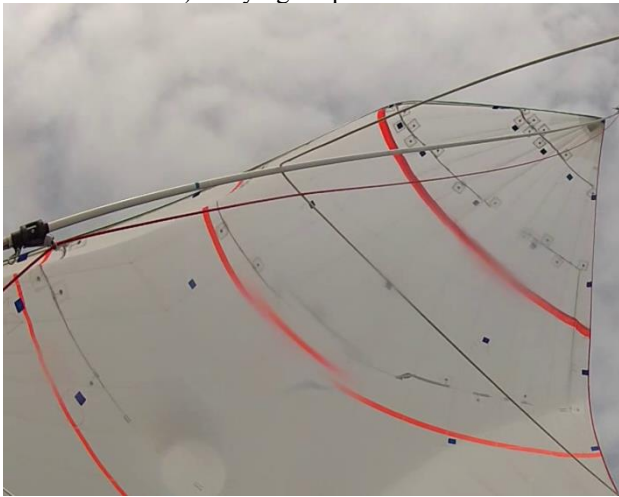
A	67.7s	Minimum of pressure and loads
B	68.1s	Intermediate step
C	68.5s	Intermediate step
D	68.9s	Maximum of pressure



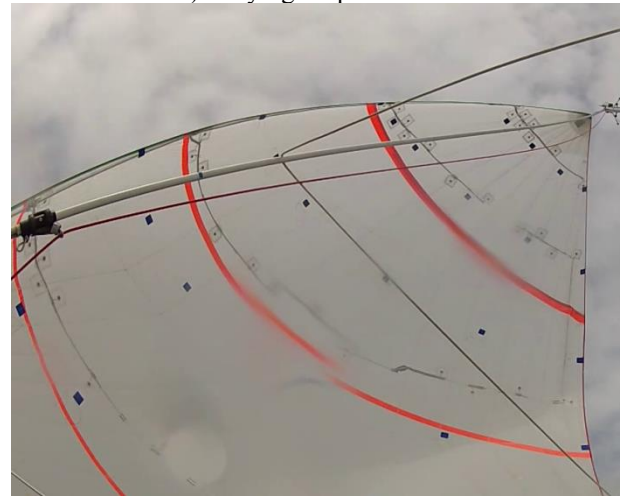
a) Flying shape for instant A



b) Flying shape for instant B



c) Flying shape for instant C



d) Flying shape for instant D

Figure 7 Snapshots of the flying shape during flapping

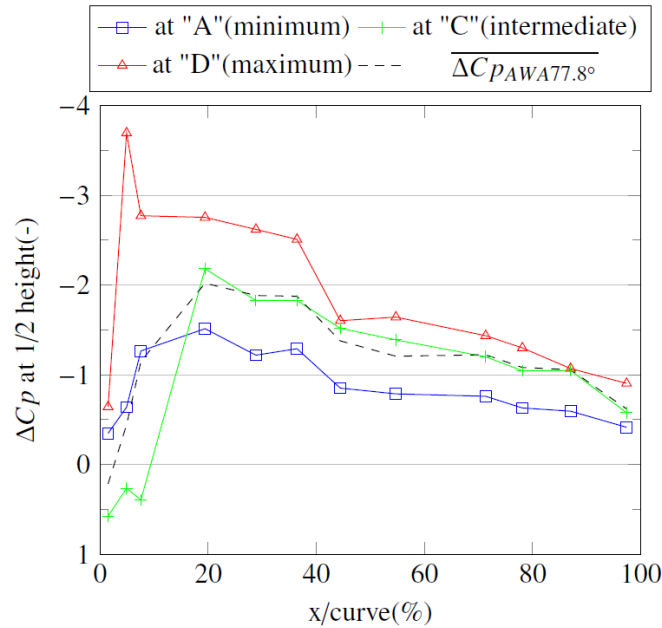


Figure 8 Details of pressure distribution at 1/2 height at minimum (A), when recovering (C), at maximum (D) and average pressure distribution for equivalent AWA for comparison

### 3.3 Spinnaker load and FEPV aerodynamic force measurement

In this section, we discuss the general trend and differences between spinnaker loads measured directly from load cells on the sail corners and aerodynamic force calculated by FEPV. For this process, FEPV calculations have been carried out every 5 frames (i.e. at 5Hz). At each instant, the force has been calculated combining the instantaneous sail shape (as obtained with VSPARS) and the instantaneous pressure distribution.

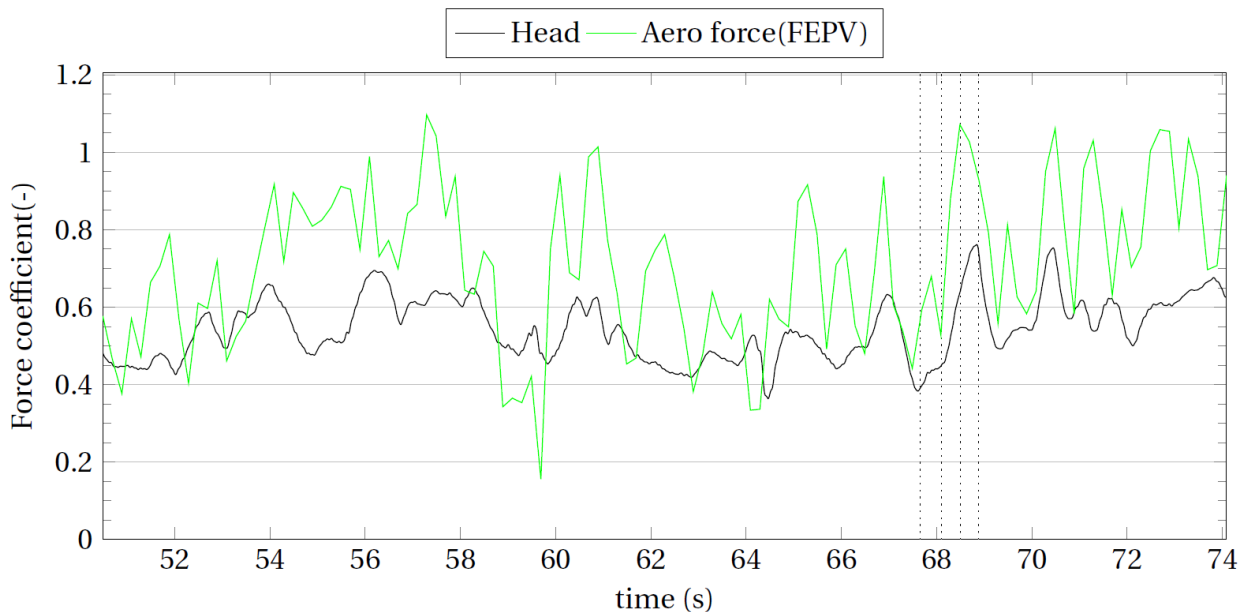


Figure 9 Evolution of dynamic force coefficient during 25s. Force coefficient measured at head of spinnaker (Head) and spinnaker aerodynamic force magnitude calculated by FEPV.

In Figure 9, the spinnaker aerodynamic force magnitude calculated by FEPV and the load measured at the head of the spinnaker are plotted. Since the directions of the loads on the corners were not measured, quantitative comparison is not relevant. However their dynamics can be observed. The trend is similar for both load coefficients. They have similar low frequency behaviour. The local maxima found in the head force coefficient also occur most of the time in the aerodynamic force. However the force coefficient calculated by an instantaneous flying shape and instantaneous pressure distribution varies on a bigger range and quicker than the force measured at the head of the spinnaker. The standard deviations explain as well the difference of dynamic attitude. For the aerodynamic force calculated by FEPV, the standard deviation is about 26% of the average, while for measured loads the standard deviations are only 13% of their mean values. The difference of

dynamics could indicate a damping effect between the dynamic pressure and the aerodynamic force given by the spinnaker to the sailboat. The dynamic viscoelastic behaviour of the sail cloth Nylon, but also of the sheets might give a structural damping. A variation of shape or the curvature itself might also absorb some energy and thus limit high speed variations of loads.

This difference of dynamic behaviour might also come from the amount of pressure taps on the spinnaker. High suction areas occur and disappear quickly in small local regions. A rough discretization might lead to overestimate or underestimate those peaks of pressure. The pressures and flying shape are highly correlated. Errors in the flying shape acquisition (especially at the leading edge) might increase the inaccuracy of force as well.

Nonetheless, the average aerodynamic force calculated by instantaneous shapes and pressures is 30% lower than the aerodynamic force calculated by an average shape and an average pressure distribution. If the FEPV computation is seen as an operator  $F$ ,  $\overline{F(P(x,t), Shape(t))} \neq F(\overline{P(x,t)}, \overline{Shape(t)})$  because pressures and flying shape are dependant variables to each other. This difference highlights the importance of the dynamic effects and the strong correlation between the flying shape and pressure distribution.

#### 4. CONCLUSIONS

Full-Scale experiments have been carried out on a J/80 sailing yacht in downwind condition where boat data, loads, pressures and flying shape on a spinnaker were simultaneously measured. From a steady approach, loads on the spinnaker decrease when running downwind. Despite clear trends according to the AWA, the variations of loads during a "stable" 20 second period are significant; the standard deviations are 10 to 20% of the average value while the standard deviation of the AWS is about 6% of the average. It is also confirmed by the pressure distributions on the spinnaker. A good repeatability of the pressure distribution is shown up to an AWA of about 120°, even though a high standard deviation is found especially at the leading edge, 30% of the differential pressure at the luff. For greater AWA, the standard deviation is in the same order of magnitude than the mean differential pressure itself; the AWS is lower and the flow around the sail more detached. Thus the entire sail shape is less stretched, more curved and less stable preventing optimal trim during long periods of time. This non-optimum trim and low dynamic pressure drive to greater pressure fluctuations increasing this instability.

Even for tighter AWA, there is a strong correlation between pressure, load and flying shape fluctuations. Minimum of suction appears just before the curling of the luff; and the recovery from the folded flying shape of the spinnaker creates a high suction peak at the leading edge. This might be due to the sudden deceleration of the sail cloth when it reaches its original full shape creating added mass of air. At that moment, the loads reach also a maximum.

However those high fluctuations of pressure are dampened. The transmission of the aerodynamic loads from dynamic pressure on the sail to tension in the lines acts as a low-pass filter maybe due to the curvature of the sail and the dynamic viscoelasticity behaviour of the sail cloth and of the sheets.

To even better assess the aerodynamic loading, FEPV system could be refined with a better discretised pressure distribution on the sail and more accurate flying shape acquisition with more VSPARS visualisation stripes. This is actually an on-going research. Further experiments will also be carried out with a more specific and stricter procedure to minimize any unwanted perturbations. Further studies will also focus on investigating the dynamics of the spinnaker for deeper AWA and analyse the influence of different parameters which could affect the spinnaker dynamic performance.

#### 5. ACKNOWLEDGEMENTS

This project has received funding from the European Union's Seventh Programme for research, technological development and demonstration under grant agreement No PIRSES-GA-2012-318924, and from the Royal Society of New Zealand for the UK-France-NZ collaboration project SAILING FLUIDS.

#### REFERENCES

- Augier, B., Bot, P., Hauville, F., Durand, M., "Dynamic behaviour of a flexible yacht sail plan", in *Ocean Engineering*, 66, pp.32–43, 10.1016/j.oceaneng.2013.03.017, 2013
- Augier, B., Bot, P., Hauville, F., Durand, M., "Experimental validation of unsteady models for fluid structure interaction: Application to yacht sails and rigs", in *Journal of Wind Engineering and Industrial Aerodynamics*, 101, pp.53–66, 10.1016/j.jweia.2011.11.006, 2012
- Augier, B., Hauville, F., Bot, P., Aubin, N., Durand, M., "Numerical study of a flexible sail plan submitted to pitching: Hysteresis phenomenon and effect of rig adjustments", in *Ocean Engineering*, (26 m), pp.1–10, 10.1016/j.oceaneng.2014.06.040, 2014
- Campbell, I.M.C., "A comparison of downwind sail coefficients from tests in different wind tunnels", in *Ocean Engineering*, pp.1–10, 10.1016/j.oceaneng.2014.06.036, 2014

- Chapin, V.G., de Carlan, N., Heppel, P., "A Multidisciplinary Computational Framework for Sailing Yacht Rig Design & Optimization through Viscous FSI", in *20th Chesapeake Sailing Yacht Symposium*, Annapolis, 2011
- Durand, M., Lothode, C., Hauville, F., Leroyer, A., Visonneau, M., Floch, R., et al., "FSI Investigation on Stability of Downwind Sails with an Automatic Dynamic Trimming", in *3rd International Conference On Innovation in High Performance Sailing Yachts*, Lorient, 2013
- Fossati, F., Muggiasca, S., "An experimental investigation of unsteady sail aerodynamics including sail flexibility", in *4th High Performance Yacht Design Conference*, Auckland, pp. 222–231, 2012a
- Fossati, F., Muggiasca, S., "Motions of a sailing yacht in large waves: an opening simple instationary modelling approach", in *22nd HISWA Symposium on Yacht Design and Yacht Construction*, Amsterdam, 2012b
- Fossati, F., Muggiasca, S., Bayati, I., "LECCO INNOVATION HUB SAILING YACHT LAB PROJECT A Sailing Research Infrastructure", in *3rd International Conference On Innovation in High Performance Sailing Yachts*, Lorient, 2013
- Herman, J.S., "A sail force dynamometer: design, implementation and data handling", Massachusetts Institute of Technology. 1989
- Hochkirch, K., Brandt, H., "Fullscale hydrodynamic force measurement on the Berlin sailing dynamometer", in *14th Chesapeake Sailing Yacht Symposium*, Annapolis, pp. 33–44, 1999
- Lombardi, M., Cremonesi, M., Giampieri, A., Parolini, N., Quarteroni, A., "A strongly coupled fluid-structure interaction model for wind-sail simulation", in *4th High Performance Yacht Design*, Auckland, pp. 212–221, 2012
- Lozej, M., Golob, D., Bokal, D., "Pressure distribution on sail surfaces in real sailing conditions", in *4th High Performance Yacht Design Conference*, Auckland, pp. 242–251, 2012
- Masuyama, Y., "The work achieved with the sail dynamometer boat "Fujin", and the role of full scale tests as the bridge between model tests and CFD", in *Ocean Engineering*, pp.1–12, 10.1016/j.oceaneng.2014.06.037, 2014
- Motta, D., Flay, R.G.J., Richards, P.J., Le Pelley, D.J., Deparday, J., Bot, P., "Experimental investigation of asymmetric spinnaker aerodynamics using pressure and sail shape measurements", in *Ocean Engineering*, 10.1016/j.oceaneng.2014.07.023, 2014
- Le Pelley, D., Modral, O., "V-spars: a combined sail and rig shape recognition system using imaging techniques", in *3rd High Performance Yacht Design Conference*, Auckland, pp. 57–66, 2008
- Le Pelley, D., Morris, D., Richards, P., "Aerodynamic force deduction on yacht sails using pressure and shape measurements in real time", in *4th High Performance Yacht Design Conference*, Auckland, pp. 28–37, 2012
- Le Pelley, D., Richards, P., "Effective Wind Tunnel Testing of Yacht Sails Using a Real-Time Velocity Prediction Program", in *20th Chesapeake Sailing Yacht Symposium*, Annapolis, 2011
- Ranzenbach, R., Armitage, D., Carrau, A., "Mainsail Planform Optimization for IRC 52 Using Fluid Structure Interaction", in *21st Chesapeake Sailing Yacht Symposium*, Annapolis, 2013
- Renzsch, H., Graf, K., "An experimental validation case for fluid-structure-interaction simulations of downwind sails", in *21st Chesapeake Sailing Yacht Symposium*, Annapolis, 2013
- Renzsch, H., Graf, K., "Fluid Structure Interaction Simulation of Spinnakers—Towards Simulation Driven Sail Design", in *21st HISWA Symposium on Yacht Design and Yacht Construction*, 2010
- Trimarchi, D., Vidrascu, M., Taunton, D., Turnock, S.R., Chapelle, D., "Wrinkle development analysis in thin sail-like structures using MITC shell finite elements", in *Finite Elements in Analysis and Design*, 64, pp.48–64, 10.1016/j.finel.2012.09.005, 2013
- Viola, I.M., Bartesaghi, S., Van-Renterghem, T., Ponzini, R., "Detached Eddy Simulation of a sailing yacht", in *Ocean Engineering*, pp.1–11, 10.1016/j.oceaneng.2014.07.019, 2014



Viola, I.M., Flay, R.G.J., "Force and pressure investigation of modern asymmetric spinnakers", in *International Journal of Small Craft Technology, Transaction RINA*, 2009

Viola, I.M., Flay, R.G.J., "On-water pressure measurements on a modern asymmetric spinnaker", in *21st HISWA Symposium on Yacht Design and Yacht Construction*, Amsterdam, 2010

Viola, I.M., Flay, R.G.J., "Sail pressures from full-scale, wind-tunnel and numerical investigations", in *Ocean Engineering*, 38(16), pp.1733–1743, 10.1016/j.oceaneng.2011.08.001, 2011

Wright, A.M., Claughton, A.R., Paton, J., Lewis, R., "Off-Wind Sail Performance Prediction and Optimisation", in *2nd International Conference On Innovation in High Performance Sailing Yachts*, Lorient, 2009

## “Can a Flapless Hydrofoil Provide a Realistic Alternative To a Standard Moth Foil With a Flap?”

James Robert Mackenzie  
Australian Maritime College Project Researcher, funkyjames99@yahoo.com.au

### *Abstract*

*Moth sailing dinghies are the first class to use hydrofoils throughout their fleet. The current main foil used on the moth has been fitted with a trailing edge flap, with a length of 30% of the chord. In 2006 Dr Ian Ward designed the first pivoting foil with an axel fitted at the quarter chord. This journal paper investigated the performance of a pivoting foil in comparison to a flapped foil. In order to compare the performance of the foils, numerical simulations were carried out and compared to experimental results. The experimental testing was carried out on a moth with full scale foils fitted and sailed at a range of True Wind Angles (TWA). During the tests, the boat speed was recorded at each heading in order to produce polar plots. The numerical simulation was carried out in a Velocity Prediction Program (VPP) called FS-Equilibrium. The simulation was carried out with a four degrees of freedom force balance. The wind strength was 8 m/s for experimental and numerical simulations. There was a variation between experimental and VPP results, with the un-flapped foil having the greatest boat speed in experiments and the flapped foil having the greater boat speed in the VPP. This variation was due to not all forces and moments been considered in the 4 degrees of freedom numerical model and turning manoeuvre's unable to be filtered from experimental results.*

**Keywords:** *Moth, Hydrofoil, Experimental, Velocity Prediction Program, Lift and Drag*

## 1. Nomenclature

<b>Symbol</b>	<b>Definition</b>	<b>Units</b>
$C_l/C_d$	Lift/Drag Coefficients	-
GPS	Global Positing System	-
h/c	Depth To Chord Ratio	-
TWA	True Wind Angle	<i>Degrees</i>
VPP	Velocity Prediction Program	-

## 2. Introduction

Sailboats fitted with hydrofoils have seen major advances over the last twenty years. The international moth class has been at the forefront of this development with world championships attracting over one hundred foil borne craft. The earliest developments were based around a tri-foiler concept and then evolved to a bi-foiler arrangement mostly developed by John Illett in Western Australia (Culnane, 2013).

In this study two types of fully submerged T-Foil hydrofoils used on a moth sailing dinghy were analysed to see which provides the optimum performance. The first foil was fitted with a flap that was located on its trailing edge at a distance of 30% of its chord length. The second foil was un-flapped and incident controlled by an axel fitted at quarter chord. The first design of T-Foil is used throughout the current fleet of moth dinghies. The second design of T-Foils tested and analysed are presently believed to be superior under some circumstances (Beaver and Zseleczy, 2009). In order to compare and verify the performance of the two foils, numerical simulations were carried out along with full scale testing. The wind strength for all tests was 8 m/s. In order to establish the hydrodynamic

performance of each tested foil an on- and off-design condition was established to show an area of operation where each foil was operating with a high drag penalty for the same baseline lift value. The un-flapped foil had one design condition due to its constant cross sectional profile. The flapped foil had two design conditions caused by varying camber created by its constant flap deflections. The numerical simulations were carried out in a Velocity Prediction Program (VPP) called FS-Equilibrium (Stewart et al., 2012). The simulation was solved for optimum Velocity Made Good (VMG) and a steady state solution in four degrees of freedom. The velocity prediction was carried out by means of a force balance, where a set of non-linear equations are solved for each degree of freedom in the simulation. These equations defined the forces and moments acting on the rig, hull and foils. The apparent wind direction and speed were determined from the boat speed and true wind direction and speed. The VPP relies on user modules to define the forces acting on the system. The main foil user module was altered for each design condition in the simulation as it is a function of lift and drag forces over a range of foil incidences. The full scale testing was conducted on a moth with full sized foils. The moth was fitted with a Global Positioning System (GPS) (Stewart et al., 2010), that recorded headings and boat speed. A support boat was fitted with an anemometer to record wind speed and direction. The data was then used to obtain TWA and boat speed by resolving the two vectors. The experimental and numerical results are represented by two polar plots that show boat speed as a function of true wind angle. Two headings were analysed to show an optimum VMG for windward leeward course racing.

### **3. Literature Survey**

#### **3.1 Experimental Research**

Beaver and Zselezky (2009) analysed hydrodynamic and aerodynamic efficiency of the foiling moth. The full scale testing showed that a foil with a ~30% flap could modulate lift up to about 45% of what would be achieved by globally changing the angle of attack of the lifting foil. This means a 2.2 degree change in flap angle is required to obtain the same result as a 1 degree foil angle change for an un-flapped foil. The best lift/drag ratios were when the flap angle is zero degrees. Experiments showed there was 11% less drag for a foil with flap at zero degrees than one with a high flap angle to achieve the same lift. The un-flapped foil also has reduced parasitic drag due to the elimination of the hinge line. In the experiments the foils were altered by operating the flap angle. If a foil with a smooth operating surface was introduced, such as the un-flapped foil, the results may have had a larger variance.

Miller (2009) investigated the merits of an electronic control system that could control the flying height of the moth. The system was designed with an un-flapped forward lifting foil. The use of the un-flapped foil was seen as an unlikely option, due to it been susceptible to damage during capsize and launching. This area needed development and testing before becoming a useable foil design. Another alternative design was the flapped arrangement. The flapped foil was concluded to be less efficient due to additional drag caused by the gaps on the hinge line.

Binns et al. (2008) studied lift and drag forces on a moth T-foil rudder for different Depth to Chord ratios ( $h/c$ ). Lift and drag forces varied with submergence from the free surface. As the  $h/c$  increased there was a decrease in drag and lift, due to free surface pressure relief. A simple design process was developed based on experimental data recorded. The design process was a function of skipper and boat mass,  $h/c$  ratio, angle of incidence, drag and lift forces. The results of the design process produce two simple curves that create the most efficient foil setup. These simple curves were used in this study to model the effect of the free surface on the performance of the T-Foils.

#### **3.2 Velocity Prediction Programs**

Previous work on hydrofoils in the moth class has been based on optimisation of foil systems and control. The use of VPP's has been a common tool used in new designs and optimisation of current systems used. Bögle et al. (2010) identified recent foil design was based on profile shape for reducing

the drag and increasing the lift coefficient. Other parameters such as plan form area and mechanical parameters of the control system had not been published at the time of writing. In order to compare different parameters of the foil and control systems, different states and sailing conditions needed to be found. The VPP was used to solve for a steady state solution. It was recommended that the outputs could be further improved by focusing on stability and not only boat speed. In order to achieve this accuracy additional force modules needed to be defined and existing ones updated. The end result would be conditions experienced by the sailor matching the solutions given by FS-Equilibrium. The work by Bögle et al. (2010) defined that by optimisation the moth could be more efficient at various points of sail. The mechanical characteristics in regards to control systems for the flapped and un-flapped foils were not investigated. The greatest difference would be wand loading and movement, which is a part of a control system based on foil angle of attack.

Hull (2011) created a VPP to model the moth and then compared results against GPS event data collected from Whaley and Alvazzi (2013) and wind speed data from Masters (2013). The modelled degrees of freedom was from four to six. The VPP predicted the performance of the moth with good accuracy. A conclusion from this work was that aerodynamic forces due to windage and sail efficiency required revision as this is a major component of the total drag force. Hydrodynamic forces could be improved by including added resistance due to waves. Ventilation is not taken in to account as studied by Emonson (2009), as ventilation only tends to affect the boat temporarily by removing all the lifting force from the affected foil. Ventilation could be a component that may need to be accounted for when studying the actuation of the two foil systems. FS-Equilibrium user modules programmed by Hull (2011), were used by the author for the numerical analysis.

Findlay and Turnock (2009) studied the use of a VPP as a design tool and the investigations were based around the moth. Upon further refinement it was found that the VPP could be used as a coaching aid to help the sailor understand the headings for the optimum VMG. The skipper placement and varied foil configuration could also be a function of optimum VMG. The studies were carried out over two years with moth foils evolving to have an elliptical profile with increases in aspect ratios. To improve performance these design characteristics were supported by empirical results from the VPP. As the moth is always evolving the computer algorithm could be evolved to include the un-flapped foil as it was not investigated in these studies.

### **3.3 Hydrofoil Configurations**

Hydrofoil configurations can be divided into two categories, fully submerged and surface piercing. This describes how the lifting surfaces are arranged and operate.

The surface piercing configuration is designed so that sections of the foil extend above the free surface while riding on the foils. Struts connect the foils to the hull of the vessel with sufficient length to support the hull free of the water surface when operating at design speeds. As speed is increased, the lifting force generated by the water flow over the submerged section of the foils increases causing the hull to rise and the submerged area of the foils to decrease. For a given speed the hull will rise until the lifting force equals the weight carried by the foils.

The foils of the fully-submerged configuration are designed to operate at all times under the water surface. The struts which connect the foils to the hull and support it when riding on the hydrofoils, mostly do not contribute to the total lifting force provided by the system. In the fully-submerged configuration, the hydrofoil is not self-levelling. A system must be installed in order to operate the effective angle of attack of hydrofoils to change the lifting force in order to respond to changing conditions of vessel speed, weight and sea conditions. Due to the hull flying in the air and supported by two struts, the hull is almost uncoupled from a seaway.

### 3.4 Types of Height Control

#### 3.4.1 Flapless foil

The flapless foil was originally built by Dr Ian Ward (Stevenson et al., 2004) and was the basis for numerous prototypes built by the author between November 2012 to March 2013. The foil has an axle at  $\frac{1}{4}$  of its chord. The foil is pivoted around the centre of pressure of the foil and allows for easy automation by a vertical push rod fitted to the trailing edge of the foil. The range of angular rotations for the foil is between 0.5 to 15 degrees. The foil used in the analysis has been built and sailed by the author over the last ten months and is shown in Figure 1. After sailing the foil for a period of time the author has found reduced gearing is required when compared to the flapped foil, as small angle changes produce large changes in lifting forces. Sailing the moth upwind the rudder lift was reduced in order to raise the bow and body weight was crucial in short step chop where the wave periods were irregular. To sail downwind the rudder lift was increased to pull the bow down and helped keep the hull in trim while running with the waves.

#### 3.4.2 Flapped Foil

The flapped hydrofoil has become the most common foil used in the moth class (Stevenson et al., 2004). It was first used in a championship by Garth Illett in 2003 in Western Australia. The flap is usually 30% of the chord and is located on the trailing edge of the lifting foil and runs the full span of the lifting surface. A positive flap deflection increases the camber of the foil and raises the maximum lifting force, while a negative flap deflection will reduce the camber and maximum lifting force on the foil. For a flapped foil the foiling height is controlled by adjusting the flap angle from positive to negative deflections usually in a range of -5 to 15 degrees. Since the first Illett design in 2003 the forward lifting foil has evolved from square tipped foil sections designed by Tom Speer to elliptical ends with bulbs around the intersection with the vertical strut. The current Mach 2 hydrofoil used on the world championship boat has all these features coupled with a smoother hinge arrangement when compared to earlier designs. The current speeds of the top boats are approaching 33 knots for a 10 second average. The flapped foil has been very successful due to the fact that it has been mass produced over many years and sailed by experienced sailors who have refined settings and control systems (Stevenson et al., 2004). The foil used in the analysis was designed by Alan Goddard. The foil is hinged on the top surface of the lifting foil with a strip of Kevlar impregnated with Sikaflex prior to the foil being laid up in the mould and a mono film fairing is placed on the lower edge of the foil as to close the gap created by the hinged surface. The author has tried quite a lot of techniques to reduce the gap, by tongue and groove arrangement, Sikaflex joint, Dacron centre hinge. The current foil has shown on the race course to be competitive with leading production moths, such as Bladerider or Prowler (Culnane, 2013). The vertical strut on the lifting foil is the same as the flapless arrangement.



Figure 1 Fully-Submerged Foil Configurations (Left), Surface Piercing design (Middle), (Stevenson et al., 2004). Un-flapped foil sailed by the author (Right).

### **3.4.3 Advantages of Flapless Foil**

The flapped foil requires significant flap movement to maintain the moth at a constant height while sailing in the water (Stevenson et al., 2004). At low speeds when the hull is in the water and low riding the flap is angled down and effectively increases the camber of the foil to induce lift of the hull. Though there is a high lifting force there is also a large amount of drag created at the same time. As the boat speed is increased the flap will assume a neutral position in order to reduce the lifting force generated by the foil. At this stage the foil is operating at its most efficient shape and the component of drag produced is at its smallest. The increasing speed will finally give rise to a requirement for a reduction of lift in order to maintain a constant ride height. This can also happen when the boat travels through wave peaks. At this stage the flap will be in the upward position and cancellation of lift is the result. In this operating condition the downward and drag forces are at their greatest values. The foil can do this more than twenty times in a minute and in effect the foil is not operating at the designed shape and has areas of operation where there is a high drag component generated.

The flapless foil uses the same theory for operation. This means a larger angle of attack at lower speeds and reduced angle of attack at higher speeds. The major advantage is that the cross sectional shape of the foil is constant at all angles of operation and will generate a smaller drag force than a flap except for when both foils are operating in their neutral positions. In sailing the flapless arrangement the author has found rather small movements of the foil is all that is required in order to control the ride height. The major refinement at this stage is the gearing to gain this control. In setting up the angles for flight of the foil the angle of attack is set at 0.5 degrees as a minimum and up to 14 degrees maximum. The concept is far removed from the methodology embraced by the flapped foil, where there is a negative flap angle needed for the down force. Essentially the key variable is boat speed. The slower the boat more angle of attack is required to lift the boat. As speed increases the angle of attack reduces to compensate the increase in speed in order to maintain a constant ride height. This means a negative angle of attack is never needed on the flapless foil.

## **4. Analysis Methods**

### **4.1 FS-Equilibrium Velocity Prediction**

The VPP software used in the analysis was FS-Equilibrium, which is distributed by Stewart et al. (2012). The velocity prediction was done by means of a force balance, where a set of non-linear equations are solved for each degree of freedom in the simulation. These equations define the forces and moments acting on the rig, hull and foils. The apparent wind direction and speed are determined from the boat speed and true wind direction and speed. The VPP relies on user modules to define the forces acting on the system. The user modules used in the analysis were originally programmed by Hull (2011). The main foil user module was altered for each design condition in the simulation as it is a function of lift and drag forces over a range of foil incidences. The main foil user module used formulas derived from experimental work done by Binns et al. (2008). Where there are four multipliers that are a function of lift and drag coefficients that are calculated and plotted against foil angle of attack. These values are then used to calculate the forces and moments on the main foil and used to obtain a steady state solution.

### **4.2 X-Foil**

X-Foil is an interactive program for the design and analysis of subsonic isolated aerofoils (Drela and Youngren, 2008). The two dimensional lift and drag coefficients used in the analysis were obtained from X-Foil. The simulations were run with a viscous solution and a free stream velocity of 8 m/s. The Ncrit command was used to model boundary layer separation and Reynolds number affects. The two dimensional lift and drag coefficients were then converted to three dimensional values by using lifting line theory (Alberte E. Von Doenhoff, 1948). Lifting line theory is a function of foil aspect ratio which accounts for geometrical properties of the foil.

#### 4.2.1 X-Foil Lift/Drag Coefficients

The range of flap deflections used in FS-Equilibrium were between -5 to 15 degrees relative to the neutral lift angle. The flapped foil was modelled using its 30% trailing edge flap and the un-flapped foil was an incident controlled surface with no flap. The theoretical X-Foil lift on drag coefficients ( $C_l/C_d$ ) are shown in Figure 2. For angles of attack between -1 to 3 degrees the un-flapped foil is the most efficient with the largest  $C_l/C_d$ . Either side of this range the un-flapped foil has a higher drag value than that of the flapped foil.

As stated earlier two dimensional lift and drag coefficients were calculated in X-Foil. The values were converted to three dimensional values by using Lifting line theory. For the range of flap deflections specified in the main foil user module lift and drag coefficient variances were specified relative to a neutral flap angle. These inputs were then used in equations derived from experimental work conducted by Binns et al. (2008). FS-Equilibrium uses the values in its four degrees of freedom force balance.

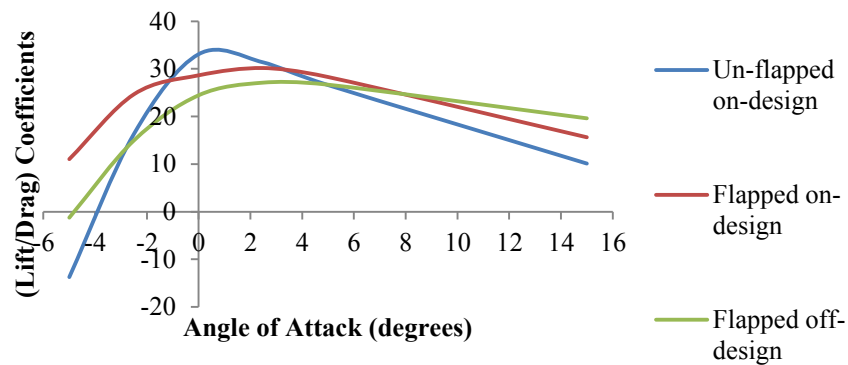
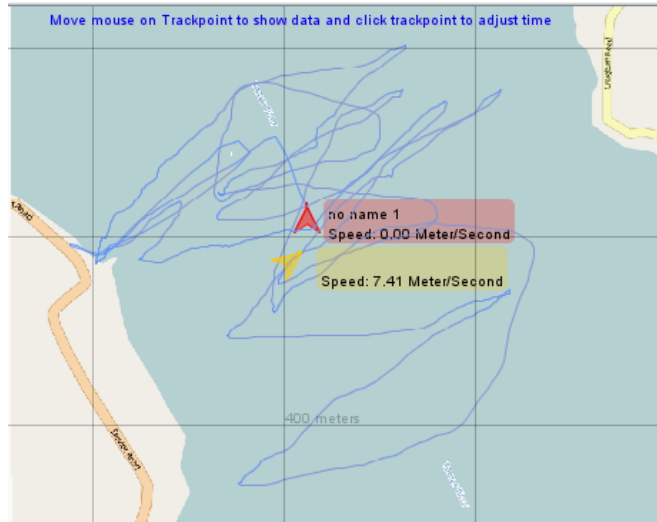


Figure 2 X-Foil coefficients for lift/drag relative to angle of attack.

#### 4.3 Full Scale Testing

The testing was carried out on the Tamar River. Three sessions were done back to back in order to test each design condition. The wind strength ranged from 9 to 20 knots. Wind data was collected from a support boat in intervals of a minute. The average wind angle had no major shift over the three test runs. The moth and support boat were both fitted with GPS. Once the testing was completed GPS data for the moth and support boat was loaded into software from Stewart et al. (2010) called GPS action replay. The data provided individual tracking points where speed and headings were tabulated for given time steps. A screen shot of the un-flapped foil session in GPS action replay is shown in Figure 3. The data was processed around a design wind of 8 m/s. Wind recordings of 1.3 m/s either side of this value were considered acceptable for the testing. The greatest distance the moth travelled from the support boat during testing was 500 meters and considered acceptable as the wind direction was constant for all given time intervals.



**Figure 3** GPS Action replay screen shot of un-flapped foil test session. The red arrow shows the position of the stationary wind anemometer boat, the yellow arrow and blue track line shows the instantaneous position and track of the moth fitted with the un-flapped foil.

#### 4.4 Foil Design Condition Selection

In order to evaluate the full performance envelope of each foil an on- and off-design condition was established for the analysis. When the foils were positioned at their neutral angle of attack they were required to lift 110 kg. The on-design condition was when the foil had the optimum setup for a wind of 8 m/s. At this wind strength the foil was in its most efficient shape where a high  $C_l/C_d$  was produced. The off-design condition was created to show an area of operation where the foil potentially had a reduction in efficiency. The condition was designed for light winds where a greater angle of attack is needed to lift the total mass. If the wind speed then increases whilst sailing (thus precluding, the ability to change design setups), a negative deflection of a control surface is required to provide the same lift force to that of the on-design condition. The flapped foil controls the lift force by altering its flap angle and acts as a control surface. This means the flapped foil has a varied cross sectional shape that is a function of flap deflection. As the foil cross sectional shape and camber vary two design conditions were established. Due to the off-design condition having a larger angle of attack, a greater negative flap deflection was required in order to produce the required lift force. The un-flapped foil had one design condition as the foil cross section was constant for all angles of operation. The ride height of the un-flapped foil is controlled by pivoting the whole foil at  $\frac{1}{4}$  of its chord. The setup of the three design conditions for a design lift of 110 kg at 8 m/s boat speed is shown in Table 1.

**Table 1** Three design conditions for a design lift of 110 kg at 8 m/s boat speed.

Foil Type	Foil Angle of Attack for 110 kg, (deg)	Flap Angle, (deg)
Un-flapped	3.86	N/A
Flapped on-design	1.54	0
Flapped off-design	10	-12.8

#### 4.5 Flap Deflection

The foiling height of the moth is controlled by altering a control surface on the main foil. The foil deflections are created in order to alter the oncoming fluid flow and alter the lifting force as a function of foiling height in the vertical plane. In Figure 4, flap deflection and angle of attack are shown for all design conditions.

The un-flapped foil only had one design condition due to the constant cross sectional shape for all angles of incidence. The zero flap angles for all foils was set for a mass of 110 kg. The un-flapped foil



had a slightly greater angle of attack due to it having a symmetrical foil section. The flapped foil was an asymmetrical foil section. The flapped off-design condition was created to show an area of operation where the foil potentially had a reduction in efficiency.








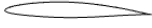

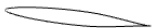








CONDITION	Un-flapped on design	Un-flapped Total lift (kg) @ 8 m/s wind	flapped on-design	flapped-on Total lift (kg) @ 8 m/s wind	flapped off design	flapped-off Total lift (kg) @ 8 m/s wind
-5 degrees		31.83		33.92		-4.06
-2.5 degrees		38.21		88.99		53.06
0 degrees		110.00		110.00		110.00
+2.5 degrees		181.23		195.72		166.31
+5 degrees		249.32		242.02		221.17
+15 degrees		391.21		341.73		398.56

Figure 4 Flap deflection & angle of attack for design conditions analysed in FS-Equilibrium.

## 5. Results

### 5.1 FS-Equilibrium Simulation

Three individual simulations were run in FS-Equilibrium. Each design condition required altering of the main foil user module in order to represent the varying change in foil cross sectional shape. Once the FS-Equilibrium simulations were completed polar plots for TWA relative to boat speed were produced. In the range of TWA there are two sailing conditions to be considered. The first is the low riding condition when the moth is predominately supported by hull buoyancy forces. The second is the foiling condition where the moth is fully supported by the two hydrofoils. Once flying on the hydrofoils the un-flapped foil outperformed the flapped foil. In respect to the flapped foil, the on-design was more efficient while foiling. In the low riding condition the flapped design conditions had a small variance on their performance with the off-design providing the greatest boat speed. The un-flapped foil produced the lowest boat speed in the low riding condition. A polar plot for all three design conditions is shown in Figure 5.

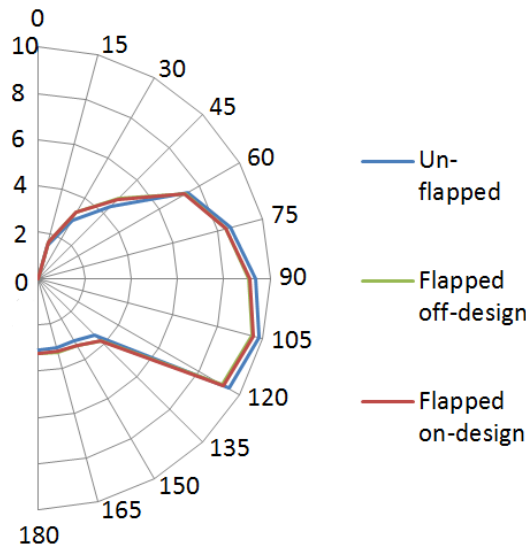


Figure 5 FS-Equilibrium polar plot of boat speed relative to TWA. Due to line weights and small variances in boat speed, the percentage differences for the flapped design conditions are also shown in Figure 6.

### 5.1.1 Optimum VMG

An optimum VMG for upwind and downwind sailing was selected in order to replicate windward leeward racing. These angles were selected as windward leeward courses are the standard course structure for all international moth championships (Stevenson et al., 2004). The wind strength for all simulations in FS-Equilibrium was 8 m/s. The two TWA selected for the optimum VMG was 60 degrees for upwind and 120 degrees for downwind sailing. For both selected TWA the un-flapped foil had the greatest VMG. The VMG and percentage variance relative to the un-flapped foil is shown in Table 2.

Table 2 The VMG and percentage variance relative to the un-flapped foil.

Foil Type	VMG,(m/s) @120 degrees	$\Delta$ speeds relative to un-flapped foil @120 degrees (%)	VMG, (m/s) @ 60 degrees	$\Delta$ speed relative to un-flapped foil @60 degrees (%)
Un-flapped	-4.81	0	3.64	0
Flapped on-design	-4.64	3.45	3.56	2.25
Flapped off-design	-4.62	4.11	3.6	1.11

### 5.1.2 Performance of Flapped Design Conditions

The flapped design conditions had two areas of operation where one out performed the other. As shown in Figure 5, the moth was foiling for TWA between 60 to 120 degrees. For TWA outside of this range the moth was low riding. For TWA between 35 to 75 degrees the flapped off-design foil had the greatest performance. This implies when wind ward sailing there is an advantage to have the foil set in the off-design condition where a greater lift force is required for the moth to remain foiling. For TWA between 75 to 130 degrees the on-design condition had a speed advantage. The greatest variance in boat speed was between TWA of 105 to 130 degrees where the on-design condition had a significant speed advantage. In this range the maximum speed was recorded in FS-Equilibrium. These headings also represented maximum angles the moth can sail without coming off its foils. This shows that a higher foil camber attracts a larger drag penalty sailing at these headings. For TWA between 130 to 180 the moth was low riding with the off-design performing the best. In Figure 6 percentage variance

for the two flapped design conditions is shown, where a positive value is a performance advantage to the flapped on-design foil.

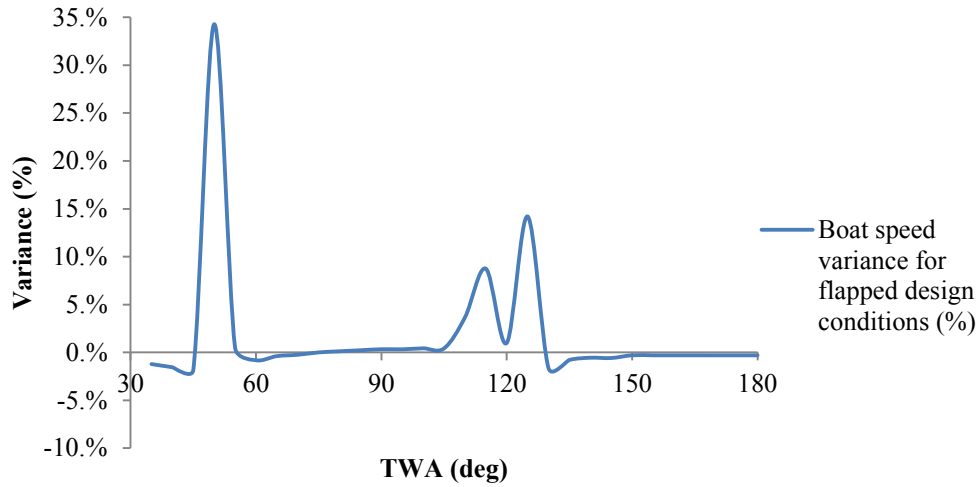


Figure 6 Percentage variance of boat speed for the two flapped design conditions. The range of TWA was between 35 to 180 degrees.

### 5.1.3 Performance of Flapped Design Conditions While Foiling

As shown in Figure 7, the flapped on-design foil has the greatest boat speed for most TWA while sailing on hydrofoils. For windward sailing angles there is a smaller variance when compared to downwind sailing angles. For sailing angles between 55 to 125 degrees the flapped on-design condition has the highest  $C_l/C_d$  value. At sailing angles where the moth is low riding the off-design condition has the higher  $C_l/C_d$  value. These results show that a higher  $C_l/C_d$  means greater boat speed for most TWA.

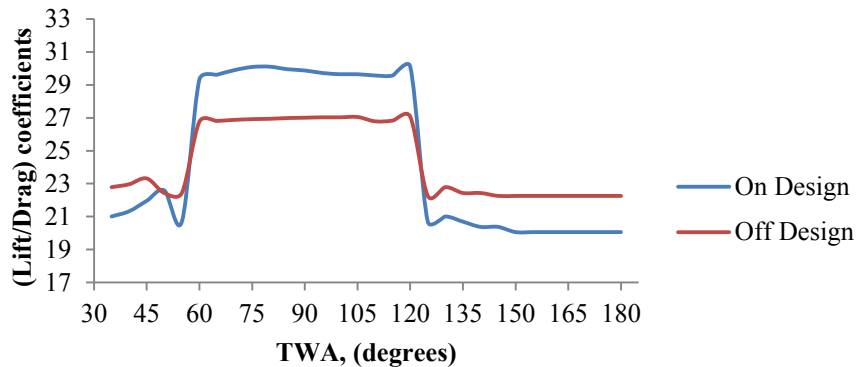


Figure 7 (lift/drag), coefficients as a function of TWA. For the 2 flapped design conditions.

### 5.1.4 Average Flap Angle

The average flap angle in FS-Equilibrium for all three design conditions is shown in Figure 8. The smallest flap deflections are for TWA of 60 to 120 degrees. In this range the moth is riding on hydrofoils and a smaller lift force is required from the main foil. For TWA outside of this range the moth is low riding and a greater flap angle is used in order to generate a greater lifting force.

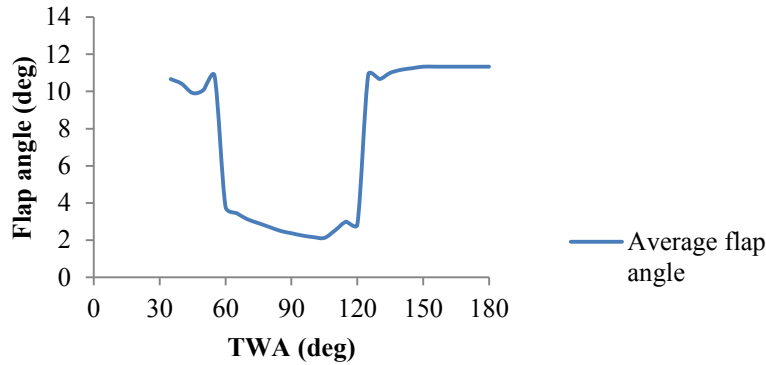


Figure 8 Average flap angle for all design conditions in FS-Equilibrium.

## 5.2 Full Scale Testing

The results showed a slight variance to that of simulation results. The flapped on-design foil had the greatest boat speed for all angles of sail. When sailing upwind the flapped on-design foil could foil at a TWA of 12 degrees while the other two conditions were not foiling till TWA of at least 30 degrees. As Beaver and Zselezky (2009) showed greater flap deflections are required to generate the same base lift value to that of the un-flapped foil. The un-flapped foil requires smaller adjustments to fly and reduced gearing than that of the flapped foil. The wand gearing was kept constant for all design conditions. This may explain why the flapped foil was foiling in testing at a greater range of TWA. This variable was not picked up in the numerical analysis as it set for a steady state solution. The flapped off-design had the worst performance across most headings and concurs with FS-Equilibrium results. In Figure 9 experimental results are represented by a polar plot of boat speed relative to TWA for all 3 design conditions.

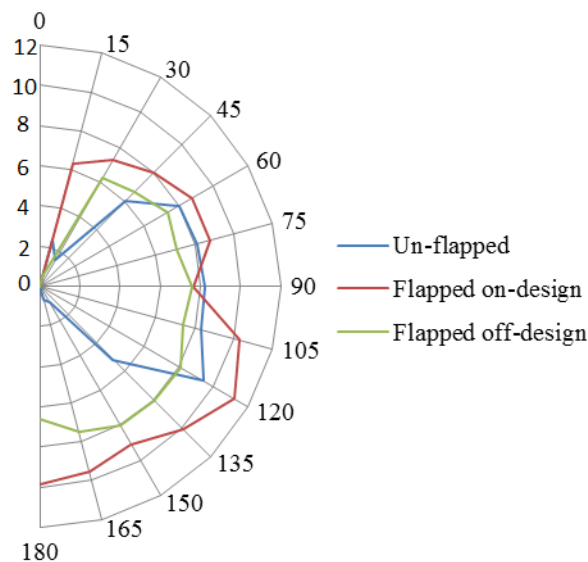


Figure 9 Polar plot of experimental results for all 3 design conditions.

### 5.2.1 Performance of Experimental Flapped Design Conditions

The flapped design conditions showed a variance to that of the numerical values. In full scale testing the moth was foiling for TWA between 30 to 180 degrees. Data for TWA between 0 to 30 degrees was inconclusive as the minimum leeway angle for upwind sailing was on average 25 degrees for both design conditions. This means only one the foiling state of the moth can be accurately

analysed. At TWA between 110 to 120 degrees both foils reached their maximum speed and was also where the greatest variance occurred between the two design conditions. The performance of the flapped on-design verifies that it was the most efficient of the two design conditions. The averaged variance for all TWA is shown in Table 3.

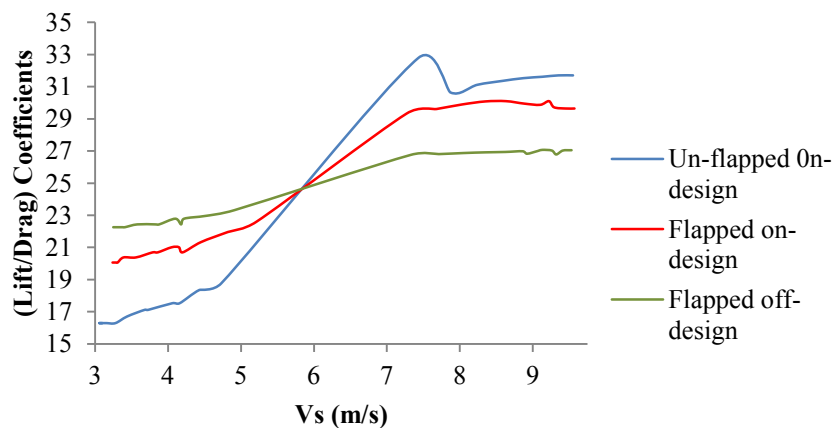
**Table 3 Experimental variance for flapped foil design conditions.**

TWA (degrees)	Description	AVG % Variance
35-75	On design foil has speed advantage.	21.254
80-105	On design foil has its smallest speed advantage	20.3
110-120	On design foil has its largest speed advantage	39.351
125-180	On design foil has speed advantage	29.071

## 6. Discussion

### 6.1.1 Foil Efficiency as a function of Hull Speed

In FS-Equilibrium user modules are used to define foil and flap deflections. This is a function of hull sinkage and is measured from the vertical datum point. In Figure 10, coefficients for  $C_l/C_d$  are graphed with respect to boat speed. For all three foil configurations analysed the range of TWA for foiling was between 60 to 120 degrees. The boat speed where the hull became airborne was around 4 m/s for all design conditions. The speed range for the moth while hydro-foiling was between 7 to 10 m/s. In non-foiling conditions the flapped off-design had the highest  $C_l/C_d$  value. The flapped foil was more efficient at low speeds when low riding and was less efficient once foiling when compared to the un-flapped foil. This shown by the  $C_l/C_d$  value being greater than the un-flapped foil until a speed of 6 m/s. At a speed of 5.8 m/s all curves crossed and therefore all speeds were identical. Once foiling the un-flapped foil has the greatest  $C_l/C_d$  value.



**Figure 10 Coefficients of lift/drag with respect to hull speed.**

## 6.2 Experimental and Numerical Variance

The comparison of boat speed for numerical and experimental results showed FS-Equilibrium under estimated on average 43% for all true wind angles. These results agree with studies by Hull (2011), that showed when comparing a four to a six degrees of freedom model a similar order of magnitude shift in results was obtained. The boat speed was always under estimated for most TWA. For TWA between 65 to 120 degrees, both analyses had their smallest variance with FS-Equilibrium over predicting the speed on average 13%. The maximum boat speed occurs between these TWA for all design conditions for both numerical and experimental analysis. For TWA outside of this range there is a larger variance between both analyses, however, it should be noted that most design

optimisation is carried out in this range due to the high sailing speeds obtained resulting in most sailing occurring in this range.

The increase in measured performance of the flapped on-design condition when compared to the un-flapped foil could be caused by the dynamic state of the moth, that is the flapped on-design condition is far more stable in the present setup than the un-flapped foil. This dynamic stability feature of the foils is not modelled in the numerical simulation which the moth was in a steady state where pitch and heave were neglected. Another cause of experimental error was due to manoeuvring into turns which caused a spike in boat speed, as the moth stayed on its foils at TWA in which a steady state solution would result in the moth coming off its foils. These turning manoeuvres were unable to be filtered from experimental results. This is a problem as the moth is not sailing in a steady state and is under the influence of rapid accelerations and decelerations. Further testing may be needed in order to verify these results. The averaged percentage variance for all design conditions is shown in Figure 11.

Despite the differences displayed between the predicted and measured differences between flapped on-design and un-flapped foils, the flapped off-design and un-flapped foils showed very close differences for the measured and predicted cases. The primary reason for this is most likely due to the fact that the flapped off-design condition does not retain the same dynamic stability superiority due to its far from optimal configuration.

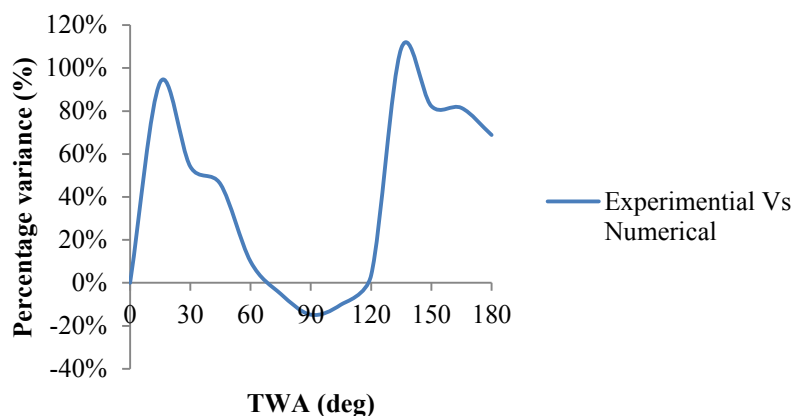


Figure 11 Average percentage variance of all design conditions for all TWA.

### 6.2.1 Explanation of Maximum Boat speed

In both analyses the greatest boat speed occurred for TWA between 105 to 120 degrees. These TWA represent sailing conditions where the main sail is in drag mode with low lift force produced. As a result there is a greater component of the wind pressure applied to mainsail which is aligned with the moth's course heading. The average flap angle for the moth at these TWA was on average 2.5 degrees, which was the lowest flap deflection for all headings as shown in Figure 8.

## 7. Conclusion

Two types of T-foils used on an international moth dinghy were tested in order to obtain optimum VMG for a windward leeward course structure. The wind strength for the analysis was 8 m/s. The first foil tested was fitted with a flap located on the trailing edge and a length of 30% of the chord. The second foil was un-flapped and was rotated about an axel at  $\frac{1}{4}$  of the chord.

In order to compare the two foils and verify results full scale testing was done along with a numerical simulation involving a VPP. The two dimensional lift and drag coefficients were obtained from X-Foil and converted to three dimensional values by using lifting line theory. These results were used to set the design conditions for all foils tested. In order to compare the efficiency of each foil an off- and on-design condition was created which was a function of the camber of the foil cross section. The flapped foil had two design conditions due to flap deflections and the varying camber of the foil

cross section in the longitudinal plane. The un-flapped foil had one design condition as the whole foil was pivoted and the foil camber remained constant through its range of operation. The minimum lift for every foil was 110 kg when setup for a neutral flap. The on-design condition for each foil involved no flap deflection and only needed inclination of the foil to the free stream flow till the required baseline lift was generated. The flapped off-design condition was created to show an area of operation where the foil potentially had a reduction in efficiency. The condition was designed for light winds where a greater angle of attack is needed to lift the total mass. If the wind speed then increases whilst sailing (thus precluding, the ability to change design setups), a negative flap deflection is required to provide the same lift force to that of the flapped on-design condition. The foil was inclined at 10 degrees angle of attack for the flapped off-design condition. Due to the large foil inclination a negative flap deflection of negative 12.8 degrees was required in order to produce the baseline lift.

The numerical simulation was done on a VPP called FS-Equilibrium. The VPP was modelled using four degrees of freedom force balance. Yawing and pitching were neglected in the analysis. The FS-Equilibrium modules were originally programmed by Hull (2011) and modified by the author. For each simulation the relative lift and drag coefficients had to be modified in order to represent the three design conditions. The simulations were run for an optimum VMG and results for boat speed and TWA between 35 to 180 degrees were produced. The results showed that at a wind speed of 8 m/s the moth will foil for TWA between 60 to 120 degrees. Once riding on the hydrofoils the un-flapped foil produced the greatest VMG and boat speed, followed by the flapped on- and off-designs. At TWA where the moth hull was low riding, the flapped foil had the greatest boat speed with the off-design performing the best. The un-flapped foil was the slowest in the low riding regime. The flapped design conditions had small variances for most sailing angles with the off-design most efficient while low riding and the on-design faster while on the foils. The greatest variance was between TWA of 105 to 130 degrees where the on-design condition had a significant speed advantage. In this range the maximum speed was recorded in both analyses. These headings also represented maximum angles the moth can sail without coming off its foils in FS-Equilibrium. This shows that a higher foil camber attracts a larger drag penalty sailing at these TWA.

The full scale testing was carried out on a moth built by the author with foils setup to their prescribed design conditions. The moth was fitted with a GPS and was sailed at all TWA with the boat speed also recorded. The wind speed and direction were recorded by an anemometer on a support boat located in the vicinity of the moth. As the design wind for the analysis was 8 m/s, wind readings that were within a 1.3 m/s range were used in the GPS analysis. The average wind angle was taken over the three separate runs with no major shift in wind direction occurring. The greatest distance the moth travelled from the support boat was 500 meters during testing. The experimental and numerical results were compared and showed a variance. The author believes this is due to FS-Equilibrium only using four degrees of freedom force balance in its simulations and neglecting pitching and yawing. Pitching can have a significant effect of the effective angle of attack of the foil. The filtering of experimental data could be improved by eliminating manoeuvring, as the moth is not sailing in a steady state and is under the influence of rapid accelerations and decelerations. For all TWA the flapped on-design performed the best followed by the un-flapped and flapped off-design conditions. The performance of the flapped on-design verifies that it was the most efficient flapped design condition. Between TWA 65 to 120 degrees, the variance between experimental and numerical results was considerably small when compared to other headings. These range of headings are also when the moth is foiling and when the maximum boat speed occurs. The flapped off-design and un-flapped foils showed very close differences for the measured and predicted cases. The primary reason for this is most likely due to the fact that the flapped off-design condition does not retain the same dynamic stability superiority of the flapped on-design, due to its far from optimal configuration.

Future work on the topic could include a six degrees of freedom force balance in FS-Equilibrium so that pitch and heave are considered. Pitch has a direct effect on the foil angle of attack as it is a rotation around the boats transverse axis. The actuation and gearing of the un-flapped foil could be reduced as to allow for smaller foil deflections as shown by Beaver and Zselezky (2009). In experimental work more accurate filtering of turning manoeuvres could help match both experimental and numerical results. The recording of boat speed and TWA could be improved if the anemometer

and GPS are fitted to the moth as one unit. This would allow actual TWA, boat heading and speed to be collected and reduce error in data collection. As the moth at times can sail at the true wind speed an apparent wind angle may need to be considered in the calculations. By matching all numerical and experimental data for all sailing conditions. This allows further refinement of the VPP and allow for more accurate numerical analysis in the future.

## 8. References

Alberte E. Von Doenhoff, IHA (ed.) 1948, *Theory of wing sections*, NASA.

Beaver, B & Zselezky, J 2009, 'Full scale measurements on a hydrofoil international moth', *19th Chesapeake Sailing Yacht Symposium*, Annapolis, Maryland, vol. 19, p. 20.

Binns, JR, Brandner, P & Plouhinec, J 2008, 'The effect of heel angle and free surface proximity on the performance and strut wake of a moth sailing dinghy rudder t-foil', *High performance yacht design conference*, Auckland, New Zealand.

Bögle, C, Hochkirch, K, Hansen, H & Tampier-Brockhaus, G 2010, 'Evaluation of the performance of a hydro-foiled moth by stability and force balance criteria', Bachelor of Engineering Master's thesis, Tu-Berlin.

Culnane, D 2013, viewed 20 March 2013, <[http://wiki.mothosphere.com/index.php?title=Main\\_Page](http://wiki.mothosphere.com/index.php?title=Main_Page)>.

Drela, M & Youngren, H 2008, *X-FOIL*, 6.97 (Unix) edn, <<http://web.mit.edu/drela/Public/web/xfoil/>>.

Emonson, JA 2009, 'An investigation into the effect of froude, weber and cavitation numbers on ventilation of surface-piercing t-foils', Bachelor of Engineering (Naval Architecture) thesis, Australian Maritime College.

Findlay, MW & Turnock, SR 2009, Development and use of a velocity prediction program to compare the effects of changes to foil arrangement on a hydro-foiling moth dinghy, Master's thesis, University of Southampton.

Hull, DPJ 2011, 'Speed sailing design and velocity prediction program', Bachelor of Engineering (Naval Architecture) thesis, Australian Maritime College.

Masters, J 2013, *Weather Wunderground*, viewed 5 May 2013, <<http://www.wunderground.com/>>.

Miller, C 2009, 'Control system for international moth on hydrofoils', Bachelor of Engineering thesis, Glasgow University.

Stevenson, P, Culnane, D & Babbage, S 2004, *Moth web forum*, viewed 23 July 2013, <<http://moth-sailing.org/imca/faces/news.jsp>>.

Stewart, A, Kurihara, K & Aldrich, C 2010, *Velocitek*, viewed 28 August 2013, <<http://www.velocitek.com/>>.

Stewart, D, Leyek, Z & Pozo, R 2012, *FS-Equilibrium user manual*, Future-Ship GmbH, Potsdam.

Whaley, L & Alvazzi, U 2013, *Trac Tac*, viewed 5 August 2013, <[http://germanmaster.traclive.dk/events/event\\_20101205\\_SailSydney/index.php?raceid=409ad480-0250-11e0-a925-406186cbf87c](http://germanmaster.traclive.dk/events/event_20101205_SailSydney/index.php?raceid=409ad480-0250-11e0-a925-406186cbf87c)>.





# THE INTERACTION BETWEEN SAILING YACHTS IN FLEET AND MATCH RACING SITUATIONS

**P.J. Richards**, Yacht Research Unit, University of Auckland, New Zealand

**N. Aubin**, École Navale, France

**D.J. Le Pelley**, Yacht Research Unit, University of Auckland, New Zealand

## SUMMARY

The interaction between yachts sailing upwind close hauled is investigated in the wind tunnel through measurement of the forces and moments on a balance mounted key boat which is experiencing interference from one or two opponent boats. For most of the tests the boats were set at an apparent wind angle of  $25^\circ$  and a heel angle of  $25^\circ$ . In addition the variation of forces and moments on the key boat, in isolation, were measured over a range of apparent wind angles and the drive to side force ratio is subsequently used as an indicator of the effective apparent wind angle when an interfering boat is present. The data from two boat testing was analysed to show that much of the reduction in drive force is due to changes in wind angle rather than wind pressure. These changes in angle and wind pressure are shown to be similar to those measured around an isolated yacht using two 3-component velocity measuring Cobra probes. With three boat interference there are too many possible position combinations to consider all of these and so tests focused on two starting line and two layline scenarios. The relative importance of each interfering yacht is investigated and the effects of separation on interference demonstrated.

## 1. INTRODUCTION AND BACKGROUND

In an earlier paper Richards et al. (2013) presented wind tunnel measurements of the interaction between two yachts when sailing upwind and downwind, with both symmetric and asymmetric spinnakers. The correct location of the negative interference and severe negative interference zones was presented for each sailing situation. In particular they pointed out that the popular understanding of interference, as encapsulated in documents such as “Racing Basics” by Mark Johnson (1995), doesn’t emphasise that the important wind vector is the apparent wind, relative to the yacht, which is calculated by the vector sum of the true wind and the reversed boat velocity. Although interference may be important during any leg of a race, it is often on the upwind legs where yachts are forced into closer proximity and hence this paper will focus on these upwind interactions. Initially two boat interference is studied in greater detail and then multiple boat interference is considered. Figure 1 shows an example of a two boat test, where the key boat, to the right, is mounted on the 6-component force balance, which sits below the black turntable, while the interfering yacht, with its white hull and sails, is moved to a variety of relative positions. For the current testing all yachts have been set up with  $25^\circ$  of heel and for most tests the apparent wind angle is  $25^\circ$ .



Figure 1 Two boat testing in the University of Auckland Twisted Flow Wind Tunnel

Marchaj (1982) provides a detailed discussion of situations similar to that shown in Figure 1, and points out that the key boat is in what is called the “safe leeward position” where it may experience both an increase in wind speed and a favourable change of local wind direction as a result of the windward yacht. In contrast he describes the position of the white yacht as the “hopeless position”, since almost any option will result in losses. He points out that “the turbulent wake behind the sail when close-hauled is deflected away from the line of the apparent wind toward the stern”. He also comments that the influence of the wind deflection and turbulence behind a yacht can be felt for up to ten boat lengths.

Marchaj also reproduces some quantitative wind tunnel data collected by M.S. Hooper using J-class yacht models. The apparent wind angle (AWA, the angle between the apparent wind and yacht velocity vectors) for both yachts was  $40^\circ$  and the yachts were heeled  $15^\circ$ . This AWA might typically occur when reaching, that is sailing approximately perpendicular to the true wind direction. The position of the “interfering” yacht was fixed while the “interfered with” yacht was moved about in relation to the fixed yacht. The data is presented as contours of the available drive force, component in the direction of motion, on the “interfered with” yacht as a percentage of the driving force which would be available in an undisturbed wind. The lowest percentages, down to 0-10%, were recorded along the line of the apparent wind downstream of the “interfering” yacht. Almost all downwind positions showed a loss of drive force which returned to nearly 100% one boat length either side of the centreline. Two regions of positive interference were identified. The strongest of these, with a gain of 20%, was located at the “safe leeward position” with the two models in-line across the apparent wind and with the “interfered with” yacht 0.6 boat lengths on the leeward side of the “interfering” yacht. The other region of positive interference (up to 5%) was half a boat length windward of the “interfering” model along the  $60^\circ$  direction (measured from the centreline of the interfering yacht).

Caponnetto (1996) used a vortex lattice code to analyse the interference between two identical IACC yachts when sailing close-hauled with an AWA of  $25^\circ$ . The heel angle was  $0^\circ$ . In this study the “key boat” was fixed at the origin while a “second boat” has been positioned at various radii ( $R=0.5, 1$  and  $2$  mast heights ( $h$ )) for all angles around the “key boat”. At all three radii the lowest drive force and side force on the key boat occurred when the second boat was at an angle of  $22^\circ$  (measured from the bow in the same manner as the AWA) which is almost along the apparent wind line. At this angle the wake of the windward yacht crosses the key boat. With the second boat in this direction the ratio of the drive on the windward second boat to that on the leeward key boat is 4.8 for  $R=0.5h$ , 2.6 for  $R=1h$  and 2.0 for  $R=2h$ , which clearly shows the reduced interference as the yachts move apart. The results are also presented as the ratio of the drive force on the affected yacht to that for an isolated yacht sailing alone in free air. It is shown that when the yachts are moderately close to each other ( $R=1h$ ) and the relative direction is  $22^\circ$  the ratio of 2.6 is produced by a 4% gain for the second boat and a 60% reduction in drive force for the key boat. The data shows that the key boat gets some positive interference if the second boat lies within a sector of  $\pm 60^\circ$  of directly astern. Caponnetto (1996) points out the interesting observation that the drive force on the two interfering yachts is equal when the relative angle is  $96^\circ$  for all three separations considered. With this relative positioning two identical yachts could maintain the same speed and hence remain in the same orientation. However the data shows that in this case the drive force is 3% lower than an isolated yacht and so if they were both part of a fleet race then while they can match each other, they will be losing ground relative to other yachts.

While most studies to date have only considered two boat interactions, Spenkuch et al. (2008) have proposed a lifting line method for modelling covering and blanketing effects for yacht fleet race simulations. With this approach the wake of an upwind sailing yacht is represented as a single heeled horseshoe vortex (and image) system. At each time step changes in vortex strength are convected into the wake as a pair of vortex line elements. These subsequently move in accordance with the local wind, self-induced velocity and velocity induced by the presence of the wakes of other yachts. The lifting line approach was compared with CFD results and showed good agreement for single and two yacht setups. While the method is intended for use in fleet race situations, no CFD results are included for situations involving more than two yachts.

In Section 2 the important multiple yacht interference scenarios are discussed, while in Section 3 the wind tunnel modelling considerations are outlined. Sections 4-6 deal with the results from 1, 2 and 3 boat testing.

## 2. FLEET AND MATCH RACING SCENARIOS

With either fleet or match races the course will typically take the form depicted in Figure 2 with the start line set up perpendicular to the true wind. The race will then consist of a number of windward and leeward legs. In this paper we will concentrate on interference between yachts during the upwind legs. With match racing the two yachts will often choose to be in close proximity to each other in order to avoid the chances of their opponent gaining a race winning advantage from being on the beneficial side of a wind shift. In fleet races it is almost impossible to cover all opponents and so interference effects tend to occur most frequently in situations such as:

1. At the starting line where all yachts are concentrated in a restricted area.
2. On occasions where a yacht on port tack encounters an opponent on starboard tack and is obliged to tack.
3. Along the lay lines leading up to the windward mark.

In such situations the most likely interactions are between two boats, then three boats and least often more than three boats, which probably only occurs near the starting line. Even if there are several yachts in close proximity, the fact that interference effects tend to weaken with distance means that each boat is only significantly affected by those boats close to it and so this study will only consider 2 and 3 boat interactions.

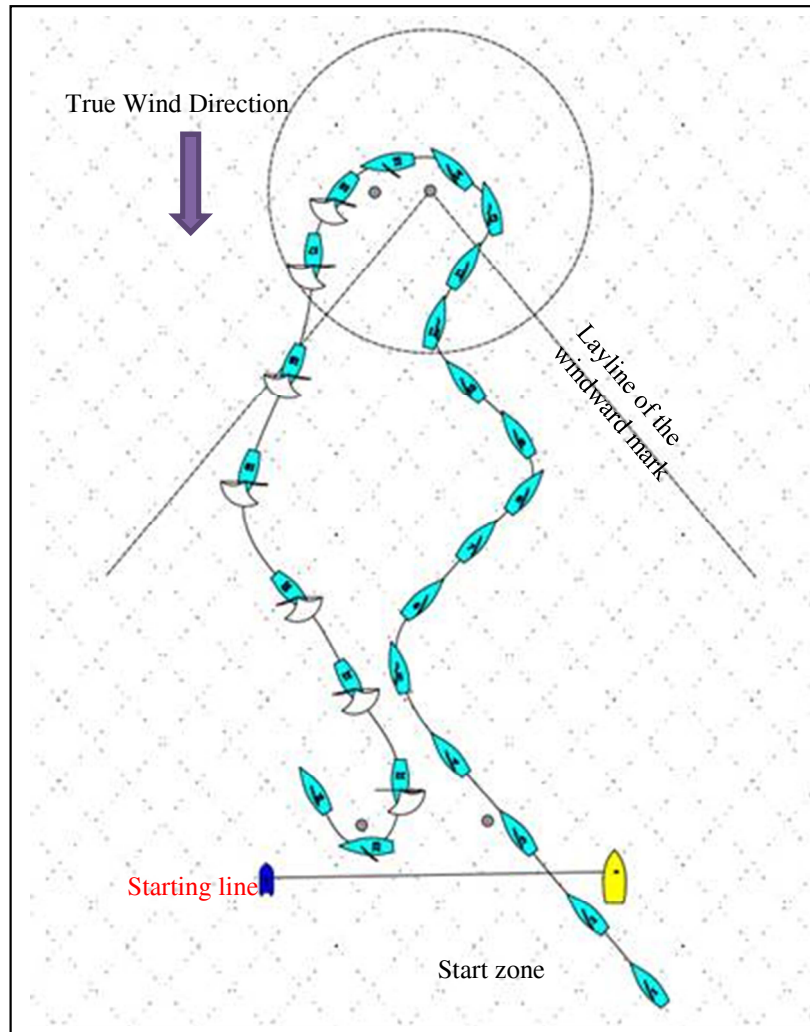


Figure 2 *Classic fleet or match race course*

### 3. WIND TUNNEL SETUP

With wind tunnel testing of the interaction between yachts there are a number of factors which need to be considered and noted. These include:

- Since all models will be stationary, the situations modelled must represent two or more yachts moving with the same velocity vector. This means that the yachts must be on the same tack (port or starboard) and travelling at or near the same boat speed ( $V_B$ ). Crossing situations cannot be accurately modelled.
- In reality the interactions between boats will mean that the forces on the various boats will be different and so one or more boats will slow down relative to the others. Fortunately the relative movements caused by these imbalances are quite slow with one yacht slowly pulling ahead of the other(s). This means that a passing manoeuvre can be considered to be a series of quasi-steady situations, where the yachts can be considered to be moving at almost the same speed, but with their relative positions changing.
- At the University of Auckland it is standard practice to carry out all testing on port tack. However, since all yachts are assumed to be symmetric, the results can be mirrored to represent starboard tack situations.
- Since the models are stationary the air movement generated by the wind tunnel represents the apparent wind (AWS), the vector sum of the true wind (TWS) and the reversed boat speed ( $-V_B$ ) as illustrated in Figure 3.
- The University of Auckland wind tunnel is known as the “Twisted Flow Wind Tunnel”, but for the tests reported here the turning vanes, which create the twist, were not used. The twist in the apparent wind is created by the changes in the vector diagram with height, since the true wind speed increases with height whereas the boat speed remains constant. For off wind sailing conditions this twist can be significant but for the upwind conditions considered here the twist is at most a few degrees and hence can be ignored. This is fortunate since the vanes would interfere with many of the locations where we wish to place models.

- In Section 6 two of starting line scenarios will be considered. As noted in Section 2 the starting line may be considered to be perpendicular to the true wind, which means that it will not lie directly across the wind tunnel but instead will be angled slightly.
- In many races the run to the starting line may be mistimed and so a yacht may have to shed speed in order to avoid crossing the starting line early. This means that the yachts on the starting line may in reality have a variety of forward speeds. However the ideal situation is that all yachts hit the starting line at full speed at exactly the right moment. It is this ideal situation which is modelled in the tests reported here.
- In order to minimise changes in sail shape, semi-rigid fibreglass sails have been used on all models. These sails generally have a more realistic upwind shape and while some trimming can be carried out they tend to be much less sensitive to unintended trim changes.

Since the current investigation is concerned with general trends rather than a specific yacht in particular situations, the conditions chosen are intended to be generic. It has been assumed that the yacht will maximise its upwind velocity made good with a true wind angle (TWA) of  $42^\circ$  and that the yacht is then sailing at an apparent wind angle (AWA) of  $25^\circ$ . Simple analysis of the velocity triangle, shown in Figure 3, shows that these angles correspond to the condition when the boat speed is about 70% of the true wind speed. Most monohull displacement yachts can achieve boat speed to true wind speed ( $V_B/TWS$ ) ratios higher than 0.7 at low wind speeds but will drop below this ratio as the wind speed strengthens. With the chosen angles the apparent wind speed (AWS) is 1.58 times the true wind speed and the starting line (assumed perpendicular to the true wind) is at an angle of  $73^\circ$  to the apparent wind (and hence the wind tunnel centreline). The heel angle was set to  $25^\circ$ . The yacht model used as the key boat had a mast height of  $h=2.2\text{m}$ , sail area  $A=1.64\text{ m}^2$  and hull length of  $L=1.5\text{m}$ . The other models were very similar.

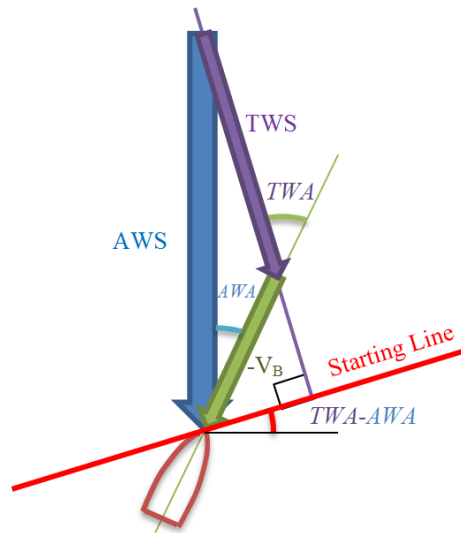


Figure 3 *Velocity Vector Diagram*

#### 4. SINGLE YACHT TESTING

In order to understand the interactions between yachts it is first necessary to understand the way in which the local flow conditions affect the forces on a yacht and the way the yacht affects the local flow field. For this reason two sets of single yacht tests have been conducted, one to determine the forces and moments on a yacht at a variety of apparent wind angles and the second to measure the flow field around the model.

##### 4.1 Apparent wind angle effects on forces and moments

In the first of these single model tests the balance mounted model was tested at apparent wind angles (AWA) from  $10-30^\circ$ . This range is deliberately asymmetric with the respect to the standard test AWA of  $25^\circ$  since the interactions are more likely to reduce the effective apparent wind angle than increase it. The general forces ( $F$ ) and moments ( $M$ ) have been reduced to coefficient form by using:

$$C_F = F / qA \quad \text{and} \quad C_M = M / qA^{3/2} \quad (1)$$

where  $q (=0.5\rho(AWS)^2)$  is the reference dynamic pressure based on the air density  $\rho$  and the Apparent Wind Speed, and  $A$  is the total sail area.

Figure 4 shows the variation of the primary force and moment coefficients with apparent wind angle. The sails were trimmed to maximise the drive force at AWA=25° and then remained in the same positions for other angles. Since the sails are made from fibreglass they retain their shape even when soft sails would distort due to back winding. As a result the data in Figure 4 is valid for the tests conducted but would be slightly different at low apparent wind angles with flexible sails.

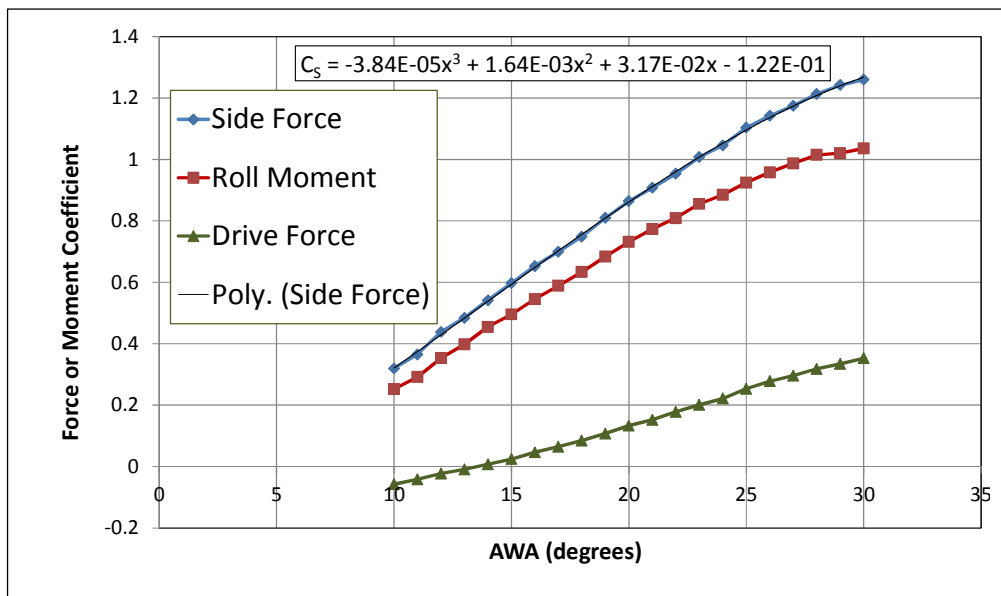


Figure 4 Force and moment coefficients as a function of apparent wind angle

For a particular trim the forces and moments on the yacht can be assumed to be a function of the effective apparent wind angle and the effective dynamic pressure. As a result the interaction between yachts can be considered to be a mixture of these two effects. Since the drive force reduces to zero more rapidly than the side force, the ratio of these forces can be used as an indicator of the effective apparent wind angle. The forces individually cannot be used for this purpose since they are modified by both changes in wind direction and strength. By using the drive/side force ratio the influence of the wind strength is removed and the results can then be used to indicate the effective apparent wind angle. In order to do this the apparent wind angle has been plotted against the drive/side force ratio and a polynomial fitted to this curve as shown in Figure 5. Once the effective apparent wind angle has been determined a corresponding side force coefficient can be obtained from the polynomial fitted to the curve in Figure 4. The measured side force can then be divided by the side force coefficient and the sail area in order to give an estimate of the effective wind dynamic pressure. In this way it is possible to differentiate between reductions in drive force caused by a change in wind direction from that caused by a reduction of wind pressure.

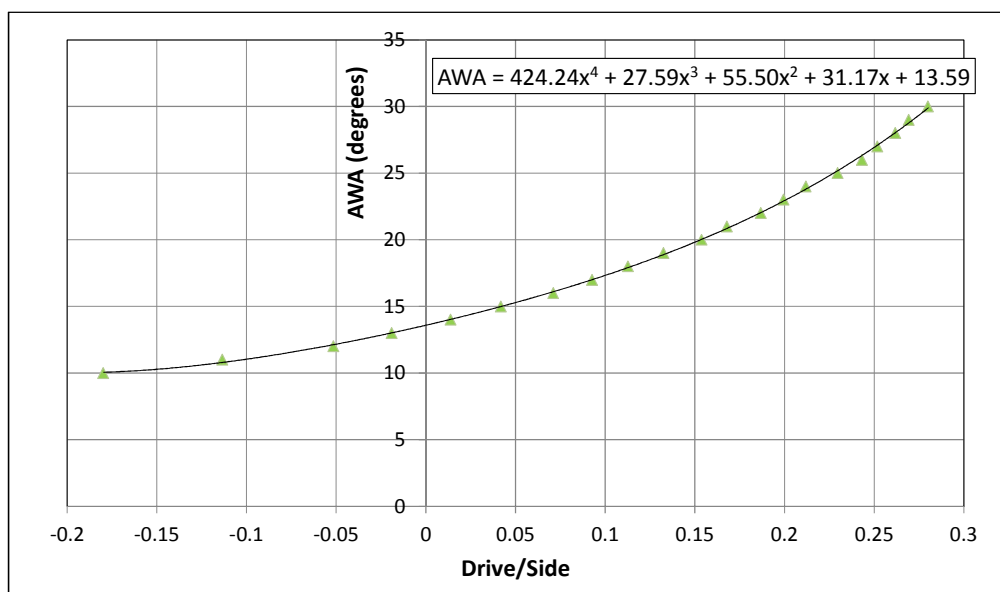


Figure 5 Apparent wind angle as indicated by the drive/side force ratio

## 4.2 Modified Flow Field

For the second single boat test two Cobra probes were mounted on a stand at heights of  $z=h/3$  and  $z=2h/3$ . These probes can measure the three components of the wind speed vector at moderate frequencies. For this test the model yacht was positioned well upstream in the wind tunnel and the probe stand moved in a regular grid around the model. Care was taken to make sure that the probe had the same alignment at all locations. There was a region close to the hull and below the heeled sails where the probes could not be positioned, this is indicated in Figure 6 by the blanked-out area around the hull.

The data collected has been processed to give contour maps of the changes in the local apparent wind angle, the percentage strength of the wind dynamic pressure ( $q$ , based on the total wind speed at each point) and the local flow elevation angle, all relative to the values measured without the model present. The results, shown in Figure 6a & b, show that upstream of the yacht the flow is deflected slightly such that a yacht in that location would experience a small increase in the apparent wind angle, whereas downstream the changes in effective apparent wind angle are much larger and extend over a greater area. At the lower level the flow deflections are highest immediately downstream of the yacht and the centreline of the affected zone seems to lie between the upstream apparent wind direction (straight down the page) and the yacht's centreline. At the higher level the deflection angles are somewhat smaller, more localised and reach their maximum value some distance downstream. The most affected zone is also more aligned with the upstream apparent wind. Figures 6c & d both show a region of increase dynamic pressure on the windward side of the yacht. This can be associated with the circulation created around the sails. In addition at the lower level there is a clear wake region with reduced dynamic pressure, which at this level coincides with the greatest changes in local apparent wind angle. The elevation angles in Figures 6e & f indicate an upward flow on the windward side of the yacht and a downward flow on the leeward side. The strong vertical flows in Figure 6f indicate the presence of the tip vortex shed from the head of the sails and carried downstream by the apparent wind. It may be noted that the change from upward to downward flow is a roughly the same location as the largest changes in AWA in Figure 6b.

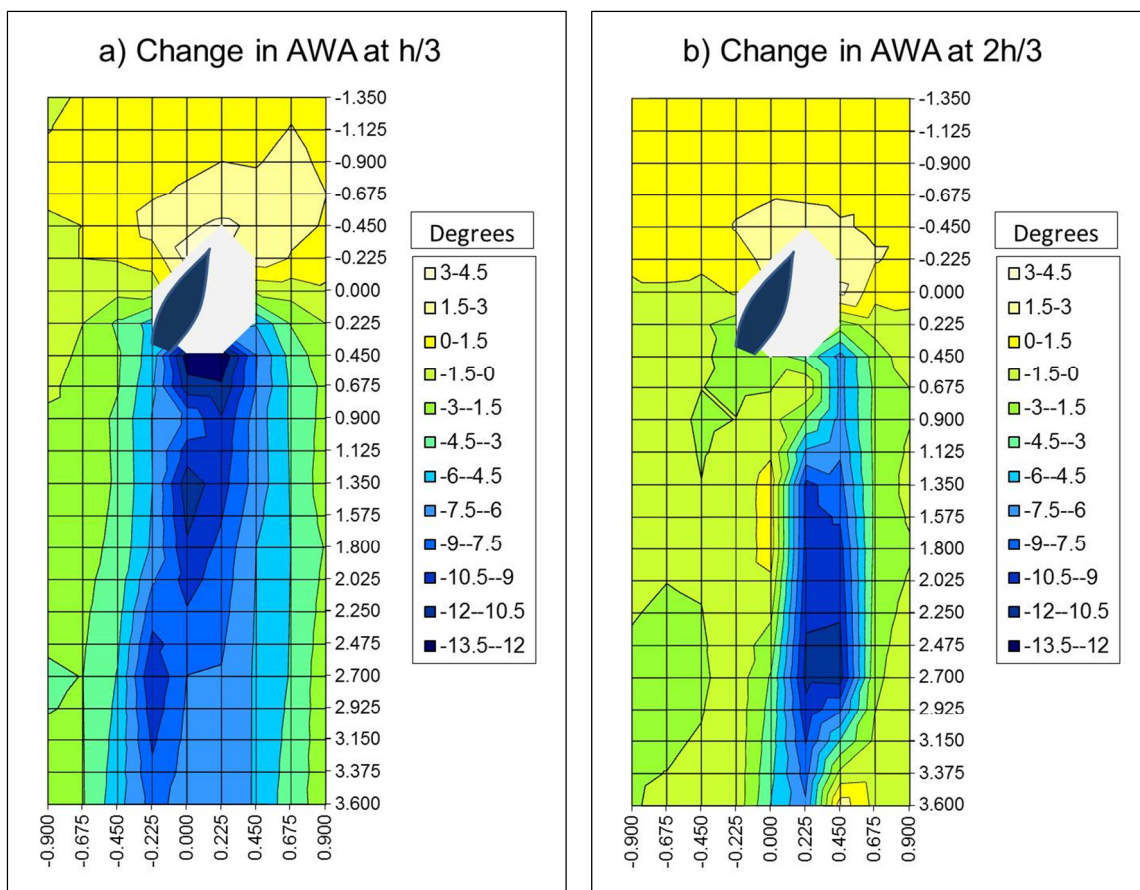


Figure 6 Changes in local wind direction, strength and elevation angle at  $z=h/3$  and  $2h/3$   
(Continued on next page)

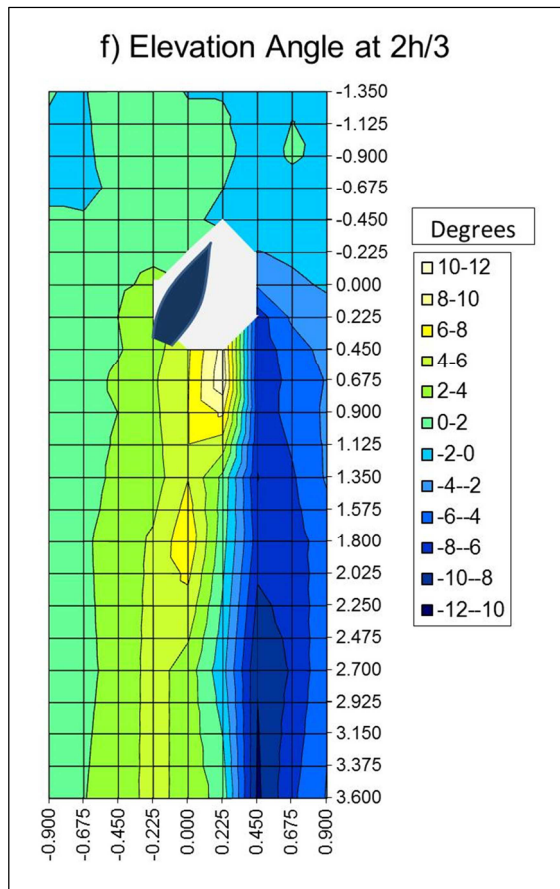
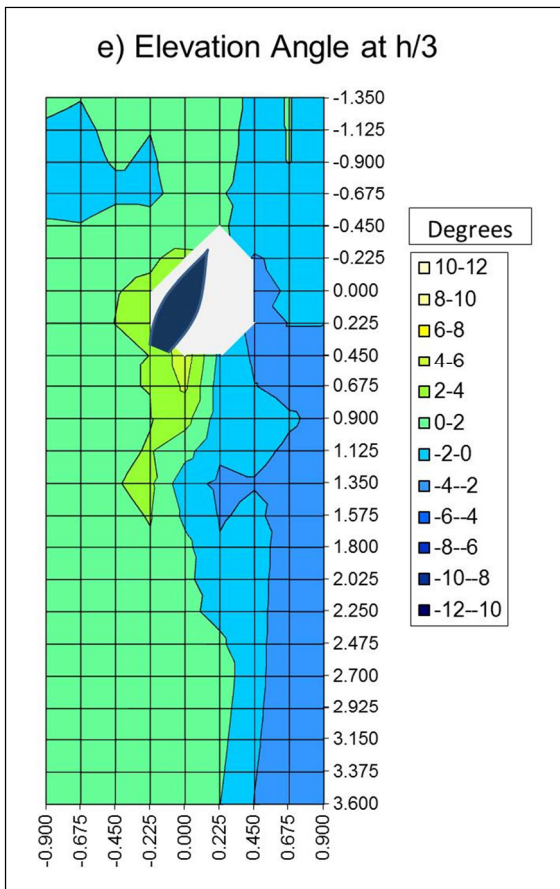
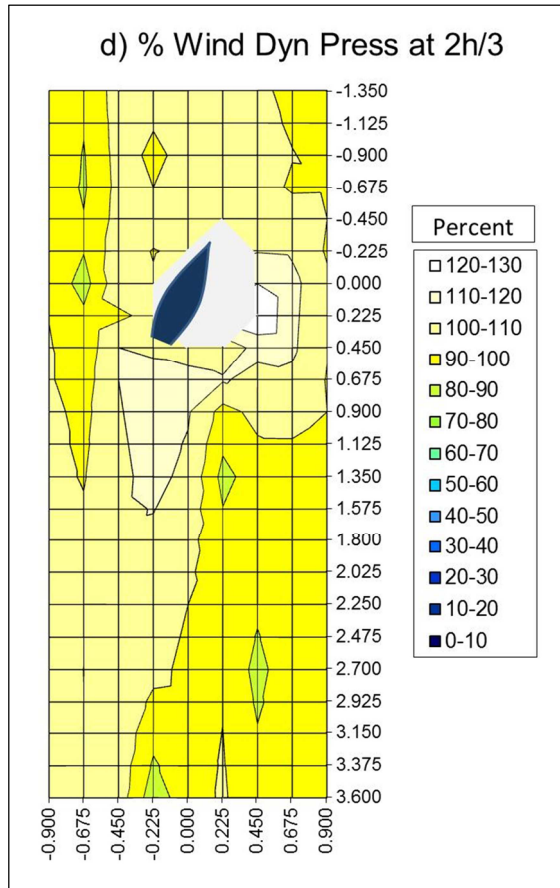
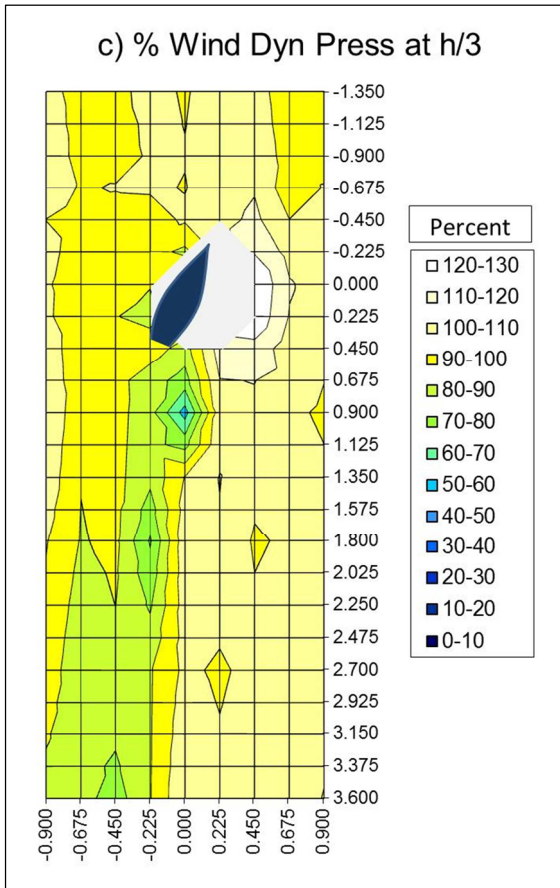


Figure 6 Changes in local wind direction, strength and elevation angle at  $z=h/3$  and  $2h/3$



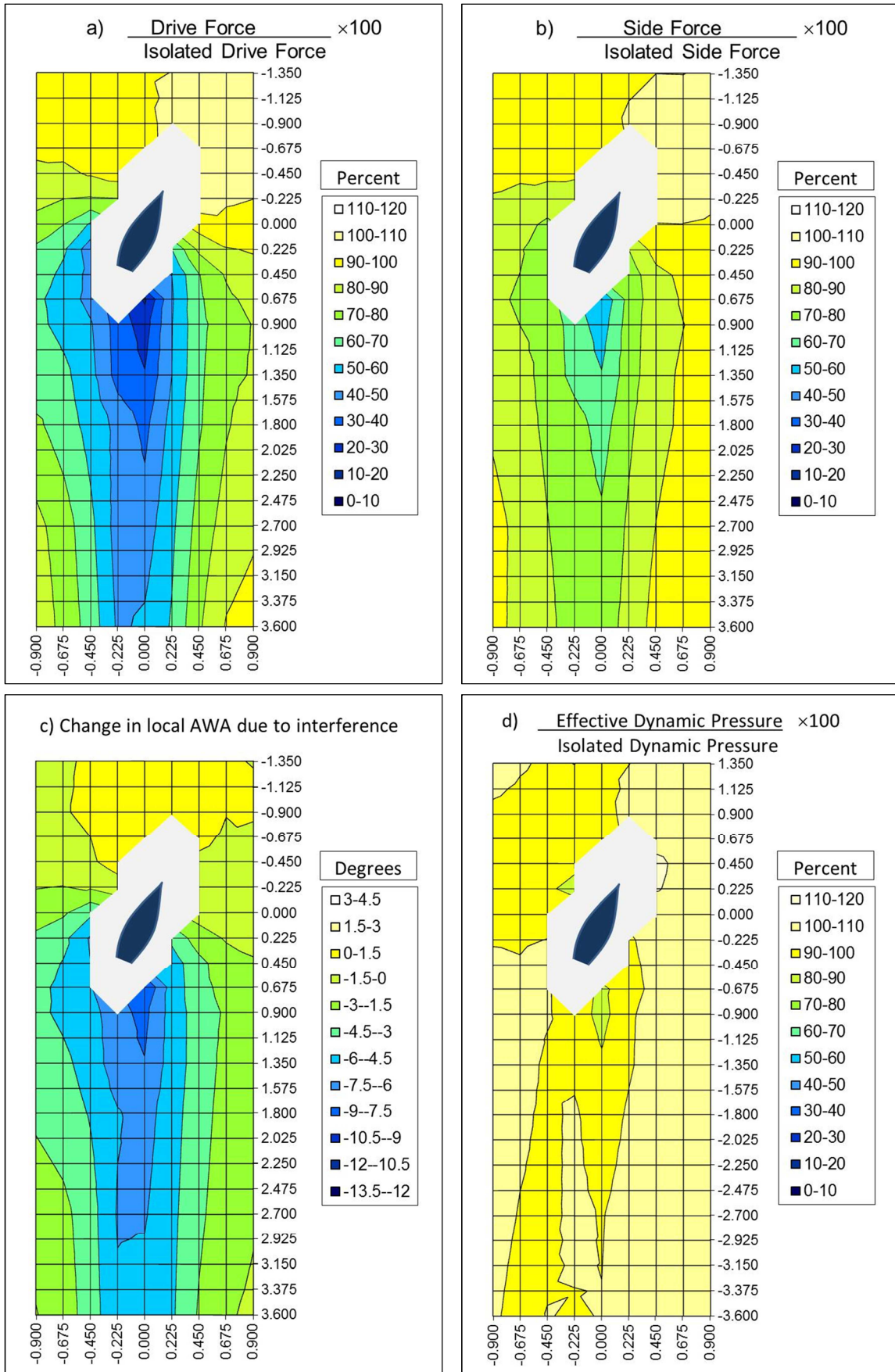


Figure 7 Reductions in a) Drive force, b) Side Force and d) Effective Dynamic pressure and c) changes in apparent wind angle for another yacht located at each point, when experiencing interference from the yacht shown.

## 5. TWO YACHT TESTING

In a manner similar to the Cobra probe measurements, two boat testing has been conducted with one model mounted on the balance and the second model moved around it. The forces measured have then been processed in order to calculate the percentage of the isolated drive force and side force that occurs with interference. In order to relate these measurements with the flow field measurements the contour maps in Figures 7a & b show the percentage of the isolated values that are felt by another yacht at each location if it is affected by the one shown. This means that the yacht shown at point 0,0 is the interfering yacht. The results show that a yacht in the lee bow position experiences a slight increase in both the drive and side force. However if the yacht is in the wake of the interfering yacht then the drive force is reduced significantly and the side force to a lesser extent. The data has been analysed using the polynomials discussed in section 4.1 to determine whether the reductions indicate a change in wind direction or a reduction in wind strength. The results in Figures 7c & d show patterns similar to those in Figure 6, though since the forces on the model are an integral of the flows at all heights the indicated changes in apparent wind angle are less severe than measured at  $z=h/3$ , as seen in Figure 6a. It is worth noting that in the region where the drive force is reduced to a level between 20-30% of the isolated value (a 70-80% reduction), the indicated dynamic pressure reduction is in the 80-90% range (a 10-20% reduction). It therefore follows that most of the reduction is due to the adverse changes in wind direction.

## 6. THREE YACHT TESTING

With more than two yachts interacting there are a huge number of possible combinations of relative positions and so it is almost impossible to consider all of these. As a consequence we will concentrate on two situations where multiple yachts are most likely to be in close proximity, namely the starting line and the layline. For each of these we will consider two slightly different scenarios and seek some guidelines on maximising relative gains, or at least minimising losses.

### 6.1 Starting line scenario 1 – Key boat between two opponents

In a fleet race situation it is inevitable that all of the yachts will try to be as close as possible to the starting line as the race begins and hence this places a constraint on their relative positions, which makes the number of possible combinations manageable. As stated earlier we will consider the ideal, if somewhat unrealistic, situation where all the yachts reach the line at the same time and at full speed. For most of the yachts this means that there will be one yacht to windward and another to leeward. In some cases the gap between neighbouring yachts may be quite small, while at other times these may be larger. Some of the obvious questions that arise for a skipper as he/she approaches a starting line might be:

- If he has a choice between a narrow gap and a wider gap, which one does he head for?
- If there is space should she keep close to the windward or the leeward neighbour?

In order to test this situation three yacht models were set up on the starting line, the central yacht was the key boat mounted on the force balance, while the others were moved along the starting line as illustrated in Figure 8. For each position of the leeward yacht, the windward yacht was moved to a range of positions, making a 2D array of position combinations. In addition tests were conducted with only the windward yacht, representing a situation where the leeward boat is far away, and with only the leeward boat. The photograph in Figure 9 shows the three models in one of the close proximity situations. It may be observed that the wind tunnel start line, the white line under the bows of the models, isn't directly across the tunnel but, as discussed in Section 3, is at an angle of  $73^\circ$  to the tunnel centreline, so that it is effectively perpendicular to the true wind direction, while the tunnel centreline represents the apparent wind direction. Also visible in Figure 9 are the wooden frames used to support the two interfering models and for the windward boat there are also weights to stop the model from tipping over. Although these may cause some disturbance to the flow it was reasoned that their relatively small size and the fact that they are near ground level would mean that any disturbance would be negligible.

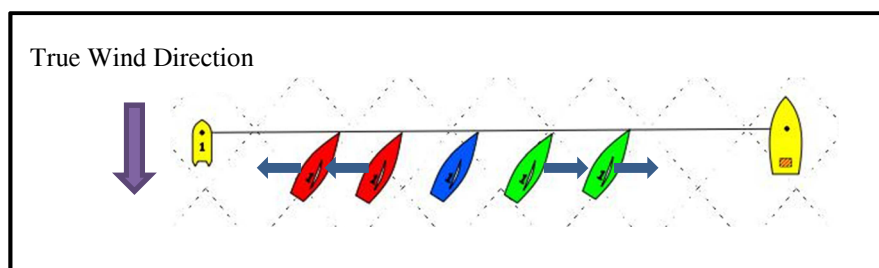


Figure 8 Starting line scenario 1, a yacht between two others.



Figure 9 Three boat interference testing in the wind tunnel.

Figure 10 shows the results from this three boat study in terms of the “Drive force interference factor” which is defined as

$$\text{Drive Force Interference Factor} = \frac{\text{Drive force}}{\text{Drive force on an isolated yacht}} \quad (2)$$

With this definition, values over 1.0 indicate beneficial interference whereas values below 1.0 are detrimental to the performance of the central key boat. Included in the figure are two sets of two-boat data. The only curve which goes above 1.0 is for the no leeward boat (LB) case, where the windward boat (white hull in Figure 9) may cause both a beneficial change in wind direction and a slight increase in wind dynamic pressure. These beneficial effects are seen to be most significant when the two boats are close to each other. The other set of two boat data is that with no windward boat (“No WB”) which is displayed as the unconnected larger symbols down the right hand side of the graph. It can be clearly seen that the detrimental effects of the leeward boat are far more significant, with reductions to levels as low as 40% of the isolated drive force. While this negative interference also decreases with separation it is still having a marked effect when the yachts are 0.86h apart.

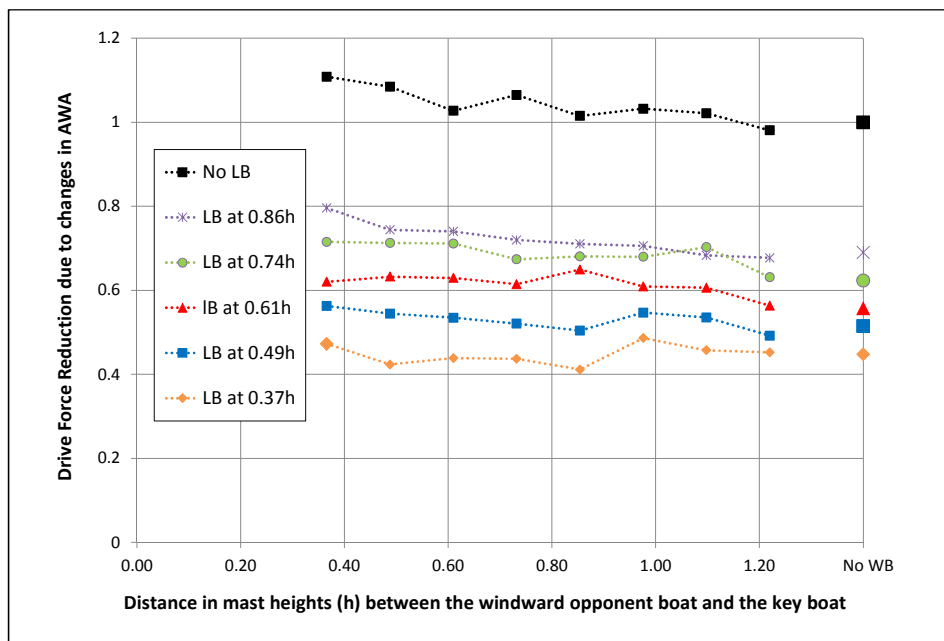


Figure 10 Drive force interference due to yachts on either side.

(Note: Larger symbols on the right-hand side indicate no windward boat and the upper line is the no leeward boat data)

The three-boat data in Figure 10 is arranged so that each line represents a particular leeward boat position while the horizontal position of the symbols indicates the simultaneous windward boat position. It shows that to a certain extent the effects from the windward and leeward boats are additive. For example if the leeward boat is at 0.86h, then bringing the windward boat close to the key boat partially improves the situation. However if the leeward boat is close to the key boat then the windward boat seems to have no beneficial effect, and possibly makes the situation slightly worse. Detailed analysis of the drive and side force data for this scenario shows that the vast majority of the effects are caused by changes in wind direction and that changes in wind strength never cause more than a 15% reduction in drive force.

The overall picture that emerges from this test is that a skipper should maximise their separation from a leeward boat. If there is a choice between a wide and a narrow gap then head for the wide gap and err towards the windward end of that gap. Some advantage may be gained by getting close to a windward boat but there are dangers with this strategy, since while there are gains to be had in the lee bow position, if you are slightly early and have to shed speed as you approach the starting line then your relative position can rapidly change from one of advantage to severe disadvantage as you drop back into the wake of the windward yacht.

### 6.2 Starting line scenario 2 – Key boat beside two opponents

In the previous section it was shown that while a windward yacht can offer weak assistance, a leeward yacht can have a marked detrimental effect. Since on a starting line there will often be multiple yachts on each side of any boat, the question arises as to whether the yacht beyond the immediate neighbour has any significant influence? This has been investigated by placing the two interfering yachts either to windward or to leeward. A variety of positions for the nearest yacht were used, and with each of these a range of positions for the further away yacht tested, including removing the second yacht completely. The single interfering boat results are represented by the larger unconnected symbols in Figure 12.

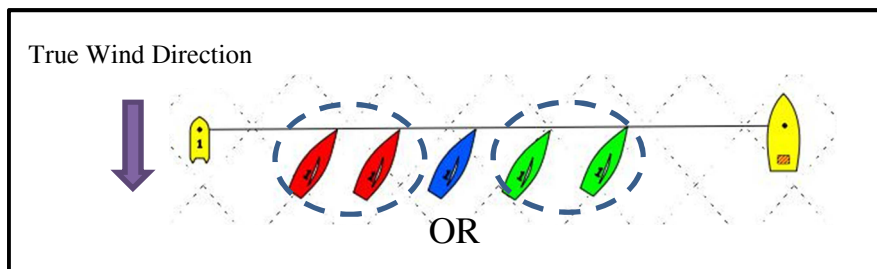


Figure 11 Starting line scenario 2, two opponent to one side or the other.

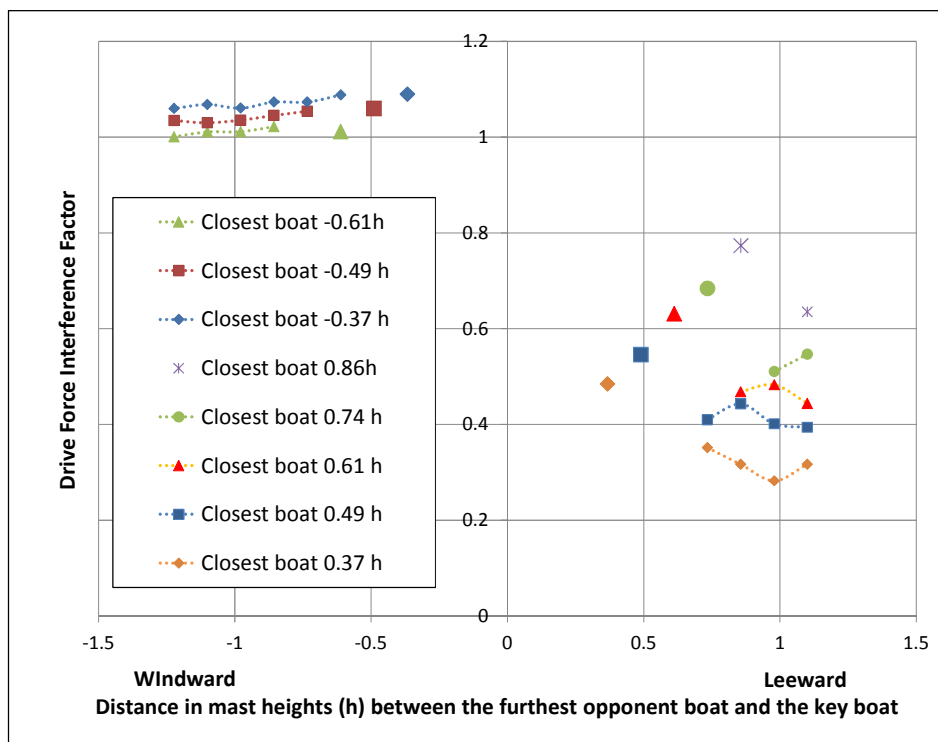


Figure 12 Drive force interference due to yachts on one side. (Larger symbols indicate only one opponent boat)

The results in Figure 12 show a difference in influence for the second windward boat in comparison with a second leeward boat. With the windward boats the second boat doesn't appear to enhance the beneficial effect given by the single windward boat, and in fact appears to weaken the effect. In contrast a second leeward boat enhances the detrimental effect with all distance combinations. It isn't clear but there is a suggestion that there may be an optimal distance for the second leeward boat in terms of their combined effect. One possible explanation for this is that if the second boat is too close it adversely affects the one in the middle, so that it then has less effect on the key boat. It would be interesting to see if a third leeward opponent would enhance these adverse effects further, however the space in the wind tunnel and the availability of similar models meant that it was not possible to extend this study to more than two leeward yachts

We therefore conclude that a second windward yacht has little influence and can be ignored, however a second leeward boat enhances the adverse effects and should be avoided if possible. The indications from an interference point of view are that the leeward end of the starting line is to be preferred, however factors such as the true wind not being quite perpendicular to the line, anticipated wind shifts etc. may negate this advantage.

### 6.3 Layline scenario 1 – Key boat between two opponents

The other upwind situation where yachts are frequently in close proximity is on the layline leading to the windward mark. In the wind tunnel the simulation is carried out for yachts rounding clockwise and leaving the mark to the starboard side. For this scenario the situation considered is one where the key boat is between two opponents, with each boat trailing the one in front of it by 1.5 boat lengths. The question considered is simply “whether there is an advantage to be gained by erring to windward or leeward of the line being taken by the other two boats”. Obviously a skipper would not choose to be on the leeward side if this resulted in not reaching the mark on the current tack as the two additional tacks required would mean a significant loss overall. For these tests the two opponent boats were always in line with each other and were moved along equal advantage lines which are perpendicular to the true wind and therefore angled in the same way as the starting line in the wind tunnel. The resulting situations are therefore equivalent to the key boat moving windward or leeward of the line taken by the leading and trailing yachts, as illustrated in Figure 13.

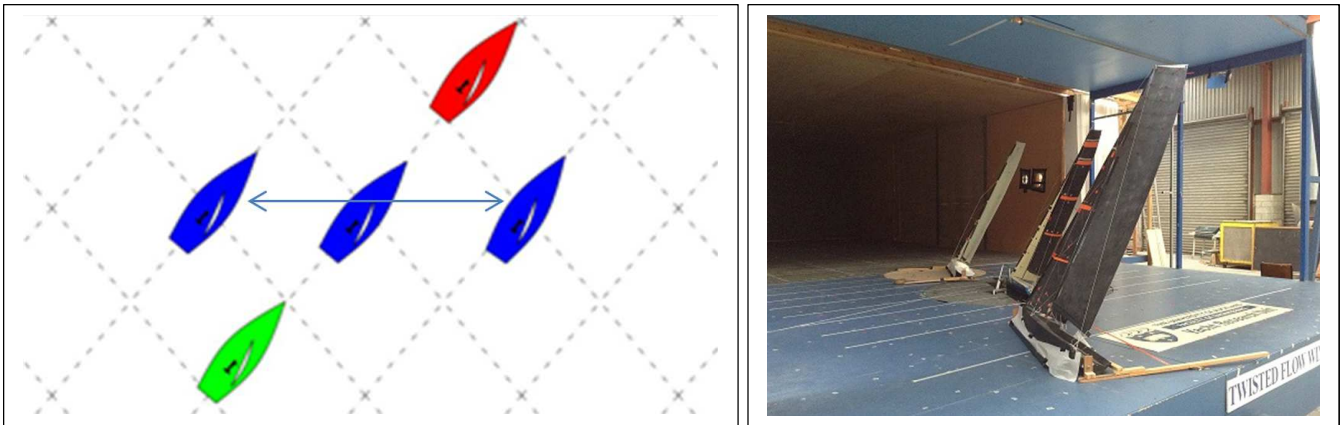


Figure 13 Layline scenario 1, key boat between two opponents.

The three boat drive force data is shown in Figure 14 along with data interpolated from the two boat testing for the situations where there is either one boat ahead or one boat behind. It is clear that the one ahead and one behind case is dominated by the presence of the leading yacht. In fact the drive force reductions with three boats are more severe than measured with just the boat ahead. From the two boat testing with only the boat behind one might expect some relief to be provided but this doesn't appear to be the case, instead things seem to be worse. It is possible that having three models in a line across the tunnel is deflecting the whole flow to the side in a manner that is not necessarily totally realistic. Although as noted by Marchaj (1982) “A particularly bad position is one behind a number of yachts sailing on a close-hauled course. The helmsman of a following yacht will find himself facing a strongly deflected wind ....”. So it may be that the combined group is enhancing the detrimental effects on the key boat.

In terms of strategy it can be concluded that with either one boat ahead or with one ahead and one behind it is better to err to windward of the direct layline. This would mean sailing a little further on the opposite tack before manoeuvring onto the lay line and thereby suffering something of a loss, but would then increase the drive force once the tack was completed. In addition since the major cause of the losses is a change in effective wind direction then sailing at a slightly higher true wind angle after the tack should increase the drive force and maintain speed, while the fact that the yacht is slightly beyond the layline will mean that the mark can still be reached while on this lower course.

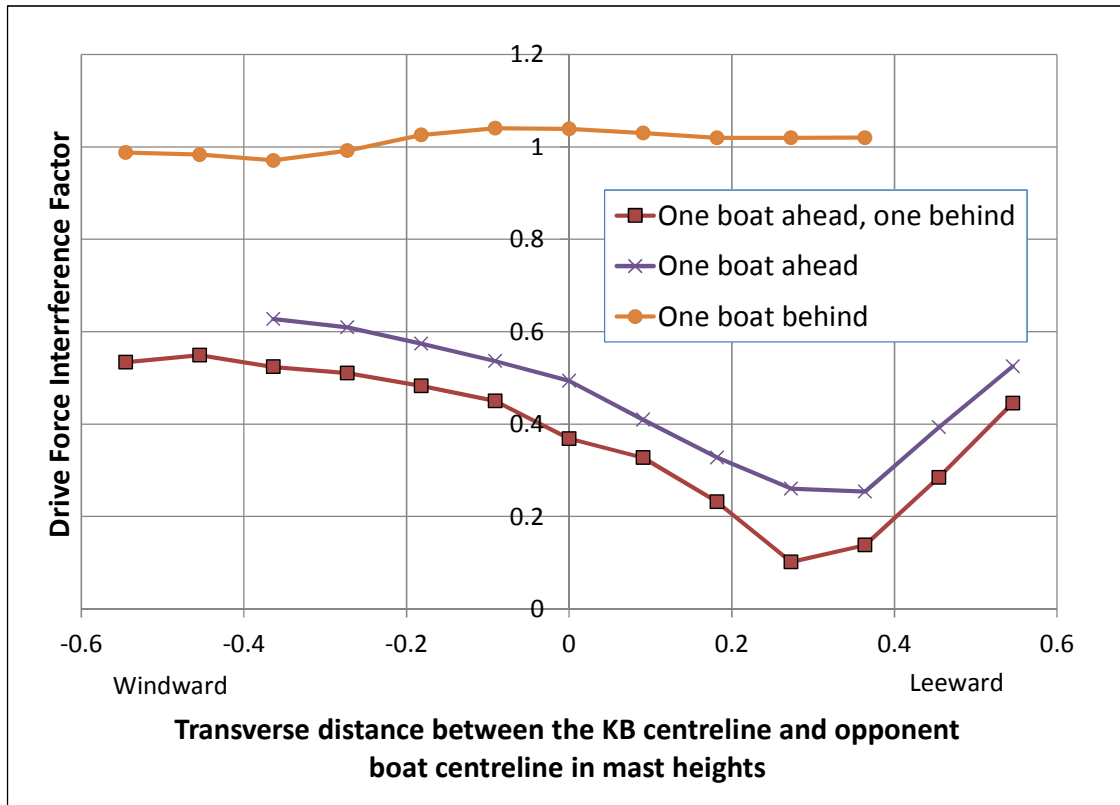


Figure 14 Drive force interference for the key boat on the layline with opponents ahead and behind.

#### 6.4 Layline scenario 2 – Key boat ahead of two opponents

Figure 14 shows that there is a slight increase in drive force that can be gained from having an opponent behind. On occasions it may be possible to get onto a layline with two boats close behind you, as illustrated in Figure 15. The questions which then arise are:

- Do the two boats offer more assistance than the single boat behind?
- Is there an optimal position relative to those boats in term of maximising drive force?

The particular situation tested assumed that the two opponents were 1.5 boat lengths behind the key boat and that they were in a position of equal advantage relative to each other. The two boats had one half-beam separation between the two hulls.

The drive force interference results shown in Figure 16 show that the fractional increase in drive force is only of the same order as that to be gained from a single opponent. It also shows that the gain will be maximised by being on the leeward side of the central axis between the pair of opponents, either by being directly ahead of the more leeward opponent or slightly leeward of that line provided the mark can still be reached by taking that line.

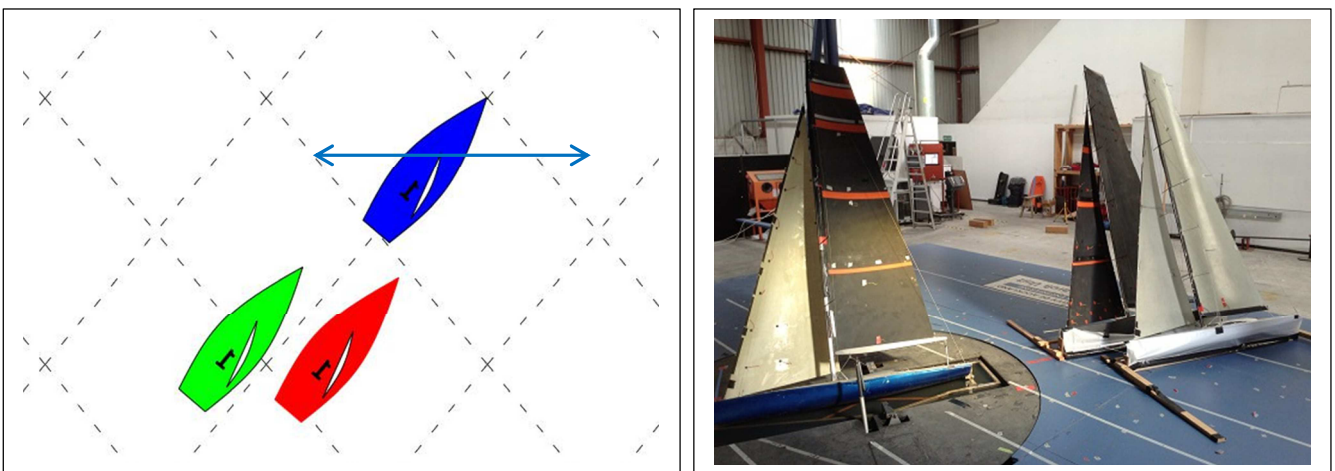


Figure 15 Layline scenario 2, key boat ahead of two opponents.

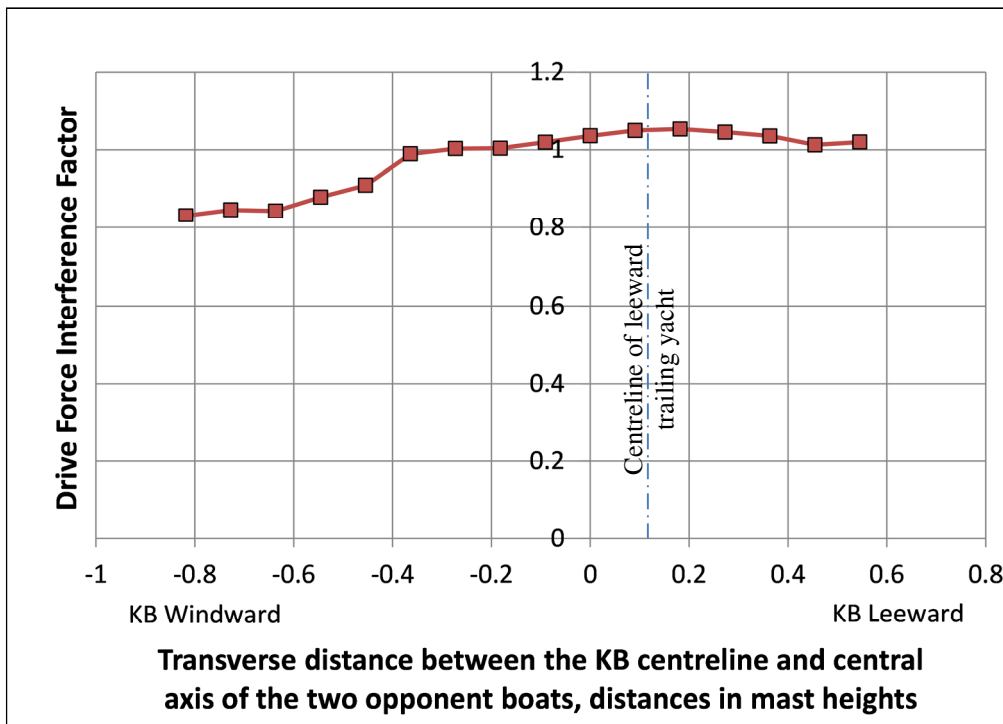


Figure 16 Drive force interference for the key boat on the layline with two opponents behind.

## 7. CONCLUSIONS

The interaction between yachts sailing upwind close hauled has been investigated through wind tunnel measurement of the forces and moments on a balance mounted key boat which is experiencing interference from one or two opponent boats. The variation of forces and moments on the key boat, in isolation, were also measured over a range of apparent wind angles and the drive to side force ratio used as an indicator of the effective apparent wind angle when an interfering boat is present. The data from two boat testing shows that much of the reduction in drive force is due to changes in wind angle rather than wind pressure. These changes in angle and wind pressure are similar to those directly measured around an isolated yacht using Cobra probes. With three boat interference there are too many possible position combinations to consider all of these and so tests focused on two starting line and two layline scenarios. It has been shown that on a starting line with one opponent to windward and one opponent to leeward the interference is dominated by the adverse effects of the leeward boat. If the leeward boat is sufficiently remote then the windward boat can offer some relief. However if the two opponent boats are to windward then the small increase in drive force primarily depends on the proximity of the nearest of the two. With two boats to leeward the second boat enhances the adverse effects of the nearer boat. Two layline scenarios have also been considered and it was found that the most significant interference occurs if there is a yacht immediately ahead, in which case drive force losses can be minimised by erring to windward.

## REFERENCES

- Caponnetto, M., The aerodynamic interference between two boats sailing close-hauled, *International Shipbuilding Progress*, 44(439), 241-256, 1996
- Johnson, M., Racing basics, available on-line at [www.uiowa.edu/~sail/skills/racing\\_basics/index1.shtml](http://www.uiowa.edu/~sail/skills/racing_basics/index1.shtml), 1995
- Marchaj, C.A., *Sail theory and practice*, Dodd Mead & Company, NY, 1982.
- Richards, P.J., Le Pelley, D.J., Jowett, D., Little, J., Detlefsen, O., (2013) 'A wind tunnel study of the interaction between two sailing yachts'. 21st Chesapeake Yacht Sailing Symposium, Annapolis, USA, 15-16 March, 2013.
- Spenkuch, T., Turnock, S., Scarponi, M., & Shenoi, A., Lifting line method for modelling covering and blanketing effects for yacht fleet race simulations, *Proceedings 3rd High Performance Yacht Design Conference*, Auckland, NZ, 1-4 December 2008.

# COMPARISON OF DOWNWIND SAILING PERFORMANCE PREDICTED FROM WIND TUNNEL TESTS WITH FULL-SCALE TRIALS FROM AMERICA'S CUP CLASS YACHTS

I M C Campbell, Wolfson Unit MTIA, UK

## SUMMARY

This paper compares of wind tunnel sail data with full-scale performance, using trials data gained during the 32<sup>nd</sup> America's Cup event. VPP calculations were made using sail coefficients obtained from the wind tunnel and sailing speeds and angles were compared with measurements of the ACC yachts' performance. Causes for the differences that were found are discussed and relate to both the modeling and difficulties with trials measurements.

Data is also presented showing the differences between different sail shapes and sizes, which is a matter of interest to designers when developing sails. The differences found between wind tunnel results and sailing trials are discussed.

## 1. INTRODUCTION

The 32<sup>nd</sup> held in Valencia in 2007 was an extraordinary event in that teams could build two America's Cup Class (ACC) Yachts without constraints on development time from the Cup Protocol. Although this class has been superseded by multihulls much of the data obtained remains unpublished although it is valid for other monohull yachts and for validation of experimental and numerical modeling methods.

By kind permission from Luna Rossa Challenge some of the wind tunnel downwind sail data was published at the INNOVSail 2013 conference, Campbell (2013), for the purpose of comparing tests from different wind tunnels to help validate the use of wind tunnels for testing of sails.

The aim of this paper is to extend the work to the comparison of wind tunnel sail data with full-scale performance, using trials data gained during the 32<sup>nd</sup> America's Cup event. This data was measured and analysed by the performance team at the time of the event but has been re-examined for this paper for comparison with VPP calculations made using the wind tunnel data.

Two questions can be posed:

Do wind tunnel tests produce sail forces representative of full-scale sailing?

And can wind tunnel tests distinguish the performance differences between different sail designs?

Other direct methods have been used to address the scaling question, e.g. by measuring sail forces on a boat, Masuyama, (2013); or comparing sail shapes, Mausolf et al. (2011); or comparing pressures, Motta et al. (2013). By comparison performance measurement is an indirect method since sail forces are compared with speed predictions based on hydrodynamic forces. Nevertheless hydrodynamic forces can be predicted with reasonable accuracy and all the methods are subject to the problems of wind measurements in the real environment.

Comparison between sails is of particular interest to designers and sailors, since competition provides the incentive to find a faster sail. Numerical modeling for performance e.g. using RANSE CFD, as distinct from just inflating mould shapes to predict flying shapes using panel codes, is now available to sail designers, Wright (2010). Whilst CFD modeling of the flow may differ from that in the wind tunnel there remains the common issue that the flying shape is under the sailors' control and the sail forces vary with the flying shape. The flying shape is adjusted in the wind tunnel to optimise sail forces but although Luna Rossa Challenge used the Sail Vision on-board system shape matching of downwind sails proved difficult.

## 2. LUNA ROSSA CHALLENGE FOR 32<sup>ND</sup> AMERICAS CUP

The challenge was launched through the Yacht Club Italiano, the oldest sailing club in the Mediterranean, established in 1879 in Genoa, Italy. The two partners in Luna Rossa Challenge 2007 were the Prada Group and the Telecom Italia Group.

In February 2004, the Luna Rossa team was the first to set up its base in Valencia, where it started training in May with ITA 74, the yacht which had raced in the semi-finals of the Louis Vuitton Cup for the 31<sup>st</sup> America's Cup in New Zealand, and ITA 80, a similar design.



The team Luna Rossa Challenge 2007 (sailing team, design team, shore team, weather team, performance team, boat builders, sail loft, logistics, administration and management) included about 110 people from 18 different countries. At the time this organization was larger than the School of Engineering Sciences at the University of Southampton where the author worked. However the competition was immense with 11 challengers, having varying resources, seeking to race the Cup Defender Alinghi and with racing in different “Acts”, in house 2-boat tuning and informal match racing.

The Cup Protocol permitted each team to build two new America’s Cup Class yachts and the Luna Rossa Challenge launched ITA 86 in 2006 and ITA 94 in 2007, with Miuccia Prada being godmother. Considerable research and development went into the design of these yachts and the author was involved in the experimental work in the towing tank, the wind tunnel and on the water.

Sadly for Luna Rossa Challenge they were beaten in the Finals of the Louis Vuitton Cup by Emirates Team New Zealand, who then lost in the races for the America’s Cup to the Defender Alinghi. The subsequent 33<sup>rd</sup> and 34<sup>th</sup> America’s Cups were raced by fewer challengers in multihulls so the pinnacle of development of the match racing displacement monohull remains the defender Alinghi’s SUI 100 from 2007.



Figure 1 Luna Rossa racing Emirates Team New Zealand

### 3. WIND TUNNEL TESTS

The new wind tunnel (galleria del vento) became available at the Politecnico di Milano in 2004 and Luna Rossa Challenge conducted 12 weeks of upwind and downwind sail testing during the 3-year campaign for the 32<sup>nd</sup> America's Cup. The data in this paper comes from the 8<sup>th</sup> session conducted in February 2006 and represents the development phase for the downwind sails but not their final configuration used in the Louis Vuitton Cup. A total of 175 measurement runs were taken on 10 different asymmetric downwind sails during this session.

#### 3.1 Wind tunnel

The Politecnico di Milano wind tunnel had a closed circuit, with a bank of fourteen fans driving the air through the final bend into the large 14m x 4m low speed section. The tunnel floor was smooth, with a 35m long section, which allowed the boundary layer to grow to a thickness of approximately 300mm. There were consistent lateral and vertical variations in flow speed across the location of the model. These were associated with the flow pattern from the individual fans and amounted to an rms variation in pitot pressure of approximately 5%. The tunnel had a high speed section on the return circuit below the low speed section with a contraction ratio of approximately 3:1, which helped produce a relatively uniform speed in this smaller section. So to avoid the problems with the flow variations and effects from the presence of the model the mean flow speed was taken from measurements in the high speed section. Campbell (2013).

The tests were conducted with a twisted flow device, Zasso et al. (2005), using a true wind gradient measured in Valencia for the prevailing sea breezes. The gradient was curve fitted by a power law of between 1/20 and 1/30, which was considerably lower than the conventional 1/7 or 1/10 curves. The twist between the centre of effort and mast head was approximately 3 degrees and between the centre of effort and the boom approximately 5 degrees. The apparent wind angles in the wind tunnel tests were referenced to the centre of effort not the mast head.

#### 3.2 Model parameters

The model particulars were:

Scale 1:12.5

Reference length 1500mm model scale, 18.75m full-scale

Reference mast height above DWL 2698mm model scale, 33.725m full-scale

Reference distance of dynamometer centre from tunnel floor 40mm model scale – for centre of effort height calculations, which have not been corrected for this distance, so needs to be added in any VPP calculations.

Test wind speeds associated with nominal dynamic pressures of  $q = 2.91\text{Pa}$ , approximately 2.2 m/s, which was similar to full-scale apparent wind speeds. This speed was selected to give representative flying shapes using the scaling criteria of the ratio of wind pressure to sail cloth weight.

The model was mounted over a 6-component strain gauged balance with a small gap between its topsides and the floor of the tunnel. The floor was a large turntable that could be rotated to present the model at different apparent angles to the wind.

The model was fitted with remotely operable sail winches with cables led to the control room where the data acquisition system was also sited. The winches allowed adjustments to be made to; gennaker/spinnaker pole height and angle, gennaker sheet, main sheet and main vang, as can be seen in Figure 2. Other adjustments were made manually before the start of a test sequence.

#### 3.3 Test sails

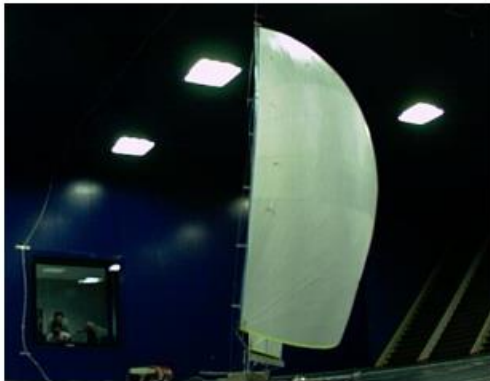
The sails were designed by Luna Rossa's sail team using North Sails' Flow-Membrane software. The model downwind sails were built by Guido Cavalazzi, one of the designers who enjoyed building sails, from the panels derived from the design mould shapes in similar manner to their full-scale construction. The model mainsails were built over a mould in a similar way to their full-scale construction with North Sails' 3DL method.

The sails referred to in this paper are listed in Table 1. The downwind sail type used for racing varied according to the true wind speed, mainly due to the different apparent wind angles associated with optimum downwind speed, as discussed later in this paper. The asymmetric gennakers have the prefix A in their code and the symmetrical spinnaker has the prefix S. Different methods of gybing applied to the asymmetrics and spinnaker, with operational advantages in different wind conditions that affected sail selection when racing.

Each new sail design was allocated a sequential letter and the sails referred to in this paper represent the best designs at the time of the tests together with the design of the original gennaker A3v5 and spinnaker S1. It should be noted that the America's Cup Class rule was revised to version 5 for the 32<sup>nd</sup> Cup, with an increase in the downwind sail area so new sail designs were developed at the start of the campaign.

Table 1 Sail dimensions

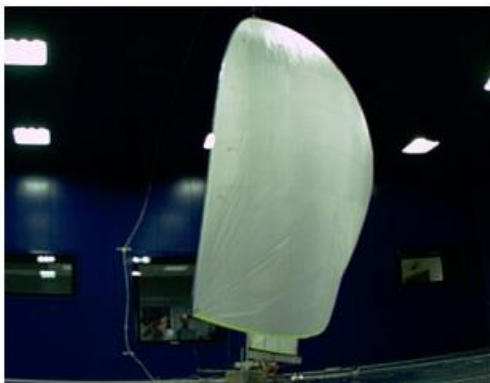
							<b>Model</b>	<b>Full-scale</b>
<b>Wind</b>	<b>Sail</b>	<b>Code</b>	<b>SLU</b>	<b>SLE</b>	<b>SF</b>	<b>Head</b>	<b>Area</b>	<b>Area</b>
<b>condition</b>	<b>type</b>		<b>m</b>	<b>m</b>	<b>m</b>	<b>m</b>	<b>m<sup>2</sup></b>	<b>m<sup>2</sup></b>
Light	asymmetric	A1-D	34.50	31.66	18.50	0.05	3.03	473
Medium	asymmetric	A2-F	35.00	31.80	18.42	0.05	3.46	541
Strong	asymmetric	A3-I	34.40	30.04	19.15	0.05	3.40	531
Strong	Original	A3v5					3.45	539
Strong	Spinnaker	S1					3.46	541
Light	mainsail	M1B					1.36	212.5
Medium	mainsail	M2A					1.36	212.5



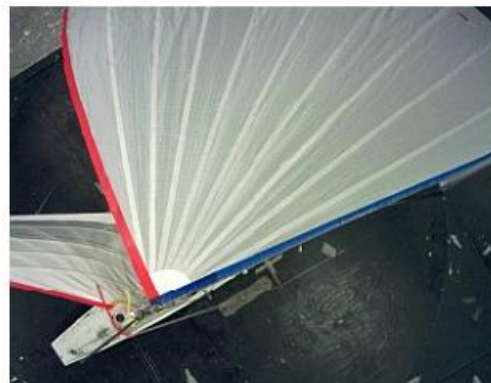
x8\_291\_front09/02/2006 16:55:27  
A2\_F, AWA = 60 deg, TWS = 9 knots



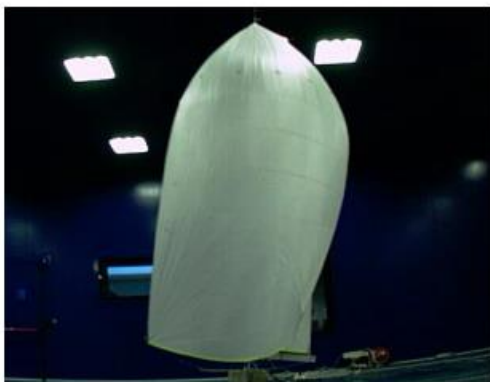
x8\_291\_overhead09/02/2006 16:55:09  
A2\_F, AWA = 60 deg, TWS = 9 knots



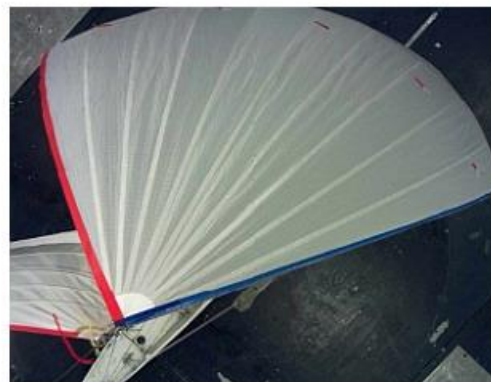
x8\_332\_front09/02/2006 20:04:43  
A2\_F, AWA = 75 deg, TWS = 10 knots



x8\_332\_overhead09/02/2006 20:04:25  
A2\_F, AWA = 75 deg, TWS = 10 knots



x8\_362\_front10/02/2006 10:54:39  
A2\_F, AWA = 90 deg, TWS = 12 knots



x8\_362\_overhead10/02/2006 10:54:27  
A2\_F, AWA = 90 deg, TWS = 12 knots

Figure 2 Images of the A2 gennaker under test at different apparent wind angles

### 3.4 Test method

The data was measured from the SF dynamometer using the Wolfson Unit Lasso system, which gave a real time display of the sail forces and was used as an aid to trimming the sails to produce the maximum driving force. The data files were analysed subsequently using the Wolfson Unit's WindCorrect program according to the process described in 3.6.

Each sail was tested over an appropriate range of apparent wind angles and the driving forces can be compared in Figure 3. Target driving forces had been obtained from previous test sessions so the sails were adjusted using the remote winches until forces were close to the target. This process could take approximately 5 to 10 minutes and data was then acquired over a period of approximately 1 minute to produce the average sail forces, moments and wind speed. Adjustments were then made in attempts to improve the driving force using the remote controls and real time force display, with acquisitions for mean values at promising settings. This process was repeated a few times within a 10 to 15 minute period before the wind was turned off to check for any zero drift in the dynamometer. Sail trimmers from the team were involved in some of the test sessions to share knowledge about sail settings.

Optimum sail settings of the A2 gennaker are shown in Figure 2, which can be compared with the boat racing in Figure 1, and it can be seen that the spinnaker pole was brought progressively aft as the apparent wind angle increased, bringing more of the gennaker in-line with the bow of the boat. However it can be seen from the fixed overhead camera image that the sail geometry remained similar relative to the apparent wind, with the boat appearing rotated under the sails.

At most angles the drive force could be increased without increasing the heeling moment and it can be seen that in many instances the maximum drive force was achieved at lower values than the maximum heeling moment. Thus the sail trim for maximum drive would produce the best boat speed.

If there were significant increases in heeling moment and heel force this might affect boat speed, due to related hydrodynamic changes in heel and induce drag, but this is only a potential issue with data from tests at 45 degrees apparent wind angle and can be resolved by VPP calculations through the optimisation of speed using the flat function, which reduces the maximum lift and drag with associated changes in driving and heeling forces.

The hydrodynamic characteristics of ACC yacht hulls were for their resistance to be lower at 20 degrees heel than when upright, due to their bow and stern overhangs increasing waterline length when heeled. As can be seen from Figure 14 the yachts tended to sail downwind slightly heeled so the wind tunnel model was tested at 5 degrees heel to represent any flow effect over the sails although at this angle the hull resistance was similar to when upright.

### 3.5 Windage tests

The windage of the hull and rig was measured without sails and the data was fitted to the VPP windage model, which resulted in drag areas of  $A_x = 9.5\text{m}^2$  and  $A_y = 50\text{m}^2$ . These data were subtracted from the measurements to derive the sail coefficients, so the VPP calculation included separately the windage and the sail coefficients.

The windage was added back for comparison of the VPP fit with the corrected driving forces and heel moments. The windage has a comparatively small effect on downwind performance since at an apparent wind angle of 90 degrees the hull generates very little lift to augment the driving force and the drag only affects the heel, which is small.

### 3.6 Sail coefficients

The measured sail forces and moments were corrected to sail coefficients and centre of effort locations by:

Correcting for wind off end zeros, following each set of runs.

Transforming the force data into the wind axes in the heeled plane using the IMS velocity vector method, which was a relatively small change for the 5 degree heel used for the downwind tests.

Subtracting the windage values, which are given in 3.5.

Calculating lift and drag coefficients based on the total sail area and dynamic pressure from the reference pitot.

Correcting the coefficients for wall boundary effects and wake blockage effects, taking due account of the induced drag due to lift in determining the separated flow for the wake blockage correction.

Recalculating the force and moment coefficients in the upright condition at the nominal apparent wind angle and comparing the results from the VPP fit.

The notation on the figures gives for each series the heel angle and apparent wind angle in the horizontal plane, as set on the turntable, i.e. not corrected to the heel plane.

### 3.7 Sail data

Test results for the basic sail force measurements on the downwind asymmetric gennakers are shown in Figure 3. There is a group of results for each sail that represents different attempts to optimise the trim for maximum drive force and it can be seen that these span approximately 5% at each apparent wind angle, which represents the scope available to the skill of good sail trimmers.

Lift and drag sail coefficients are related to the driving forces and heeling moments and these are shown in Figure 4 and Figure 5. Spline curves were fitted to these coefficients for VPP calculations and the associated VPP curve fit is shown in Figure 3. It can be seen that this fit is matched below the maximum values of driving force from each group of measurements, which was chosen to predict speeds when sailing with off-optimum sail trim.

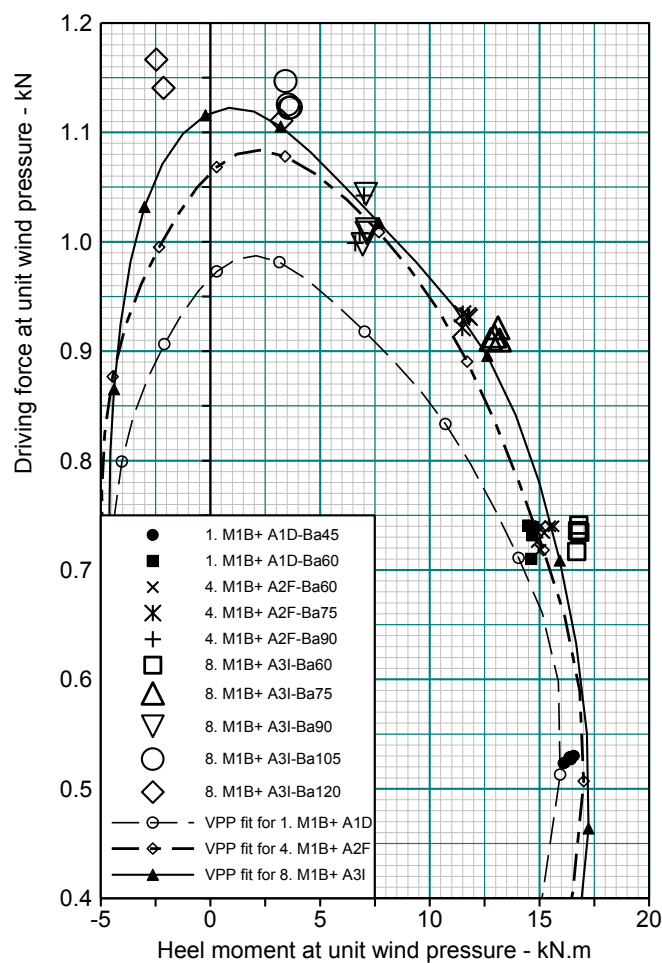


Figure 3 Variation of driving force with heel moment

The data in Figure 3 represents the better sails tested at that time, i.e. A1D, A2F and A3I. The A1-D sail had slightly lower area than the other two asymmetric sails and produced lower forces.

It can be seen from Figure 4 that the lift coefficients were relatively similar for all the sail types between apparent wind angles of 75 to 120 degrees but the A1 sail produced higher lift coefficients at angles of 45 and 60 degrees. The America's Cup Class benefitted in downwind sailing from the allowance of a pole as distinct from a bowsprit used in many sports boat classes. This enabled the gennaker sail luff to be orientated to an optimum angle to the wind at each apparent wind angle with the mainsail

accordingly adjusted. The sail geometry therefore remained similar relative to the wind, whilst being different relative to the boat, which accords with the relatively small variation of lift coefficient with apparent wind angle.

The drag coefficients, shown in Figure 5, tended to increase with apparent wind angle and were lower with the A2 gennaker compared to the A3. The relative location of the mainsail to the gennaker changed with apparent wind angle, being most closely coupled with the A1 gennaker at an apparent wind angle of 45 degrees. This geometric difference could relate to the higher lift coefficients produced by the A1 gennaker and the higher drag coefficients produced by the A3 gennaker but the drag also contributed to the driving force at apparent wind angles of greater than 90 degrees so it is possible that the sails were trimmed to produce more drag at these angles.

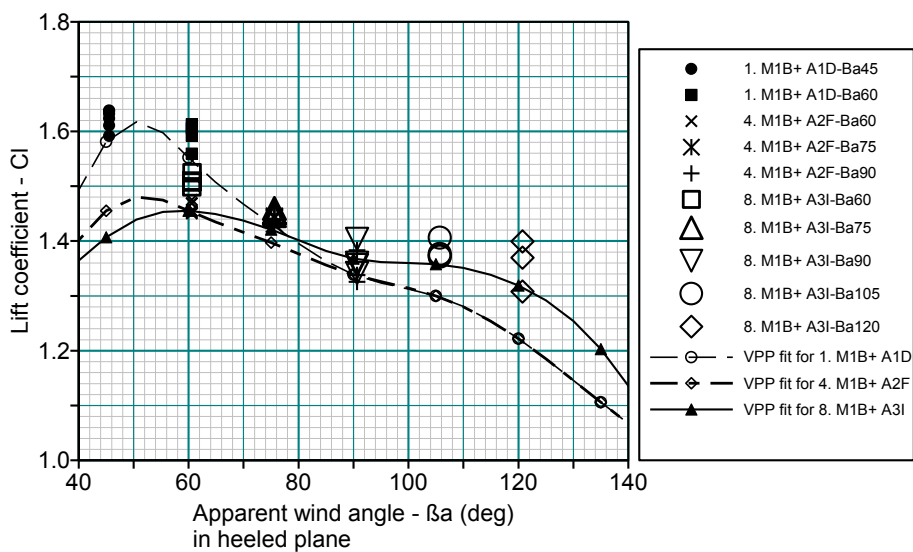


Figure 4 Variation of lift coefficient with apparent wind angle

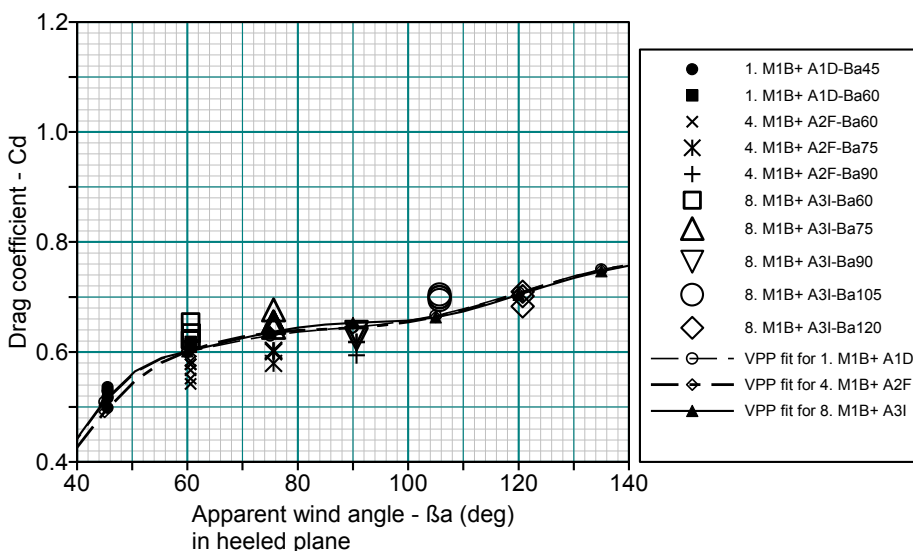


Figure 5 Variation of drag coefficient with apparent wind angle

The VPP fits were adjusted to lower values of lift outside the test data ranges to promote the VPP to iterate to values within the test range.

The centre of effort heights associated with the heeling moments are shown in Figure 6. These have been plotted on a different axis to the lift and drag coefficients to show the influence of heel force. The heeling moment is low at low values of heel force so has little influence on the hull hydrodynamics and sailing performance. The centre of effort height has been obtained from the transverse force to match how the VPP calculates heel equilibrium; however the longitudinal driving forces and pitch moments are considerably higher for downwind sailing at apparent wind angles of 90 degrees and would provide an alternative centre of effort height since the reason for the lower centre of effort height at low heel force is unclear.

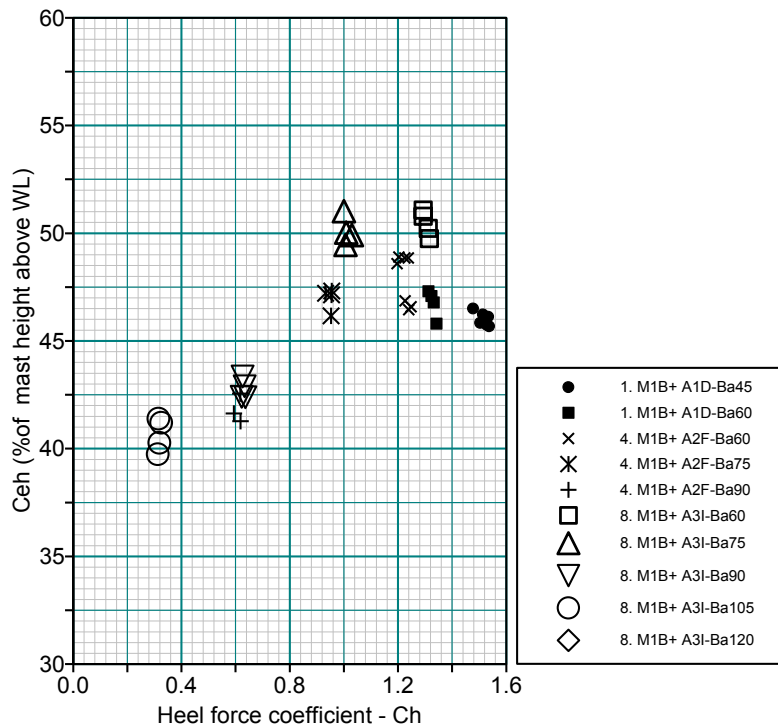


Figure 6 Variation of centre of effort height with heel force coefficient

The wind tunnel was used to compare different sail designs and a large number of shapes were tested, as indicated by the sail code letters. It is therefore of interest to compare sails with significantly different shapes to determine the level of discrimination that can be provided in wind tunnel tests and examples are shown in Figure 7.

The 2006 design of the A3-I gennaker produced approximately 5% more driving force at apparent wind angles of 105 and 120 degrees than the original A3v5 gennaker design from 2005 and similar driving force but at a lower heeling moment at an apparent wind angle of 90 degrees. These are clear differences despite the 5% variations in driving force found during the sail tuning process. The differences found between other sail shapes were, however, smaller but although the designs had different mould shapes their flying shapes were adjusted to produce the best sail forces and may have been similar.

It is also clear that the asymmetric gennakers produced significantly higher driving forces than the symmetrical spinnaker, of up to 15% at the larger apparent wind angles of 120 and 135 degrees.



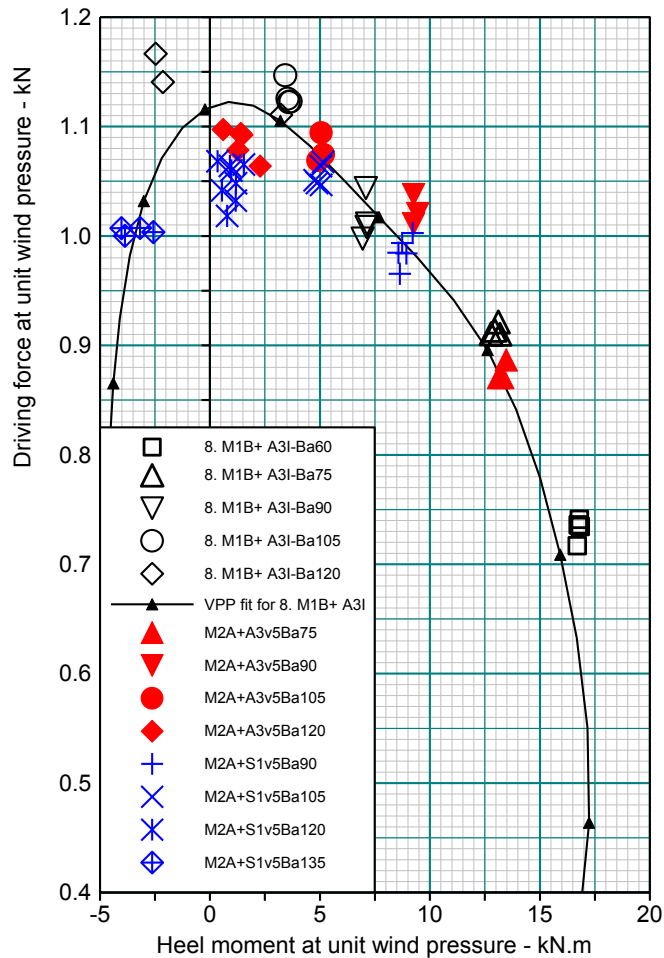


Figure 7 Variation of driving force with heel moment for Spinnaker and Gennakers

#### 4. VPP CALCULATIONS

VPP calculations were performed using the WinDesign WD4 software package developed by Yacht Research International and the Wolfson Unit MTIA, Oliver and Robinson (2008). This program had the facility to input experimental hydrodynamic data for the hull and aerodynamic data for the sails.

The hydrodynamic data for the hull was obtained from tank tests on a 1:3 scale model. This data currently remains confidential to the Luna Rossa Challenge however other generic data on America's Cup Class yachts has been published, e.g. Viola et al. (2012) The hydrodynamic characteristics for downwind performance prediction are, however, relatively simple compared to upwind predictions because downwind heel angles are small so heel and induced drag components are also small compared to the upright resistance characteristics of the hull, which dominate the speed calculations.

The VPP essentially iterates to a force balance between the hull drag and the sail driving force at wind speeds and angles that also match the wind vector triangle shown in Figure 8 using the geometric Equation 1. The VPP calculations take account of the variation of driving force with apparent wind angle shown in Figure 3. The result for downwind sailing always occurs with the maximum sail force coefficient and, unlike in upwind sailing performance prediction, the flattening and reefing functions are not required so the optimization element of the VPP calculations is also not required.

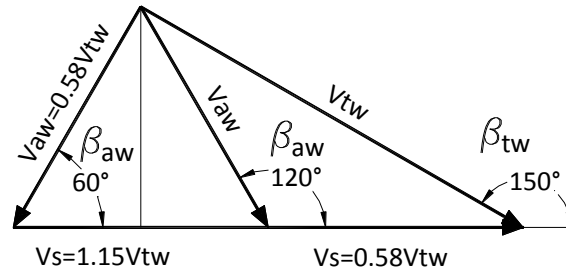


Figure 8 Wind vector triangle for downwind sailing

$$V_{AW} = \sqrt{(V_{TW}(Z) \sin(\beta_{TW}) \cos(\phi))^2 + (V_{TW}(Z) \cos(\beta_{TW}) + V_S)^2}$$

$$\beta_{AW} = \tan^{-1} \left\{ \frac{V_{TW}(Z) \sin(\beta_{TW}) \cos(\phi)}{V_{TW}(Z) \cos(\beta_{TW}) + V_S} \right\}$$

Equation 1 relating true and apparent wind speeds and angles

The aerodynamic characteristics for the sails were obtained from the wind tunnel tests and the inputs required for the VPP were straightforward, being the variation with apparent wind angle of lift and drag coefficients, as shown in Figure 4 and Figure 5 and centre of effort height, shown in Figure 6. The variation of drag with lift was obtained in the VPP calculations from an input of the effective rig height and an associated variation of centre of effort height with lift was also an input. However because the heel angles associated with downwind sailing were small and also the apparent wind angles were large reducing drag had little effect on driving force and the maximum lift produced the fastest speeds. Therefore the effective rig height and variation in centre of effort height did not affect the performance predictions.

A set of lift and drag coefficients were provided as inputs to the VPP for each downwind sail in combination with the mainsail. That is separate coefficients were not produced for asymmetric gennaker and mainsail as is the case when the VPP calculates sail forces from sail dimensions using generic data held within the program. The range of true wind speeds and angles associated with each sail was specified, which ensured that the VPP calculations were based on the same sail selection that was used by the sailors on the boats.

As described in paragraph 3.7 the sail coefficients were set slightly lower than the maximum values obtained from the wind tunnel tests. This was to allow for the sail trimming on the boats to be below optimum since the sailors did not have the benefit of sail force measurements that were available in the wind tunnel. However, to investigate sensitivity, VPP calculations were also performed with a 5% increase in lift coefficient and an associated increase in induced drag. These results are also shown in the performance comparisons given in Section 6 of this paper.

The VPP output is normally given as the speed polars, Figure 9, showing the variation of boat speed with true wind angle for Figure 3 increments of true wind speed. The polars provide a good visual indication of the true wind angles for optimum speed made good downwind and these are marked by square symbols in Figure 9.

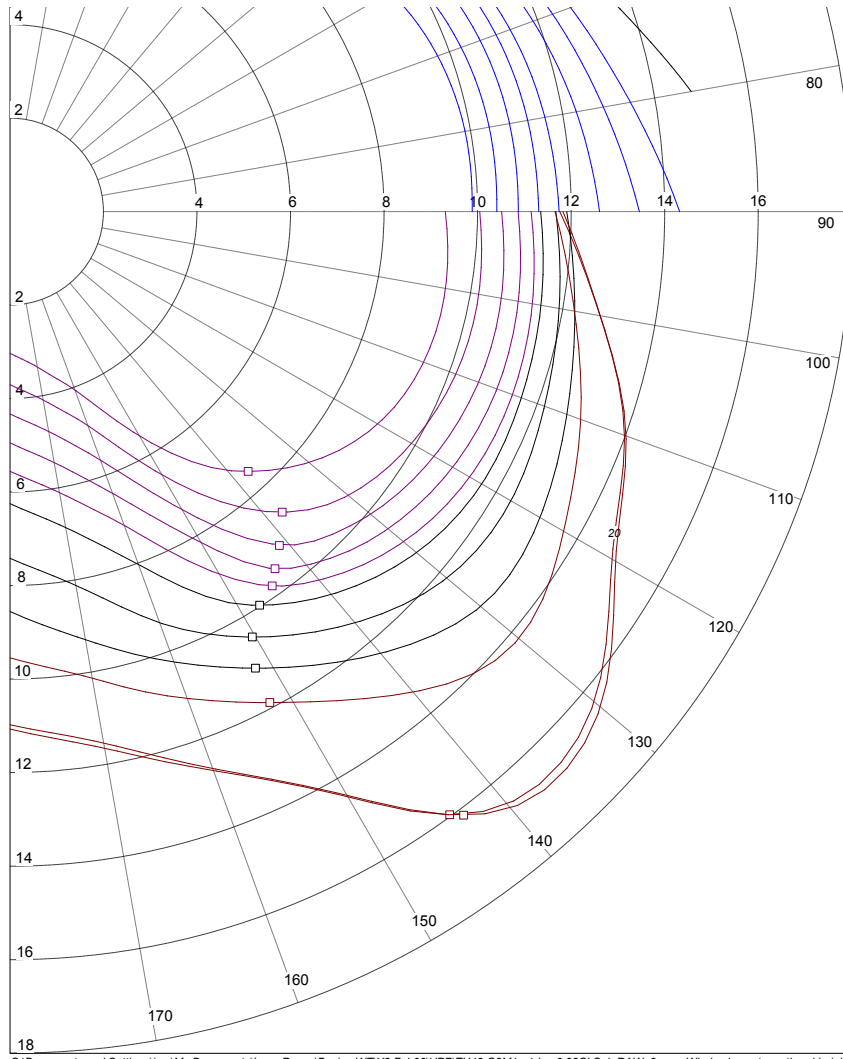


Figure 9 VPP polar speeds downwind

There are, however, other parameters in the VPP output including apparent wind speeds and angles and heel angle, which is important for upwind sailing but is also an indicator of apparent wind angle for sailing downwind. In Figure 10 the speed made good downwind is shown plotted against heel angle for fixed true wind speeds to show both the optimum heel angle and the loss in speed when not at optimum heel. It can be seen that the optimum heel tends to reduce with increasing wind speed but the speed loss is great at heel angles less than optimum than at greater heel angles.

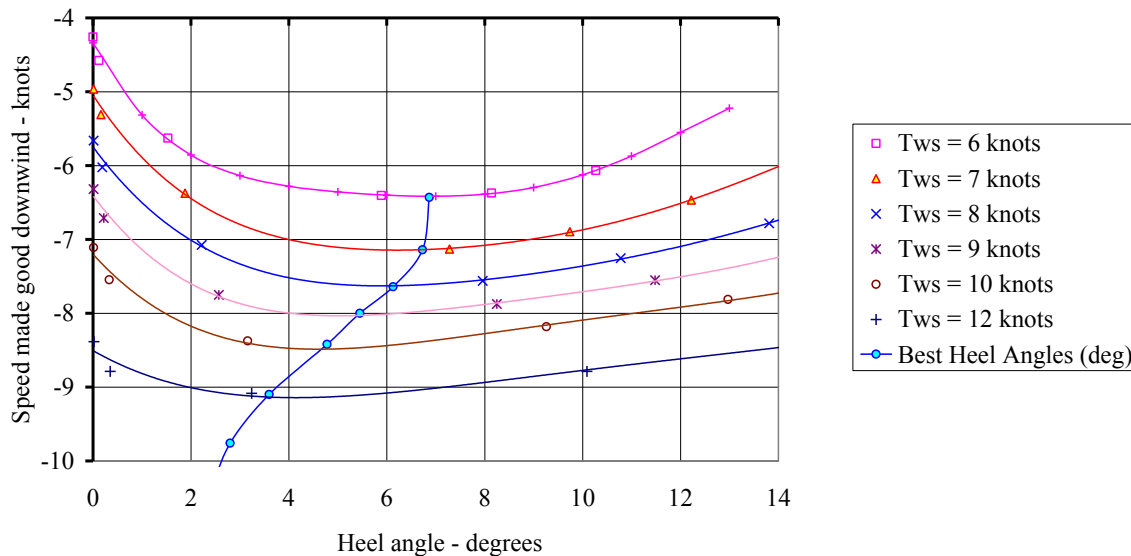


Figure 10 Variation of speed made good downwind with heel angles and true wind speed

## 5. SAILING TRIALS

2-boat sailing trials were conducted throughout the 3-year campaign but these were limited by a number of factors: e.g. the sailing season in Valencia, periods away from Valencia for racing in “Acts”, bad weather with light winds or storms and informal racing with other teams. The trials were conducted for a variety of purposes: e.g. to obtain baseline performance data, to test hull components including fins bulbs and rudders, to test rig components including mast booms and sails, to tune the new boats as they arrived and for crew and race training. Despite the 3-year campaign and a protocol for the Cup that permitted unrestricted sailing, time on the water was a limiting resource for the team and more time would have allowed more development.

Emphasis was placed on upwind sailing performance, since in match racing it is important to get to the windward mark first and control the boat behind, so downwind sail evaluation was limited and sometimes performed in conjunction with other trials, e.g. fin and bulb evaluation. Baseline target speeds and wind angles were developed from sailing trials in 2005 but the data presented in this paper is from trials conducted between April and July 2006. ITA74, Luna Rossa’s race boat from the 31<sup>st</sup> Cup, was sailed against ITA86, their first new design for the 32<sup>nd</sup> Cup, and approximately 30 downwind sailing trials have been analysed for comparison with VPP predictions based on wind tunnel data. Mausolf et al. (2011) reported on the difficulties of conducting full-scale downwind trials to measure flying shapes on one boat sailed over a three day period. By comparison Luna Rossa’s trials were conducted over a much longer period, with greater resources, using 2 boats but with comprehensive performance monitoring equipment to measure speeds and angles. Nevertheless it proved to be a difficult task to obtain definitive measurements of differences to the desired level of accuracy.

The trials were conducted with the boats operated by the sailing team, crewed and helmed by sailors with America’s Cup experience and other yacht racing pedigrees. The performance was monitored both on-board and remotely by the performance team using equipment set-up and calibrated with the help of the shore team and the sailing conditions were monitored by the weather team operating from their own boats. The trials techniques had been developed during previous Cup campaigns with input from members of different teams in previous campaigns so it was a well rehearsed process. The results were reviewed following each day’s sailing at a STEP meeting, so named because it had originated on steps during previous Prada and Luna Rossa Challenges in New Zealand. So considerable efforts were made to improve the accuracy of the measured data throughout the trials periods.

The trials process involved setting the two boats off on parallel courses for a 6 to 8 minute period, with the crews concentrating to obtain the best relative performance from each of the boats. Measurements of speeds, angles and distances were averaged over this period. The two boats would then swap sides and the trials repeated then, when time and position on the course permitted, the boats would gybe and the trials repeated with the wind on their opposite side giving four separate measurements of sailing performance for each configuration of the boat.

Corrections were applied to the trials measurements to improve their consistency. Wind measurements from the mast head instruments presented particular difficulties for downwind sailing due to; the proximity of the masthead gennaker, the boat's motions, twist in the apparent wind gradient and the low apparent wind speed of approximately half the true wind speed. Normal upwash corrections applied when sailing upwind with the fractional genoas were inaccurate for downwind sailing with masthead gennakers so tests were conducted on the wind tunnel model by observing angles on the masthead wand from an overhead camera to obtain corrections for downwind sailing. However, the masthead wand could be observed oscillating through large angles when the boats were sailing downwind.

Correlations were made between the wind measurements upwind and down, from port and starboard gybes and from weather boats stationed on the course. The relationship between the true and apparent wind speeds and angles must conform to the wind triangle, Figure 8, and this improved during the trials period but discrepancies remained of up to 0.5 knots and 5 degrees. In addition the twist in the wind gradient varied and was noticeable to the navigators on the boats so particular corrections were applied. These issues complicate the correlation between the measurements and VPP calculations.

## 6. PERFORMANCE COMPARISONS

Comparisons between results from the VPP calculations and measurements from the sailing trials are shown in Figure 11 to Figure 14. The true and apparent wind angles are shown in Figure 11 and a number of points can be noted:

The distribution of measurements represents the wind speeds during the 4-month period of the trials, with preponderance in the 10 to 15 knot range, the sea breeze conditions. Only a few trials were conducted in lighter wind conditions, with little interest in wind strengths below 7 knots as it was the minimum for starting Cup races. There were a significant number of trials in stronger winds of 17 to 22 knots where the spinnaker would be used.

The apparent wind angle increased with true wind speed from less than 60 degrees in light winds to greater than 120 degrees in strong winds whilst the boats were being sailed downwind on courses aimed best speed made good downwind. There were significant variations of 5 to 10 degrees in the apparent wind angle in the true wind range of 12 to 15 knots, which was indicative of the boats being sailed differently from trial to trial. There was also variation in the higher wind speeds but at greater apparent wind angles of the order of 120 degrees.

Apparent wind angles from VPP calculations are shown for both the optimum speed made good downwind and at the trend through the measured true wind angles. The VPP optimum gives a good fit up to a true wind speed of 15 knots although it is associated with lower true wind angles than the trend. Increasing the sail coefficients made little difference to the VPP optimum true and apparent wind angles so it would appear that the differences with the measurements were either due to the trials measurements or the sailing style.

The optimum downwind angles from VPP calculations in a true wind speed of 20 knots, Figure 9, were considerably smaller than those sailed during the trials. This was known at the time of the races but the boats continued to race at the higher angles, i.e. sailing angled closer to the leeward mark. This may have been due to operational or structural reasons, e.g. match racing tactics, sail handling issues when gybing or to lower the apparent wind speed to avoid blowing out the sail. Alternatively there may have been an issue with the VPP but without further races with ACC Yachts in 20 knots of wind the issue remains unresolved.

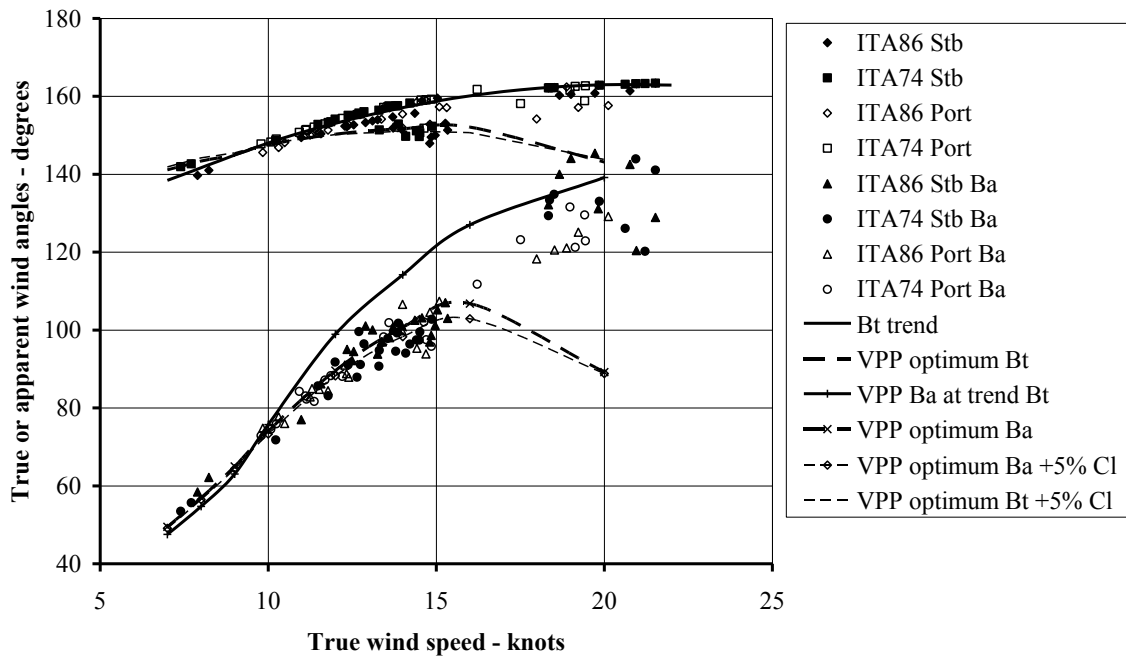


Figure 11 Variation of true and apparent wind angles with true wind speed

The differences between predicted and measured boat speeds are shown in Figure 12, where the baseline was taken as a curve fit through the measured boat speeds. There is less variation in the speed than in the angles, which may be because boat speed measurements are more straightforward than wind measurements.

Comparisons with VPP calculations showed the measurements lying between the predictions at the trend through measured true wind angles and at optimum true wind angles. The predicted optimum in 20 knots true wind speed was a high boat speed, which is associated with the smaller apparent wind angle, shown in Figure 11 and higher apparent wind speed, shown in Figure 13. Increasing the sail coefficients improved the correlation between the VPP optimum and measured boat speeds in the true wind range of 10 to 14 knots.

Of particular note are the low boat speeds in light winds compared to the predictions and the reason for this is unclear. It is unlikely that the hydrodynamic drag was incorrect since it is dominated by friction drag at these lower boat speeds, which can be reliably predicted. There was generally good correlation of speeds and angles at 10 knots true wind so it is unlikely that the sail coefficients were incorrect to the extent required to give the discrepancy in the lighter winds, although it is possible that the sails did not fly properly in the light winds due to the motions imposed by the wave action on the boat.

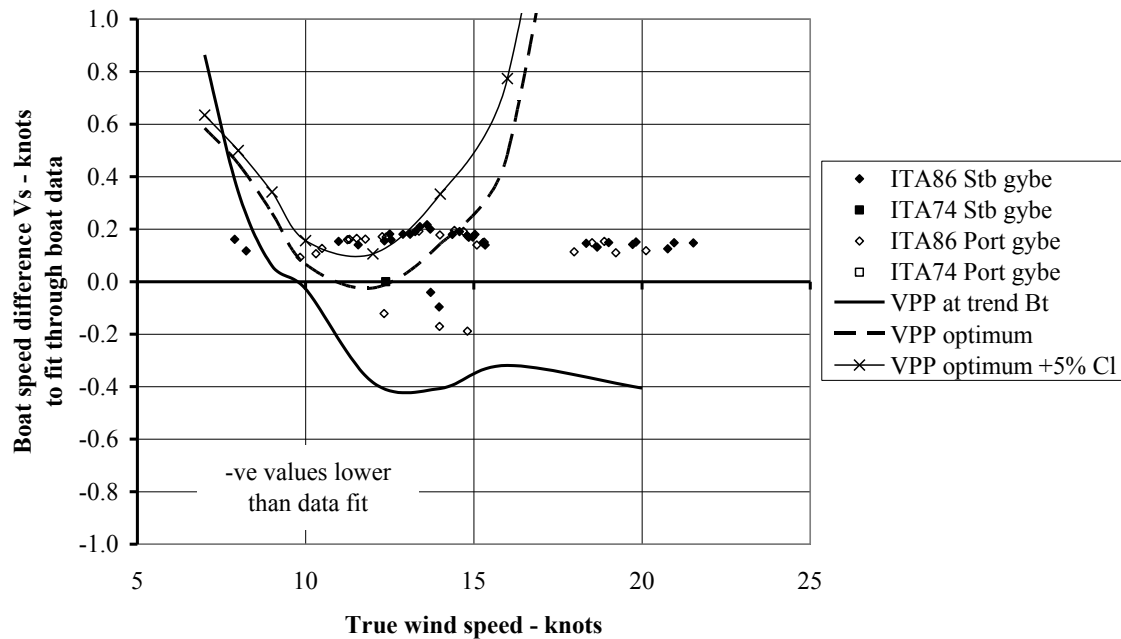


Figure 12 Variation of boat speed differences with true wind speed

Comparisons of the differences between predicted and measured apparent wind speeds are given in Figure 13, where the baseline was taken as the VPP optimum values so there is no curve shown for the optimum as in the previous Figure 11 and Figure 12, and it can be seen that there is considerable variation in the measurements at particular true wind speeds.

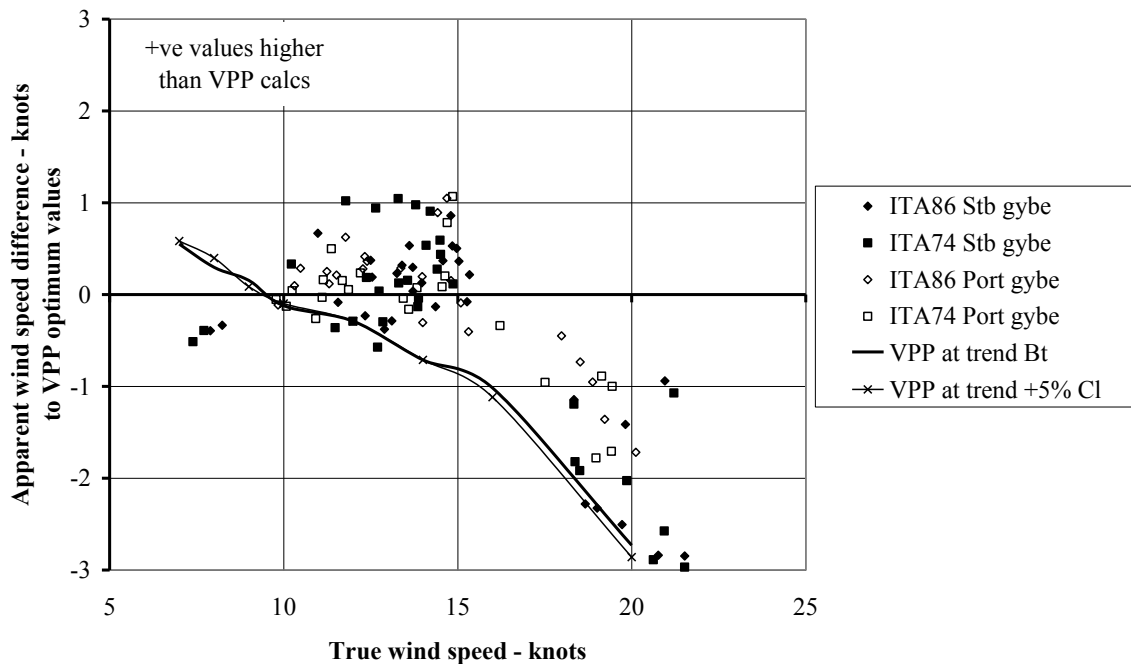


Figure 13 Variation of apparent wind speed difference with true wind speed

The apparent wind speeds were best matched by the optimum VPP calculations up to a true wind speed of 15 knots. As discussed previously the optimum VPP calculation at 20 knots occurred at lower angles and higher speeds than the measurements so the apparent wind speeds obtained from the trend through the measured true wind angle is a better match to the trials measurements for true wind speeds around 20 knots. Increasing the sail coefficients made a relatively small difference to the apparent wind speed although it should be noted that the scale of this figure is much coarser than for the boat speed shown in Figure 12.

The final comparison, given in Figure 14, is of heel angles and it can be seen that the measurements were generally higher than the predictions. Consideration of these measurements can be made together with the VPP output shown in Figure 10 and the wind tunnel data shown in Figure 3. Zero heel moment from the wind tunnel tests occurred at an apparent wind angle of approximately 120 degrees and this is consistent with the measurements shown in Figure 11 in around 20 knots true wind speed.

The higher heel angles in the true wind speed range of 10 to 15 knots are indicative of the boat sailing at a smaller apparent wind angle than optimum, which would also be associated with a smaller true wind angle and this does not appear to be the case from the data shown in Figure 11.

Increasing the sail coefficients in the VPP resulted in a relatively small change to the predicted optimum heel angles.

As in the previous plots the high VPP optimum heel in a true wind speed of 20 knots represents sailing at higher boat speeds and smaller apparent wind angles.

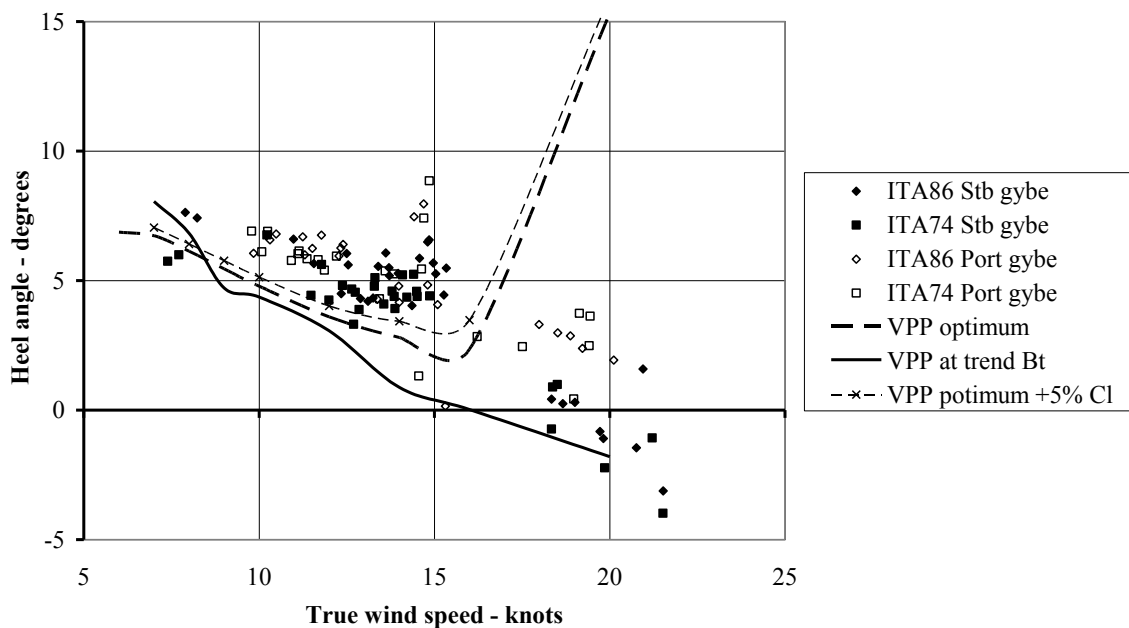


Figure 14 Variation of heel angle with true wind speed

The data in the preceding figures is of measurements of absolute performance from both the boats sailing in the trials. However the important measurements at the time of the challenge were their relative speeds, as shown in Figure 15, because these were used to tune the boats and set up their configuration, including rig, sails and appendages.

Improvements were sought in downwind speed made good of 1m/minute, since this would give an advantage of approximately a boat length on a downwind leg, which could be sufficient to gain an overlap in a match race and take control of the race.



1 m/minute speed difference equated to approximately 2% increase in driving force or reduction in drag but it can be seen in Figure 15 that the speed differences varied by up to 10 m/minute or 20% difference in force. This is considerably greater than the 5% difference due to sail trim found in the wind tunnel, as can be seen in Figure 3. The relative speed differences could be measured with greater accuracy than the absolute speeds and angles shown in the preceding figures so it is therefore clear that significant variations could be attributed to the wind environment and the sailing operation. These are essential ingredients of yacht racing but unfortunately they cloud the analysis of yacht performance.

It should also be noted that each downwind trial was conducted for a different purpose and that the crews' observations, which are not included in this paper, formed an important part of the trials evaluation.

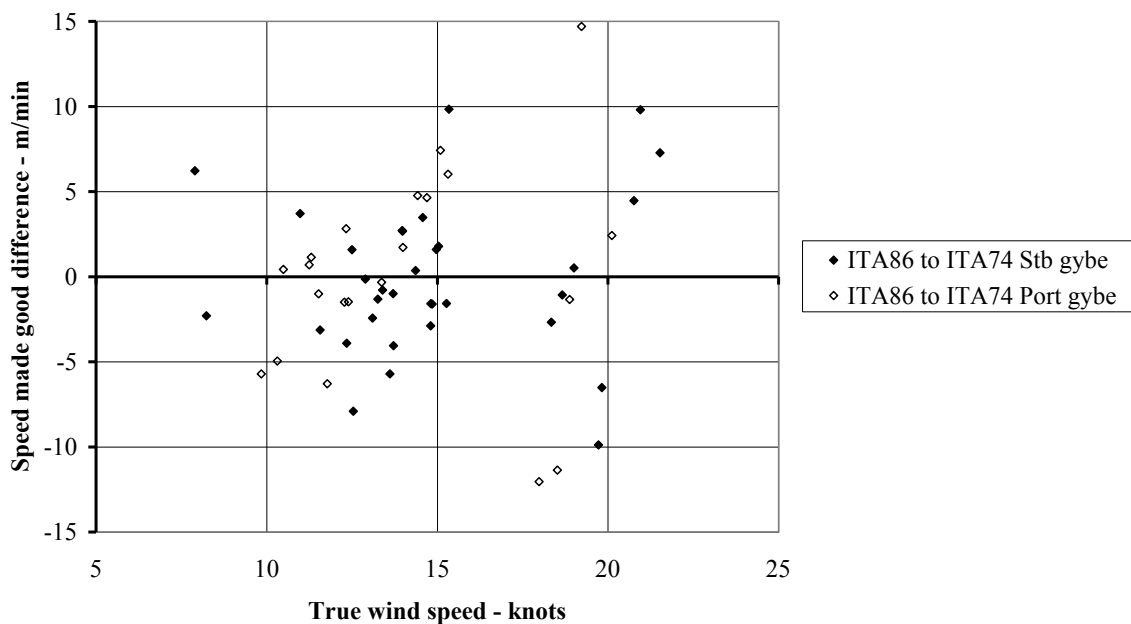


Figure 15 Variation of difference in speed made good with true wind speed

## 7. CONCLUSIONS

The aim of this paper was to investigate whether wind tunnel tests on downwind sails provide a reliable measure of their full scale sailing performance and it has been shown that there is reasonable agreement between VPP calculations and trials measurements provided performance is compared at related sailing angles and not just the optimum predicted by the VPP. There remains some uncertainty about the accuracy of the trials results that makes it difficult to assess the source of any errors that may exist within the wind tunnel results.

It is clear that adjustments to the sail settings alters their flying shapes, which changes the sail forces by the order of 5% near to the maximum driving force. Wind tunnel tests have provided a reliable method to measure these sail forces with good repeatability.

The forces for a particular sail combination show a reasonably smooth variation with apparent wind angle and with relatively small changes in the lift coefficient, which is consistent with the flying shapes of the sails as viewed in the wind axes.

Significantly different downwind sail shapes produce different forces, e.g. forces from gennakers can be distinguished from those from spinnakers. The effect of smaller shape changes are more difficult to distinguish once the sheeting has been adjusted to optimise their flying shape.

When comparing VPP calculations with sailing trials data the output needs to be interrogated to match measured sailing angles and it is not sufficient to compare speeds from the VPP optimum downwind points. It is also necessary to compare all the output results, including true and apparent wind speeds and angles and heel angle, not just boat speed and wind speed and to ensure that the trials measurements conform to the wind vector triangle.

Trials measurements are difficult even with the best equipment and systems. Variations remained within trials data gathered carefully over a prolonged period even where corrections were applied.

Increasing the value of the sail force coefficients in the VPP increased the predicted boat speed but did not significantly improve the correlation with true and apparent wind angles from the trials. It is unlikely that the source of differences in wind tunnel measurements since the apparent wind angle is set in the tunnel without reference to wind instruments mounted on the model.

Relative differences in downwind sailing speeds from the 2-boat trials, which could be measured with greater accuracy than absolute performance, showed much greater variation than could be attributed to the sail force variations measured in the wind tunnel.

In stronger wind conditions of around 20 knots the ACC boats were sailed at much wider true and apparent wind angles than the optimum from VPP calculations, possibly for operational or tactical match racing reasons and possibly for structural reasons and in lighter winds of around 7 knots the measured boat speeds were considerably lower than predicted.

## 8. REFERENCES

Campbell, I.M.C., The Performance of Offwind Sails Obtained from Wind Tunnel Tests. *R.I.N.A. International Conference on the Modern Yacht*.1998

Oliver, J.C. and Robinson, J., Development of a VPP Based Rating for J-CLASS Yachts”, *20th International HISWA Symposium on “Yacht Design and Yacht Construction”*, Amsterdam, November, 2008

Wright, S., Claughton, A., Paton, J., Lewis, R., Off-Wind Sail Performance Prediction and Optimisation. *2nd International Conference on Innovation in High Performance Sailing Yachts (INNOV’SAIL)*, Lorient, France. 2010

Campbell, I.M.C., A Comparison of Downwind Sail Coefficients From Tests in Different Wind Tunnels. *3<sup>rd</sup> International Conference on Innovation in High Performance Sailing Yachts (INNOV’SAIL)*, Lorient, France. 2013

Zasso, A., Fossati, F., Viola, I.M., Twisted Flow Wind Tunnel Design for Testing Yacht Sails. *4th European and African Conference on Wind Engineering (EACWE4)*, Prague, Czech Republic. 2005

Mausolf, J., Deparday, J., Graf, K., Renzsch, H., and Böhm, C., Photogrammetry Based Flying Shape Investigation of Downwind Sails in the Wind Tunnel and at Full-Scale on a Sailing Yacht, *20<sup>th</sup> Chesapeake Sailing Yacht Symposium*, Annapolis, Maryland, USA. 2011

Claughton, A., Fossati, F., Battistin, D., Muggiasca, S., Changes and development to sail aerodynamics in the ORC International Handicap Rule, *20th International Symposium on “Yacht Design and Yacht Construction”*, Amsterdam, 2008

Motta, D., Flay, R.G.J., Richards, P., Le Pelley, D., An Experimental Investigation of Asymmetric Spinnaker Aerodynamics Using Pressure and Sail Shape Measurements, *3<sup>rd</sup> edition of the conference INNOV’SAIL*, Lorient France, 2013

Y. Masuyama, The Work Achieved with the Sail Dynamometer Boat “Fujin”, and the Role of Full Scale Tests as the Bridge between Model Tests, *3<sup>rd</sup> edition of the conference INNOV’SAIL*, Lorient France, 2013

Viola, I. M., Flay, R. G. M., Ponzini, R., On the CFD Modelling Uncertainty of ACC Yachts, *4<sup>th</sup> High Performance Yacht Design Conference*, Auckland, NZ, 2012

## **9. ACKNOWLEDGEMENTS**

It has only been possible to publish the previously confidential results due to the kind permission of Sig Patrizio Bertelli, although Luna Rossa Challenge retain their Intellectual Property Rights to the data in accordance with their agreement with the Wolfson Unit MTIA.

The work was originally performed for the Luna Rossa Challenge with the aim of winning the prestigious America's Cup and many of its team members played their part in enabling the work described in this paper to be conducted.

Thanks are particularly extended to the North Sails' designers; Grant Spanhake, Henrik Søderlund and Guido Cavalazzi, for designing and manufacturing the model sails and their assistance in the wind tunnel.

The wind tunnel tests were also conducted with the helpful assistance from staff at the Politecnico di Milano under the guidance of Fabio Fossati.

My work was contracted through the Wolfson Unit MTIA with thanks to my colleagues for their contribution in the development of the systems used for the tests.

# EXPERIMENTAL AND NUMERICAL ASSESSMENT OF MEGA-YACHT AERODYNAMIC PERFORMANCES AND CHARACTERISTICS

**F. Fossati, F. Robustelli, P. Schito**, Politecnico di Milano – Department of Mechanical Engineering, ITALY  
**A. Cuoci, M. Derudi**, Politecnico di Milano – Department of Chemistry, Materials, and Chemical Engineering, ITALY  
**S. Dellepiane** Azimut - Benetti, ITALY

## SUMMARY

In this paper an overview of the methodologies developed at Politecnico di Milano in order to assess mega-yacht aerodynamics in terms of aerodynamic loads, comfort analysis, pollutants dilution and re-ingestion analysis are provided. Experimental approach using wind tunnel tests is described as well as numerical tools developed by the authors in the open-source fluid-dynamic framework OpenFOAM. Several different approaches are investigated for modeling the dispersion of exhaust gas stream around the boat aiming to find the best compromise in terms of accuracy and computational cost. In addition effects of temperature and gravity on the pollutant dilution are investigated and discussed.

## 1. INTRODUCTION

Large yacht design is obviously driven by aesthetics, but, in order to achieve the designer's wishes, a lot of engineering and technology is required. Typically the aspects that are being studied during the design stage are those related to seakeeping, noise and vibration. For these problems, well established analysis techniques exist, ranging from towing tank tests to computer simulation by means of CFD, FEM and SEA software. Larger main dimensions, superior comfort requests and higher manoeuvrability characteristics focus mega-yacht designer attention towards hull and superstructure aerodynamic performance. Windage evaluation of very high superstructure, aerodynamic load assessment, and accurate air flow simulation are considered very important in the design procedures to get optimal layout and opening position, to support Dynamic Positioning Systems design and in general to evaluate comfort and exhausts gases issues which are obviously a key features on board a luxury yacht. More in details, the interaction between large superstructures and air flow may cause annoying local increases in wind speed (speed up) in open decks and guest relax area and an increasing number of owners are requesting aerodynamic analysis as a contractual commitment for new yachts, especially larger ones; another aspect related to the aerodynamic performances of the yacht is the potential discomfort or health hazard caused by the diesel engines exhaust gases: on large yachts, the required power for propulsion and hotel loads can vary from 3000 to 8000 kW, generated by diesel engines. The exhaust ducts are usually lead partly underwater, and partly lead to the main mast, so that when the yacht is at anchor, no exhaust will go at water level, where guests could be swimming. However, the design of mast exhaust outlets and the surrounding superstructure must be done very carefully, in order to avoid uncomfortable concentrations of exhaust gas in open areas, or, even worst, re-ingestion of pollutants (exhaust gas) by the various HVAC inlet grills that are located on the yacht.

Aerodynamic resistance and wind effects have been considered in naval architecture as regards large ship superstructure influence on propulsion and manoeuvring. In Lewis (1988) extensive experimental research performed in the early 30s by Hughes are reported [Hughes (1930,1932)].

In Baker (1942) presented a formula for the assessment of aerodynamic resistance of merchant ships considering the different shapes of hull and superstructure. The topic was described by Saunders (1957) that considers air resistance due to pressure effects only and by Isherwood (1973) who developed a multiple linear regression analysis of experimental tests to get non dimensional coefficients for longitudinal and transverse aerodynamic components as well as for yaw moment.

Similar analysis based on a wider and updated set of data was presented by Fujiwara et al. (2001, 2006). Further reference data relative to aerodynamic forces on marine structures and ship superstructures are available in Haddara et al.(1999) and in Koop et al. (2012), but relative to shapes very different to mega yachts. Only recently aerodynamic specific matters related to maxi yacht design have considered, extensively reported in Wallis et al. (2013) and in Harries et al. (2010).

Dynamic Positioning System (DPS) is a computer controlled system to automatically maintain the ship position and heading by using her own propellers and thrusters. Position reference sensors, combined with wind sensors, motion sensors and gyro compasses, provide information to the system about the ship position and the magnitude and direction of the acting external forces [Det Norske Veritas (2001)]. The system software contains a mathematical model of the ship that includes information relative to its hydrodynamic and aerodynamic characteristics and to the location and propulsive characteristics of the thrusters. This knowledge, combined with the sensor information, allows the computer to assess the steering angle and thruster output for

each thruster. In Balchen et al. (1980) a mathematical model of a Dynamic Positioning System based on Kalmar filtering is described.

This allows operations at sea where mooring or anchoring is not feasible due to deep water, congestion on the sea bottom (pipelines, templates) or other problems. Dynamic positioning may either be absolute in which case the position is locked to a fixed point over the bottom, or relative to a moving object like another ship or an underwater vehicle. It's also possible to position the ship at a favourable angle towards the wind, waves and current (weathervaning).

While a detailed description of the system is outside the aim of this paper, any DPS contains an aerodynamic - as well as hydrodynamic model of the ship. DPSs have been applied since the early seventies when drilling has become interesting also in deep sea where no anchoring system could be considered. In this case, and more in general in the offshore drilling field, DPS development has been focused mainly on the hydrodynamic aspects as wave loads and current were predominant. For maxi and mega-yacht applications the scenario is quite different. DPS is used to get and maintain a fixed point or to maintain a defined course at very low speed, mostly in good weather conditions or in any case in low Beaufort sea states. Typical applications are maintaining ship position and orientation in sheltered waters without anchoring, or course keeping in narrow passages. In this case aerodynamic forces are very important and, in the first case mentioned above, can be predominant. The ship aerodynamic behaviour assessment through wind tunnel tests or numerical simulations can be very significant for the performance of the installed DPS system.

In addition as previously mentioned comfort on board a luxury yacht is obviously a key feature in all its aspects, like ship motions, noise and vibrations, windage and exhausts gases issues. The on board comfort assessment on the various living areas of the yacht decks can be performed by two point of view. The first one is related to the flux acceleration and can be considered by means of local wind speed measurements, i.e. speed up comfort. The second one is connected to the air pollutant concentrations of gases released from the stacks of the yacht: it can be taken into account by means of pollutant concentration measurements.

Since the speed-up comfort results are heavily dependent on the yacht exterior profile, these measurements are to be carried out at an early stage: excessive speed-up values in external areas like sunbathing or dining may be overcome by modifying the exterior shape, or by inserting glass or plexiglass windscreens, which can be fixed or removable. These elements usually have an impact on the aesthetics of the yacht, so they must be carefully designed together with the exterior stylist.

The positioning of HVAC external grids and generator exhausts can also be dependent on the aerodynamics of the flow around the yacht. Grids are usually placed according to the exterior profile design, so that they have the smallest possible aesthetic impact, and by using common practices [Hajra et al. (2013)] in order to avoid pollution between exhaust and intake air (for example, usually the intake air grids are put on the opposite side from the exhausts). However, exhausts gas flow around the yacht superstructure may not be intuitive, therefore an experimental evaluation is very useful in order to detect possible re-ingestion problems. Most of the yachts now have diesel generator exhausts running up to the stack, as high as possible, but limitations come from the maximum allowable backpressure and from the fact that they often have to be incorporated into the mast or superstructure design, so that they are not directly visible. Although exhausts are usually provided with particle soot filters and/or catalytic filters, great care is to be taken in order to ensure that gas is diluted or is flowing far enough from the external guest living areas. If there were a certified helideck on-board, wind tunnel tests would be required by the rules stated by the Safety Regulation Group of the UK Civil Aviation Authority (CAA) and the Offshore Safety Division of the Health & Safety Executive (HSE) in [CAA Paper (2004/02)] to estimate the temperature rise, due to the exhausts gases, in way of the helideck, in order to make sure that the helicopter can develop enough lift.

The lack of data concerning the peculiar mega-yacht forms and the required accuracy lead to set up scaled model wind tunnel tests similarly to testing the underwater hull in a towing tank. However, there is a subtle difference in the design of underwater and above water hull and superstructures: in the former, the hull design is mainly performed by the naval architect, whilst in the latter a lot of other inputs are required, the biggest one being the exterior designer's, but also the air conditioning system design, the antennas and mast layout. This means that model for the wind tunnel test can be built only when all this processes are almost finished (i.e. the design has already gone through many laps of the so called "design spiral"), because it is very expensive and time consuming, so it must be done only when the project is well defined. However, if a potential problem would be detected with the wind tunnel tests at this advanced stage, it would probably mean going back to the designer's drawing board to modify the structure or the layout, and consequently a new discussion with the owner.

A way to overcome this problem and have a more efficient and integrated design of the superstructure with the comfort requirements is the computer simulation by means of computational fluid dynamics (CFD). CFD gives lots of advantages during the design process in terms of cost, speed and ability to simulate real conditions. In fact many flow and heat transfer processes cannot be easily experimentally tested while CFD gives a deeper insight into the flow, predicting what will happen under a given set of circumstances, answering quickly to many design issues. Using this numerical tool is it possible to predict how a design will affect the flow, and it allows to modify the model until getting an optimal result.

Actually CFD is increasingly applied in related industries for aerodynamic design problem and has been recently applied also to ship and offshore structures where an accurate prediction of the wind loads play an important role in almost any operation at sea.

Also aerodynamic specific matters like aerodynamic flow simulation for smoke tracing and thermodynamics analysis of the exhaust of funnels or design of superstructures with respect to safe helicopter operation have been investigated using CFD covering different ship types (containerships, cruise vessels, fast ferries and surface effect ships) but relative to shapes very different to mega yachts. Bertram (2003) provides a detailed review of recent advances in CFD based applications in naval architecture and offshore engineering and from the literature review a substantial lack of data concerning the peculiar mega-yacht forms is highlighted.

The procedure for producing a reliable numerical model for the assessment of yacht aerodynamics features, as wind comfort and re-ingestion of exhaust gases, expects a comparison with results obtained by means of wind tunnel tests. The validation of numerical model against available experimental data allows to calculate the full scale aerodynamic forces and wind speed-up on specific locations and to detect potential discomfort due to exhausts produced by diesel fuel combustion as well as potential plume re-ingestion problems at full scale including exhausts temperature effects. Furthermore the validated CFD model can also be used to investigate potential effects due to some changes on the yacht.

From these premises an experimental and numerical research program has been jointly carried out at Department of Mechanical Engineering and at Department of Chemistry, Materials and Chemical Engineering of Politecnico di Milano: as a first step of the research program an experimental approach has been developed at Politecnico di Milano Wind Tunnel in order to assess mega-yacht aerodynamics in terms of aerodynamic loads, comfort analysis, pollutants dilution and re-ingestion analysis using wind tunnel tests on a scale model.

Then as a second step of the research program a CFD model has been developed by the authors aiming to provide an effective design tool for mega-yacht aerodynamics and on board comfort assessment.

In the following an overview of the overall research activity will be provided: in particular after a brief summary of the experimental approach, the CFD method developed by the authors to investigate yacht aerodynamics and on board comfort assessment including wind comfort and re-ingestion of exhaust gases will be presented.

The proposed numerical model has been validated against experimental wind tunnel tests performed on a scaled model of a 270' LOA mega-yacht and some results are presented and discussed.

## **2. YACHT AERODYNAMICS AND ON BOARD COMFORT ASSESSMENT**

### **2.1 Experimental Approach**

In the following, for reader's convenience, a summary of the experimental approach to assess mega-yacht aerodynamics in terms of aerodynamic loads, comfort analysis, pollutants dilution, and re-ingestion analysis using wind tunnel tests is provided.

In addition, some results obtained using a scale model of a 270' LOA (~90 m) mega-yacht at different wind exposures, are shown: these data have been used to validate the CFD model described in details in section 2.4.

### **2.2 Experimental set-up**

With reference to maxi and mega-yacht application, tests are generally performed in the low speed Wind Tunnel Boundary Layer test section taking into account atmospheric turbulent flow characteristics.

As well known, the atmospheric wind properties are a function of the environmental characteristics at full-scale: in the wind tunnel they can be achieved by using passive turbulence generators placed into the test section (typically spires and roughness elements), as reported in Figure 2-1.



Figure 2-1 [Politecnico di Milano boundary layer test section]

Given the considerable dimensions of the Politecnico di Milano Wind Tunnel, the optimal scale for super and mega yacht models is in the order of 1:20 – 1:30. These dimensions derive from a series of considerations, including reducing blockage as far as possible (normally less than 5%), while at the same time it is possible to reproduce with a good level of detail many of the elements of the boat that are useful for determining superstructure drag or windage effects. This geometric scale is also compatible with the scaled simulation of the boundary layer: wind tunnel tests are generally carried out considering scaled simulation of the natural wind characteristic of the site according with turbulence and boundary layer similitude law. As an example, with reference to the 1/30 scale factor, in Figure 2-2 measured mean wind velocity and wind turbulence intensity vertical profiles are shown in comparison with the reference profiles relevant to marine areas, according to the Eurocode specs.

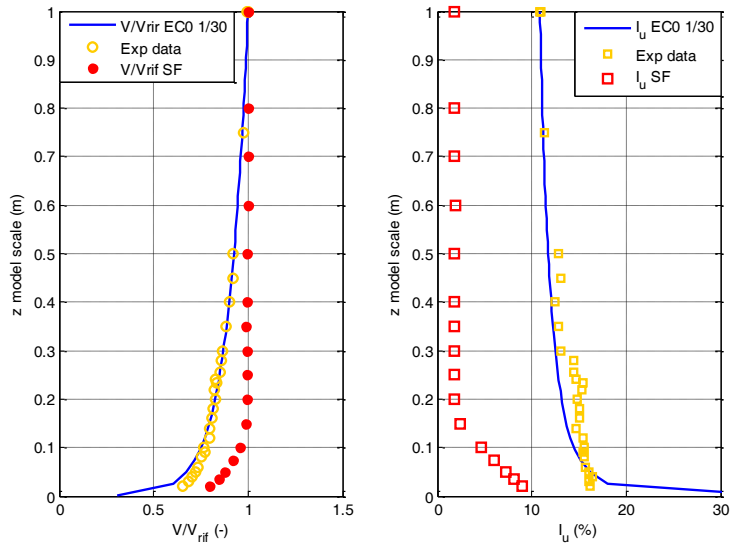


Figure 2-2 [Mean wind velocity and turbulence intensity vertical profile. Turbulent flow & smooth flow (SF)]

The yacht model is manufactured as a “rigid aerodynamic model”, i.e. a static model that reproduces the geometry of the full-scale structure (aerodynamic surfaces and details). Figure 2-3 shows an example of a mega-yacht scale model.



Figure 2-3 [*Mega-yacht scale model*]

The measurement of the overall wind loads on the hull and yacht superstructures is achieved using a six component force balance, which is generally placed inside the hull and permit highly accurate measurement of the three forces (vertical, longitudinal and lateral) and the three moments around the three principal axes. The model is usually manufactured using an internal structural frame that is rigidly connected to the dynamometer. The yacht aerodynamic forces are generally measured at different angles of attack, from  $0^\circ$  to  $180^\circ$  and results are presented in terms of aerodynamic coefficients as functions of the exposure angle ( $\alpha$ ).

Comfort evaluation on the various yacht decks and recreational areas are performed by means of wind speed measurements carried out in different positions according to yard and designer specifications (typically on yacht terraces and yacht decks) considering different wind exposures.

More in details, local wind speed measurements are performed by means of Irwin probes: these instruments are driven by means of a pressure scanner and allow measuring the magnitude of the wind speed at a given position at the desired height from the floor level. Figure 2-4 shows an example of the Irwin probes layout chosen for the yacht sun deck and the relevant instrumentation set-up on the yacht model, while in Figure 2-5 an Irwin probe is represented.



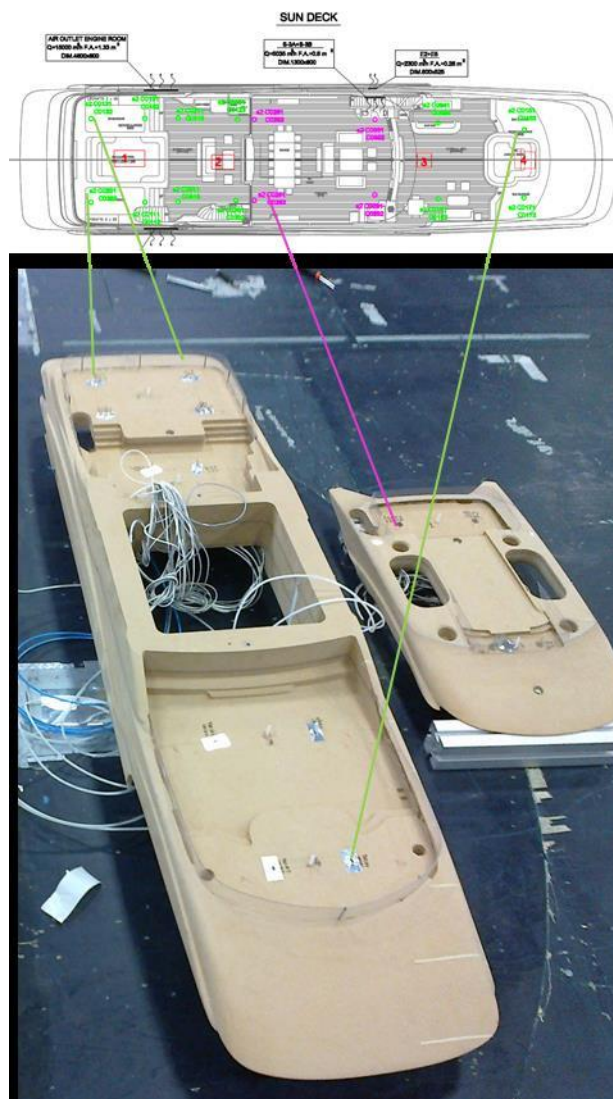


Figure 2-4 [Irwin probes on the scale model Sun Deck and measurement set-up]

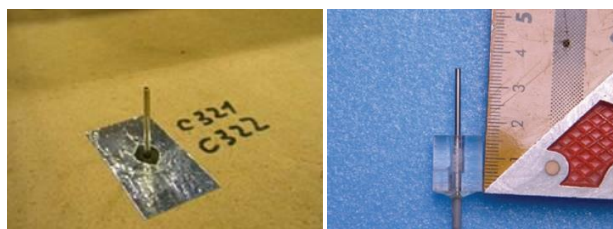


Figure 2-5 [Irwin probe]

For more details on the experimental and yacht model set-up readers can refer to Fossati et al. (2014).

### 2.3 Numerical Model

As a further step of the research program, a CFD model has been developed by the authors aiming to provide an effective design tool for mega-yacht aerodynamics and on board comfort assessment.

The numerical tool is developed within the open-source fluid-dynamic framework OpenFOAM Computational Fluid Dynamic (CFD) framework by using the Reynolds Averaged Navier-Stokes (RANS) equations. With reference to aerodynamic loads and

wind comfort assessment, a standard solver is firstly used and validated against the experimental data available from the wind tunnel tests.

The RANS equations are solved in terms of mean values, while the unsteady fluctuations are modelled by using a turbulence closure model. The  $k-\omega$  SST model, which gives good performances in separated flows and is often used on this kind of problems [Menter (1994) and Wilcox (2006)], was chosen to close the RANS equations.

In particular *simpleFoam* solver, based on the SIMPLE approach [Patankar (1980)], was adopted. More in details, a first order discretization scheme is used for the first part of the simulation in order to have numerical stability. When the aerodynamic coefficient have reached a quite stable trend, the second order discretization is implemented to get more accurate results.

For the present study, the adopted convergence criterion consists in monitoring the aerodynamic coefficients values obtained at each iteration: the number of iterations required for convergence depends on a series of parameters like the geometry under investigation, the wind angle of exposure, the turbulence model and the setting of the initial values. In order to increase the numerical stability and the convergence speed *potentialFoam solver*, an *OpenFoam* utility designed to generate a starting flow field by solving the potential flow equation, was used to generate the first guess solution.

An Infiniband platform was used for running all the simulations. In its current configuration, it is made up of 16 nodes, each of them having 36 GB of RAM memory and 12 Intel® Xeon® X5675 (12Mb cache, 3.06 GHz, 6.40 GT/s Intel® QPI) processors. To perform the validation of the numerical model against the experimental data, the numerical domain geometry (30 [m] length with a cross section of 15[m] x 4 [m]) was realized, aiming at reproducing the wind tunnel facility physical features as shown in Figure 2-6. The computational domain size and the refinement levels on the model surface are built by taking into account the boat model length overall (LOA). The hull is positioned in the domain center with the inlet placed at certain distance from the yacht bow, in order to match at the best the onset wind velocity profile obtained during the experimental tests as better described in section 2.2

The computational mesh is built using the open-source meshing tool *snappyHexMesh* provided within OpenFOAM.

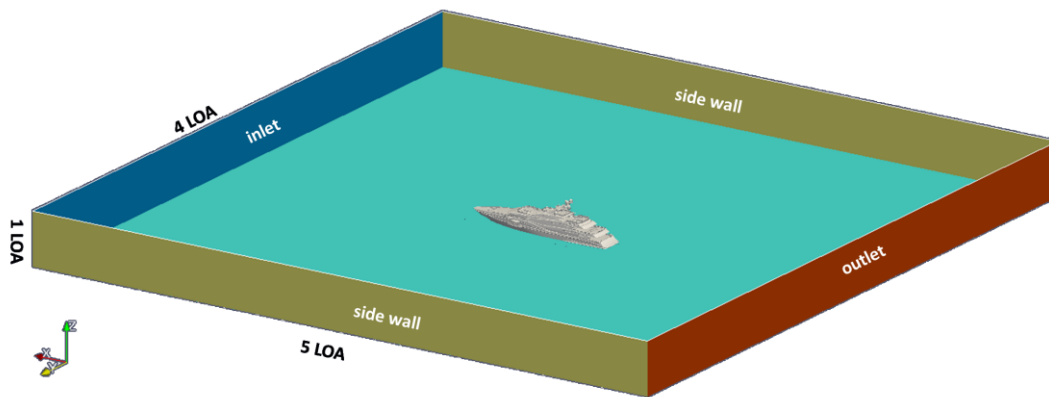


Figure 2-6 [The computational domain]

The approach of this mesh generator is the local refinement and the snapping of the mesh on the surface of the considered geometry. In order to use this tool it is necessary to create a background hexahedral mesh which defines the extent of the computational domain and a base level mesh density. The preliminary mesh is created starting from the rectangular prism block described before, defining cube blocks with edge maximum size related to the boat LOA (in particular equal to  $1/25$  LOA).

The model geometry is provided in STL file format. The meshing tool generates automatically three-dimensional mesh containing hexahedral cells and split-hexahedra from this triangulated surface geometry.

The quality of the mesh is improved by adopting suitable refinement in the zones where the most important gradients and flow changes are expected ( $1/800$  LOA) (Figure 2-6).

A mesh sensitivity analysis is performed with two aims: to reproduce correctly the forces on the hull and to reproduce correctly the incoming wind profile.

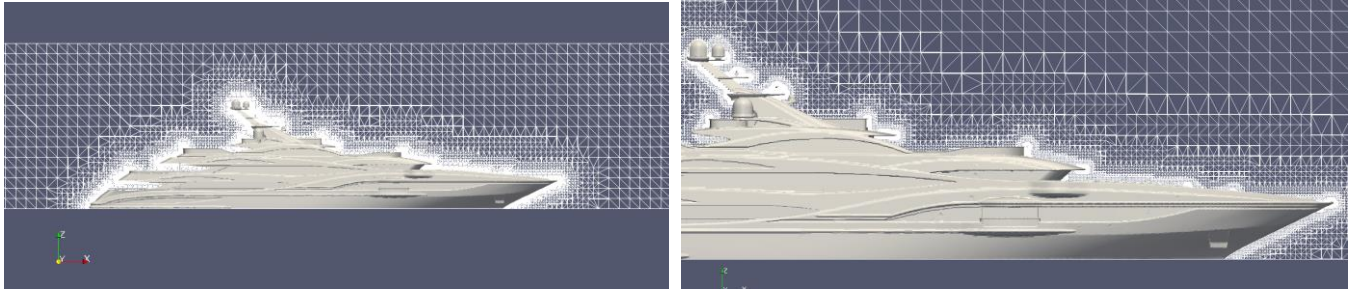


Figure 2-7 [Mesh visualization]

Once the numerical domain and mesh realization are assessed, boundary conditions must be defined. With reference to the above mentioned computational domain boundaries (Figure 2-6), the following boundary conditions are applied:

- Inlet boundary: Dirichlet conditions for onset wind speed  $U$ , turbulent kinetic energy  $k$ , and specific dissipation rate  $\omega$ . The initial values of  $k$  and  $\omega$  at the inlet are set in order to reproduce the wind tunnel flow turbulence level. For pressure, a Neumann zero gradient condition is assumed.
- Outlet boundary: flow is considered fully developed. Therefore, Neumann zero gradient condition is used for all variables, except for pressure, where a fixed (zero) value is set.
- Top and side walls: symmetry plane condition. This condition assumes a zero flux of all quantities across the symmetry boundary. The symmetry boundary condition consists therefore in a zero normal velocity at the symmetry plane and also a zero normal gradients of all variables at the symmetry plane. As stated above, these conditions determine a zero flux across the symmetry plane. Since the shear stress is zero at a symmetry boundary, it can also be interpreted as a “slip” wall when used in viscous flow calculations.
- Bottom: fixed wall condition. This is the domain boundary which represents the sea surface. The first step is to simulate the flat plane used in the wind tunnel tests. An efficient way to model the near wall behavior of the flow is the use of the wall functions approach. This method allows to bridge the troublesome region near the wall without increasing the numbers of cells and the consequent computational effort. It also increases the numerical stability and convergence speed. The requirements of this approach led to a mesh resolution where the first grid points should be located in the inertial sub-layer, which means that the  $y^+$  values fall within the range of  $50 < y^+ < 500$  [Giovangigli (1999)]. Thus, it is possible to use the law-of-the-wall to specify the boundary condition for the dependent variable as  $U$ ,  $k$  and  $\omega$ . The rough wall functions are set for  $k$ ,  $\omega$  and the turbulent viscosity  $\nu_t$ . For this surface, no slip condition is assumed ( $U=0$ ) while for pressure  $p$  a Neumann zero gradient condition is given.
- Yacht surface: no slip condition with standard wall functions and zero gradient for pressure.

#### 2.4 Numerical model validation

The numerical model previously described had been validated against experimental result available from tests carried out using a scale model of a 270' LOA (~90 m) mega-yacht.

Figure 2-9 shows an example of aerodynamic loads measured at different wind exposure angles. Global forces are presented through non-dimensional aerodynamic coefficients. Mean values of the aerodynamic force coefficient  $C_{Fi}$  and the aerodynamic moment coefficient  $C_M$  are defined according to the following equation:

$$C_{Fi} = \frac{\overline{F_i}}{qDL} \quad i = x, y; \quad C_M = \frac{\overline{M}}{qD^2L} \quad (1)$$

where  $F_i$ , and  $M$  are respectively the mean values of forces and moment,  $q$  is the onset flow mean dynamic pressure,  $D$  and  $L$  are reference dimensions.

In the same figure, for each tested wind exposure, measured values of aero coefficients standard deviation related to the wind turbulence effect are superimposed to the mean coefficient values.

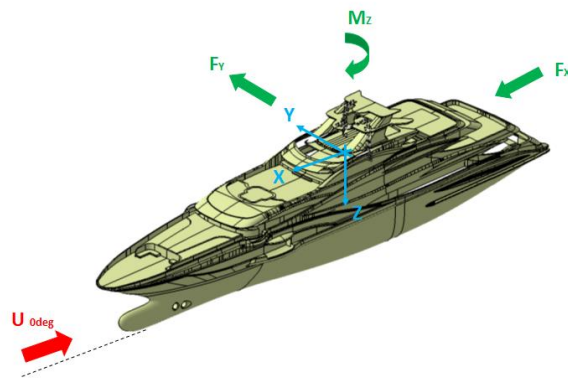


Figure 2-8 [Yacht reference system and aerodynamic loads]

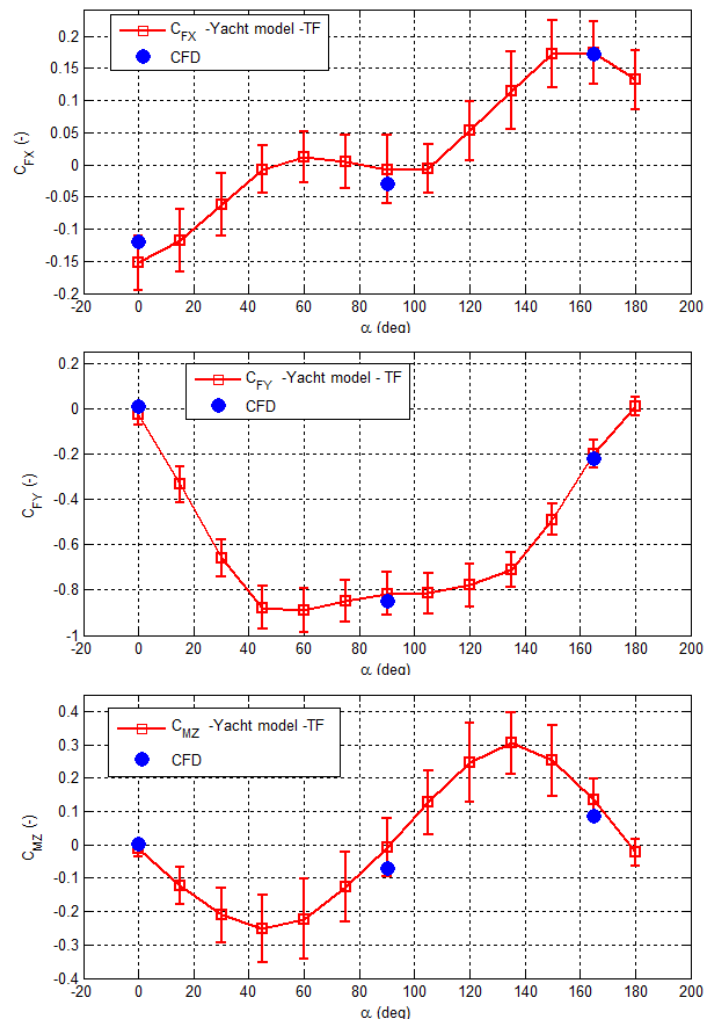


Figure 2-9 [Aerodynamic coefficients vs wind angle of incidence]

As mentioned above comfort evaluation on the various yacht decks and living areas are performed by means of local wind speed measurements carried out in different positions according to yard and designer specifications (typically on yacht terraces and yacht decks) at different wind exposures. Figure 2-10 shows an example of the results obtained in turbulent flow at  $90^\circ$  wind exposure with reference to the yacht main deck level.

The results are presented in a dimensionless form by means of the speed-up factor.

The speed-up factor  $S$  is defined as the ratio between the local mean wind speed  $V$  in the measurement position and a reference wind velocity ( $V_{ref}$ ):

$$S = \frac{V}{V_{ref}} \quad (2)$$

The assumed reference wind velocity in this case is the onset flow mean wind speed measured in the wind tunnel test section at 10m full scale height above the sea.

In the following, as an example, some results relevant to the wind incidence of 90° off the bow are reported: in particular the comparison between measured and calculated speed up values are shown in several position on the various yacht terraces and yacht decks.

The position of the local wind speed measurement points are sketched in the upper part of the figures, which also show the label relevant at each probe placed on the scale model in the same position.

Figure 2-10 shows the experimental measures obtained on the main-deck: the speed-up values are plotted in a top view sketch of the yacht main-deck and the histogram graph in the lower part of the figure shows the speed up values on the vertical-axes while on the x-axes the probes labels are reported. The colour of each point in the deck region is determined by the value of the speed up quantity, which can be read in the coloured scale to the right of the figure.

Figure 2-11 shows the same quantity obtained from the numerical simulation: in particular a top view of the yacht is superimposed to the calculated speed-up contour map. The color of each point is determined by the value of the speed up quantity according to the scale placed in the bottom part of the figure.

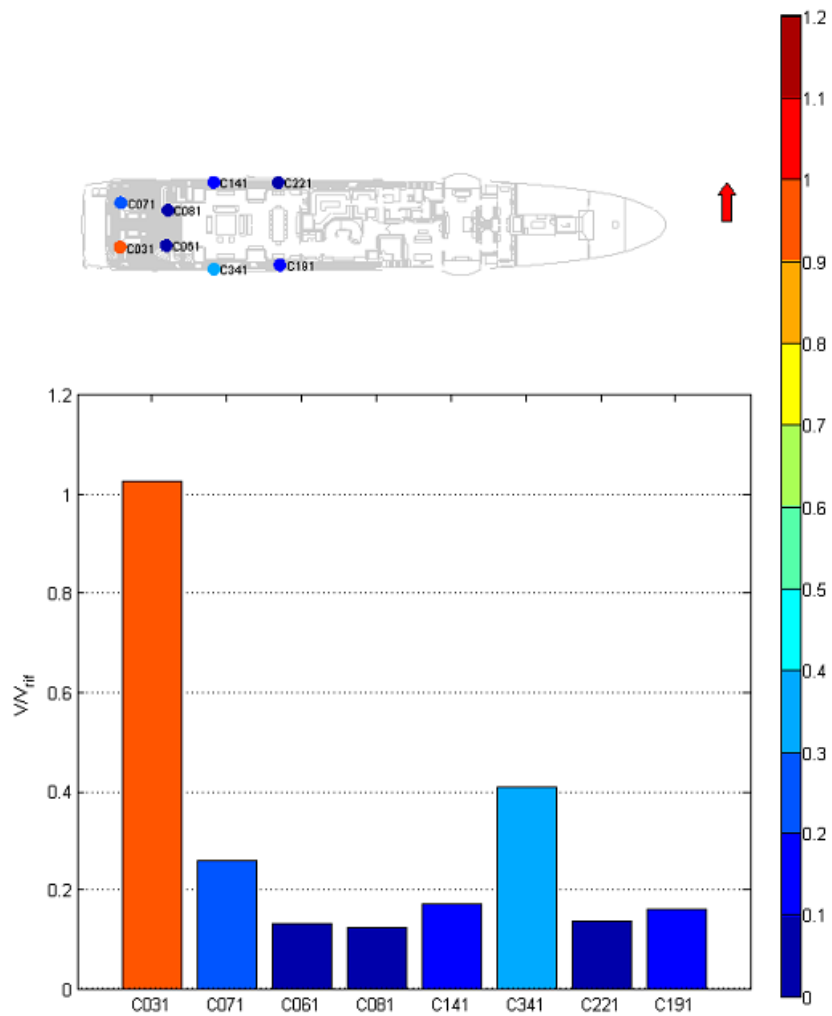


Figure 2-10 [Speed Up - Main Deck - wind angle 90 deg - experimental results]

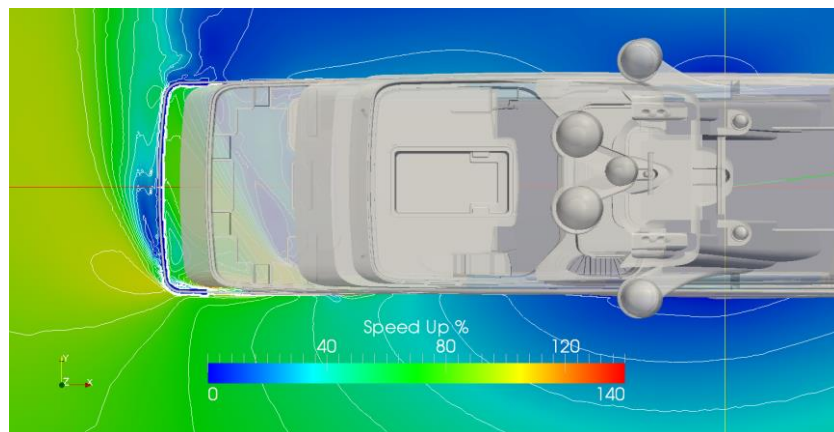


Figure 2-11 [Speed Up - Main Deck - Top view]

More in details Figure 2-12 and Figure 2-13 show for each level of the main deck the calculated speed-up contour map and the corresponding position of the measurement points on the yacht scale model with the relevant label.

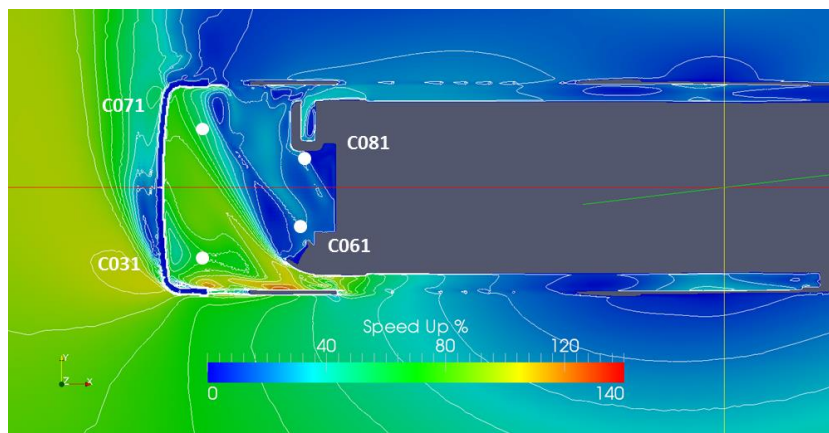


Figure 2-12 [*Speed Up - Main Deck first level - numerical results*]

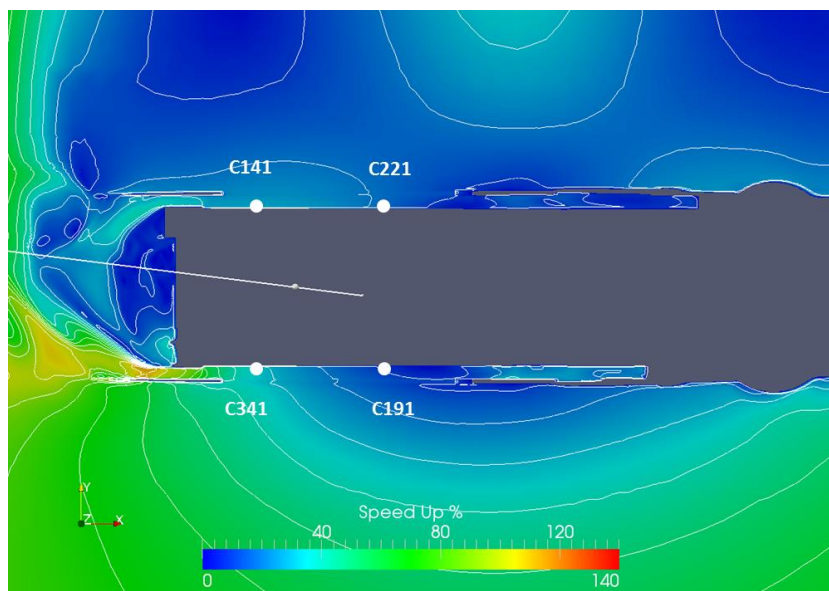


Figure 2-13 [*Speed Up - Main Deck - second level - numerical results*]

Figure 2-14, Figure 2-15 and Figure 2-16 refer to the wheelhouse deck.

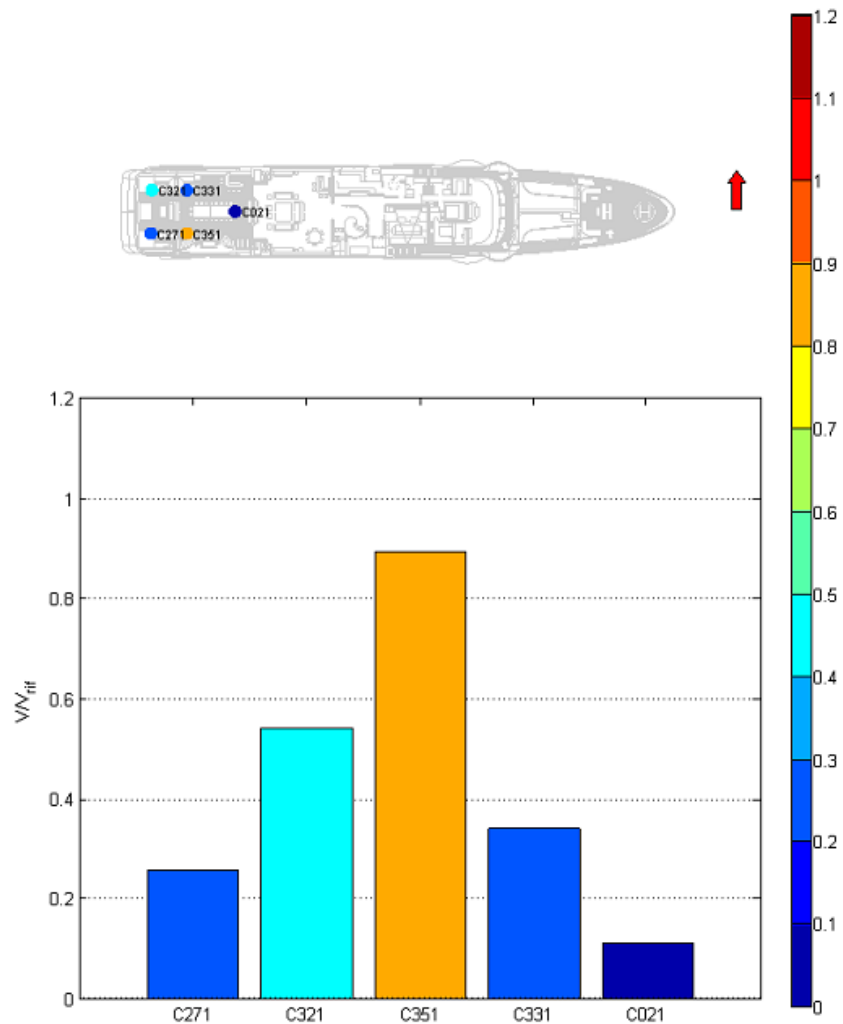


Figure 2-14 [*Speed Up - Wheelhouse Deck - wind angle 90 deg - experimental results*]

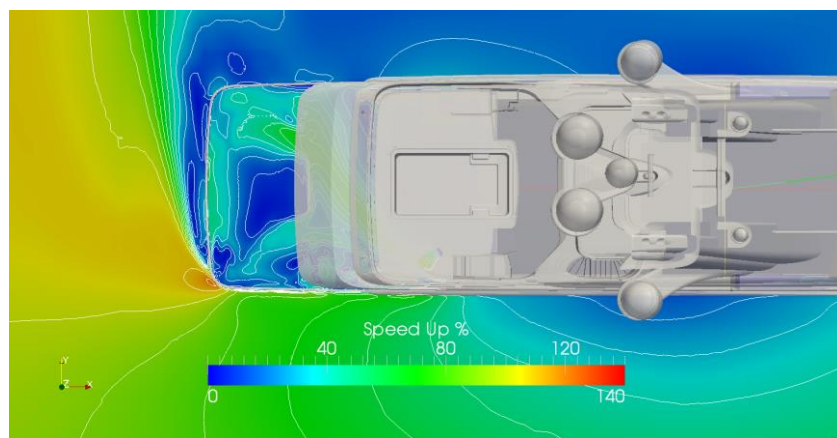


Figure 2-15 [*Speed Up - Wheelhouse Deck - wind angle 90 deg - numerical results*]



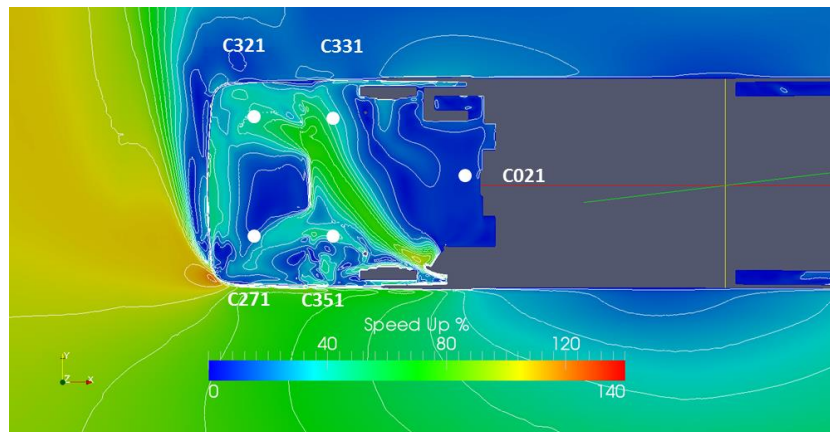


Figure 2-16 [*Speed Up - Wheelhouse Deck - wind angle 90 deg numerical results*]

Comparison between numerical and wind tunnel measurements show a satisfactory agreement both in terms of aerodynamic coefficients and of speed up.

### 3. POLLUTANT DILUTION AND RE-INGESTION OF EXHAUST GASES ASSESSMENT

#### 3.1 Experimental approach: Wind Tunnel Experiment on Scale Models

The main requirement for the pollutants dilution lab-scale experiments is related to release from the stacks of a gas having well defined properties in terms of density (to reproduce a particular buoyancy effect) and content of a suitable tracer gas, which is used to gain information about its dilution and dispersion in the ship wake [Carpentieri et al. (2004)]. In the wind tunnel environment, a mixture consisting of air and carbon dioxide, at room temperature, with a CO<sub>2</sub> concentration equal to 20% by volume, is fed to the yacht model stacks with the objective to reproduce the emission of exhausts produced by diesel fuel combustion. The tracer flow-rate is controlled by means of a mass flow meter. The CO<sub>2</sub> concentration into the feed flow-rate is generally checked prior to the start of each experimental session by sampling a small amount of gas directly from one of the stacks (Figure 3-1) and analyzing it directly in order to verify the tracer gas composition.

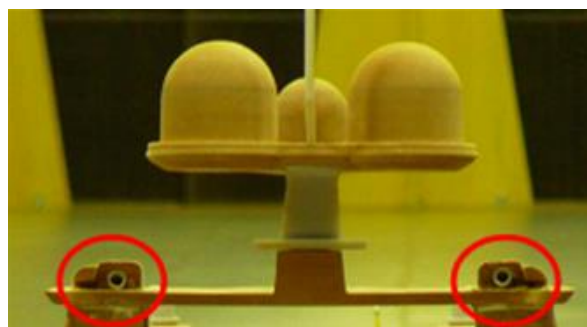


Figure 3-1 [*Stacks of the yacht model*]

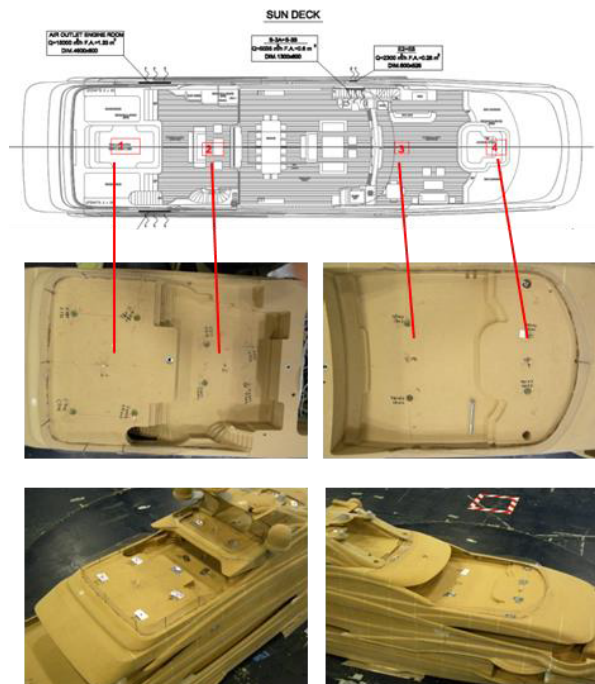


Figure 3-2 [Map of sampling points for the pollutant dilution analysis and model measurement set up]

The gas analysis is carried out in real time by means of an on-line analyzer (Figure 3-3), equipped with several detectors, including a non-dispersive IR for detecting continuously the concentration of CO<sub>2</sub>. In order to obtain a quantitative measure of the pollutant dilution conditions and the potential presence of the tracer gas into the ship wake or its possible accumulation in some parts of the vessel, a certain number of sampling ports are realized on the yacht model, placing them on decks or in areas that can be potentially critical for the dispersion of the tracer gas.

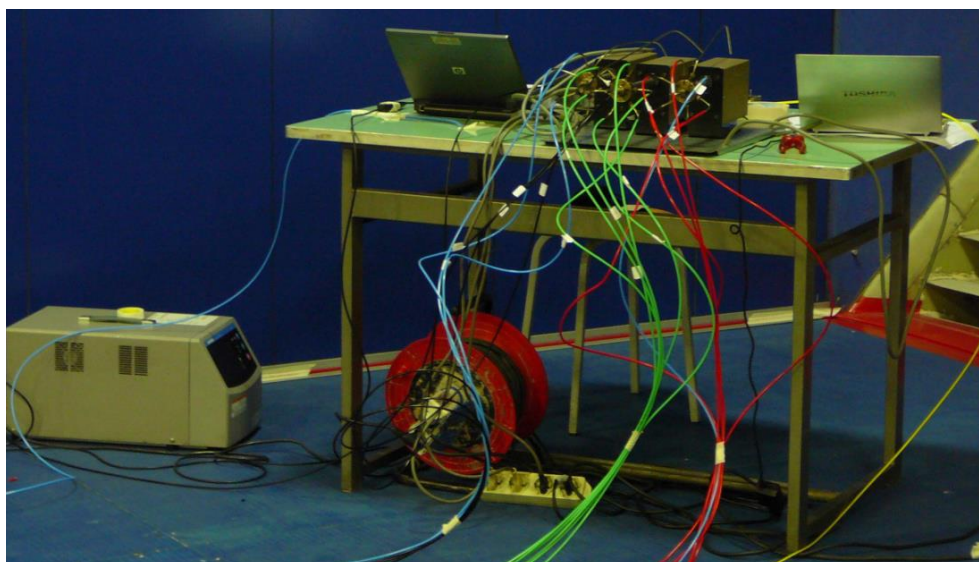


Figure 3-3 [Gas analyzer for continuous detection of CO<sub>2</sub> concentration]

### 3.2 Scaling Rules

As previously said the wind tunnel reproduces the atmospheric boundary layer characteristics at model scale. Therefore, the conditions necessary to ensure the flow similarity are obtained from the dimensional analysis of exhausts flow motion equations.

Geometric similarity must be ensured by the homogeneous scaling of all lengths that can be relevant for the system under investigation (e.g. those of the model). The dynamic similarity is obtained by acting on the equations of conservation of mass, momentum and eventually of energy. In this case it is necessary to accurately control the scaling of the emissions, ensuring the similarity of the mixing conditions of the released exhausts. Dimensional analysis of the parameters that mainly affect the behavior of the exhausts discharged from a stack requires the conservation of a series of dimensionless parameters involving both the properties of the emission and those of the flow itself. In particular, the complete scaling is based on the following equation:

$$\frac{CU_{ref}L_{ref}^2}{Q} = f\left(\frac{\rho_s}{\rho_a}, \frac{W}{U_{ref}}, \frac{gL_{ref}}{U_{ref}^2}\right) \quad (3)$$

where  $W$  is the outlet speed of the gas released from the model,  $\rho_a$  and  $\rho_s$  represent, respectively, the density of the ambient air and of the emission,  $C$  is the volume concentration and  $Q$  is the volumetric flow-rate of the contaminant emitted by the source, at standard conditions of temperature and pressure. The above equation expresses the dimensionless concentration field as a function of three dimensionless parameters relating the physical properties of the emission with those of the flow field in which it is dispersed. This implies that in order to have a perfect similarity between the full scale and the lab-scale model the following parameters should be kept constant:

- Speed ratio:  $\frac{W}{U_{ref}}$
- Density ratio:  $\alpha = \frac{\rho_s}{\rho_a}$
- Froude Number:  $Fr^2 = \frac{U_{ref}^2}{gL_{ref}}$

The Froude number, which can be also expressed as:

$$Fr^2 = \frac{\rho U^2 L^2}{\rho g L^3} \quad (4)$$

represents the ratio between the inertia and gravity forces in the considered flow. This type of scaling (complete scaling) cannot be easily obtained due to speed or temperature conditions required in the wind tunnel for the small-scale model. For this reason, the complete scaling, is often not used.

In order to be able to simulate a real scenario with a good representation of the main physical aspect of the problem, in a way that is consistent with the requirements of the complete scaling, some restrictions must be eliminated using what are called "enhanced scaling relationships".

This is how it is possible to combine different process variables in several dimensionless parameters which are not necessarily a complete set of parameters allowing for the definition of new scaling rules.

A parameter which is not essential is the ratio of density between the gas emitted and the surrounding air,  $\alpha$ . It is not important by itself but it can affect the momentum of the emission and its buoyancy. The non-conservation of  $\alpha$  results in several possible scaling rules, based on the consideration that the trajectory of the plume that is transported from the local wind is mainly determined by the ratio between the inertial and buoyancy forces. Therefore, this can lead to the following approximated equation:

$$\frac{CU_{ref}L_{ref}^2}{Q} = f\left(\frac{\rho_s W^2}{\rho_a U_{ref}^2}, \frac{(\rho_s - \rho_a)gL_{ref}}{\rho_{ref}U_{ref}^2}\right) \quad (5)$$

in which  $\rho_{ref}$  is a reference density which can be that of air, or that of the gas emitted.

In the wind tunnel experiments the choice is to follow a conservative approach by performing a scaling of the ratio between the emission and wind momentum, so as to reproduce consistently the interaction and the dilution/mixing conditions between flue gas and the external flow field, without obtaining a complete scaling of the buoyancy contribution. In practice, the density of the emission, which in the real case is less than that of air (given the high temperature of the flue gas), in the experiments is considered equal to that of the air. This leads to a negative buoyancy of the plume, with the aim to better highlight the potential entrainment of the exhausts in areas of interest of the model. Indeed the effect of a higher temperature of the fumes at full scale would be to facilitate the dispersion in the atmosphere of the fumes themselves, thereby reducing the chances of having re-ingestion phenomena or of discomfort in the areas of relevance of the vessel and its superstructure. Accordingly, the scaling of the gas discharge conditions is carried out as follows:

$$\left( \frac{W_0}{U_{stack}} \right)_m = \frac{W_0}{U_{stack}} \sqrt{\frac{\alpha}{(\alpha)_m}} \quad (6)$$

where  $W_0$  is the exhaust speed at the stack tip,  $U_{stack}$  the wind speed at the actual stack height above the sea surface and  $\alpha$  the density ratio. The subscript  $m$  indicates the parameters related to the small-scale model.

This point and in particular the temperature effects has been investigated in more details by means of numerical simulations as described in section 5.

During the wind tunnel tests tracer gas dispersion measurements are then performed using wind speed scaled accordingly to Froude number similarity law (i.e. maintaining the ratio between the inertia forces and the weight force).

## 4. POLLUTANT DILUTION NUMERICAL SIMULATIONS

In the following a description of exhaust gas mixture and its dilution numerical modelling will be given. Several different approaches are taken into account for modeling the dispersion of exhaust gas stream around the boat, with the aim to find the best compromise in terms of accuracy and computational cost.

### 4.1 Exhaust gas modeling

The chemical and physical features of the exhaust gases mixture must be properly characterized in order to perform reliable CFD simulations. In particular, the density (i.e. the molecular weight) of exhaust gas stream has to be estimated with sufficiently high accuracy, to properly quantify the role of the buoyancy.

In the present work, it was assumed that the exhaust gas mixture is the result of combustion reactions of a diesel fuel. Diesel is typically composed of about 75% saturated hydrocarbons (primarily paraffins including *n*, *iso*, and cycloparaffins), and 25% of aromatic hydrocarbons (including naphthalenes and alkylbenzenes). For the purposes of the present work, only the average composition is needed, and details about the chemical composition are negligible. The average chemical formula for common diesel fuels is  $C_{12}H_{23}$ , ranging approximately from  $C_{10}H_{20}$  to  $C_{15}H_{28}$ .

In this work we assumed the complete combustion of fuel in air to the main combustion products ( $CO_2$  and  $H_2O$ ), i.e.:



In stoichiometric conditions neither fuel, neither oxidizer are present in the exhaust gases, whose composition can be easily calculated from reaction (7):

$$\begin{cases} x_{N_2} = 73.9\% \\ x_{H_2O} = 12.7\% \\ x_{CO_2} = 13.4\% \end{cases} \quad (8)$$

where  $x_i$  is the molar fraction of  $i$ -th component. The molecular weight of the exhaust gas mixture reported above is equal to 28.88 kg/kmol, which is very similar to the molecular weight of regular air (28.85 kg/kmol).

Actually, the exhaust gas composition depends on the equivalence ratio  $\phi$  (or fuel-to-oxidizer ratio) at which the engine works.  $\phi$  is defined as the current molar ratio between the fuel and the air and the same ratio in stoichiometric conditions:

$$\phi = \frac{n_F n_O^{st}}{n_O n_F^{st}} \quad (9)$$

where  $n_F$  is the number of moles of fuel ( $C_{12}H_{23}$ ),  $n_O$  the number of moles of oxidizer ( $O_2$ ) and the “st” superscript refers to the stoichiometric conditions. If the equivalence ratio at which the boat engine works is known, the exhaust gas composition can be easily calculated again from the stoichiometric constraint (7). Unfortunately, the equivalence ratio characterizing the engine under investigation is not available, which means that a complete characterization of exhaust gas stream is not possible. However, from Equation (7) it is quite easy to demonstrate that, if we limit our attention to the typical equivalence ratios adopted for diesel engines ( $\phi = 0.7 \div 1$ ), the molecular weight of the exhaust gas mixture changes only in a very limited amount. As an example, for  $\phi = 0.7$  (i.e. the lower limit of the range reported above), we have the following composition:

$$\begin{cases} x_{O_2} = 6.0\% \\ x_{N_2} = 75.4\% \\ x_{H_2O} = 9.2\% \\ x_{CO_2} = 9.4\% \end{cases} \quad (10)$$

The resulting molecular weight (28.83 kg/kmol) is also in this case very similar to the molecular weight of regular air.

In conclusion, the difference between the molecular weight of air and exhaust gases is always within 0.2%, independently of the equivalence ratio. This has some important consequence on the numerical modeling, as better explained in the following.

## 4.2 Numerical modeling of exhaust gases

Several different approaches are taken into account for modeling the dispersion of exhaust gas stream around the boat. The aim is to find the best compromise in terms of accuracy and computational cost. The different approaches we used are listed in the following, in decreasing order of complexity and accuracy.

### 4.2 (a) Multicomponent mixture with gravity effects

This is the most comprehensive and accurate approach, but it is characterized by the largest computational cost. The exhaust gas stream is described as a multicomponent mixture of main combustion products ( $H_2O$  and  $CO$ ) and  $N_2$ , according to the molar composition reported in (8). The transport properties (thermal conductivity, viscosity, and mass diffusion coefficients) of the single species are calculated on the basis of the kinetic theory of the gases [Curtiss et al. (1949), Chapman et al. (1970)]. In particular, the preferential diffusion effects are taken into account, in order to better describe the molecular diffusion process in regions close to the walls, or where the convective becomes small. The transport properties of the mixture are calculated using the conventional mixing rules for mixtures of ideal gases [Dixon (1968), Coffee et al. (1981)]. The thermodynamic properties are calculated under the hypothesis of ideal mixture.

The governing transport equations to be solved are discussed in the following. Their derivation can be easily found in the literature e.g. Poinsot (2001). Obviously, the Navier-Stokes equations are written including the term associated to the gravity:

$$\begin{cases} \frac{\partial \rho}{\partial t} + \frac{\partial}{\partial x_i} (\rho v_i) = 0 \\ \frac{\partial}{\partial t} (\rho v_i) + \frac{\partial}{\partial x_j} (\rho v_i v_j) = -\frac{\partial p}{\partial x_i} + \frac{\partial}{\partial x_j} \left[ \mu \left( \frac{\partial v_i}{\partial x_j} + \frac{\partial v_j}{\partial x_i} - \frac{2}{3} \delta_{ij} \frac{\partial v_l}{\partial x_l} \right) \right] + \rho g_i + \frac{\partial}{\partial x_j} (-\rho \overline{v_i v_j}) \end{cases} \quad (11)$$

In the equations above,  $\rho$  is the density of the mixture,  $v_i$  is the  $i$ -th component of the velocity vector,  $p$  is the pressure,  $\mu$  the dynamic viscosity,  $\delta_{ij}$  the Kronecker delta, and  $-\rho \overline{v_i v_j}$  the Reynolds stresses, and  $g_i$  the  $i$ -th component of the gravity vector. In order to close the Navier-Stokes equations (11), a proper turbulent model must be adopted. In the present work (as previously reported) the  $k$ - $\omega$  SST model was adopted. This model is based on the Boussinesq assumption, to relate the Reynolds stresses to the mean velocity gradients, i.e.:

$$-\rho \overline{v_i v_j} = \mu' \left( \frac{\partial v_i}{\partial x_j} + \frac{\partial v_j}{\partial x_i} \right) - \frac{2}{3} \left( \rho \kappa + \mu' \frac{\partial v_l}{\partial x_l} \right) \delta_{ij} \quad (12)$$

where  $\kappa$  is the turbulent kinetic energy, and  $\mu'$  is the turbulent dynamic viscosity, which is calculated as a function of  $\kappa$  and  $\varepsilon$ , the dissipation rate of the turbulent kinetic energy:

$$\mu' = \rho C_\mu \frac{\kappa^2}{\varepsilon} \quad (13)$$

The  $k$ - $\omega$  SST model requires the solution of two additional transport equations, for the turbulent kinetic energy  $\kappa$  and the specific dissipation rate  $\omega$  (i.e. the ratio of  $\varepsilon$  to  $\kappa$ ), from which the turbulent dynamic viscosity can be estimated:

$$\begin{cases} \frac{\partial}{\partial t}(\rho \kappa) + \frac{\partial}{\partial x_j}(\rho v_j \kappa) = \frac{\partial}{\partial x_j} \left( \Gamma_\kappa^{eff} \frac{\partial \kappa}{\partial x_j} \right) + G_\kappa - D_\kappa \\ \frac{\partial}{\partial t}(\rho \omega) + \frac{\partial}{\partial x_j}(\rho v_j \omega) = \frac{\partial}{\partial x_j} \left( \Gamma_\omega^{eff} \frac{\partial \omega}{\partial x_j} \right) + G_\omega - D_\omega \end{cases} \quad (14)$$

In these equations,  $G_\kappa$  represents the generation of  $\kappa$  due to mean velocity gradients.  $G_\omega$  represents the generation of  $\omega$ .  $\Gamma_\kappa^{eff}$  and  $\Gamma_\omega^{eff}$  represent the effective diffusivity of  $\kappa$  and  $\omega$ , respectively.  $D_\kappa$  and  $D_\omega$  represent the dissipation of  $\kappa$  and  $\omega$  due to turbulence. Additional details can be found in Wilcox (2006).

The transport equations of species account only for convection and diffusion, since no chemical reaction occur:

$$\frac{\partial}{\partial t}(\rho Y_k) + \frac{\partial}{\partial x_i}(\rho Y_k v_i) = - \frac{\partial}{\partial x_i}(\rho Y_k V_{k,i}) - \frac{\partial}{\partial x_i}(\rho \overline{Y_k' V_{k,i}'}) \quad k = 1, \dots, N \quad (15)$$

In the equations reported above,  $N$  is the total number of species (5 in this particular case),  $Y_k$  is the mass fraction of species  $k$ -th, and  $V_{k,i}$  is the  $i$ -th component of the laminar diffusion velocity of species  $k$ -th. Both Fickian and thermal diffusion (Soret effect) are taken into account for evaluating the diffusion velocities:

$$V_{k,i} = - \frac{\Gamma_k}{\omega_k} \frac{\partial \omega_k}{\partial x_i} - \frac{\Gamma_k \Theta_k}{X_k} \frac{1}{T} \frac{\partial T}{\partial x_i} \quad (16)$$

where  $X_k$  is the mole fraction and  $\Theta_k$  the thermal diffusion ratio of species  $k$ -th.  $\Gamma_k$  is the individual species mixture averaged diffusion coefficient, related to the binary diffusion coefficients  $\Gamma_{jk}$  through the expression [Giovangigli (1999)]:

$$\Gamma_k = \frac{1 - Y_k}{\sum_{j \neq k}^N \frac{X_j}{Y_{jk}}} \quad (17)$$

The contribution due to the pressure-gradient diffusion was neglected for all the simulations performed in this work. The species turbulent fluxes  $\overline{\rho Y_k' V_{k,i}'}$  are closed using the usual gradient assumption:

$$\overline{\rho Y_k' V_{k,i}'} = -\frac{\mu}{\mathbf{Sc}_k^t} \frac{\partial Y_k}{\partial x_i} \quad (18)$$

where  $\mathbf{Sc}_k^t$  is the turbulent Schmidt number for species  $k$ -th ([Poinsot (2001)]).

The transport equation of energy is solved in terms of total, non-chemical enthalpy, and includes the enthalpy contribution from the mass diffusion fluxes. Since no chemical reactions occur, the chemical heat release is accounted for:

$$\frac{\partial}{\partial t}(\rho H) + \frac{\partial}{\partial x_i}(\rho v_i H) = \frac{\partial p}{\partial t} + \frac{\partial}{\partial x_i} \left( \lambda \frac{\partial T}{\partial x_i} \right) - \frac{\partial}{\partial x_i} \left( \rho v_i \overline{h_s'} \right) - \frac{\partial}{\partial x_i} \left[ \rho \sum_{k=1}^N h_{s,k} \omega_k V_{k,i}' \right] \quad (19)$$

In this equation  $\lambda$  is the laminar thermal conductivity of the mixture, and  $h_{s,k}$  are the sensible enthalpies of species  $k$ -th.  $H$  is the total (non-chemical enthalpy), defined as:

$$H = h_s + \frac{1}{2} v_i v_i \quad (20)$$

where  $h_s = \sum_{k=1}^N h_{s,k}$  is the sensible enthalpy of the whole mixture. The enthalpy turbulent fluxes  $\overline{\rho v_i h_s'}$  are closed using the usual gradient assumption:

$$\overline{\rho v_i h_s'} = -\frac{\mu}{\mathbf{Sc}^t} \frac{\partial T}{\partial x_i} \quad (21)$$

In conclusion, the total number of equations to be solved when the multicomponent mixture model with gravity effects is adopted is equal to 12, namely: the Navier Stokes (11), the  $k$ - $\omega$  SST equations (14), the species (15) and the energy (19) equations.

The multi-component mixture is fed into the computational domain at the temperature of 633 K and pressure of 1 atm. In these conditions its density is equal to 0.555 kg/m<sup>3</sup>. Significant buoyancy effects may be expected in these conditions, since the density of environment air (at the temperature of 298K) is 1.179 kg/m<sup>3</sup>.

#### 4.2 (b) Single-component (pseudo-species) with gravity effects

In this approach the exhaust gas stream is modeled as a single-component mixture (or single pseudo-species EG), with averaged properties. The mixture of O<sub>2</sub> and N<sub>2</sub>, corresponding to the regular air, is also considered a pseudo-species (A). The main difference with respect to the approach reported above is that no preferential diffusion effects can be taken into account. However this simplification is expected to have a negligible impact on the final results, because of the following two main reasons:

- from one side, as reported in Figure 4-1, the difference between the Fick's diffusion coefficients of CO<sub>2</sub> and H<sub>2</sub>O with respect to the N<sub>2</sub> is relatively small, at least in the range of temperatures of our interest. This means that the preferential diffusion effects play a minor role in the problem under investigation;
- from the other side, since the flow under investigation is turbulent, the laminar diffusion coefficients are usually much smaller than the turbulent diffusion coefficient. This means that, especially in the regions where the intensity of turbulence is large, the error arising from neglecting the preferential laminar diffusion effects is minimum. This is therefore a further element to support the idea that preferential diffusion is not so relevant for the problem under investigation.

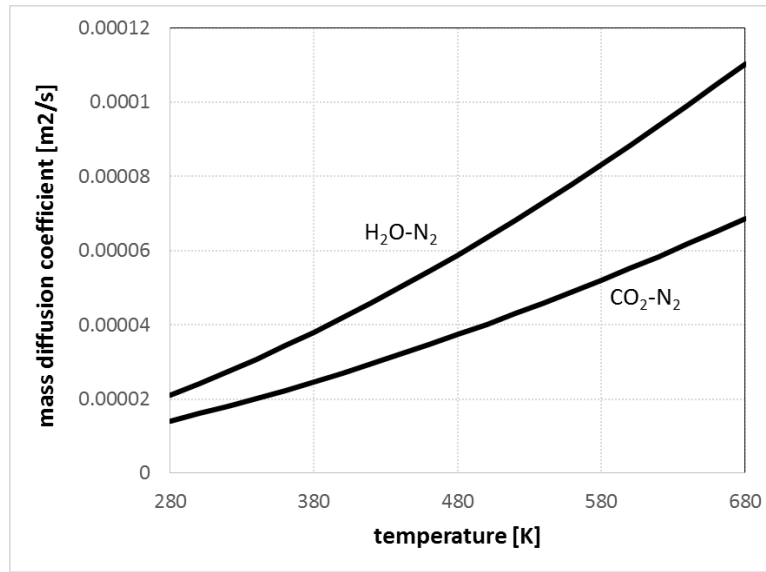


Figure 4-1 [Binary mass diffusion coefficients of H<sub>2</sub>O and CO<sub>2</sub> with respect to N<sub>2</sub> as a function of temperature]

The gravity effects are still retained, since the exhaust gas pseudo-species is injected in the computational domain at the temperature of 633 K.

The main advantage of this approach is the possibility to reduce the total number of equations to be solved. Indeed, instead of solving 5 equations for the real chemical species (fuel, O<sub>2</sub>, N<sub>2</sub>, CO<sub>2</sub> and H<sub>2</sub>O), we can solve only two equations for the 2 pseudo-species, i.e. air (A) and exhaust gas (EG). Therefore, the total number of equations to be solved is only 9 (instead of 12), with a theoretical gain in terms of computational time of about 25-30%.

#### 4.2 (c) Passive scalar with gravity effects

This approach is based on two additional simplifications of the model reported above:

- the molecular weight of the exhaust gas stream is sufficiently close to the molecular weight of air.
- the transport and thermodynamic properties of the exhaust gases are sufficiently close to those of air.

If the two hypotheses reported below are acceptable, there is no need to introduce an additional pseudo-species (EG) for modeling the exhaust gas stream. From a fluid dynamic point of view, it can be modeled as regular air at the temperature of 633 K.

The validity of the first assumption was already demonstrated in the previous section, when it was shown that the expected molecular weight is very similar to those of air, within an error of less than 1%. Regarding the second assumption, since both air and exhaust gases have almost 80% of N<sub>2</sub>, it is obvious to expect similar transport and thermodynamic properties. Figure 4-2 reports a comparison between the main properties of exhaust gas and air, to clearly demonstrate the feasibility of assumption (b).

Instead of solving the transport equation for the EG pseudo-species, which is now removed, a transport equation for a passive scalar  $\psi$  is taken into account:

$$\frac{\partial}{\partial t}(\rho\psi) + \frac{\partial}{\partial x_i}(\rho\psi v_i) = -\frac{\partial}{\partial x_i}(\rho\psi V_{\psi,i}) - \frac{\partial}{\partial x_i}(\rho\overline{\psi'V'_{\psi,i}}) \quad (22)$$

The total number of equations is equal to 8, because no species equations (15) have to be solved, since the gas phase is pure air. This means that no mixing rules have to be applied to estimate the mean transport properties of the gaseous phase. This means that the saving in computational cost with respect to model 4.2 (b) is about 15% and with respect to model 4.2 (a) is about 35-40%.



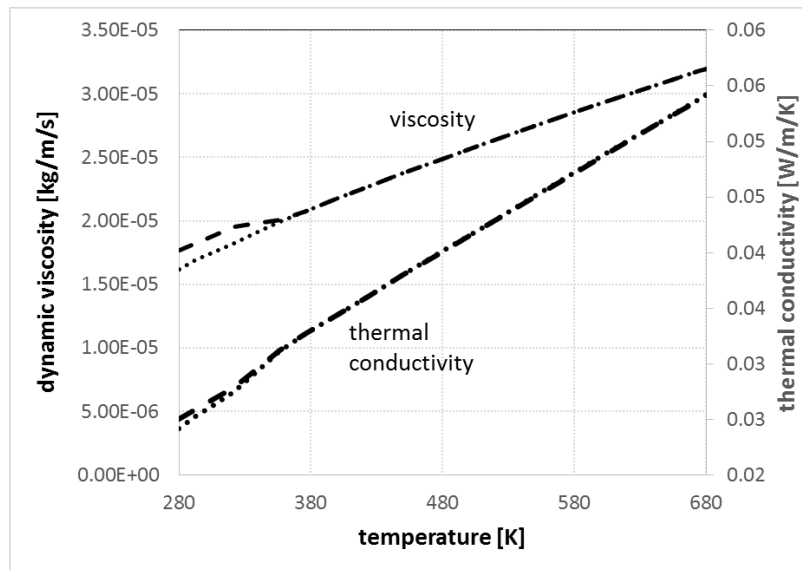


Figure 4-2 [Thermal conductivity and dynamic viscosity of exhaust gas stream (8) (---) and air (...)]

#### 4.2 (d) Passive scalar without gravity effects

The last approach under investigation is based on the previous one, with the additional, conservative hypothesis of no gravity effects. Of course this is a strong simplification of the model, since the gravity effects are expected to play an important role (because of the large difference of density between air and exhaust gas). If gravity effects are neglected, no buoyancy acts on the hot exhaust gases stream. This results in the worst scenario in terms of pollutant dispersion, because the exhaust gas is not able to move upwards and tends to remain around the boat. However, even if the assumption of no buoyancy is unphysical, it can be useful for the objectives of the present work, since it leads to very conservative results. Indeed, one should expect that if no discomfort is detected under the no gravity assumption, this must be also true for the more complex models.

Under the assumption of the present approach, the exhaust gases can be modeled as a passive scalar with a fixed (arbitrary) value on the boundary corresponding to the inlet of exhaust gases in the computational domain.

The main advantage of this kind of approach is the possibility to decouple the simulation of the flow field from the calculation of the exhaust gases dispersion. In other words, the governing equation governing the passive scalar, can be solved as a post-processing step, after the solution of the flow field (continuity and momentum equations). This means that the total number of equations to be solved is only 7, with a saving of computational time of about 50% with respect to the most accurate approach (Section 4.2 (a)).

### 4.3 Numerical model validation

For numerical model validation purposes, available experimental results have been compared with the numerical results.

As an example Figure 4-3 shows the results obtained during the wind tunnel tests tracer gas dispersion measurements with reference to 90° wind incidence from the bow: each sampling port available on the scale model is identified by an ID number and a short description indicates the placement on the ship model. In the column on the right the measured CO<sub>2</sub> concentration values are reported.

As can be seen, the concentration values obtained are very close to the detection limit of the instrument, (0.01% by volume) meaning that no problem with the dilution of the exhaust or their stagnation in critical parts of the yacht should be expected.

Exhausts horizontal discharge,  $u = 1 \text{ m/s}$ , angle with respect to the wind direction: 90°

ID sampling port	Sampling port position			CO <sub>2</sub> [% vol.]
	deck	bow -stern	port -starboard	
1	Sun deck	Stern	Middle	<0.01
2	Sun deck	Stern	Middle	0.01
3	Sun deck	Bow	Middle	0.01
4	Sun deck	Bow	Middle	<0.01
5	Wheelhouse deck	Stern	Middle	<0.01
6	Wheelhouse deck	Stern	Middle	<0.01
7	Mast plan	Stern	Middle	0.02
8	Mast plan	Bow	Middle	0.01
9	Wheelhouse deck	Bow	Starboard	<0.01
10	Main deck	Stern	Middle	0.01
11	Main deck	Stern	Middle	<0.01
12	Main deck	Stern	Starboard	<0.01
13	Main-Wheelhouse decks	Stern	Starboard	<0.01
14	Wheelhouse deck	Stern	Port	0.02
15	Wheelhouse deck	Stern	Starboard	0.01
16	Main-Wheelhouse decks	Middle	Starboard	<0.01
17	Wheelhouse deck	Middle	Starboard	<0.01
18	Mast plan	Middle	Port	<0.01

Figure 4-3 [Example of table reporting the pollutant dilution for each sampling port, angle 90 deg]

Numerical analyses of the flow field have been performed at the same wind incidence exposure angle solving the incompressible steady state RANS equations.

Then, according to the numerical model described in section 4.2(d), exhaust gases have been modeled as a passive scalar which is released from the computational domain boundary corresponding to the yacht model stacks and equation governing the passive scalar has been solved as a post-processing step.

The passive scalar transport concentration value ' $\eta$ ' can be evaluated in each point of the computational domain in terms of percentage by volume and compared to the measures.

As an example Figure 4-4 shows the pollutant concentration values at the wheelhouse deck level (% mean value) obtained from the numerical simulation. In particular a top view of the yacht is superimposed to the calculated pollutant concentration contour map, where the color of each point is determined by the local concentration value according to the scale placed in the upper part of the figure. In addition, in the same figure the ID sampling points position on the yacht scale model and the relevant labels have been superimposed to the calculated pollutant concentration contour map.

For reader's convenience Figure 4-5 shows the experimental results table where the corresponding ID sampling points values have been highlighted.

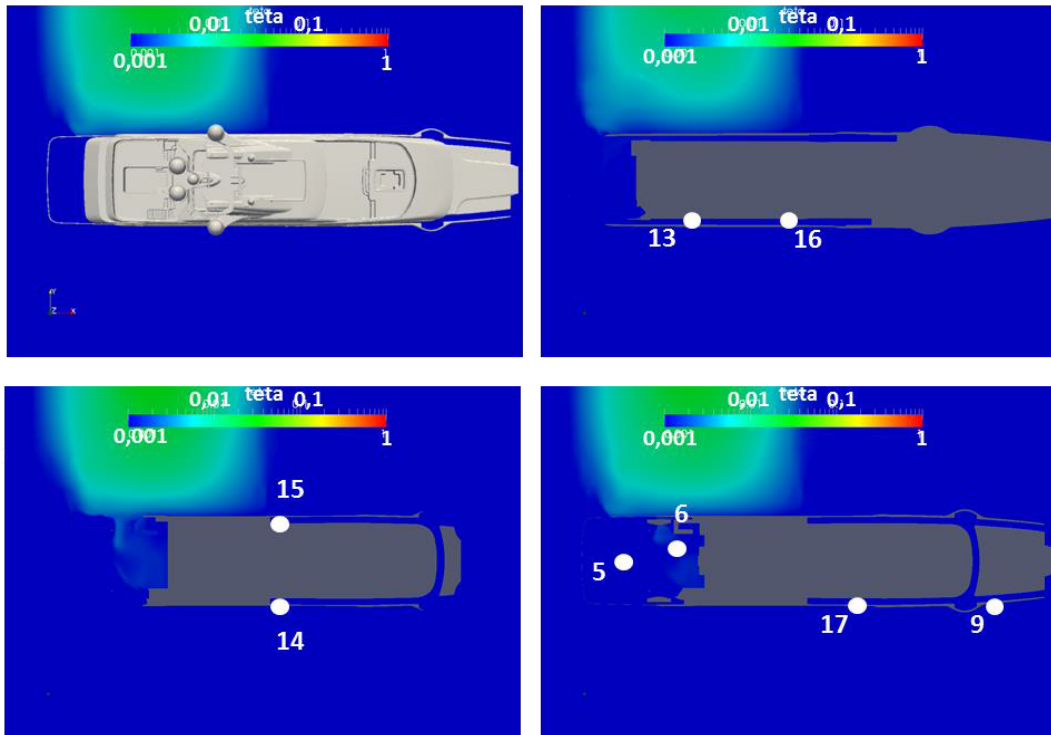


Figure 4-4 [Pollutant dilution - Wheelhouse deck - angle 90 deg]

Exhausts horizontal discharge,  $u = 1 \text{ m/s}$ , angle with respect to the wind direction:  $90^\circ$

ID sampling port	Sampling port position			CO <sub>2</sub> [% vol.]
	deck	bow -stern	port -starboard	
1	Sun deck	Stern	Middle	<0.01
2	Sun deck	Stern	Middle	0.01
3	Sun deck	Bow	Middle	0.01
4	Sun deck	Bow	Middle	<0.01
5	Wheelhouse deck	Stern	Middle	<0.01
6	Wheelhouse deck	Stern	Middle	<0.01
7	Mast plan	Stern	Middle	0.02
8	Mast plan	Bow	Middle	0.01
9	Wheelhouse deck	Bow	Starboard	<0.01
10	Main deck	Stern	Middle	0.01
11	Main deck	Stern	Middle	<0.01
12	Main deck	Stern	Starboard	<0.01
13	Main-Wheelhouse decks	Stern	Starboard	<0.01
14	Wheelhouse deck	Stern	Port	0.02
15	Wheelhouse deck	Stern	Starboard	0.01
16	Main-Wheelhouse decks	Middle	Starboard	<0.01
17	Wheelhouse deck	Middle	Starboard	<0.01
18	Mast plan	Middle	Port	<0.01

Figure 4-5 [Pollutant dilution - Wheelhouse deck, angle 90 deg]

Figure 4-6 and Figure 4-7 show the same comparison with reference to other yacht terraces and levels (sun deck and mast plan).

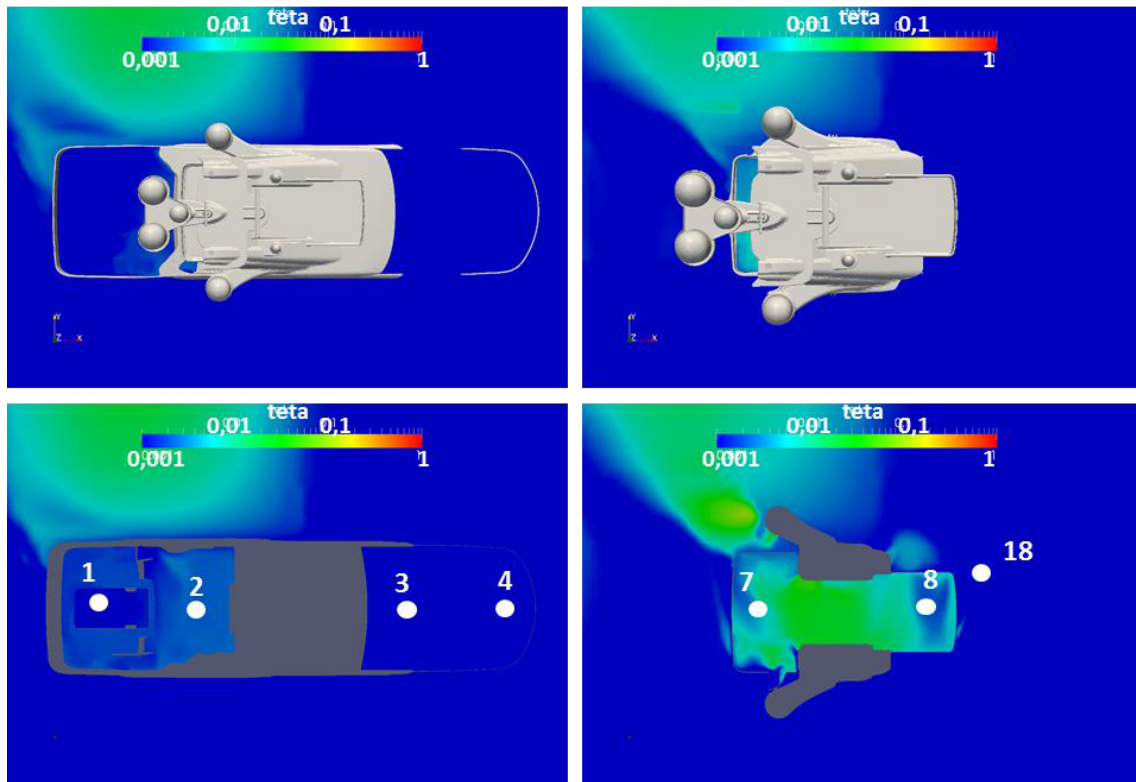


Figure 4-6 [Pollutant dilution - Sun deck & Mast Plan- angle 90 deg]

Exhausts horizontal discharge,  $u = 1$  m/s, angle with respect to the wind direction:  $90^\circ$

ID sampling port	Sampling port position			CO <sub>2</sub> [% vol.]
	deck	bow -stern	port -starboard	
1	Sun deck	Stern	Middle	<0.01
2	Sun deck	Stern	Middle	0.01
3	Sun deck	Bow	Middle	0.01
4	Sun deck	Bow	Middle	<0.01
5	Wheelhouse deck	Stern	Middle	<0.01
6	Wheelhouse deck	Stern	Middle	<0.01
7	Mast plan	Stern	Middle	0.02
8	Mast plan	Bow	Middle	0.01
9	Wheelhouse deck	Bow	Starboard	<0.01
10	Main deck	Stern	Middle	0.01
11	Main deck	Stern	Middle	<0.01
12	Main deck	Stern	Starboard	<0.01
13	Main-Wheelhouse decks	Stern	Starboard	<0.01
14	Wheelhouse deck	Stern	Port	0.02
15	Wheelhouse deck	Stern	Starboard	0.01
16	Main-Wheelhouse decks	Middle	Starboard	<0.01
17	Wheelhouse deck	Middle	Starboard	<0.01
18	Mast plan	Middle	Port	<0.01

Figure 4-7 [Pollutant dilution - Sun deck & Mast Plan, angle 90 deg]

In order to have a better insight on the pollutant propagation and to figure out the relevant cloud, pollutant iso-concentration surface can be plotted: as an example in Figure 4-8, Figure 4-9 and Figure 4-10 the 3D iso-concentration surfaces sketch are reported respectively with reference to 1%, 0.01%, 0.001% tracer concentration levels for the 90 [deg] wind exposure scenario. In each of these figures the coloured cloud represents the 3D region boundary which is interested by a pollutant concentration less or equal to the associated percentage concentration value by volume; obviously the lower the concentration level is the larger the region affected by the pollutant presence.

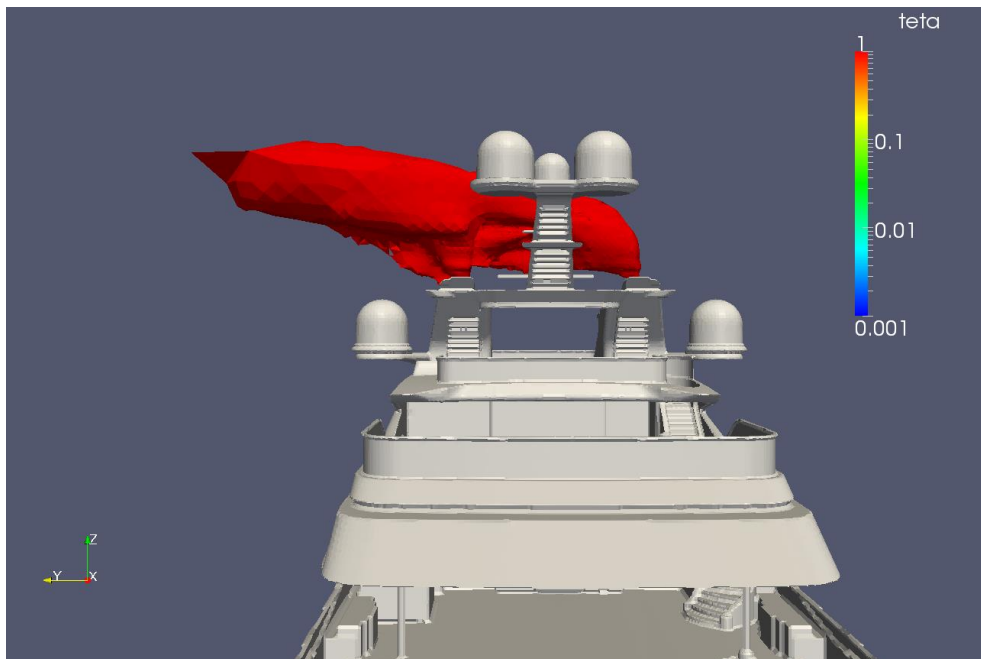


Figure 4-8 [Pollutant dilution - Back view -angle 90deg - Isosurface teta=1%]

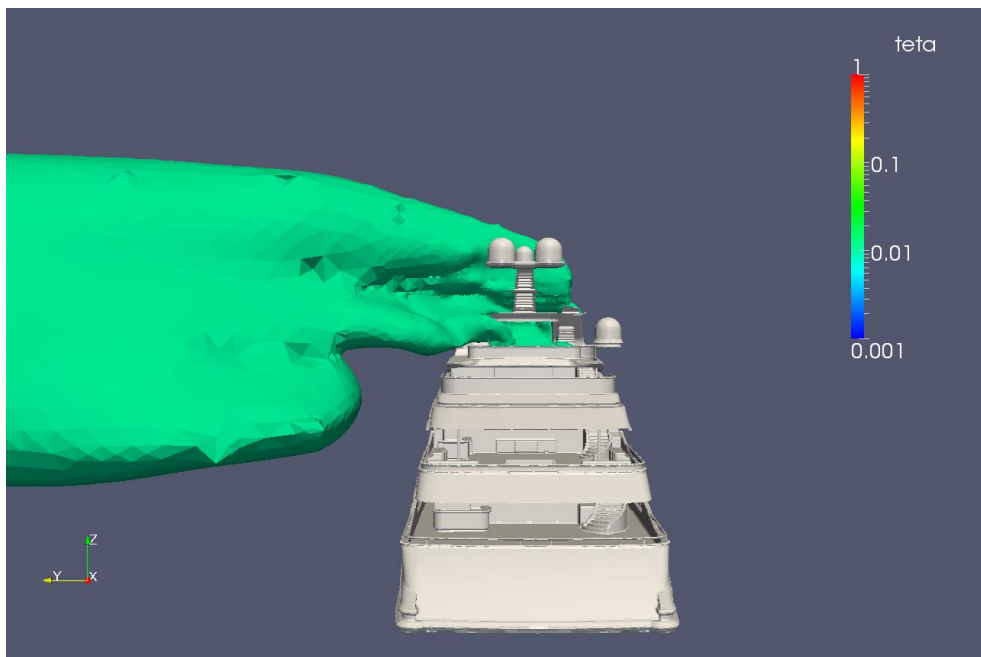


Figure 4-9 [Pollutant dilution - Back view -angle 90deg - Isosurface teta=0.01%]

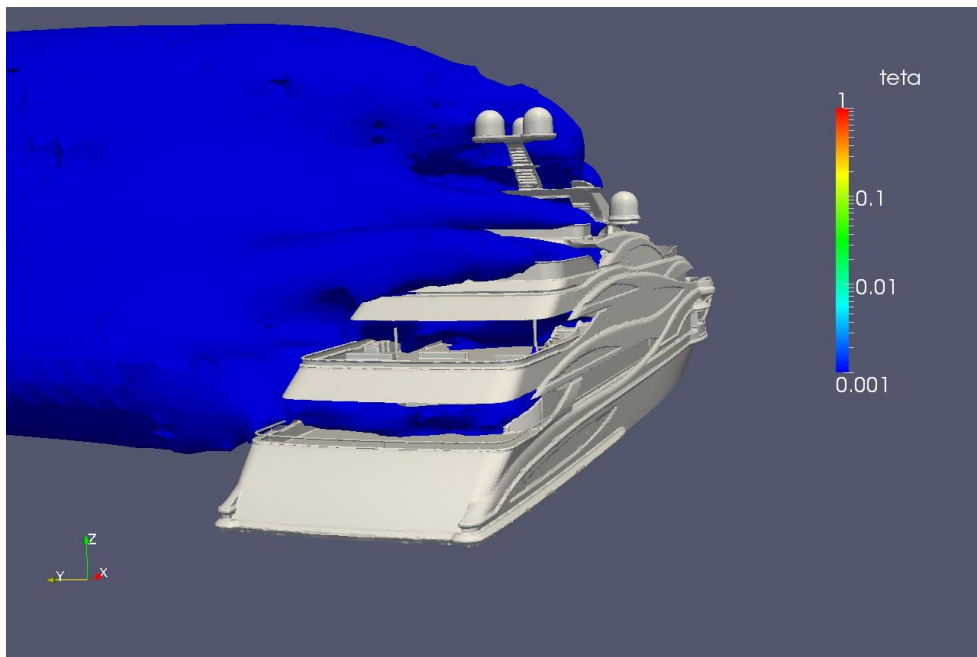


Figure 4-10 [Pollutant dilution - Back view -angle 90deg - Isosurface teta=0.001%]

The pollutant concentration isosurface sketch provides a clear and quantitative picture of the pollutant dispersion phenomenon and of the fallout region allowing to have an insight about any potential discomfort and/or re-ingestion of exhaust gases problem during the design process at advanced stage.

## 5. TEMPERATURE AND GRAVITY EFFECTS ON POLLUTANT DILUTION ASSESSMENT

As previously explained, in the wind tunnel experiments, having to reproduce the emission of exhausts produced by diesel fuel combustion, a mixture consisting of air and carbon dioxide, at room temperature, with a  $\text{CO}_2$  concentration equal to 20% by volume, is fed to the yacht model stacks.

The effect of the higher temperature of the fumes at full scale should facilitate the dispersion in the atmosphere of the fumes themselves, thereby reducing the chances of having re-ingestion phenomena or of discomfort in the areas of relevance of the vessel and its superstructure.

In order to have a better insight of the temperature and gravity effects, the numerical model has been upgraded including these parameters in the numerical model. More in details the numerical simulations of the flow field have been carried out solving the compressible steady state RANS equations and the pollutant dilution has been simulated again by means of the transport of a passive scalar on a fully calculated flow field.

This has been accomplished by means of a custom solver which has been set-up in the open-source fluid-dynamic framework OpenFOAM that for its nature allows to customize the numerical code in order to get custom tailored solution for the particular need of the problem.

In particular, the passive scalar transport equation routine has been adapted in order to include the compressible steady state solution according to section. 4.2c. Then numerical simulations have been repeated with the updated model and compared with the results relevant to the incompressible solution.

As an example, Figure 5-1 shows a comparison between results in terms of 3D iso-concentration surfaces (1%, and 0.01% tracer concentration levels) respectively obtained including temperature and gravity effects (left) and neglecting the same effects (right).

As can be seen from one side neglecting temperature and gravity effects leads to wider regions interested by the considered pollutant concentration level due to the higher pollutant propagation which increases the region affected by the tracer dispersion. On the other side neglected temperature and gravity effects leads to a negative buoyancy of the plume which increase the exhaust fallout in the yacht areas of interest.

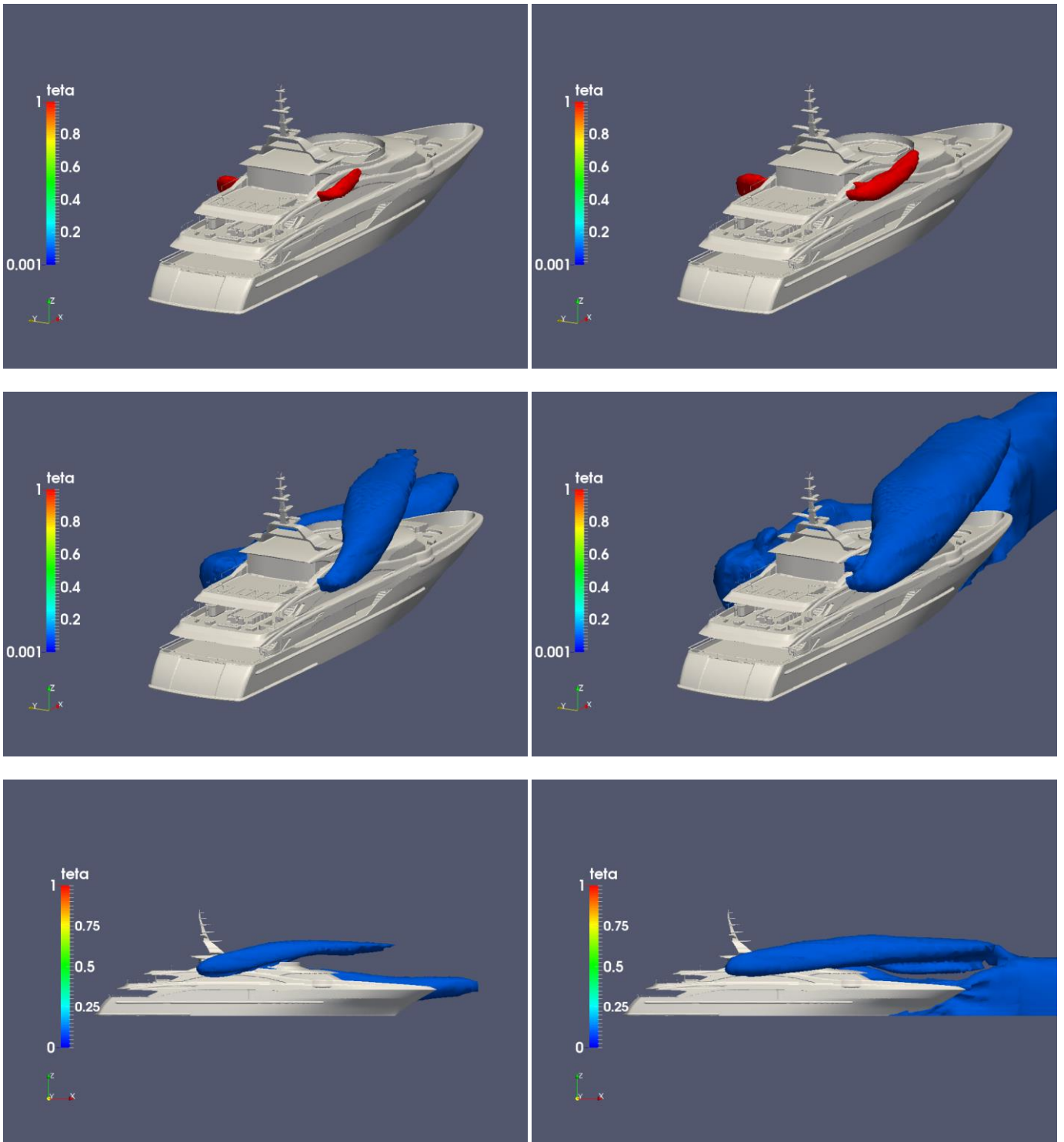


Figure 5-1 [Isosurfaces - Left: Passive Scalar, gravity ON, Temperature ON - Right: Passive Scalar gravity OFF, Temperature OFF]

More quantitative information can be extracted considering the pollutant concentration contour maps in the various yacht decks and terraces as shown in Figure 5-2.

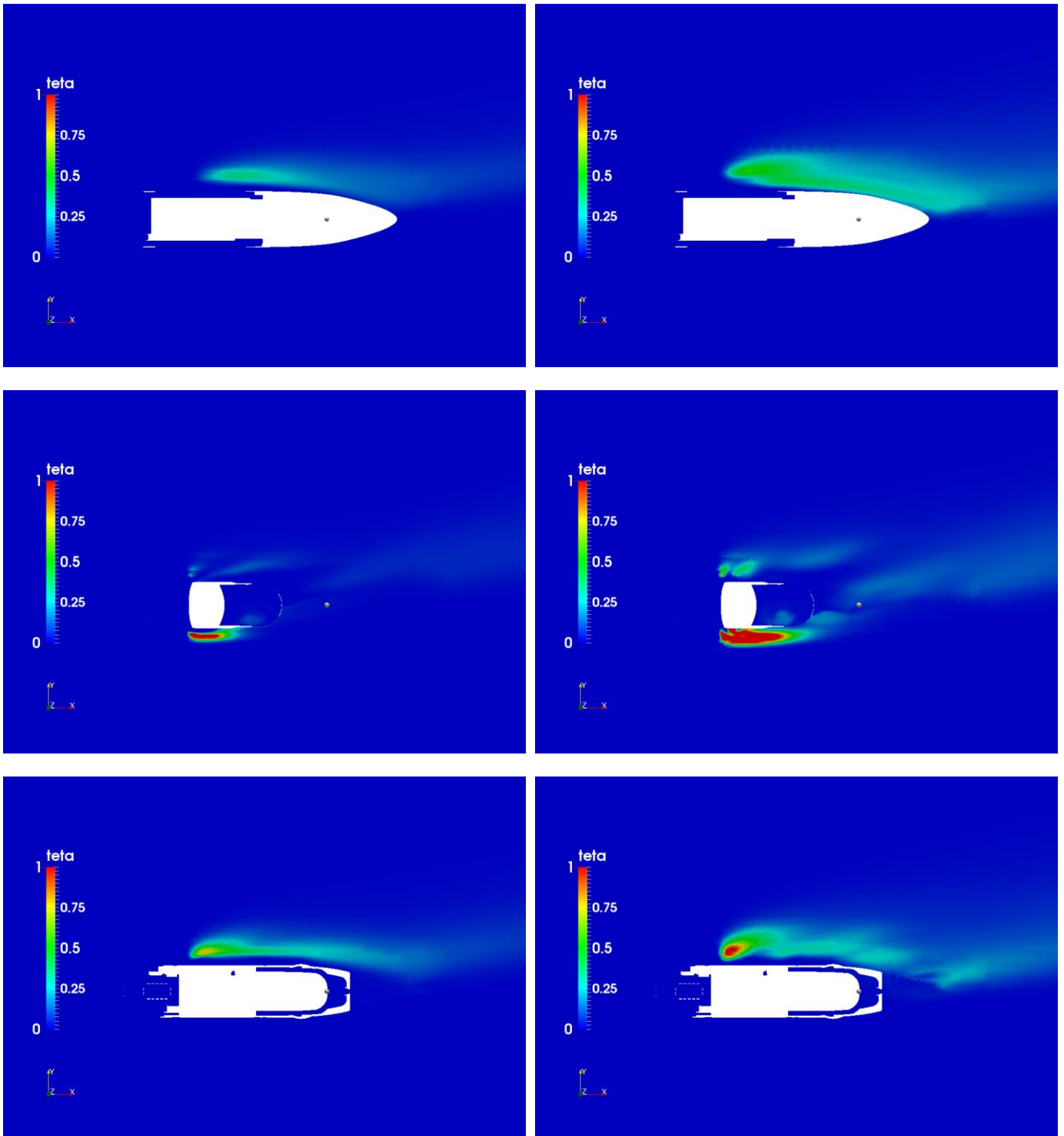


Figure 5-2 [Passive scalar concentration contours - Left: gravity ON, Temperature ON - Right: gravity OFF, Temperature OFF]

The comparison between results obtained solving the incompressible vs the compressible (RANS) equations and the transport equation for the passive scalar leads to the two following main conclusions:



1. Neglecting temperature and gravity effects leads to a negative buoyancy of the plume and represents a more conservative approach allowing to better highlight the potential entrainment of the exhausts in areas of interest of the yacht
2. As far as the wind tunnel experiments the choice to perform a scaling of the ratio between the emission and wind momentum, so as to reproduce consistently the interaction and the dilution/mixing conditions between flue gas and the external flow field, without obtaining a complete scaling of the buoyancy contribution is actually a conservative approach.

As a final step of the research in order to validate the proposed approach of the transport of a passive scalar on a fully calculated flow field some numerical simulations have been carried out using the most comprehensive and accurate approach where the exhaust gas stream is described as a multicomponent mixture of main combustion products.

As explained in par. 4.2 (a) using this numerical model the multi-component mixture is fed into the computational domain at the temperature of 633 K and pressure of 1 atm.

Then the Navier Stokes (11) the  $k-\omega$  SST equations (14), the species (15) and the energy (19) equations have been solved simultaneously using Fluent CFD software.

Finally results obtained with the multi-component mixture model have been compared with the passive scalar transport approach

As an example

Figure 5-3 shows a comparison in terms of 3D iso-concentration surfaces (0.1% tracer concentration), respectively obtained by the passive scalar transport approach (left) and by the multi-component mixture model (right).

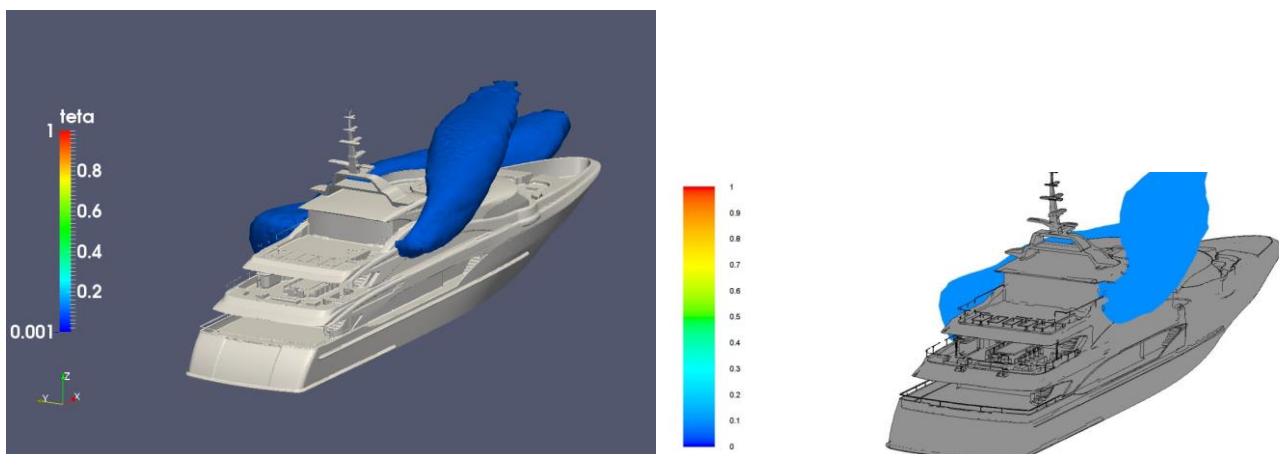


Figure 5-3 [0.1% pollutant concentration isosurfaces - Left: Passive Scalar OpenFOAM, gravity ON, Temperature ON - Right: Fluent, combustion multicomponent mixture]

Finally Figure 5-4 shows the same comparison in terms of pollutant concentration contour maps in the various yacht decks and terraces.

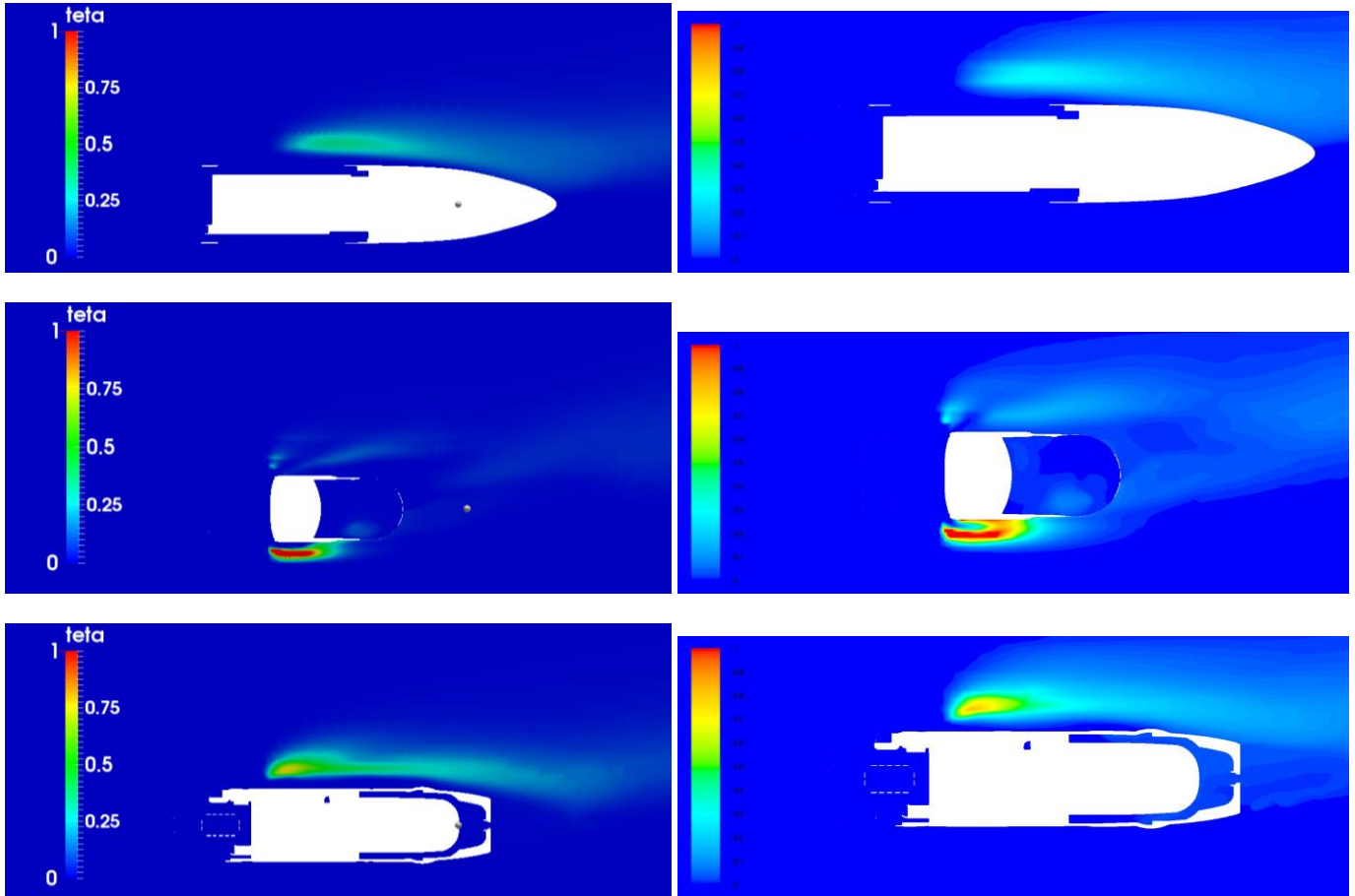


Figure 5-4 [Concentration contours - Left: Passive Scalar OpenFOAM, gravity ON, Temperature ON - Right: Fluent, combustion multicomponent mixture]

As can be seen results obtained by means of the most sophisticated approach do not differ substantially from the results obtained by means of the transport of a passive scalar on a fully calculated flow field.

Aiming to have a more efficient and integrated tool for the mega-yacht design process, in particular for the superstructure assessment, the small differences highlighted by the two different methods can be actually considered not so critical.

In addition taking into account the saving of computational time of about 50% with respect to the most accurate approach based on the multi-component mixture model, it can be concluded that the approach of simulating transport of a passive scalar on a fully calculated flow field represents the most effective approach from an operational point of view allowing also to include temperature and gravity effects in the pollutant dilution assessment.

## 6. CONCLUSIONS

In this paper an overview of the methodologies developed at Politecnico di Milano in order to assess mega-yacht aerodynamics in terms of aerodynamic loads, comfort analysis, pollutants dilution and re-ingestion analysis has been provided.

Experimental approach using wind tunnel tests has been described as well as a numerical tools which have been developed by the authors in the open-source fluid-dynamic framework OpenFOAM.

Several different approaches have been investigated for modeling the dispersion of exhaust gas stream around the boat aiming to find the best compromise in terms of accuracy and computational cost.

In addition effects of temperature and gravity on the pollutant dilution have been investigated and discussed.

The research carried out reveals that from an operational point of view the most effective approach for an efficient and integrated design of the superstructure taking into account the comfort requirements is to decouple the simulation of the flow field around the yacht from the calculation of the exhaust gases dispersion. This can be accomplished solving the transport equation of a passive scalar on a fully calculated flow field previously obtained solving the compressible steady state Reynolds Averaged Navier-Stokes (RANS) equations.

The proposed numerical model has been validated against experimental wind tunnel tests performed on a scaled model of a 270' LOA mega-yacht designed and built by Azimut-Benetti-boatyard and some results have been presented and discussed.

## REFERENCES

- Lewis, E.V., "Air and wind resistance" *Par 5.2, pp. 29-34, Principles of naval Architecture, Second Revision, SNAME*, Jersey City NJ, 1988
- Hughes G., "Model Experiments on the Wind Resistance of Ships", *Trans. RINA, Vol. 72*, 1930
- Hughes, G., "The Air Resistance of Ships' Hulls with Various Types and Distributions of Superstructure", *Trans. IESS*, 1932
- Baker, G.S., "Ship Efficiency and Economy", 1942
- Saunders, H.E., "Hydrodynamics in Ship Design", *Three Volumes, New York, SNAME*, 1957
- Isherwood, R.M., 'Wind resistance of Merchant Ships', *Trans RINA Vol 115, UK*, 1973
- Fujiwara, T., Ueno, M., Nimura, T., "An estimation method of wind forces and moments acting on ships", *Proceedings of the Mini-Symposium on Prediction of Ship Manoeuvring Performance, pp.83-92*, 18 Oct. 2001
- Fujiwara, T., Ueno, M., Ikeda, Y., "Cruising Performance of a large passenger ship in heavy sea", *Proceedings of the Sixteenth International Offshore and Polar Engineering Conference, pp. 304-311, The International Society of Offshore and Polar Engineers*, 2006
- Haddara, M.R., Guedes Soares, C., "Wind Loads on Marine Structures" *Marine Structures 12:199-209*, 1999
- Koop, A., Rossin, B., Vaz, G., "Predicting Wind Loads on Typical Offshore Vessels Using CFD", *Proceedings of ASME 31th International Conference on Ocean, Offshore and Arctic Engineering OMAE 2012*, 2012
- Wallis, S. M., "Factors Affecting the Performances of Motor Sailing Super Yachts", *Design and Construction of Super 6 Mega Yachts, 8-9 May 2013, Genoa Italy*, 2013
- Harries, S., Vesting, F., "Aerodynamic Optimization of Superstructure and Components", *2010 COMPIT, The 9th International Conference on Computer Applications and Information Technology, Gubbio, Italy April 12 to April 14*, 2010
- Det Norske Veritas, "Dynamic Positioning Systems", *Rules for Classification of Ships, Special Equipment and Newbuildings System Additional Class, Part 6 Chapter 7* January 2011
- Balchen, J.G., Jenssen, N.A., Mathisen, E., Saelid, S., "A dynamic positioning system based on Kalman filtering and optimal control", *Modelling, Identification And Control 1980 Vol. 1 No. 3, 135-163*, 1980
- Hajra, B., Stathopoulos, T., Bahloul, A., "A wind tunnel study of the effects of adjacent buildings on near-field pollutant dispersion from rooftop emissions in an urban environment", *Journal of Wind Engineering and Industrial Aerodynamic, 119(2013)133-145*
- CAA PAPER 2004/02, "Helideck Design Considerations – Environmental Effects"
- RUAG Aerospace Defence Technology, 'Politecnico di Milano: Sg-Balance 192-6i Version B02, Calibration Report', 2006
- Irwin, H.P.A.H., "A simple omnidirectional sensor for wind-tunnel studies of pedestrian level winds", *Journal Of Wind Engineering and Industrial Aerodynamics, 7*, 1981
- Carpentieri M., Corti A., Zipoli L., "Wind tunnel experiments of tracer dispersion downwind from a small-scale physical model of a landfill", *Environmental Modelling & Software 19 (2004) 881-885*
- Bertram, V.; (2003), "CFD for Aerodynamics of Fast Ships", *International Workshop AMC*
- Fossati F. et al; (2014), "Experimental Assessment of Mega-Yacht Aerodynamic Performance And Characteristics", *Journal International of Small Craft Technology -Transactions of The Royal Institution of Naval Architects - Part B, Vol 156, UK*, 2014
- Chapman, S., Cowling, T.G., "The Mathematical Theory of Non-Uniform Gases", *Cambridge University Press*, Cambridge, 1970

- Curtiss, C.F., Hirschfelder, J.O., "Transport properties of multicomponent gas mixtures", *Journal of Chemical Physics* 17, p. 550, 1949
- Coffee, T.P., Heimerl, J.M., "Transport algorithms for premixed laminar steady-state flames", *Combustion and Flame* 43, p. 273-289, 1981
- Dixon-Lewis, G., "Flame Structure and Flame Reaction Kinetics. II. Transport Phenomena in Multicomponent Systems", *Proceedings of the Royal Society* 307, p. 111-135, 1968
- Ern, A., Giovangigli, V. "Thermal Diffusion Effects in Hydrogen-Air and Methane-Air Flames", *Combustion Theory and Modelling* 2, p. 349-372, 1998
- Giovangigli, V., "Multicomponent Flow Modeling", *MESST Series, Birkhauser Boston*, 1999
- Patankar, S.V., "Numerical Heat Transfer and Fluid Flow", *Taylor & Francis, London*, 1980
- Poinsot, T., Veynante, D., "Theoretical and numerical Combustion", *Edwards, Philadelphia*, 2001
- Wilcox, D.C., "Turbulence Modeling for CFD", *DCW Industries, Inc.*, 2006

# Advanced Propulsion Trains for Superyachts

*Simon Brealey, Mechanical Engineer, BMT Nigel Gee Ltd*

*James Roy, Yacht Design Director, BMT Nigel Gee Ltd*

*Franz Hoppe, General Manager, RENK AG*

## SUMMARY

The paper examines the benefits of advanced propulsion trains for the specific demands of large superyachts with specific focus on hybrid systems utilising a combination of both diesel-electric and diesel-mechanical propulsion.

The technical characteristics of a hybrid system are compared to diesel-mechanical and diesel-electric systems. For a basis yacht of 110m a study of predicted fuel consumption is undertaken against a number of load profiles for each propulsion system. This indicates a potential of 10% saving in annual fuel use for a typical operating profile. Fuel savings are considered against the additional high investment costs of a hybrid system which indicate that hybrid would be a long term investment.

The effects of each propulsion systems on the yachts layout are discussed and the ability to allow increased luxury interior volume by careful optimisation of the required technical space is demonstrated for the hybrid system.

Whilst the conclusions demonstrate that the hybrid system will offer technical advantages and allow an improved layout the choice of the optimum propulsion system for a given yacht will be dependent upon the individual characteristics of the yachts design and the intended operating profile.

## 1. INTRODUCTION

Marine propulsion systems continue to evolve and improve incrementally to meet the ever increasing industry demands of greater efficiency, reduced fuel costs and improved packaging. The use of new technology has been eagerly adopted in many applications for defence, cargo, offshore and passenger vessels. The scope of these advancements has been wide with new fuels, energy storage and alternative propulsion layouts all being investigated and brought to market.

In that context this paper sets out to look at some of the options suitable and available for use considering the specific demands of the modern large superyacht. The paper examines the benefits of a propulsion train consisting of a diesel-electric hybrid system. Whilst it is recognised that other 'advanced' propulsion systems are available the hybrid system is an option that is based on mature and proven technology that can deliver demonstrable benefits.

## 2. HISTORICAL BACKGROUND

Hybrid propulsion for marine applications is not in itself a new idea and various systems have been designed and utilised. With naval vessels hybrid was introduced with the German mine hunters class 332 in the 1980s, where a 2 MW high speed diesel engine was married with a 75 kW electric motor for low noise loiter speed, both transmitting their power through epicyclic gears. With frigate propulsion the British Navy set a path in hybrid propulsion technology with the Type 23 Duke Class frigates featuring electric motors of 1,5 MW per shaft line for loiter and cruise married to 11 MW gas turbines for sprint speed. A more recent example is the Holland class OPVs of the Netherlands Navy, commissioned in 2011 with a system comprising of a 5,5 MW diesel engine and a 400 kW electric motor in CODELOD (COmbined DiSel ELectric Or Diesel) per shaft line.[1]

In commercial ship building, hybrid propulsion has a wealth of historical development. The large cruise ferry Finnjet of 1977 was reengined in the early 1990s with large 28 MW gas turbines and 5 MW electric motors per shaft line in parallel. In this particular case the propulsion system not only served slow speed modes but also operated as CODELAG (COmbined DiSel ELectric And Gas) to provide a continuous maximum speed of 33 knots (this was a 30.000 tonne displacement vessel). The system featured a 100 ton reduction gearbox with three stages on the electric motor side as pictured in Figure 1. Until decommissioning in 2006, seamless and unproblematic operation over the years proved the reliability of the installation.

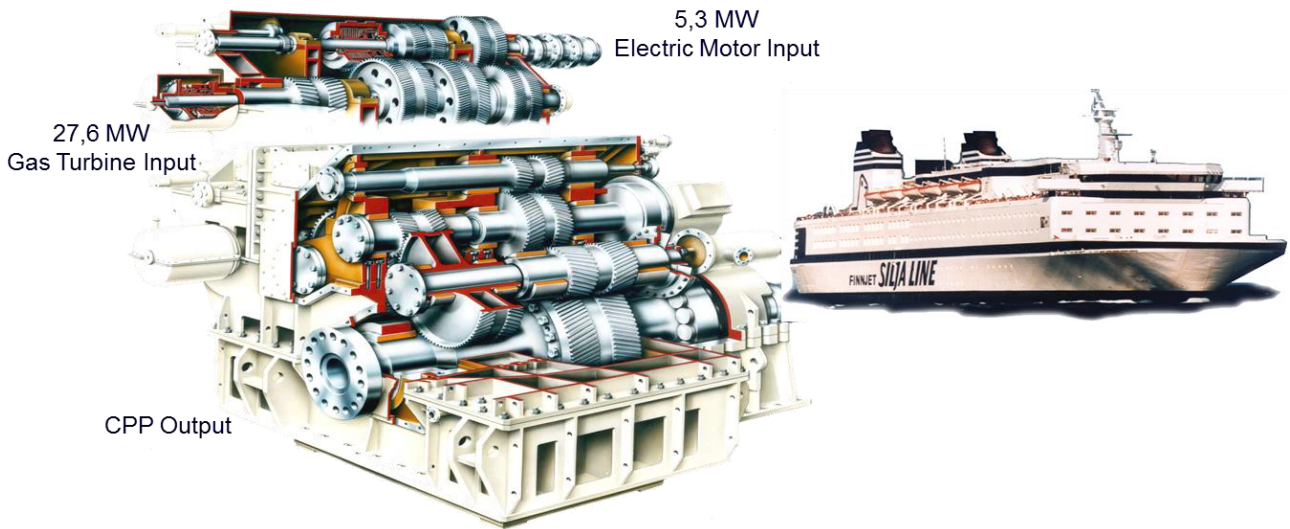


Figure1: High powered cruise ferry Finnjet with hybrid electric CODELAG propulsion.

### 3. PROPULSION SYSTEMS DESCRIPTION

In recent years electric propulsion has become increasingly popular as technology has improved. For example hotel loads and propulsion power can now be handled with modern electronic management very efficiently. Electric motors are also becoming more compact with a higher reliability and improved efficiency compared to previous generations. The availability and use of compact high torque permanent magnet motors is also widening the range of applications.

Electric motors can be arranged in hybrid configurations, together with diesel engines, or as stand-alone propulsors. The three configurations indicated in Figure 2 represent the most common considered for use in large superyachts.

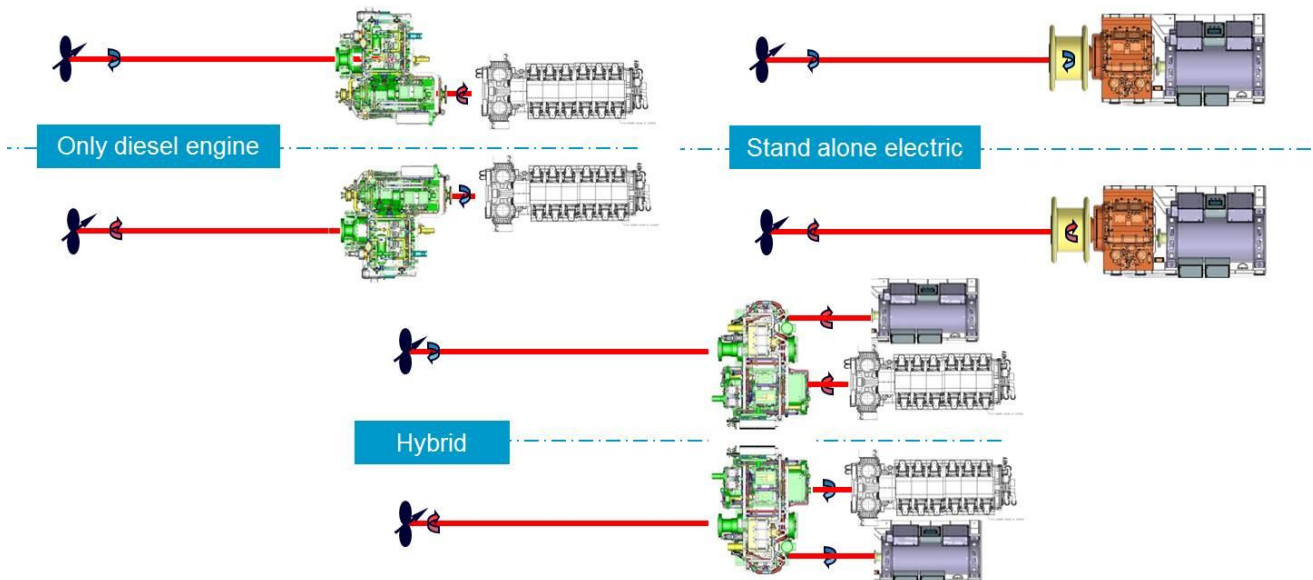


Figure 2: Basic arrangement of propulsion trains as mechanical diesel engine drive, single electric motor drive, or combined CODELAG (hybrid propulsion), power range up to 6 MW.

The straight forward diesel-mechanical engine drive provides for standard technology (and is still the most commonplace), for which there are a very wide range of available diesel engine sizes. With no complex reduction gears these systems are simple and reliable, however compromises have to be accepted regarding noise performance and efficiency in the low power range, especially where manoeuvre and loiter operation requiring power below 10% idling of a diesel engine need to be performed by propeller blade pitch adjustment (if CPP is even fitted).

Alternatively pure electric propulsion benefits from the torque-speed behavior of electric motors where full torque is available over practically the entire speed range. The depicted design show in Figure 2 is a high speed motor combined to a reduction gear to the propeller shaft line, more details of the benefits of this arrangement are given in Figure 6. By nature of electric motor operation noise and vibration characteristics are very good, and could be further improved by specifically designed elastic supports. Electric motors available today include advanced mechanical properties and insulation materials with high temperature resistance giving good reliability at low maintenance costs.

The essence of a hybrid system is the marrying of the benefits of both diesel-electric and diesel-mechanical systems. This results in a system which has the ability to operate at low speed as an electric propulsion only system or at higher speeds as diesel-mechanical. For cruise speeds the electric motors can operate as shaft generators (i.e as a PTO system) and it is possible to operate without running any generators, in this mode the engines can be made to work at their most optimum efficiency by adjusted the combinator curve to suit engine performance. To provide the best possible top speed for the yacht the electric motors can operate in conjunction with the main engines (i.e. as a PTI system). This either allows additional top speed or a reduction in size of the main engines. The ratio of EPM/Main engine power will vary between 10-50% and the speed range availability of the various modes of operation will be dependent upon hotel load and installed generating capacity. All these factors need to be carefully considered alongside the yachts likely operating profile when conceiving the architecture of a hybrid system.

Figure 3 indicates the power requirement for a typical yacht. It is useful to compare the requirements for top speed with the timeshare at 100% MCR and it can be seen that 100% MCR is used very rarely. Prime movers, such as diesel engines or electric motors, need to cover speeds through the entire range at good efficiency. This can be difficult to achieve with a single prime mover.

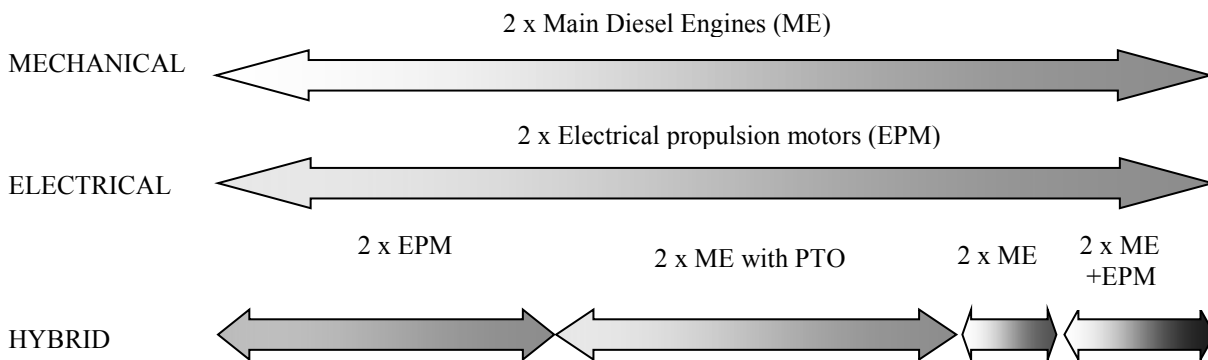
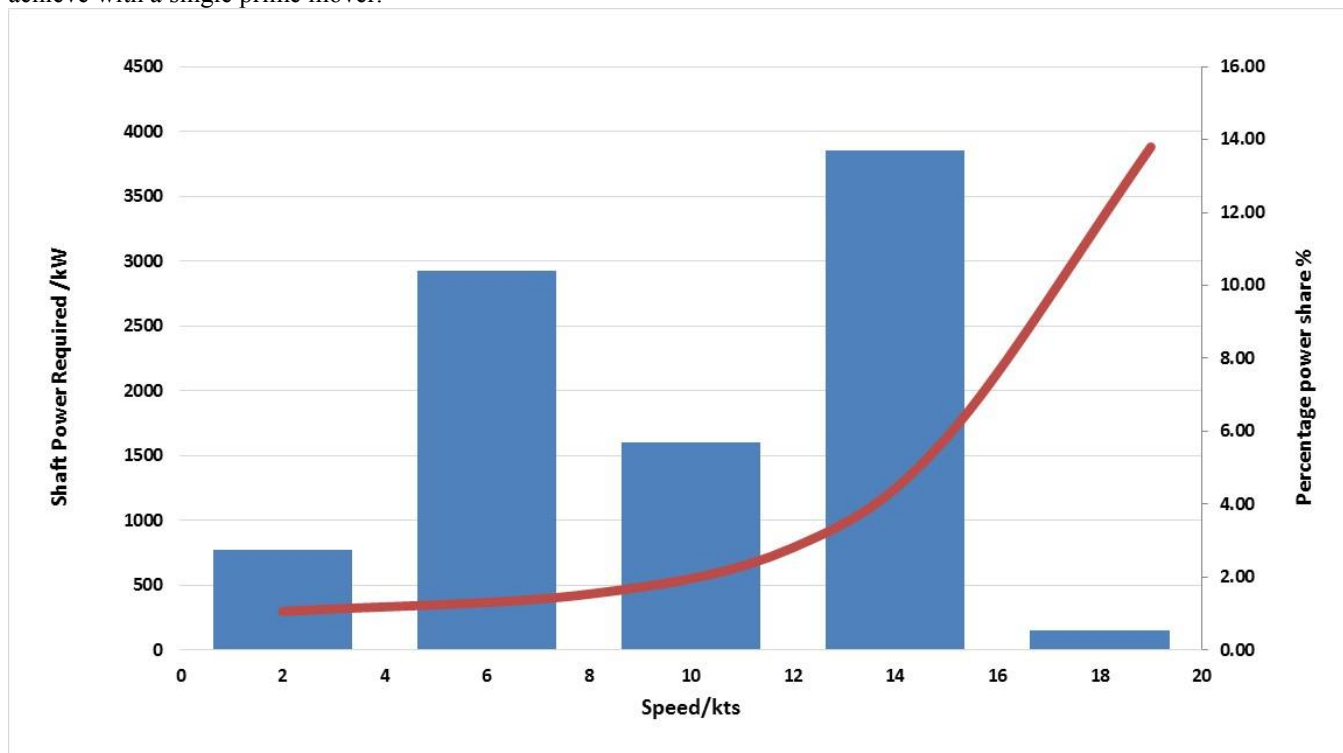


Figure 3 Comparison of combined propulsion systems at a given time vs. speed profile for a superyacht.

The example hybrid CODELAD system as shown in Figure 4 operates such that electric motors would cover speeds up to 8 knots, this point is realistically assumed as the idling power of the diesel engines. At speeds of 8-15kts the main engines would be used with the electric motors in PTO mode. Above 15kts the motors would also serve as an additional driver at top speeds knots providing a high degree of efficiency across the whole speed range.

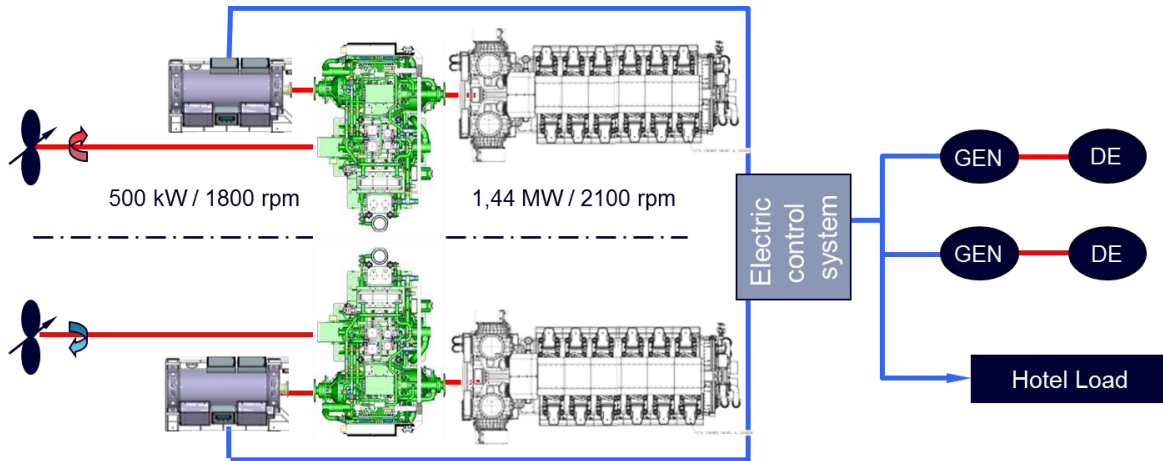


Figure 4: Hybrid propulsion with diesel engines and electric motors connected to onboard power generation.

The reduction gear used with hybrid propulsion is typically fairly simple as per the example for the Netherlands Navy Holland class OPVs, Figure 5. This consists primarily of the main gear set related to the diesel engine torque transmission, and of an additional smaller gear stage on the motor side. Both inputs are equipped with multi disc clutches and sleeve type shaft bearings. Normally the propeller thrust bearing is internally arranged to the output shaft. With double helical gearing and rigid foundations noise is within the acceptable limits of commercial levels and this can be further reduced for yacht requirements by use of viscoelastic mounts.

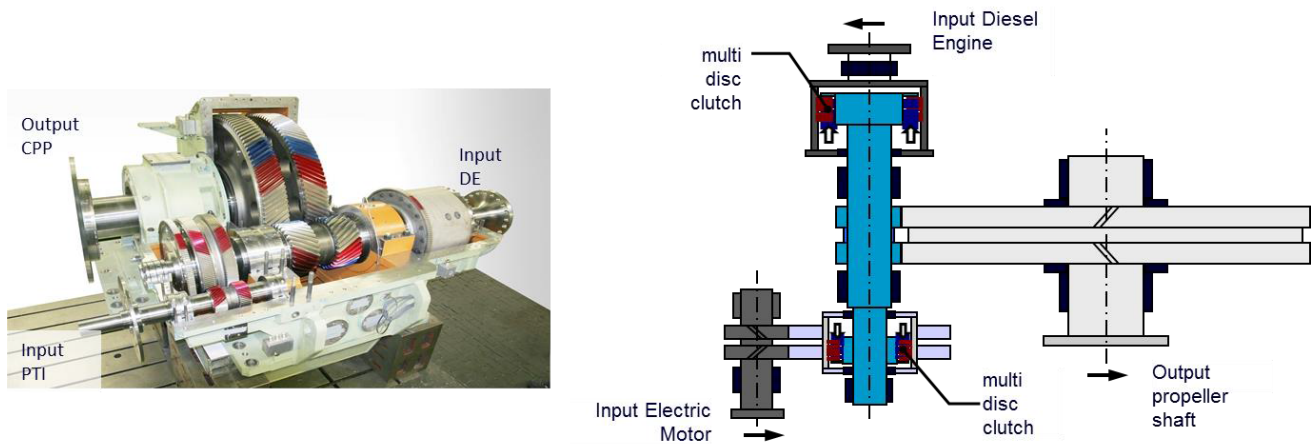


Figure 5: Main reduction gear for the Holland class OPVs.

#### 4. ADVANCED ELECTRIC DRIVE MODULE (RENK AED)

A particular advantage of diesel electric propulsion is the ability to package the propulsion to suit a specific arrangement and achieve low noise and vibration. In yacht applications this is often compromised by the size and weight of direct drive electric motors rotating at shaft speed. To overcome such disadvantages, and for low noise operation, a drive module was recently developed by RENK, the principle of which is given in Figure 6.

It features a high speed electric motor located on a raft and combined with a speed reducer gear, where the entire rafted module is positioned on a specifically calibrated soft elastic support system against the vessels foundation. This so-called Advanced Electric Drive (RENK AED) is connected to the shaft line via an internally arranged sophisticated coupling joint enabling larger displacement and, simultaneously, extreme noise suppression between module and shaft



line. In addition the reduction gear mounted on the raft is perfectly noise optimised. Weight savings of 40% are gained over the use of a direct drive motor.

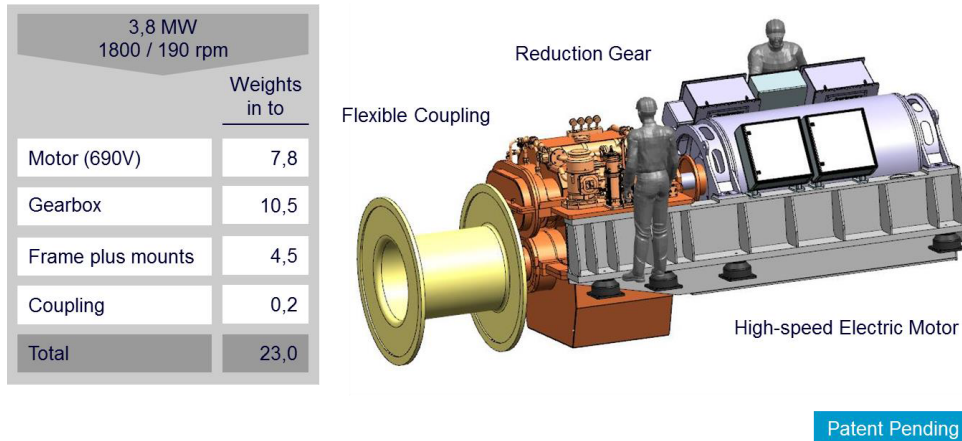


Figure 6: The Advanced Electric Drive (RENK AED), example for 3,8 MW maximum power.

## 5. LARGE YACHT PROPULSION SYSTEM DEMANDS

The specific demands from propulsion systems of large modern superyachts are unique in comparison to other vessels.

The delivery of the maximum volume of luxury guest accommodation is a key driver for the greater majority of yacht designs. In addition to traditional luxury areas, large tender bays, beach clubs, fold down shell doors and helipads will be required. Crew and staff numbers are likely to be considerable in relation to guest numbers and their accommodation will generally be designed to a high standard with ample space allowed above and beyond minimum statutory requirements.

All of these aspects fight for space and volume during the conceptualisation, design and engineering process. The effects of styling on a cutting edge modern yacht can often lead to a drive for a smaller proportioned superstructure which further places increased importance on utilising available hull volume.

It is clear that in order to deliver the best possible yacht technical space must be minimised to provide the best ratio of guest and crew volume in relation to technical volume. Whilst minimising technical volume alone offers benefits there are also significant benefits to be gained from achieving a more flexible distribution of technical space around the yacht. By taking the approach of trying to re-distribute technical space around the yacht “prime real estate” can be freed up around the yacht for provision of features directly benefiting the guest/owner.

It should be noted that minimising or re-distributing technical spaces must not be done at the expense of making the vessel unserviceable. This consideration plays an important role in achieving the correct balance between technical and luxury areas to achieve the ‘best possible’ yacht.

In the context referenced “prime real estate” can be defined as volume within the hull above the waterline on the ships side such that either windows or shell doors can be provided. Changing the purpose of quite small volumes of these areas can provide a dramatic benefit to the general arrangement of a yacht.

The types of technical spaces that typically “intrude” into these areas are:

- HVAC rooms.
- Engine room ventilation and exhaust casings.
- The upper engine room.

The size and distribution of HVAC rooms is a separate topic beyond the scope of this paper.

The size of the ventilation and exhaust casing can be effectively reduced by utilising direct at source cooling within the engine room. This can however also be further reduced by minimising the size and number of prime movers together with careful consideration of the type and configuration of the exhaust system.

The upper engine room in a typical yacht arrangement occupies approximately 25 % of lower deck volume. This space includes a significant ship side above the waterline. Reduction in both of these areas can provide significant gains in prime usable luxury area as a result of considering a sympathetic propulsion arrangement.

Another key demand is the requirement for low noise and vibration throughout the accommodation of the yacht, this requires careful consideration and design of the entire propulsion line from the propeller, prime movers and into the structure and outfit details.

A yacht is typically specified with high manoeuvrability characteristics and will typically be expected to operate autonomously in tight marinas and anchorages with good crabbing performance. Increasingly large yachts will also be expected to have a notional Dynamic Positioning (DP) capability such that either station keeping can be performed in areas where traditional anchoring is not possible or the system can be used to maintain specific headings whilst at anchor. This manoeuvrability is typically provided by fixed tunnel bow thrusters and stern thrusters.

There will be variations in the type and size of the required thrusters' dependent upon the propulsion system selected and DP capability specified. However in a typical direct mechanically driven yacht with a fixed pitch propeller it is likely that the size of the thrusters will have a dominant effect in the sizing of the overall electrical generating capacity. Thus it is likely that a yacht will have either 3 or 4 generators to meet the peak manoeuvring load-condition with only 1 or 2 required to meet normal operating conditions.

Whilst the definition of a 'typical operating profile for a yacht is very subjective it is clear that significant time is spent in harbour and at anchor. Therefore one of the most important aspects of any propulsion system should be the ability to operate effectively in conjunction with efficient hotel load generation when standing still. This is relevant when sizing generators for vessels featuring electrical propulsion as it is possible to design systems optimised for propulsion that will also operate at very low engine loads when in harbour, or be reliant upon a specific generator for long periods which may result in very short overhaul periods.

## 6. OPERATING PROFILE

Compared to many of the marine applications already mentioned the operating profile of a yacht will vary dramatically dependent upon the owners preferences, and to an extent the background and experience of the crew. This variation in operating conditions, when coupled with the privacy of typical yacht owners makes the gathering of comprehensive data logged operating profiles very difficult.

To investigate the relative merits of propulsion systems presented in this paper a typical operating profile has been generated based on broad assumptions. The profile was developed based on anecdotal evidence collected from crew, equipment manufacturers, owners' representatives and open source material and is shown in Figure 7.

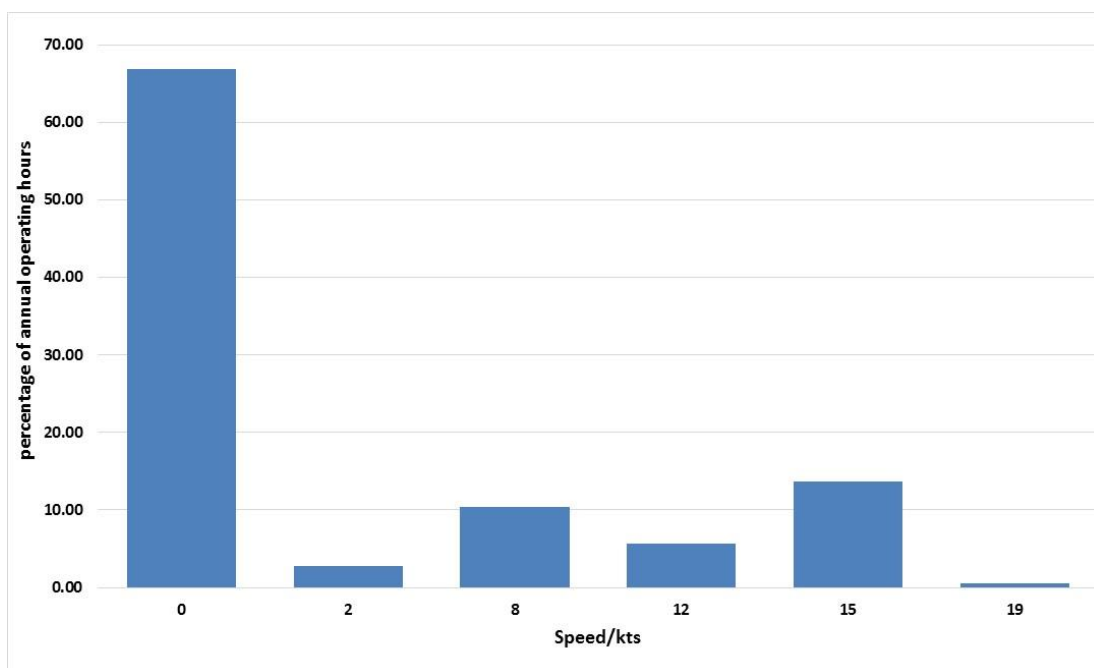


Figure 7 Operating profile indicating percentage time share vs. speeds.

The profile envisages operating in typical yacht environments all year round with transits between summer and winter destinations i.e. Mediterranean and Caribbean. Guest occupancy is considered as relatively frequent with guest usage reflecting comfortable cruising with extended stops in anchorages/harbours. The profile indicates a propulsive usage of 33% against 67% usage at harbour and anchor.

In the profile it is considered that the use of full speed will be a relatively infrequent occurrence. It is an interesting consideration that the normal new yacht specification will focus on the delivery of a single number top speed and cruise speed only. This drives propulsion system design to selection of prime movers suited to the achievement of top speed only rather than considering optimisation across the entire operating profile.

## 7. BASIS VESSEL

In order to analyse the benefits of the various propulsion systems a basis vessel has been utilised as depicted in Figure 8. The basis vessel is a 110 metre, low gross volume yacht developed by Oceanco and BMT Nigel Gee (styling by McPherson Yacht Design).

The design features a relatively narrow beam combined with a modest superstructure to provide a gross tonnage of approx. 3300 tons. As a result of the efficient hull design overall powering is approximately 4MW to provide a top speed of 19kts.



Figure 8 Illustration of the basis yacht design 110m, 3300GT 19kts.

Through the development of the basis vessel, direct drive, diesel-electric and hybrid drive propulsion systems have been developed.

As has been seen previously in Figure 3 it is possible to allocate different propulsion modes to each speed range and then analyse corresponding Specific Fuel Consumption (SFC) values and efficiencies for the prime movers. This subsequently allows for an estimate of the annual fuel usage dependent upon propulsion configuration.

## 8. ANALYSIS OF OPERATING PROFILES FOR FUEL EFFICIENCY

For the majority of large yachts (including the basis vessel) both main engines and generator sets will be high speed diesel engines chosen for their compact size and good noise and vibration characteristics. In general the specific fuel consumption (SFC) for a high speed diesel engine will follow the characteristics shown in Figure 9. Namely that the engine will operate much more efficiently when loaded above 60-75% of its MCR. The exact relationship between SFC and load will vary depending on a range of factors including the specific engine manufacturer and mode, given operating position on the engine speed/power curve and sequential turbo switching zones.

In the case of the diesel-mechanical arrangement, operation at low yacht speed will require the engines to operate at low load which in turn will result in high specific fuel consumption.

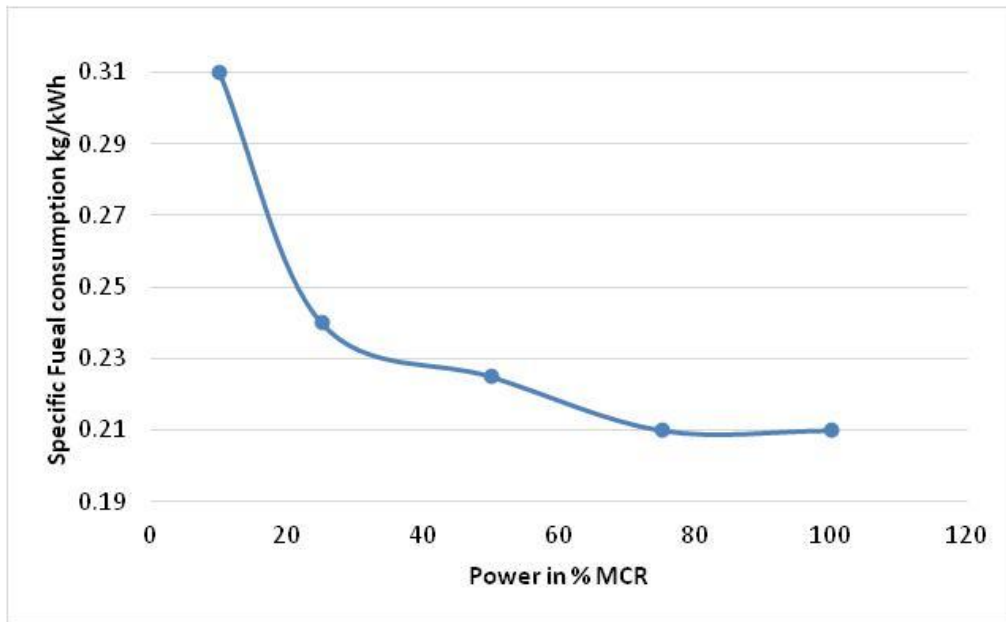


Figure 9 Typical variation of Specific Fuel Consumption against MCR for high speed diesel engines.

A diesel-electric system will be able to bring generator sets online to match the required propulsion capacity and ensure that generators are operated in a highly loaded condition. In addition to this the operation of the engine can be optimised for constant speed such that specific fuel consumption is improved. In general this will result in the diesel-electric arrangement producing a consistently low specific fuel consumption across the entire vessel speed range.

The hybrid system operates effectively as a diesel-electric vessel at low speed with a comparable low specific fuel consumption. As the speed increases the main engines are used for propulsion and PTO, in combination with the CPP propeller the operating position of the engines can be adapted to allow operation at the most optimum specific fuel consumption point. At the highest speeds when operating with the EPM's in boost mode the SFC will increase as the engines follow the power curve, but all prime movers will remain highly loaded resulting in a relatively low SFC.

The efficiency of the system is defined as the brake power generated at the prime movers in relation to the available shaft power. A diesel-mechanical drive will have a high efficiency which will only be affected by gearbox losses. The diesel electric drive will have a low efficiency due to losses in the electrical generation and control components i.e. alternators ,frequency drives and motors. The hybrid system efficiency will vary between low efficiency when operating in diesel electric mode, high efficiency when acting as a mechanical drive system only, and at a compromise efficiency when operating in electric boost mode.

The actual amount of fuel used will be dependent on both the SFC and the system efficiency. As per the relationship below;

$$\text{Fuel consumption [kg/hr]} = \text{SFC} \times \text{power [kW]} \times \text{efficiency}$$

Considering all the these factors the overall fuel consumption for the basis vessel at various speeds can be considered and is plotted in Figure 10.

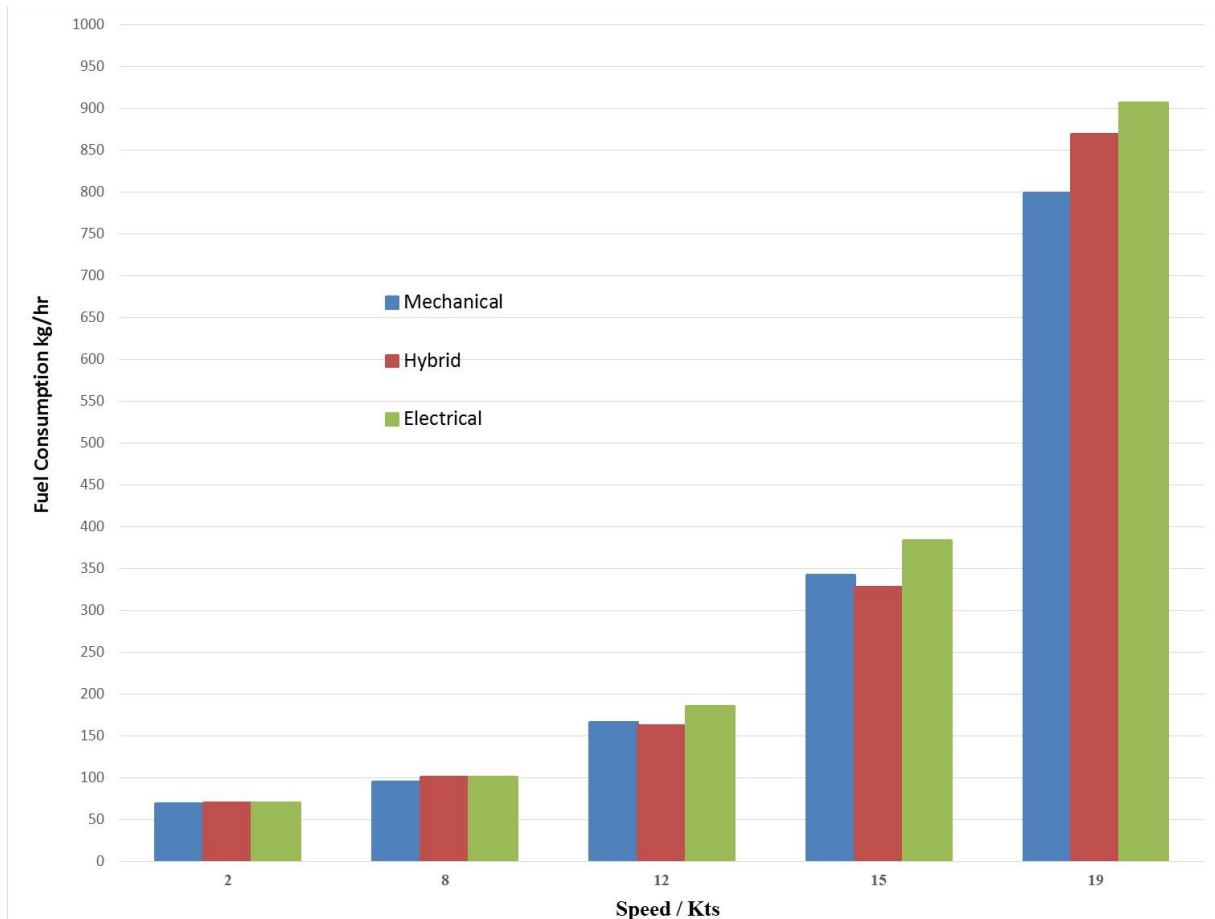


Figure 10 Fuel consumption [kg/hr] for each propulsion system at the range of operating speeds.

In general the differences between direct drive and diesel electric are small. Diesel electric uses slightly less fuel at lower speed and direct drive uses less at higher speeds. Hybrid is comparable to both systems at the ends of the speed range but uses considerably less fuel at medium speeds.

Medium speed tends towards the dominant mode in the assumed operating profile. When assessed against an annual period the hybrid system will use approximately 10% less fuel as shown in figure 11.

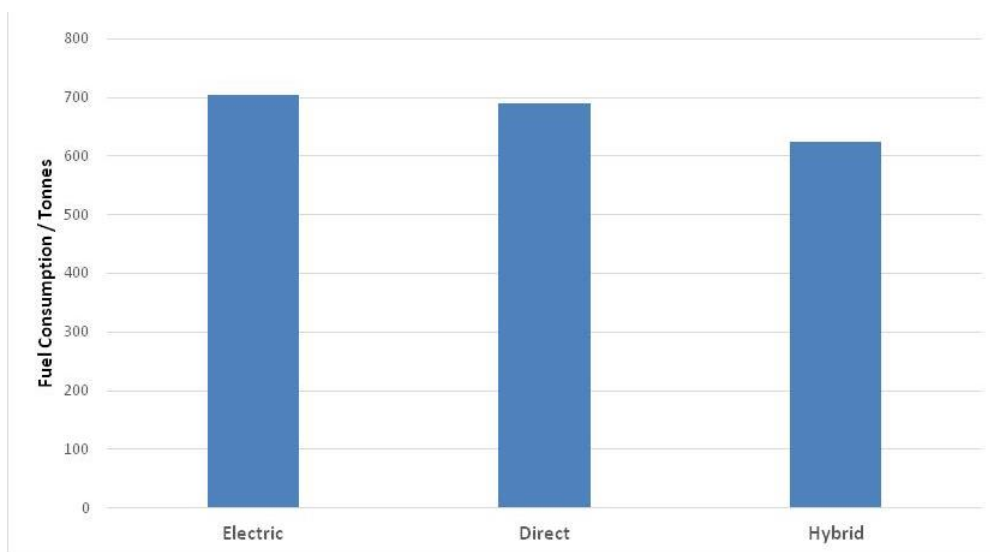


Figure 11 Variation of annual fuel consumption [tonnes] for alternative propulsion systems.

When examining other factors it can be seen that by efficient use of the main engines in regeneration mode (PTO) and low speed diesel-electric use, the annual operating hours for engines and generators can be increased resulting in the need for less frequent major overhaul and maintenance.

The hybrid system and the diesel-electric will however have higher initial costs over a direct drive diesel-mechanical system. For a hybrid system this will include a more complicated gearbox, cost of additional EPM, cost of additional frequency drives, increased complication of the control system and possibly the introduction of a CPP system. It is difficult to quantify the extent of these costs across the variety of equipment suppliers and shipyards within the industry.

It is also likely that within the annual operating budget of a large yacht the fuel costs may not be the dominant cost, or a driver for the owner. Personnel costs, mooring and other operating costs are likely to be a significant portion of overall operating costs.

It is therefore likely that the economic basis for using a hybrid system over a diesel or diesel electric would need to be based on a medium to long term investment or be judged against predictions of considerably higher bunker prices in the near future.

It can be seen that in this analysis the diesel electric yacht is less fuel efficient than the conventional direct drive yacht. This shows that the generally held opinion regarding diesel-electric systems being more efficient than diesel-mechanical is a misconception.

This misconception is in part due to the efficiency of modern high speed direct drive diesel engines across a much wider speed range than the traditional lower speed engines fitted in other marine sectors. In this case the losses inherent in the electric system are not competitive against the SFC advantages of the diesel-electric system

The diesel-electric system will however be advantageous in terms of noise and vibration and can be configured to provide exceptional DP/manoeuvring performance with large amounts of power available at low speeds. An electric system also opens the opportunity to use podded propulsion systems thereby delivering fully azimuthing thrust and greatly enhanced station keeping ability.

## **9. EFFECT OF EXTREME OPERATING PROFILES AND YACHT SIZES**

As discussed the operating profile of a yacht is likely to be highly variable. To test the robustness of the conclusions derived by analysis based on the operating profile two extreme (but credible) operating profiles were developed. These represent an 'heavy' and 'light' usage profile.

Light is designed to reflect a profile which involves low guest occupancy considerable time spent at harbour and anchor punctuated by short duration cruises to nearby alternate harbour destinations.

Heavy reflects the requirements of a world cruising yacht making a multi stop world tour. Therefore this profile would include a significant portion of time at transit speed navigating between various worldwide cruise destinations. Once at these destinations it is envisaged that the yacht would await the arrival of guests followed by undertaking a normal guest profile of comfortable cruise speeds interspersed with significant time at anchor for guest enjoyment.

The heavy scenario represents a 43% propulsive power share whilst the light profile represents a 9% propulsive power share as shown in Figure 12.

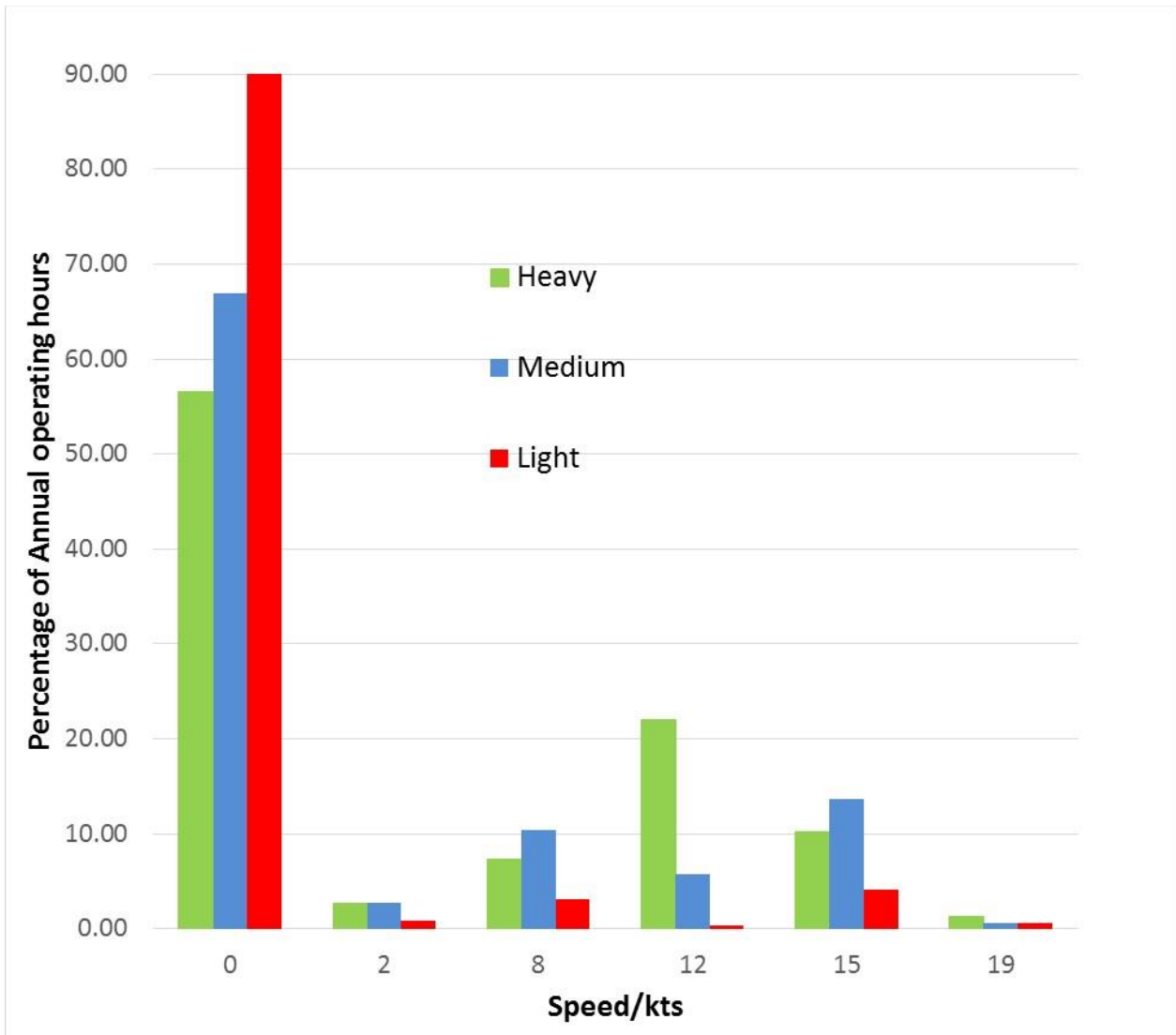
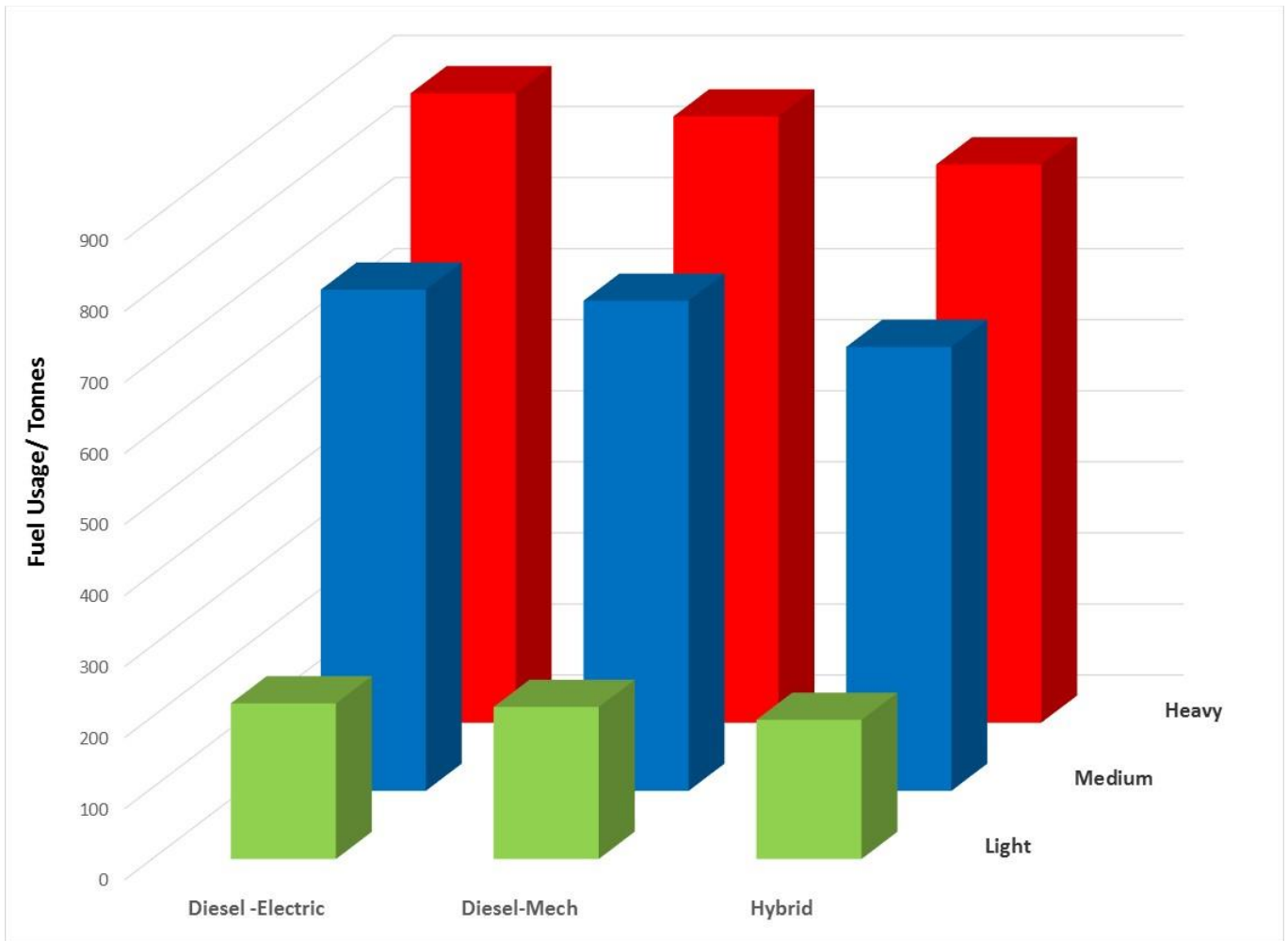


Figure 12 Variation in time share vs. speed for different operating profiles.

Generally these additional profiles (like the original) result in a dominant slow-medium speed operation. Analysing these for the basis vessel Figure 13 shows that the hybrid arrangement still uses the least fuel whilst the direct drive and diesel electric systems use very similar amounts of fuel. The savings presented by the hybrid system increase as the proportion of propulsion hours run vs anchor/ harbour hours increase. For yachts with lower propulsion hours the propulsion system with the lowest initial cost is clearly the best economic choice.



F

Figure 13 Annual fuel usage [tonnes] variation across operating profile and propulsion configuration.

The basis vessel is configured with EPM's which are sized such that with the normal generating capacity that would be installed for a diesel mechanical system there is sufficient power to support PTI top speed operation of the EPM's. This generating capacity is the capacity that is usually held in reserve for manoeuvring.

Larger yachts will require larger propulsive loads and it is likely that additional generating capacity (above the reserve held for manoeuvring) will need to be installed such that a useful PTI boost can be achieved. Compared to the basis vessel this will require more technical space and additional exhaust system/ventilation space allowance. However this increase in space required can often be considered against the range of engines available at larger power ranges. Above approximately 7MW the choice of high speed diesel engines is reduced and it is likely that the Main engines will either need to be significantly larger slower engines or a quad main high speed engine arrangement will be required.

For the larger hybrid system the additional high speed generating capacity can be installed in a more flexible way than larger or more numerous main engines. Therefore the technical space requirement space on the lower deck of a hybrid yacht can be reduced as engine heights can be contained within a single deck and generator exhaust packages can be flexibly arranged to fully utilise available uptake spaces.

In terms of fuel usage it can be seen that the ratio of EPM size to main engine size is critical for the hybrid arrangement. A high EPM to main engine power ratio will give increase propulsion mode flexibility but the requirement for additional control electronics and generating capacity will impact the technical space required. Additionally the efficiency of the vessel will be reduced across the speed range effectively shifting the vessel to operate primarily as a diesel-electric vessel.

If the EPM to Main engine power ratio is too small then the benefits of the hybrid propulsion in terms of speed increase at top speed are reduced considerably such that the additional complications caused by twin input gearbox and control electronics do not provide sufficient benefit.



The correct ratio of EPM to main engine power will vary dependent upon individual vessel size, hotel load, manoeuvring load and propulsion power requirements. Therefore careful analysis of all propulsion options are required to find the optimal space/speed/flexibility/efficiency combination specific to each yacht project.

## 10. ANALYSIS RELATED TO TECHNICAL SPACE DEMANDS

When considering the basis vessel configured for approximately the same shaft power for each system it can be seen that the hybrid version has less installed power and smaller main engines as shown in Figure 14. Substantial additional generating capacity is not required as the additional electrical propulsive power is provided by the spare capacity generating capacity that is reserved for manoeuvring.

The mechanical direct drive system has more installed power as the EPM PTI power present in the hybrid system now needs to be provided by increased main engine sizing. The diesel-electric system will require more installed power due to the lower overall system efficiency.

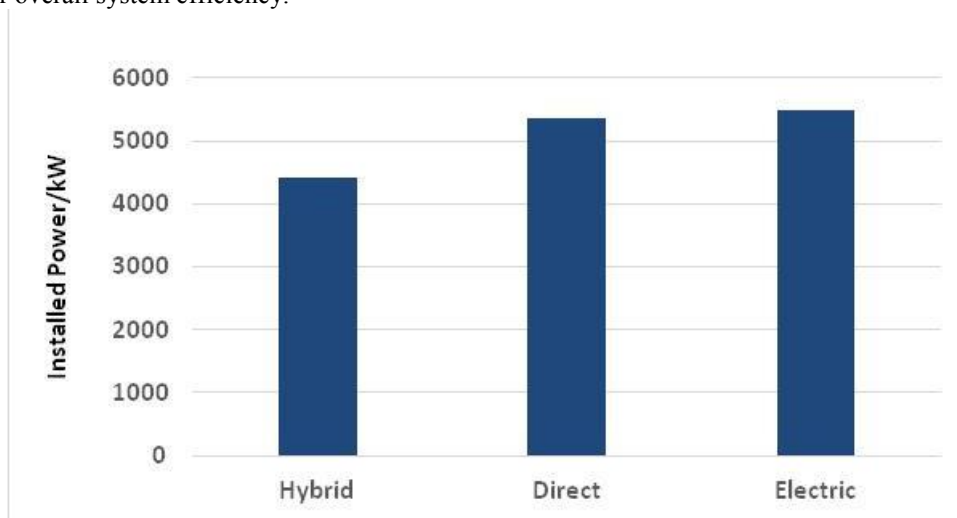
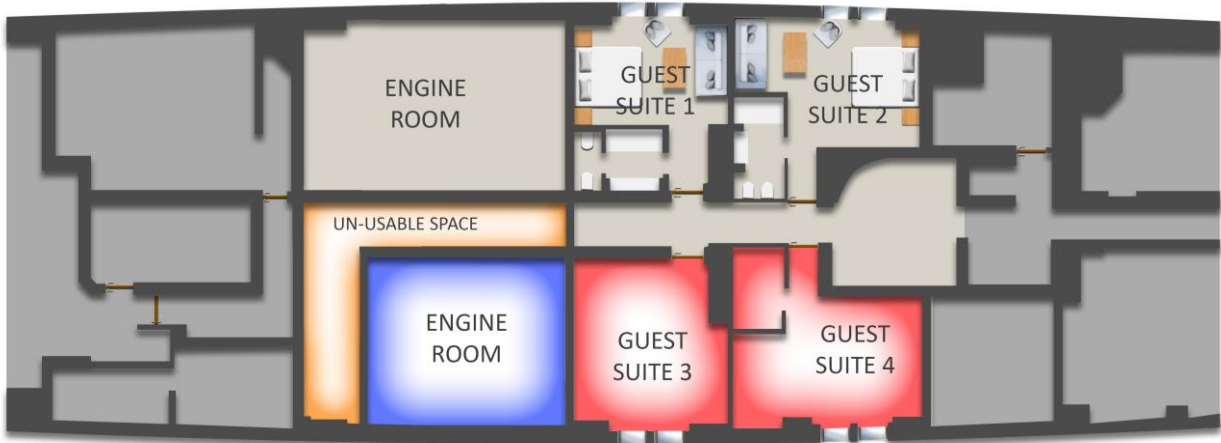


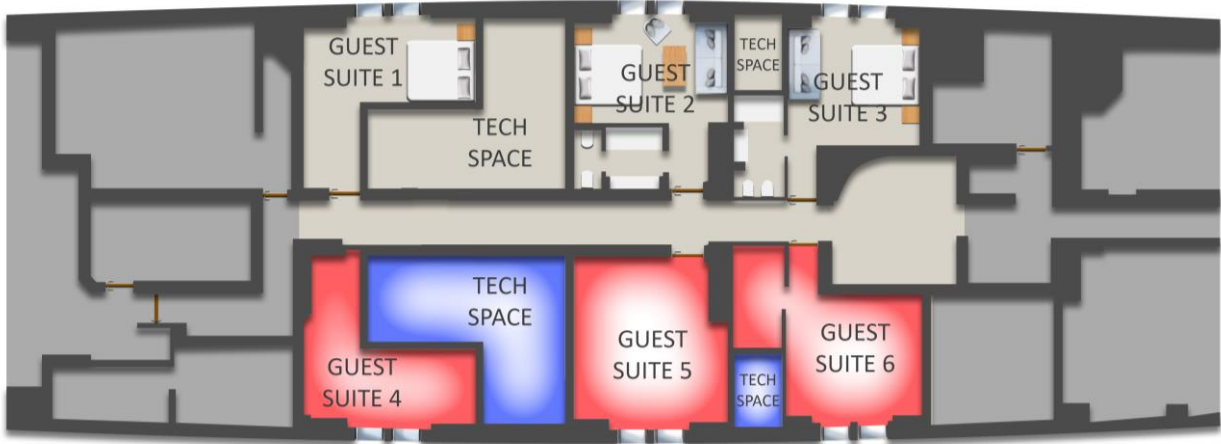
Figure 14 Total installed power variation across propulsion systems.

The amount of installed power will have subsequent effects on exhaust and ventilation arrangements. Additionally the use of smaller main engines will affect the overall engine room height requirements. As previously mentioned a key advantageous design feature for a yacht is reducing the size of the upper engine room. Figure 15 indicates the increase in lower deck space available by using the hybrid configuration with a near single tier engine room configuration. This is compared to a typical direct drive arrangement with correspondingly larger main engines, and a diesel electric system with a larger installed power. This philosophy is scalable across much larger yacht projects with proportional gains of the same magnitude capable of being demonstrated in yachts of up to approximately 6000 GT and 12MW.

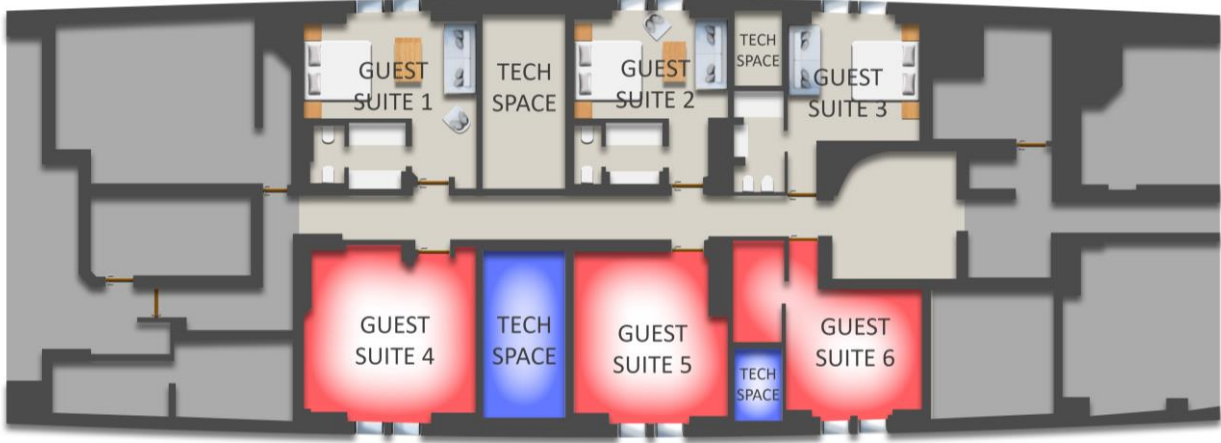
The coloured areas on the starboard side of the arrangement in Figure 15 indicate the specific space envelopes that would be developed during initial design development, the port side indicates a possible outcome produced by the designer of the GA. For the diesel mechanical system a large area on the lower deck is required and the distribution of the space required means that the areas of space required for technical space becomes unusable for guest usage, it is likely that this area will be adopted as an enlarged upper engine room. The diesel-electric option has a reduced foot print on the lower deck but the requirements of the larger machinery mean that the space allocated to the designer results in a compromised and unusually shaped cabin. The hybrid system can be arranged very flexibly due to the reduced size of the prime movers resulting in the delivery of 2 additional generously sized guest cabins.



Lower deck arrangement for Mechanical Diesel propulsion system



Lower deck arrangement for electric propulsion system



Lower Deck arrangement for Hybrid Propulsion System

	Technical space allocated to propulsion system in concept design
	Space allocated to Guest/Luxury areas in concept design
	Un allocated space not usable for accommodation

Figure 15 Illustration of lower deck Technical space requirements for mechanical, electrical and hybrid propulsion arrangements.

## **11. FUTURE TRENDS APPLICABLE TO YACHTS**

Considerable advancements are being undertaken in the field of energy storage, primarily in batteries. Battery technology is being rapidly developed to meet not only demanding automotive industry applications for electric and hybrid vehicles but also for large scale use in marine passenger vessel applications. This technology can be combined with increasingly sophisticated power control electronics which allow the introduction of DC bus electrical systems. This arrangement allows for the integration of battery energy sources with traditional 50 or 60Hz AC sources.

Energy storage potentially offers all yachts the ability to offer zero generator running whilst at anchor and allows the possibility of reducing generator sizing by use of peak load shaving. However in the context of electric or hybrid yachts there also exists the possibility to use the batteries to support PTI modes to allow boost speeds with reduced gen set capacity or provide silent low speed propulsion for short ranges.

The use of a DC grid system also offers the increased possibility of variable speed gensets and/or operating at 60Hz frequency such that additional power density can be achieved from the generators

The battery technology to allow these benefits is still developing and the cost (and weight and volume requirements) of application of very large scale installations is currently prohibitive but it is likely that these system will become both economic and technically viable in the short term to medium term.

## **12. CONCLUSIONS**

The work presented has examined the benefits of advanced propulsion trains for the specific demands of large superyachts.

A historical background has been presented which illustrates a broad range of applications of marine hybrid technology since the 1980's across a broad spectrum of vessel types and power levels.

The relative merits of hybrid, diesel-electric and conventional diesel-mechanical systems are presented and the ability of a hybrid system to flexibly meet the needs of a variable operating profile have been demonstrated.

Through the discussion of the specific demands of large modern superyachts it is demonstrated that there are clear advantages to propulsion and power generation systems which can minimise the total installed power demand coupled with offering flexibility in distribution of technical spaces.

To support this a case study has been presented using a 110m basis yacht which has been analysed for required installed power demand, fuel use and technical space requirements. To support the case study a hypothetical operating profile has been generated for a typical yacht based on anecdotal operational evidence.

The results of the case study support the case that a hybrid system can offer advantages in minimising the total required installed power, fuel burn and demand lower technical space in critical areas of the yacht (upper engine room).

The robustness of these conclusions have been tested by analysing two further extreme operating profiles with positive results.

It has been demonstrated that despite widespread misconception pure diesel electric systems are not always more efficient than diesel mechanical. It has also been demonstrated that for yachts envisaging with low propulsion hours the key consideration will be the initial cost of the system.

Future trends are discussed with reference to energy storage devices and the impact that the emergence of better battery technology and power distribution systems may have on designs of the future.

Large yachts feature many unique design requirements. The key for yacht propulsion system design is to provide a flexible and efficient system that is sympathetic to the specific general arrangement requirements whilst being as efficient as possible across a broad range of speeds.

The most optimum propulsion system will be dependent upon individual, project specific properties of speed/power, cost, space and layout.

### 13. REFERENCES

- [1] Hoppe, Franz; Herdt, Waldemar: Advanced Propulsion Gears for Super and Mega Yachts. Proceeding Conference RINA, Genova, May 2011

### 14. AUTHORS' BIOGRAPHIES

**Simon Brealey** is a Mechanical Engineer at BMT Nigel Gee. He has worked in variety of shipyard roles in the defence and yacht industry. His current focus is supporting the detailed engineering of new build yacht design projects in the 100m+ range whilst playing a lead role in the mechanical development of new concept designs.

**James Roy** is the Yacht Design Director at BMT Nigel Gee Ltd. He is responsible for development of the company's yacht design activities and managing conceptual, preliminary and detail design work as well as consultancy services.

**Franz Hoppe** is General Manager Marine at RENK AG. He graduated in mechanical engineering at the Technical University of Munich, Germany, and subsequently was appointed as assistant teacher, responsible for experimental and theoretical investigations in propulsion system technology. After finishing his university career with a PhD, he joined the industry covering various managing positions in engineering and sales of propulsion systems.

# SOLVING VIBRATIONAL RESONANCE ON A LARGE SLENDER BOAT USING A TUNED MASS DAMPER.

A.W. Vredeveltdt, TNO, The Netherlands

## SUMMARY

In luxury yacht building, there is a tendency towards larger sizes, sometime even beyond  $L_{pp}$  100 m. As a consequence, the structure becomes slender and hence flexible. In some cases this tendency causes a hull girder natural frequency to coincide with propeller rotation frequencies, with annoying resonance as a consequence. The main issue is usually the vibration decay rate, which is very low. This indicates low structural damping, which is common in steel (ship)structures. Due to slight uncertainties in ship weights and structural damping, such a resonance can only be observed during sea trials. When it can be shown that the vibrations are indeed associated with a particular vibration mode, a Tuned Mass Damper (TMD) is a viable option to deal with the phenomenon. Recently, TNO applied a TMD on a large luxury yacht for combatting a hull girder resonance. The system was developed in close cooperation with the shipyard. This paper presents the theoretical background in a easy to understand, intuitive fashion and explains the practicalities of the design, fitting and commissioning of a TMD on board a yacht.

## 1. THE TWO MASS SPRING DAMPER SYSTEM

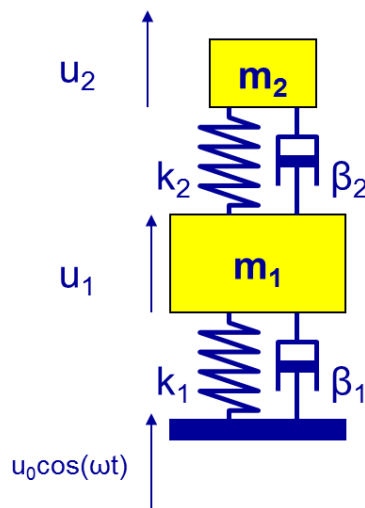


Figure 1 The two mass spring system

In order to understand the mechanism which governs a 2-node hull girder bending vibration in conjunction with a tuned mass damper, the mechanical model as depicted in Figure 1 must be characterised. In this paper  $M_1$  is the effective mass of the boat associated with the 2-node horizontal bending vibration,  $M_2$  is the mass of the TMD. Springs  $k_1$  and  $k_2$  are the respective stiffness elements, while  $\beta_1$  and  $\beta_2$  reflect the respective damping constants.

When the damping  $\beta_1$  is set at 1% of critical damping while the TMD is inactive, a frequency response function as shown in Figure 2 by the line with one maximum (green) characterised the system. As can be seen an amplification of 50 occurs at resonance. When a tuned mass damper is fitted with a mass of  $1/100^{\text{th}}$  of the main mass and a damping of 6% of critical damping, the response as shown by the line with two maxima (red) characterises the system. The dynamic amplification reduces roughly by a factor of five. The two maxima and the minimum in between are typical.

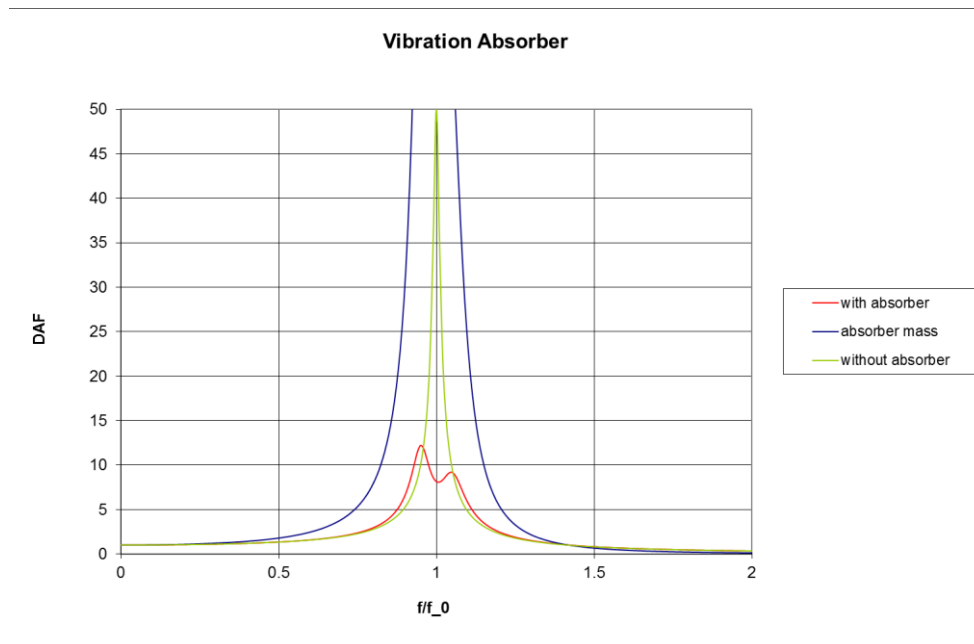


Figure 2 Typical dynamic amplification main mass, without and with absorber

As can be seen, in this case the response level reduces by a factor of almost five.

There are many splendid books on mechanics which also deal with the tuned mass damper, e.g. Den Hartog (1934) which deals with mechanical vibrations in general and Todd (1961) which is dedicated to ships.

## 2. THE 2-NODE HORIZONTAL BENDING HULL GIRDER VIBRATION

### 2.1 Observations

The annoying horizontal vibration was suspected to be associated with a horizontal 2-node hull girder vibration. This suspicion was based on a vibration contour plot (Figure 3) established during sea trials. The x-axis is the frequency in Hz while the vertical axis is the time axis during which the boat speed gradually increased. The colours indicate the vibration level (RMS) in [mm/s]. The yellow arrow points the line of increasing propeller blade excitation frequency. The blue arrow clearly indicates a natural frequency because it does not vary with the propeller blade frequency.

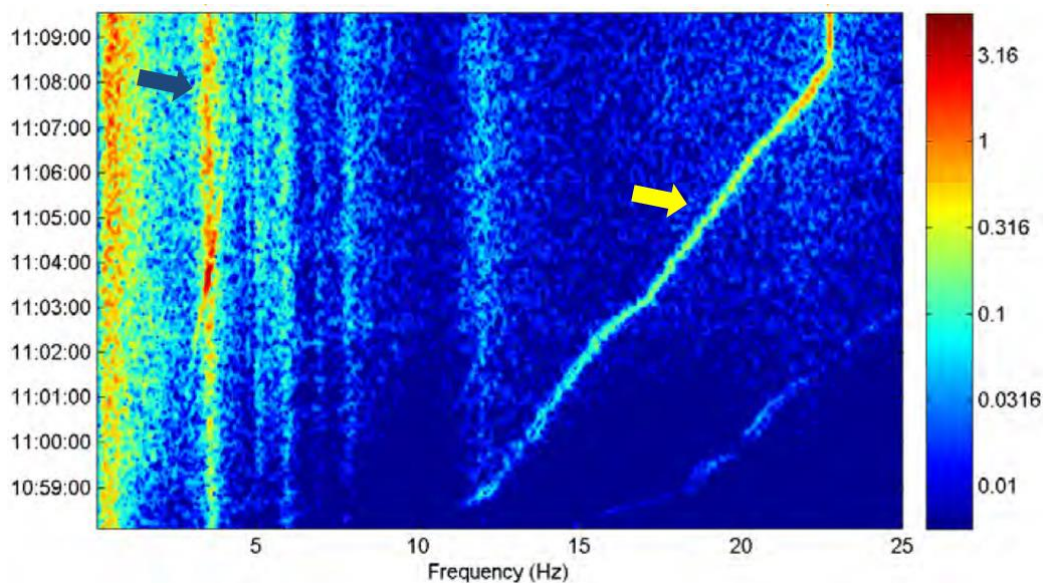


Figure 3 Countour plot measured transverse vibrations during sea trials (source: Lloyds Register, ODS)

This frequency lies at 3.6 Hz. Although the sea trial vibration measurements already indicated that this natural frequency was associated with the 2 node horizontal hull girder bending mode, it was decided to conduct an impact excitation test for confirmation purposes. Moreover, in order to investigate the effectiveness of a TMD it is essential to know the vibration mode shape and the damping associated with the vibrating main mass, which can also be determined through impact response tests.

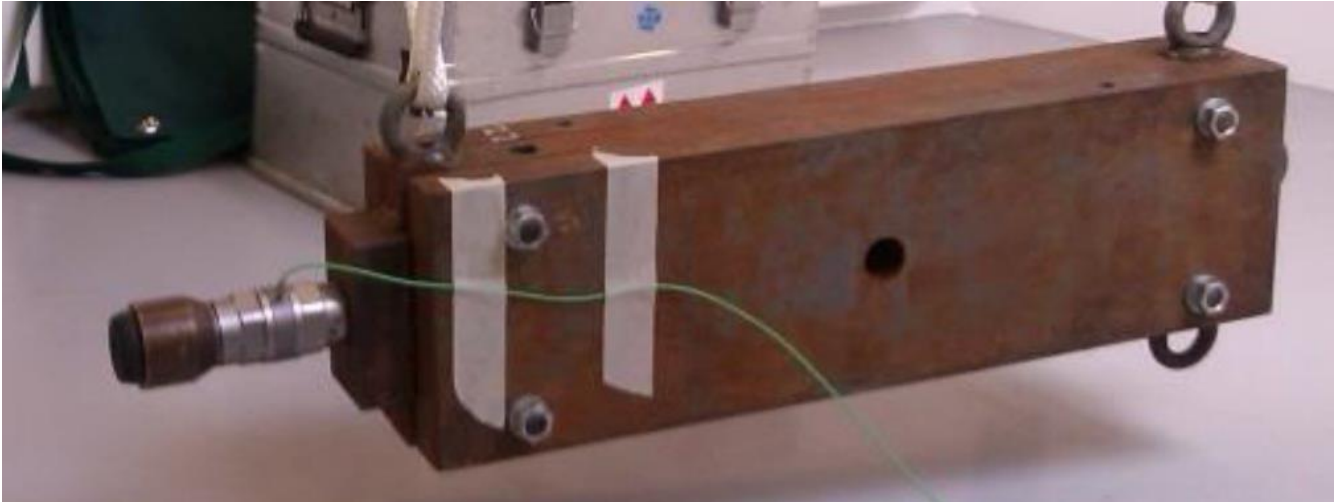


Figure 4 Typical excitation hammer, for horizontal impact

## 2.2 Impact test

Figure 4 shows the horizontal swinging hammer which was used to conduct the impact tests. The mass of the hammer was 120 kg. The hammer was fitted with a transducer for measuring the actual impact. The impact was applied at a stiff location on the ship structure, in this particular case the PS boulder foundation as the fo’c’sle deck. The longitudinal location was chosen in the forward location of the ship in order to make sure that the 2-node horizontal hull girder bending mode would be excited. Impacting at a vibration mode shape node would not excite the vibration mode of interest.

Along the boat’s length eight accelerometers were located. The impact response at each location was recorded simultaneously. By ‘dividing’ the measured acceleration by the measured impact force, frequency response functions (FRF) are obtained for each location. Figure 5 shows such a typical FRF, in this case a location at the stern of the boat. There are three graphs which must be interpreted. The amplitude graph shows the actual response in terms of acceleration level per unit of force ( $[(m/s^2)/N]$ ). Clearly there is a resonance associated amplification at 3.6 Hz.

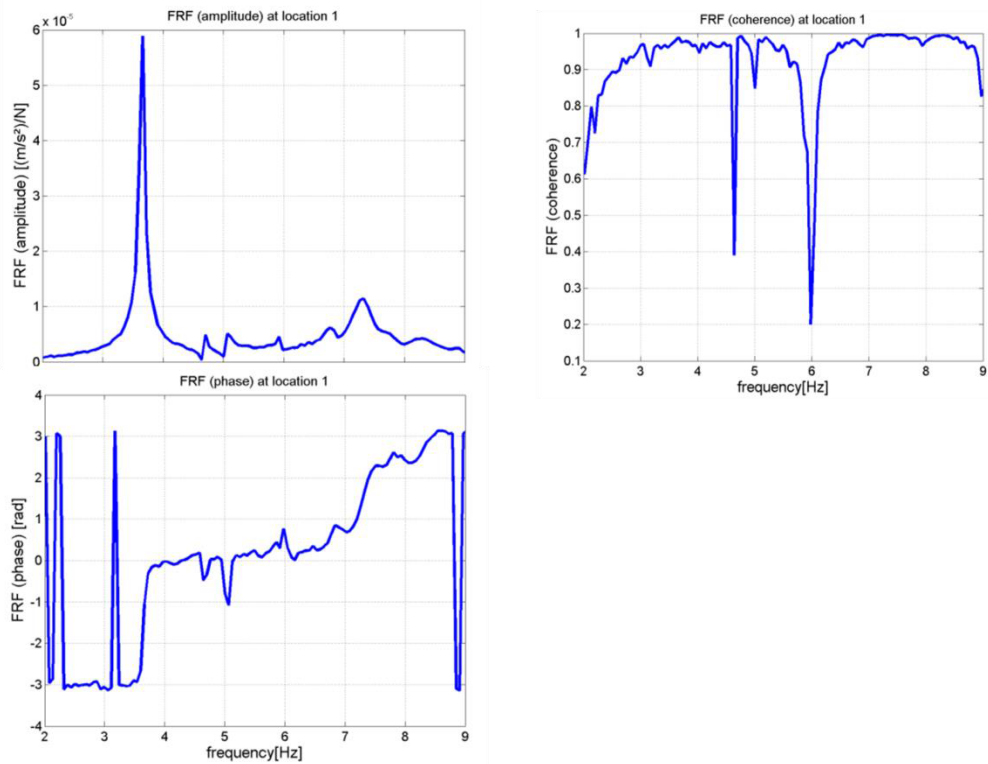


Figure 5 Typical frequency response function

The presence of resonance is confirmed by the phase graph which clearly shows a phase shift of  $\pi$  radians. Such a phase shift is in line with theory. Finally attention must be drawn to the coherence graph which is used to verify the quality of the measured FRF. Values above 0.9 indicate a real correlation between impact and response, which is clearly the case at the resonance frequency. Values below this figure should be mistrusted.

### 2.3 Mode Shape

These FRF graphs are available for each measuring location. Plotting the response values, with regard of the phase, along the length of the boat, yields a curve as shown in Figure 5, which is the vibration mode associated with 3.6 Hz.

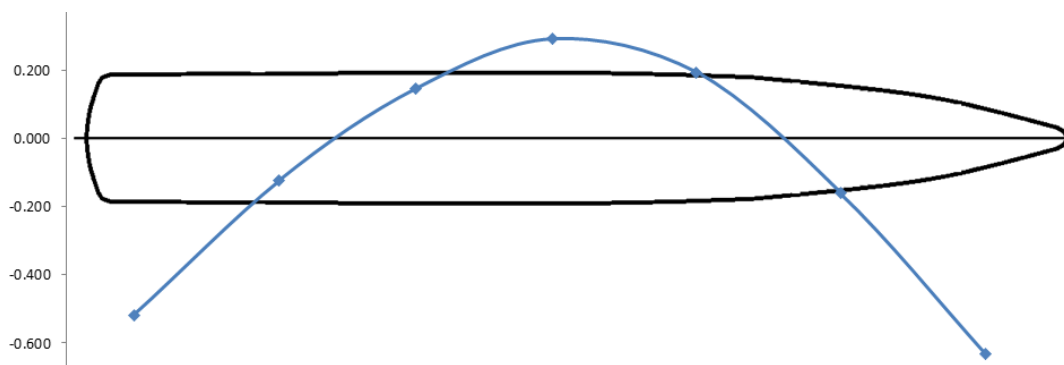


Figure 6 Vertical 2-node vibration mode at around 3.6 Hz

### 2.4 Damping

An FRF as shown in Figure 5 is also required for determining the actual structural damping, which is crucial for the choice of the TMD characteristics. In this particular example a damping is observed of (only) 1% of the critical damping of the system. Please note Figure 2 which shows the dynamic amplification of a mass spring damper system in case of damping equal to 1% of critical damping. The amplification amount to up to 50!



## 2.5 Effective mass

Another extremely important parameter is the effective mass associated with the given vibration mode. It actually depends on the planned location of the TMD. In order to explain this it is convenient to consider a mechanical system as shown in Figure 7. It shows a hinged beam with a mass  $M$ . The beam is infinitely stiff. The vibration mechanism is a pivoting motion of the beam about the hinge where the spring is compressed/ extended. If no other additional masses are present, the mass which the spring ‘experiences’ is only half of the mass of the beam, i.e.  $M/2$ . So the effective mass associated with the beam with mass  $M$  and the pivoting vibration mode equals  $M/2$  when it is considered located right above the spring (solid box in figure). If a TMD were to be fitted at this location, the main mass  $M_1$  (Figure 1) would be this mass. The effective mass would double if it were located at mid span of the beam (dashed box). A further shift towards the hinge would shift the effective mass towards infinite.

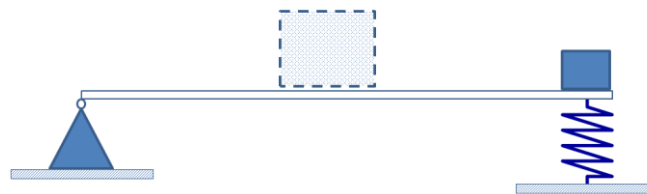


Figure 7 Explaining effective mass

A similar effect is pertinent to the 2-node horizontal vibration mode, as depicted in Figure 8. It shows that the effective mass associated with this vibration mode would be about 10000 tonnes when the mass is considered to be located amidships. If the reference mass is considered to be located at 90% of  $L_{pp}$  forward of the transom, the effective mass reduces to 2600 tonnes.

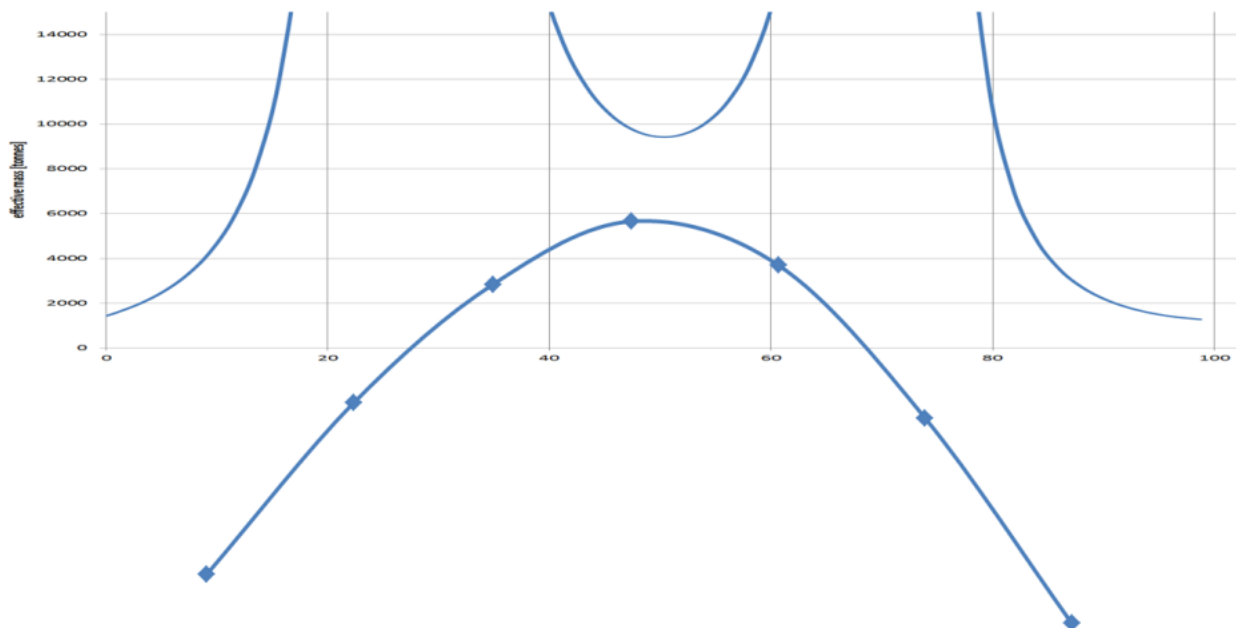


Figure 8 Effective mass as function of longitudinal location and mode shape

This results shows the importance of the location of the TMD in the boat. Apparently a location in the forepeak or near the transom is most attractive because the main mass  $M_1$  is the smallest. Hence fitting a TMD at one of these locations will prove to be most effective.

## 3. CHOICE OF TMD PROPERTIES

Once having determined the mechanical characteristics of the boat at 4.6 Hz, a TMD can be designed. The effective mass i.e. the main mass  $M_1$ , equals 2600 tonnes, while the structural damping lies at 1 % of critical damping. A very basic, but

valid, calculation model is the single mass spring system. Since effective mass and frequency are known, a spring stiffness can be calculated. Also because the damping is known, a damping coefficient can be calculated.

$$K_1 = M_1 (f_0 2\pi)^2 \tag{1}$$

$$C_c = 2\sqrt{K_1 M_1} \tag{2}$$

With :  $M_1$  main mass [kg],  
 $K_1$  stiffness [N/m],  
 $f_0$  natural frequency [Hz],  
 $C_c$  critical damping [N/m/s].

Having calculated these values a theoretical frequency response function can be calculated as shown in Figure 10 with the green curve (maximum dynamic amplification factor equal to 50). Consecutively a TMD mass ( $M_2$  in Figure 1) is to be chosen. Which means determining TMD mass and damping. The frequency of the TMD is already known; it must be tuned to (almost) the natural frequency of the boat. Due to space constraints on board, as shown in Figure 9, a mass of 2600 kg is considered feasible.

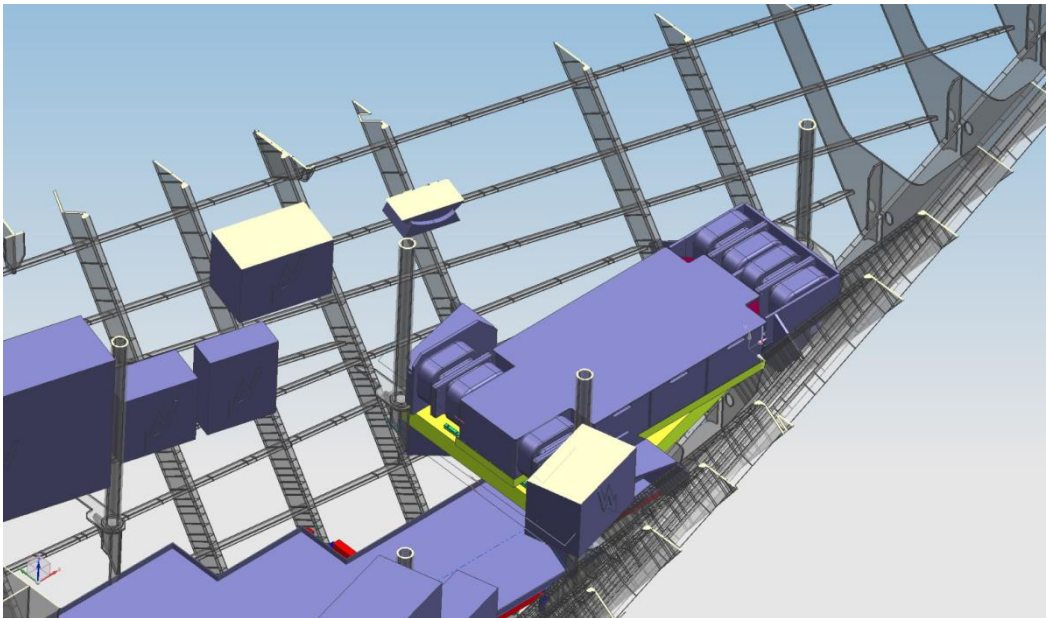


Figure 9 TMD in forepeak

When the TMD stiffness  $K_2$  is tuned toward a natural frequency of 3.6 Hz and the damping is adjusted to 2 % of critical damping (of the TMD), a theoretical analysis gives the result as shown in Figure 10., the curve with two maxima (red).

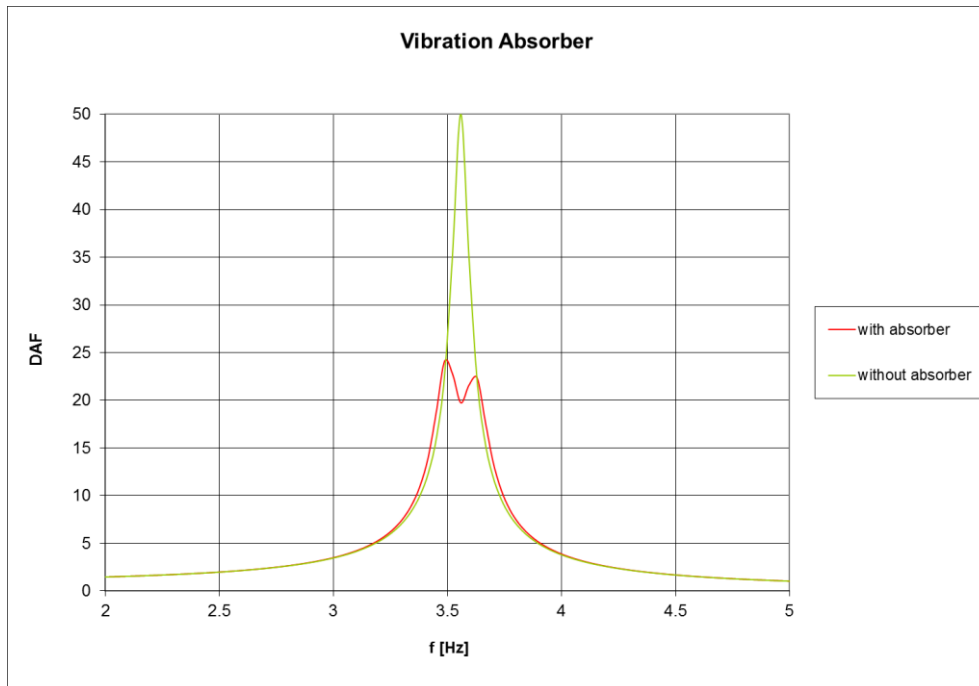


Figure 10 Dynamic amplification 2-node horizontal vibration, without and with absorber

As can be seen the amplification factor reduces by a factor of two, which implies an equal vibration level reduction. However the TMD must be tuned rather accurately to the natural frequency of the boat, which is illustrated in Figure 11.

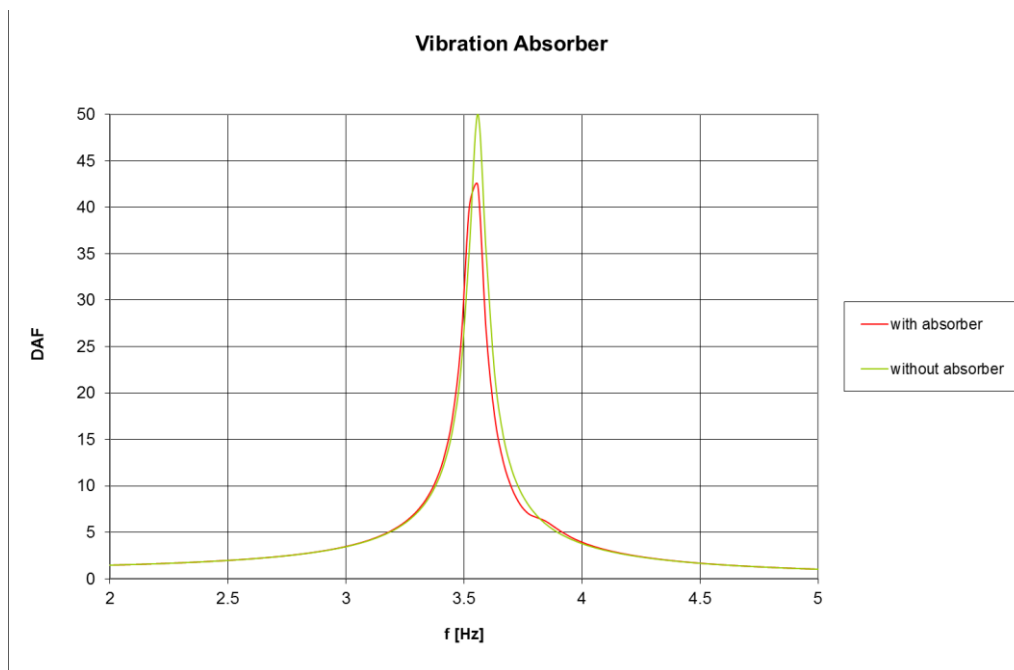


Figure 11 Dynamic amplification 2-node horizontal vibration, without and with absorber 0.20 Hz above target

The effect of the absorber is shown when the TMD is tuned 0.20 Hz off target. The reduction is then 16% only. It is also interesting to consider the dynamic response of the boat and the TMD in the time domain. When the boat (main mass) and the TMD are excited manually, a time trace as shown in Figure 12 is predicted. While being located inside the ship it is possible to excite the TMD manually. Obviously when the TMD is excited by a force, the reaction force excites the boat as well.

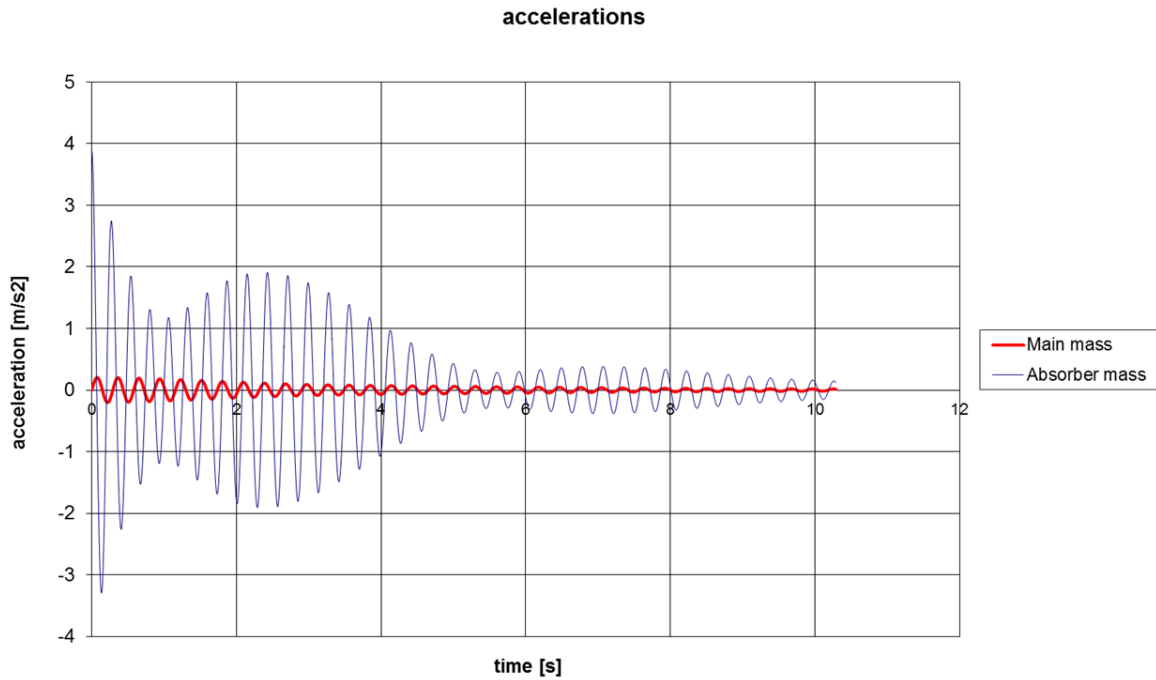


Figure 12 predicted acceleration time traces, boat and TMD, manual excitation

As can be seen, the TMD and the boat clearly interact.

Based on these findings, it was decided to install a 2600 kg TMD in the fo'c'sle. Since the boat is already operational, the device had to be assembled on board, which required the components to be appropriate for man-handling.

The building blocks which are assembled and which are to be loaded with lead ingots, are shown in Figure 13. One of the four spring assemblies is shown in Figure 14, together with an air cylinder which acts as damping element.



Figure 13 TMD building blocks



Figure 14 TMD, one of the four spring assemblies and damper

The assembly mounted in the boat is shown in Figure 9.

#### 4. PRELIMINARY RESULTS

Although the fine-tuning of the TMD has not been finalised, already some positive effect is reported by the crew. Moreover a short time slot was available for sea trials which gave the opportunity to sail the boat in a moderate breeze with approximate wave heights of 1 m ( $H_{1/3}$ ). Vibration response spectra could be measured, averaged over 120 seconds measuring time. Results are observed for the TMD blocked and operational, as shown in Figure 15 and Figure 16 respectively. It can be seen that when the TMD is active the vibration level on the boat reduces from 2.5 mg to 2.0 mg, i.e. a reduction of 20%. This is in accordance with the predicted reduction of the amplification factor in case of the TMD being tuned slightly off target (Figure 11). Once the TMD is fully tuned, a reduction of 50% is expected.

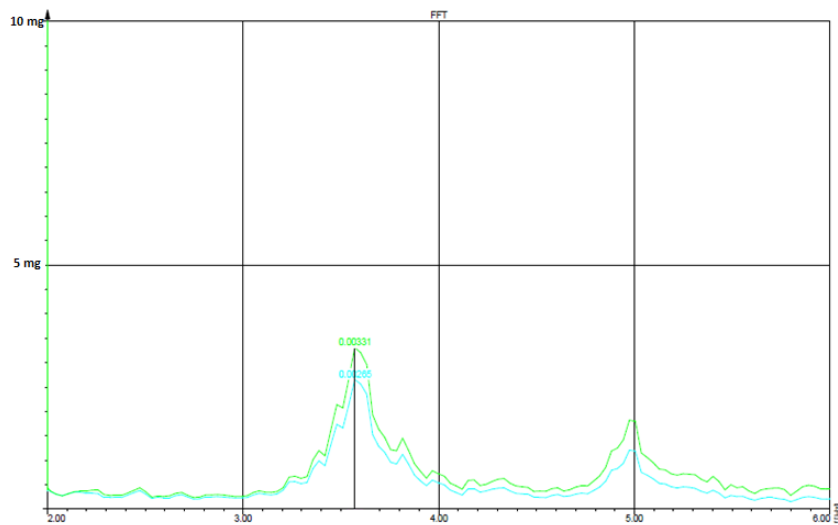


Figure 15 Measured response level, TMD blocked

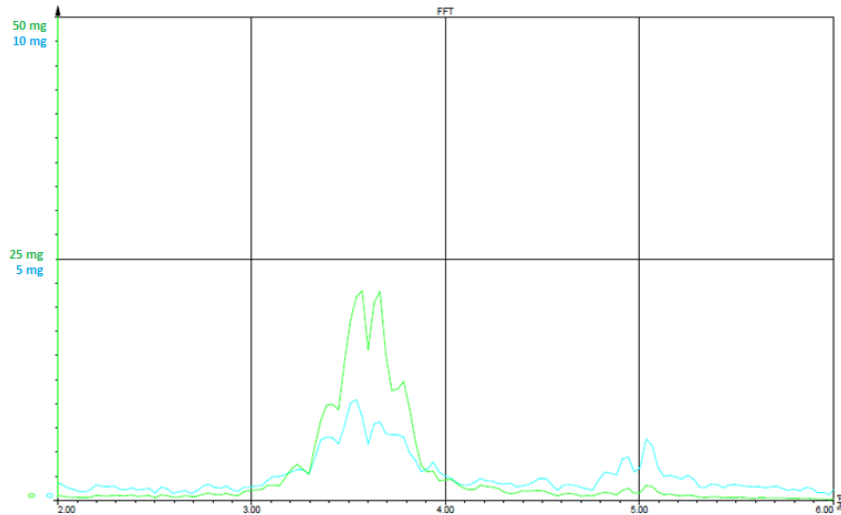


Figure 16 Measured response level, TMD active

In order to verify the proper working of the TMD, manual excitation in harbour has also been conducted. Figure 17 shows the result. The blue line shows the acceleration of the boat at the fo’c’sle, while the green line shows the acceleration of the TMD. The predicted interaction between TMD and boat is clearly visible. The results is in accordance with the prediction (Figure 12).

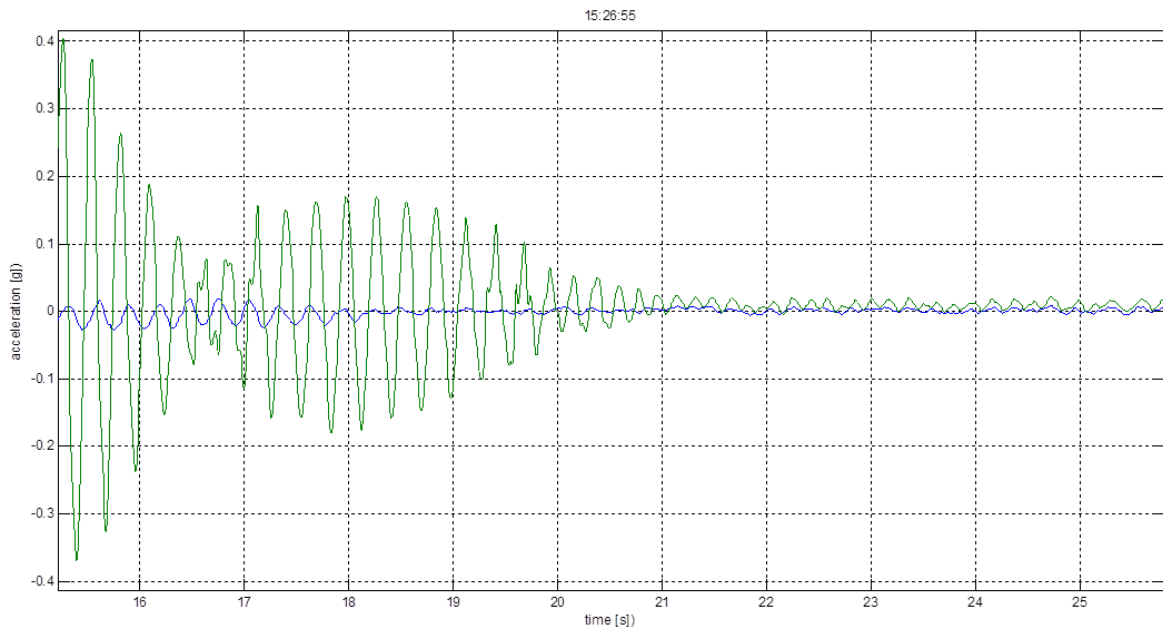


Figure 17 measured acceleration time trace, TMD-boat manually excited

## 5. DISCUSSION

Compared to the conventional use of TMD’s, the mass ratio between TMD mass and main mass is rather low. This is clearly a trade-off between effect of the system on vibration reduction and practicalities associated with fitting a deadweight conveniently somewhere in a ship structure. In the case of the slender yacht a mass of 2.6 tonnes was considered the maximum feasible (Figure 9). There are however two consequences;

1. the effectiveness of the TMD becomes very sensitive to proper tuning of its natural frequency,
2. the effect of the TMD reduces with a decreasing TMD mass.

In the other way round, a change of the natural frequency of the boat, e.g. due to a changing loading condition, causes a mismatch of natural frequency of the boat and the TMD and hence a reduction of the TMD's effectiveness. When a natural frequency shift due to loading conditions, of more than 0.5 Hz is expected, a TMD which can be tuned by the crew, must be considered.

As can be seen in Figure 10, the frequency range of interest lies well within a span of 1.0 Hz. This implies that the frequency resolution during measurements must be better than say 0.03 Hz. This is much higher than the usual resolution, often only 0.6 Hz. This requirement causes long measuring times, i.e. minutes rather than seconds.

## **6. CONCLUSIONS AND RECOMMENDATIONS**

The main conclusion is that a TMD can be effective for reducing resonance related vibration on board a boat.

Even an unusual low ratio between TMD mass and main mass (effective mass) of say 1/1000 can still yield satisfactory results, however the correct tuning of the TMD becomes even more important than it already is in case of conventional ratios ( $>1/100$ ).

Proper frequency tuning is crucial to the success of a TMD.

It is important to determine the relevant vibration mode shape and damping experimentally.

## **REFERENCES**

- Hartog Den J.P., Mechanical Vibrations, Courier Publications, January 1<sup>st</sup> 1985 (first published in 1934)
- Todd F.H., Ship Hull Vibration, Edward Arnold Publishers, first edition (1961), ISBN-10: 0713131489

# GLASS AS A LOAD BEARING MATERIAL IN YACHT STRUCTURES

K. M. Jansen BEng, Feadship, the Netherlands

## 1. INTRODUCTION

The use of glass on board of Feadship yachts has increased significantly in the past 50 years and it is expected to increase even more in the future. Glass enables more light and sight at the inside and from the outside it gives the yacht a modern impression. However, glass adds a lot to the ship's weight without contributing to the stiffness of the vessel.

In the building construction sector, glass has already been used as a load bearing material. In the shipbuilding sector this has not been done yet as the dynamic loads coming from the ship's motions make it more complicated to calculate the response of the glass application. Also the material properties of glass are a significant obstacle. Metal has a crystalline structure, this means that the atoms can move relative to each other without breaking the bonds. Therefore metal can deform plastically. Glass has an amorphous structure, so it cannot deform plastically. This makes a construction with glass much less forgiving.

Due to the movements of the vessel the loads on a yacht will be different than on a building. A yacht is loaded locally by the weight of the superstructure and the onboard equipment and globally by the ship's deformations as a result of wind and water forces on the yacht. In order to use glass as a load bearing material a connection system between the glass and the rest of the vessel's structure needs to be able to transfer these loads.

In 2011 de Voogt naval architects conducted a research 'stiffness through glass' on the use of glass as a load bearing material on yachts in order to indicate the possibilities and effects of structural glass on yachts, Mendes de Léon (2011). A connection system between the glass and the hull was designed and tested to determine the strength criteria of it. These tests were done with normal float glass, as testing with laminated toughened glass was too expensive and time consuming. Float glass is 'normal' glass that is used in everyday applications. Toughened glass is approximately 3 to 4 times stronger because of a pre-stress in the glass.

This research showed that it could be possible to use glass to increase the stiffness of the vessel. However, at specific locations in the ship's structure, the glass panels have to become very thick in order to fulfill the strength criteria. This will most likely result in an increased ship's weight. Therefore in 2013, Feadship decided to conduct another research on a realistic, local, first application of load-bearing glass using toughened glass as a test material.

### 1.1 Research goal

This project is a sequel to the research conducted by Feadship in 2011 and has the purpose to investigate the realistic design possibilities of load bearing glass on board yachts. Included in the end result will be a first application with which the structural use can be shown to parties within Feadship and to possible clients.

This paper shows the steps taken to reach this research goal.

- Chapter 2 summarizes a literature review on the properties of glass. The different ways to improve the mechanical behavior of glass are investigated.
- Chapter 3 determines the location for the first application of load-bearing glass together with the loads that act on this location.
- Chapter 4 calculates the required glass thickness with hand calculations and FE-models.
- Chapter 5 describes the experimental investigations that were supported by glass manufacturer Seele and were conducted at the University of München. The results of the tests are used to validate the hand calculations and FE-models.
- Chapter 6 lists the current regulations on glass and the aspects that need to be considered when using glass as a structural material.
- Chapter 7 specifies the changes needed in the construction and building process of the yacht when using load bearing glass instead of 'normal' glass in order to determine if the load bearing glass application is realistic or not.

## 2. GLASS PROPERTIES

Glass is an amorphous material, it consists of an irregular network of silicon and oxygen atoms with alkaline parts in between. It is a homogeneous and isotropic material with linear elastic material behavior that fails with a brittle fracture in case of overload.

The most common used type of glass is soda-lime silicate glass, this is used for centuries to produce glazing. Borosilicate glass is often used in special applications such as fire protection, as it is well resistant to alternating temperatures. A sheet of glass is made by floating liquid glass of 1100 °C in a bath of molten metal, this will flow out of the melting batch and solidifies at approximately 600 °C. Usually tin or another low melting point alloy is used, tin has a higher specific weight than glass, so the glass floats on the tin. The glass sheet will have a uniform thickness and very flat surfaces. This is called



the float glass process and was invented in 1950 by Alastair Pilkington. Without further treatment glass made with this process is called annealed glass, Schittich (2007).

### 2.1 Mechanical properties of glass

The theoretical tensile strength of glass is due to molecular bonding forces and is about 20.000 MPa, Pankhardt (2010). However, the practical tensile strength of glass depends on randomly located surface flaws. The degree and the size of the damage of the surface, as well as the duration of loading and environmental conditions are of influence. The Griffith crack theory proposes that tiny flaws result in stress peaks in the glass, Maniatis (2005). As soon as this stress peak reaches the critical value the glass element will fail instantaneous. Therefore the practical tensile strength is much less than the theoretical strength (about 100 MPa). When this stress peak is below the critical value the crack will grow very slowly. Glass under a continuous tensile load has a significantly lower strength.

Under compressive stress the flaws are compressed and no stress peaks will occur. Hence the compressive strength of glass is quite high (about 800 MPa).

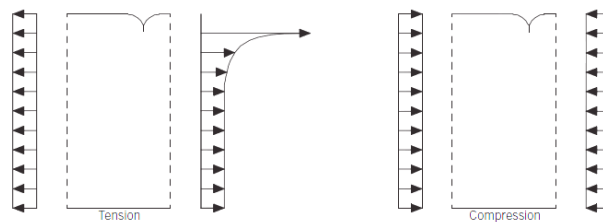


Figure 1: stress distribution around flaw, Wurm (2007)

### 2.2 Pre-stressed glass

During the post-processing phase, glass with different properties can be manufactured. By introducing a certain pre-stress in the material, any high tensile stresses will be counteracted.

#### Fully tempered glass

When the annealed glass is heated to 650 °C and subsequently cooled rapidly, a residual stress is induced which places the outer surface in compression and the core in tension. This is called fully tempered or toughened glass. An applied tension stress will have to overcome this compression before the flaws can cause failure. Another benefit of this treatment is that the glass breaks into small harmless pieces if failure does occur, therefore it is also called safety glass, Fröling (2011). According to ISO 11336, ISO (2012), the characteristic failure strength of fully tempered glass is 160 N/mm<sup>2</sup>.

#### Heat strengthened glass

Heat strengthened glass is produced similarly as fully tempered glass. The glass is cooled more slowly from the same initial temperature and the internal stresses are less. This is therefore also called partial tempered glass. The characteristic failure strength depends on the rate of cooling, and will be approximately half the strength of fully tempered glass. The fragments are larger than for toughened glass, Fröling (2011).

#### Chemically strengthened glass

Higher resistance against mechanical and thermal stress is achieved by ion exchange. The glass sheet is immersed in a chloride bath where the small sodium ions from the surface of the glass are exchanged with the larger chloride ions. Hence the structure is expanded in the surface layer which causes a compression, Wurm (2007). The characteristic failure strength of chemically strengthened glass is 160 N/mm<sup>2</sup>, ISO (2012).

As shown in figure 2, the compressive stress layer in the chemical pre-stressed glass is much thinner, it will therefore be more sensitive for surface damages compared to thermal strengthened glass.

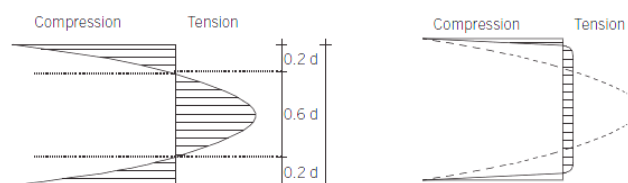


Figure 2: Stress cross-sectional diagram of fully tempered glass (left) and chemically strengthened glass (right), Wurm (2007)

The distribution of pre-stress in glass panels is not constant. The stress distributions shown in figure 2, Wurm (2007), can only be created when the panel was cooled from two sides. At the edges the surface cools down on three sides, hence the entire edge surface will be compressed. The influence of the edge reaches to a depth of 1 to 2 times the glass thickness. This is shown in figure 3. The corners of a panel even cool down on four sides, therefore the influence of a corner is even more. The strength of the glass around edges and corners is less as there are possible surface damages or micro cracks that occurred during the manufacturing.

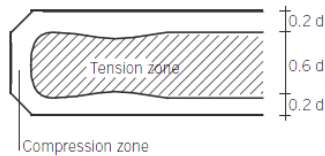


Figure 3: compression and tension zones in edges, Wurm (2007)

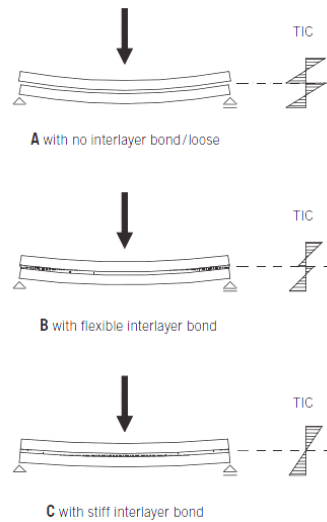


Figure 4: stress distribution in laminated glass , Wurm (2007)

### 2.3 Laminated glass

Laminated glass consists of at least two glass panels bonded by interlayers and provides opportunities to modify the mechanical and optical properties and thickness of the glass construction. Glass is produced in standard thicknesses ranging from 2 – 22 mm. When thicker windows are required to sustain a normal load it is more practical to attach two standardized panels. Laminated glass remains in one piece when one glass layer fails, keeping the system watertight.

Two materials often used for the interlayers are polyvinylbutyral (PVB) and SentryGlass Plus (SGP). Both materials are viscoelastic thermoplastics, the shear modulus is dependent on the ambient temperature and the load duration. PVB is a flexible material, hence the stress distribution will be as shown in figure 4b. The stiffness of a SGP interlayer is up to 100 times higher than that of PVB. The stress distribution will therefore be almost uniform, which makes it better resistant against forces perpendicular to the window surface.

The elasticity is also a difference between the two interlayer materials. When one glass panel breaks it is likely that another panel connected with SGP breaks as well, as broken glass takes up more space and will initiate a tension stress in the other glass layer. If the interlayer is of PVB, the elasticity of this material will absorb these stresses. In this project a few tests with full scale glass panels with SGP interlayer were done. Breakage of one layer did not initiate failure of the adjacent glass layers. Once all panels are broken, the residual load bearing capacity depends on the fracture pattern of the glass.

Annealed or chemically strengthened glass breaks into big pieces, so a bit of integrity is remained. Thermally strengthened glass (safety glass) will scatter into very small pieces, so the laminate will not have any strength left at all. However, in both cases the system will remain watertight.

Another possibility is laminated glass made from glass and polycarbonate (PC). This consists of a PC sheet as the core with thin heat or chemically treated glass sheets on the outside faces, Wurm (2007). An advantage of plastics is that they have a yield criterion and are therefore safer to use. However, plastics do not have a natural look like glass has, and plastics become pale because of scratches at the surface.

### 3. LOCATION OF THE FIRST LOAD-BEARING APPLICATION OF GLASS

As an example, the wheelhouse windows of a 45-metre Feadship were designed to be load-bearing. A bridge without mullions would be very beneficial, as the view of the captain is high priority of the regulatory bodies. Feadship has already done quite some research in reducing the area of the mullions, but leaving them out completely would be ideal.



Figure 5: Photograph of F45

### 3.1 Design loads at the wheelhouse

The wheelhouse of the F45 consists of nine separate windows of width 1150 mm and height 978 mm. According to ISO 11336, ISO (2012), the normal load on the windows can be calculated with:

$$p_D = 10.05 \cdot a \cdot k_s \cdot (b \cdot f - h) \cdot c \quad (1)$$

With:

a	=	1.33	-	factor relating to location and vessel length
$K_s$	=	1	-	service factor
b	=	1.26	-	factor based on longitudinal location
f	=	2.27	-	factor based on vessel length
h	=	6.735	m	height of centre of window from dsw
c	=	0.85	-	given constant

This gives a very small value for the design pressure. However, the design pressure is not to be less than 30 kN/m<sup>2</sup> for front positions on the uppermost deck of ships less than 50 m of length.

The deck load is calculated according to the Lloyd's Rules for Special Service Crafts, Lloyd's Register (2010), and causes a compressive force of 29.3 kN per window.

The pressure acting on weather decks,  $P_{wh}$ , is determined with:

$$P_{wh} = f_L(6 + 0.01L_{wl})(1 + 0.05\Gamma) + E \quad (2)$$

Where:

$f_l$	=	1.0	-	location factor
$L_{wl}$	=	38.65	m	length waterline
$\Gamma$	=	2.28	-	Taylor Quotient = $\frac{v}{L_{wl}^{0.5}}$
v	=	14.20	kn.	allowable speed
E	=	2.30	kN/m <sup>2</sup>	(0.07+0.08Lwl)/(D-T) but not greater than 3 kN/m <sup>2</sup>
D	=	4.55	m	depth
T	=	2.90	m	scantling draught

The pressure on the deck is 9.4 kN/m<sup>2</sup>.

The area of the deck above the load bearing glass is 28 m<sup>2</sup>, so the total force on the glass is approximately 265 kN. With nine separate windows this concludes in a force of 29.3 kN per window.

## 4. DETERMINATION OF GLASS THICKNESS

As the properties of glass are better in compression than under tension loads, the windows are subject to a constant compression force. Each glass panel is loaded with a combined in- and out-of-plane load, due to the deck load and the design pressure on the window. The buckling of the glass in combination with the normal load needs to be analysed in order to determine the glass thickness of the panel. A simplified calculation is done by hand and this is checked with non-linear FEM analysis.

### 4.1 Load assumptions

As determined in section 3.1 the normal load on the window is 30 kN/m<sup>2</sup>. The compressive load due to the deckload is 29.3 kN per window. Also the extra compressive force that prevents tension in the glass needs to be taken into account. Therefore the compressive force on each window is 39.3 kN.

The laminate consists of 3 x 10 mm fully tempered glass with a SentryGlass interlayer of 1.52 mm. According to ISO 11336 the design flexural stress of fully tempered glass is 40 N/mm<sup>2</sup>. As the characteristic failure strength is 160 N/mm<sup>2</sup> a design factor of 4 is taken into account. In building industry the allowable tensile strength is 50 N/mm<sup>2</sup>.

## 4.2 Hand calculations

The hand calculation is done according to Luible (2004), Blauwendraad (2007) and Shama (2013). In order to keep the calculation simple, the laminate is considered as a monolithic glass pane of 30 mm thick. This neglects the shear in the interlayer.

The total deflection of the glass panel depends on the initial deflection of the panel due to imperfections, the deflection caused by the normal load and an extra deflection due to the buckling effect. The total deflection can be calculated with:

$$y_t = \frac{y_0 + y_n}{1 - \frac{P}{P_E}} \quad (4)$$

Where:

$y_0$	=	2.445	mm	initial deflection due to imperfections = $\frac{h}{400}$ , this is a standard value used for imperfections in glass panels.
$h$	=	978	mm	height of window
$y_n$	=	2.27	mm	deflection due to normal load = $\frac{5qh^4}{384EI}$
$q$	=	34.5	kN/m	Distributed load over complete width = $P_D * b$
$P_D$	=	30	kN/m <sup>2</sup>	Normal load (according to section 3.1)
$b$	=	1150	mm	width of window
$E$	=	70000	N/mm <sup>2</sup>	Youngs-modulus of glass
$I$	=	25.875	$\times 10^5$ mm <sup>4</sup>	moment of inertia = $\frac{1}{12} b t^3$
$t$	=	30	mm	glass thickness
$P$	=	39.29	kN	compressive force per window
$P_E$	=	1868.96	kN	critical buckling load according to Euler = $\frac{\pi^2 EI}{h^2}$

The total deflection can therefore be calculated as 4.82 mm under the design loads.

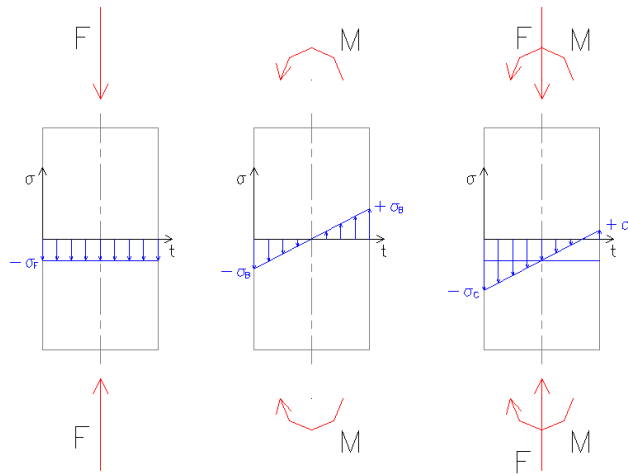


Figure 6: Stresses over the glass thickness

The stress in the glass is caused by the bending of the panel and the compressive force, see figure 6.

$$\sigma = -\frac{P}{A} + \frac{M \cdot d}{I} \quad (5)$$

Where:

$A$	=	34500	mm <sup>2</sup>	area of the cross section = $t * b$
$M$	=	4314.03	Nm	moment = $P y_t + \frac{q h^2}{8}$
$d$	=	15	mm	Distance from neutral axis = $t/2$

The stress in the glass will be 23.9 N/mm<sup>2</sup>.

In this calculation the initial deflection due to imperfections only cause an extra deflection due to the buckling effect. This deflection does not cause any stresses in the glass panel.

### 4.3 Simplified monolithic glass FE-model

A simple numerical model was made with ANSYS 10 to validate the simplified hand calculations and the non-linear analysis method within ANSYS.

#### *Construction of the model*

The full-size glass panel numerical model is shown in figure 7 . The glass thickness is 30 mm.

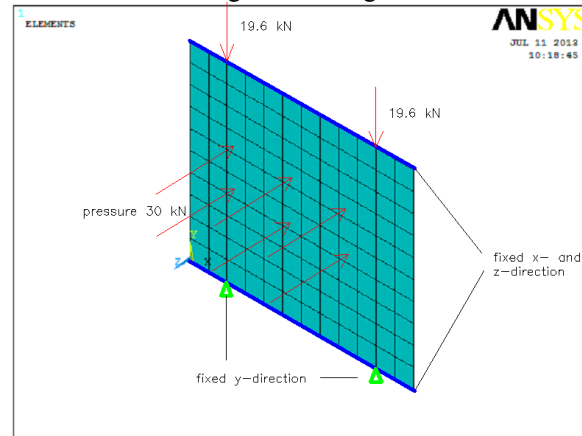


Figure 7: Monolithic glass panel FE-model

#### *Element type*

SHELL93 element was used to model the glass panel. This element has eight nodes with six degrees of freedom at each node. Translation in x, y and z directions and rotations around the x, y and z-axes. SHELL93 elements have large deflection capabilities.

#### *Material properties*

For the glass a linear isotropic material model is used, with E-modulus  $70000 \text{ N/mm}^2$  and Poisson's ratio 0.22.

#### *Meshing of the model*

A mesh size of 100 mm is used for the calculation. After refining the mesh several times, the results did not alter at this element size.

#### *Boundary conditions*

The upper and lower edge are restricted in the x- and z-direction. The connection with the frame is simulated as two point supports and is fixed in y-direction.

#### *Load introduction*

The initial deflection of 2.445 mm is simulated by applying an extra normal load of  $31 \text{ kN/m}^2$  on the surface. Simulating the initial deflection like this keeps the model very simple. Hence a total pressure  $61 \text{ kN/m}^2$  is applied on the surface. The compressive force of 39.3 kN is applied as two concentrated forces on the nodes 200 mm from the edges.

#### *Solution procedure*

A geometric nonlinear analysis can be calculated in ansys with the large displacement static option in the analysis type menu. ANSYS uses the Newton-Raphson algorithm, where the load is applied gradually in a number of substeps, Cook (2001).

#### *Results*

Figure 8 shows the total deformation of the glass panel. This deformation is 4.96 mm. Figure 9 shows the corresponding stresses in y-direction in the glass. The maximum stress occurs at the location of the maximum deflection and is a tension stress of  $51.3 \text{ kN/m}^2$ . This is more than the results of the simplified hand calculations. In this FE-model the initial deflection, which is simulated with an extra normal load, causes stresses in the glass. When the initial deflection in the hand calculations is simulated in the same manner, a total normal load of  $61 \text{ kN/m}^2$ , the maximum stress will be  $48.6 \text{ kN/m}^2$ .

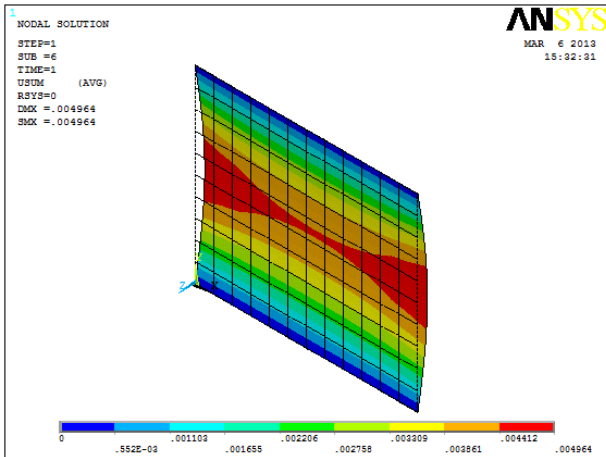


Figure 8: Monolithic glass panel FE-model; deformation

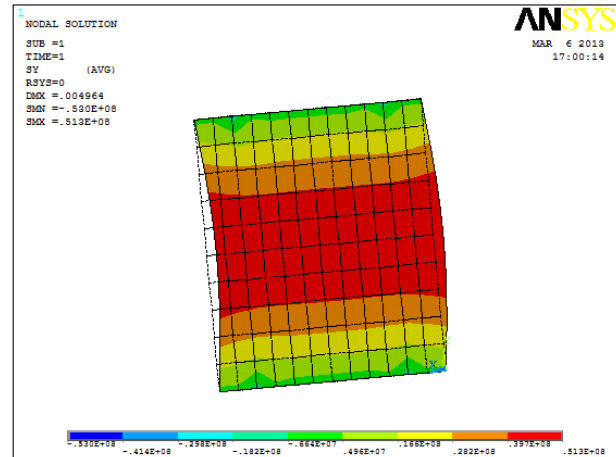


Figure 9: Monolithic glass panel FE-model; stresses in y direction

#### 4.4 Detailed layered glass FE-model

A more detailed numerical model was made with ANSYS 14. In this model the initial deflection does not cause any stresses and the different layers of the laminated are modeled.

##### *Construction of the model*

The initial deformation due to imperfections is simulated by shaping the glass panel as a part of a cylinder. The dimensions of the panel are as specified in 3.1, width 1150 mm and height 978 mm. In order to get an initial deflection of 2.445 mm the radius is 48.9 m and the angle  $0.58^\circ$ . Every layer of the laminate is modeled as a volume. These volumes are glued together with Booleans.

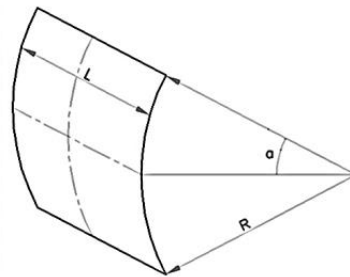


Figure 10: Construction of curved panel

##### *Element type*

SOLID186 elements are used to define the glass and SGP interlayer. This element type is defined by 20 nodes having three degrees of freedom per node: translations in the x, y and z directions. It has large deflection capabilities.

##### *Material properties*

The material model used for the glass is linear isotropic with E-modulus  $70000 \text{ N/mm}^2$  and poisson's ratio 0.22. For the SGP interlayer the properties used is a linear isotropic material model with E-modulus 283.4 MPa and Poisson's ratio 0.476.

##### *Meshing of the model*

In Ansys the length ratio of the element edges should not be less than 1:20 in order to get convenient results. The thickness of the SPG interlayer is 1.52 mm, consequently the maximum element length is 30 mm. A mesh size of 25 mm was used in order to be able to apply the loads and constraints easily.

##### *Boundary conditions*

The glass panel is assumed to be simply supported. The middle of the upper and lower edge of the panel are restricted in the x- and z-direction. The connection with the frame is simulated as two point supports and is fixed in y-direction.

##### *Load introduction*

A pressure of  $30 \text{ kN/m}^2$  is applied on the surface of the volume closest to the virtual center of the cylinder. The compressive force of 19.6 kN per setting block is applied as concentrated forces on the nodes 200 mm from the edges.

##### *Solution procedure*

To solve the nonlinear buckling analysis of the glass panel the same procedure as described in 4.3 was used.

## Results

Figure 11 shows the total deformation of the glass panel which is 2.17 mm. This is comparable to the deformation found in sections 4.2 and 4.3, as the deformation including the initial deflection is  $2.17 + 2.445 = 4.62$  mm. The deformation found with the simplified model is 4.96 mm and with the hand calculations 4.82 mm. It is remarkable however that the deformation found with the layered model is less than the monolithic model. According to chapter 2.3 figure 4 it should be the other way around. This difference can possibly be assigned finer mesh over the glass thickness and more detailed volume elements. In the simple FE-model only one shell element is used for the complete glass thickness.

Figure 12 shows the corresponding stresses in y-direction in the glass. The maximum stress occurs at the location of the maximum deflection and is a tension stress of  $28.5 \text{ kN/m}^2$ . This is less than the results found with the simple FE-model. This is because the initial deflection does not cause any stresses in this model. A high compressive force can be seen at the location where the loads are introduced. The force was modeled as a concentrated force, in reality this will be distributed over the contact area of the glass and frame. Therefore it can be expected that the local stresses will be slightly less and more distributed.

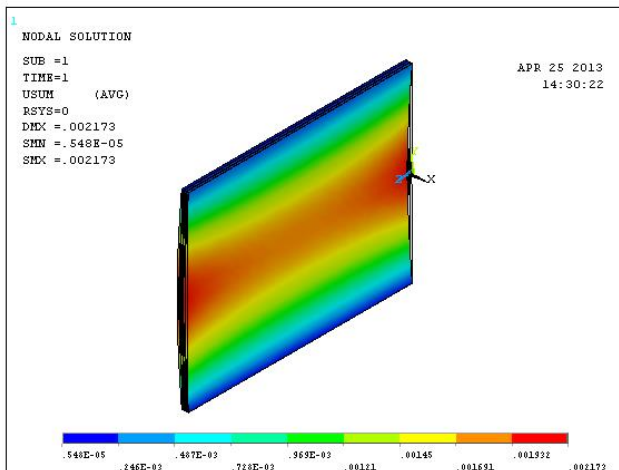


Figure 11: Laminated glass panel FE-model; deformation

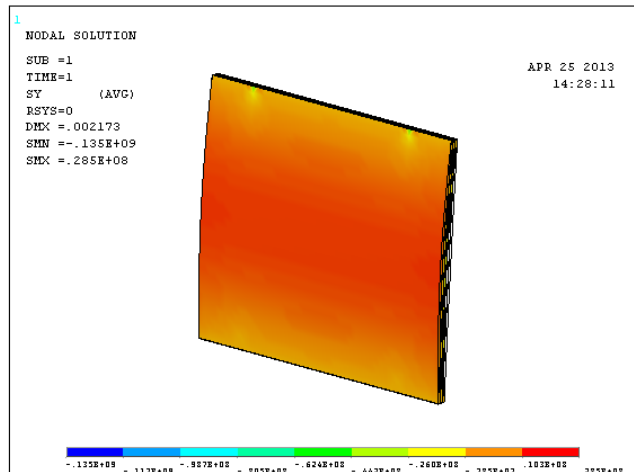


Figure 12: Laminated glass panel FE-model stresses y direction

## 5. Experimental investigation

This chapter contains the experimental investigations that were conducted at the University of München. The results of the tests are used to validate the hand calculations and FE-models.

### 5.1 Goal of the testing

By testing the glass panels of a wheelhouse we would like to achieve a gain in confidence in glass as a load bearing material. The ultimate goal is to be able to build a wheelhouse without mullions. In order to do that, the glass needs to be able to sustain the same loads as the construction would normally hold. Furthermore, the authorities need to be convinced that using glass as a load bearing material is a safe option on board yachts.

The global behavior of the full-size glass panel will be studied, focusing on the following points:

#### *Global deformation of the glass panel*

The deformation of the glass panel will be measured at specific points. This way the test results can be compared with the FE-models.

#### *Stress distribution in the glass panel*

By measuring the stress distribution over the glass panel, the location of the peak stresses can be determined. It would be interesting to see if the failure is initiated at the middle due to the bending stresses, or near the supports due to splitting tension. (Splitting tension: perpendicular to a high compression field Poisson's ratio causes tensile stresses, Mocibob (2008))

#### *Failure mode of the glass panel*

Two different failure modes can be expected:

- Failure cracks perpendicular to the applied compressive force as a result of the stresses caused by the out of plane deflection.
- Cracks in line with the compressive force as a result of splitting tension.

However, the failure mode will not show which stress initiated the failure. When one failure has occurred, other cracks will form due to the impact.

## 5.2 Specimen description

The specimen provided specifically for the tests by Seele consists of a glass panel with width 1150 mm and height 978 mm. The laminate consists of 3 x 10 mm fully tempered glass with a SentryGlass interlayer of 1.52 mm. Five identical specimen were tested under different conditions:

- T1 all plies intact
- T2 all plies intact and with strain gauges
- T3 upper layer (exterior side) broken
- T4a all plies intact
- T4b\* lower layer (interior side) broken
- T5 upper layer (exterior side) broken

\* As only the lower layer broke of the fourth specimen, this panel was tested again.

The design normal load of 30 kN/m<sup>2</sup> concludes in a vertical force of 30 kN/m<sup>2</sup> x 1.15 m x 0.978 m = 34 kN. The dead load of the load introduction frame is 1.7 kN. The applied vertical design force V is therefore 34 kN – 1.7 kN = **32.3** kN.

The horizontal load H is **39.2** kN, simulating the compressive force on the window as calculated in chapter 4.

For all specimen the initial deflection due to imperfections is measured first. In addition the temperature of the specimen was determined.

Every panel was subjected to two tests. For the first test the panel was firstly loaded with the horizontal load H and then with the vertical load V. The horizontal load was then increased up to 3 or 4 times H with steps as shown in table 2.

For the second test the panel was also loaded with first the horizontal and then the vertical load. Both loads were increased with steps as shown in table 3. Until breakage of one or more layers.

Table 1: Load steps test 01

Test 01		
load step	H [kN]	V [kN]
1	39.2	0.0
2	39.2	32.3
3	57.6	32.3
4	77.2	32.3
5	96.8	32.3
6	116.4	32.3
7*	136.0	32.3
8*	155.0	32.3
9	0.0	0.0

\* Specimen 1,4 and 5

Table 2: Load steps test 02

Test 02		
load step	H [kN]	V [kN]
1	39.2	0.0
2	39.2	32.3
3	57.6	48.4
4	77.2	48.4
5	77.2	64.6
6	96.8	64.6
7	116.4	64.6
8	136.0	64.6
9	155.0	64.6
10	96.8	64.6
11	96.8	80.8
12	116.4	80.8
13	136.0	80.8
14	155.0	80.8
15	116.4	80.8
16	116.4	97.0
17	136.0	97.0
18	155.0	97.0
19	136.0	97.0
20	136.0	114.0
21	155.0	114.0
22	155.0	130.0
23	0.0	0.0

## 5.3 Testing frame and load introduction devices

A special testing frame that allows the application of a combined normal and compressive load was designed. The glass will be installed vertically on board of the yacht. However, the panel will be tested horizontally in order to apply the normal load in a convenient manner and to avoid glass pieces to fall down from a large distance in case of failure of the panel.

The frame consists of two steel profiles connected with four hydraulic jacks, two on each side, that apply the in plane force H. The horizontal load was regulated manually. The glass is placed in this frame by means of four supports. The distributed normal load is simulated with two loads applied over the total width. It is general practice to simulate a distributed load with a four point bending test. The vertical load V was applied by a force controlled load jack, which keeps the load constant on a given value. A slight deformation can therefore cause a fluctuation in the applied vertical force, this is corrected automatically by the jack, but may take some time.



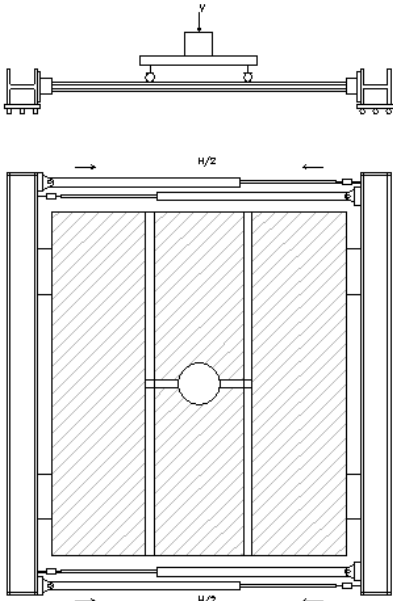


Figure 13: Test setup

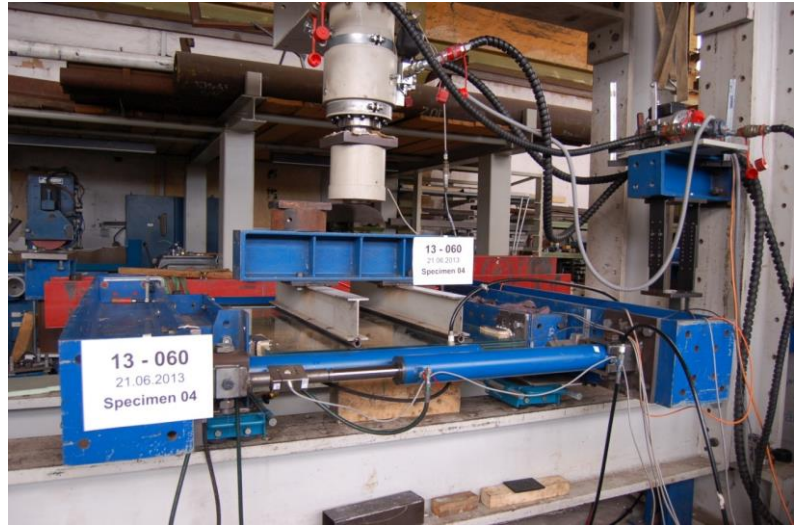


Figure 14: Testing frame

### 5.4 Test set-up and test instrumentation

The force introduction is measured with load cells located on the hydraulic jacks. Three displacement transducers constantly measure the out of plane deformation of the glass panel. The location of these displacement transducers are shown in figure 15. The out of plane deflection of the panel can be determined by taking the difference between SV2 and the average value of SV1 and SV3.

$$W = SV2 - \frac{SV1 + SV3}{2} \quad (6)$$

The transducers SV1 and SV3 were needed to ensure that a bending of the complete steel frame would not cause an inaccuracy in the measurement of the deflection. The deflection of the first specimen was only measured with transducer SV2.

The in-plane deformation is measured on both sides of the glass panel with transducers SH1 and SH2.

Additional to the measurement of the forces and displacements of the panels, the strains/stresses on the glass surface of specimen 2 were measured. The position of the strain gauges are shown in figure 15. 10 strain gauges were placed, 7 gauges on the bottom and 3 on the top side of the panel.

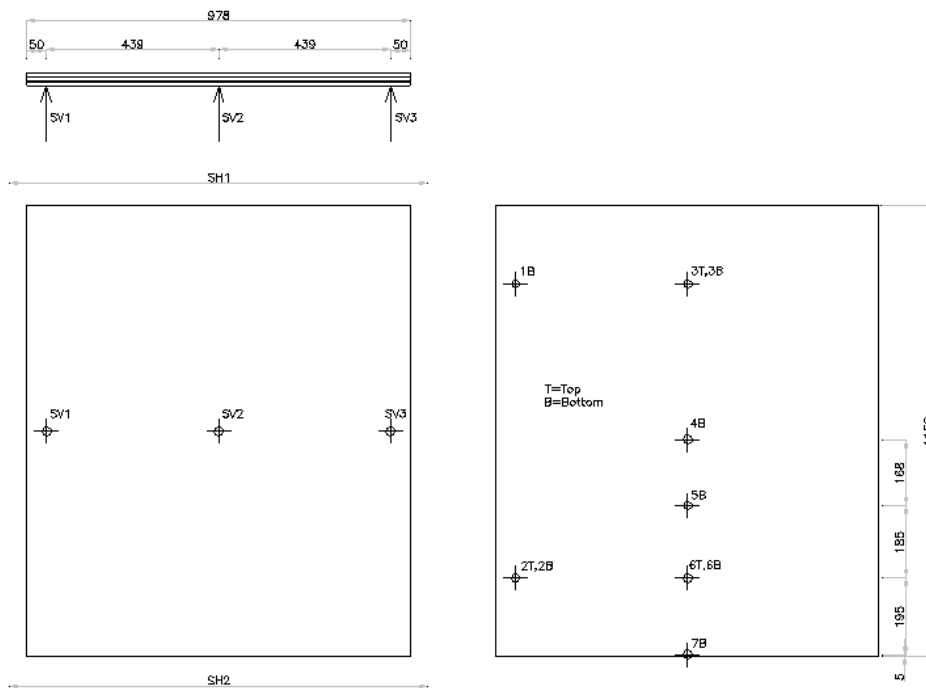


Figure 15: Position of displacement transducers (left) and strain gauges (right)

### 5.5 Test results

The following table shows a summary of the test results. The load steps 2 and 6 (see table 2) of the first test are stated so they can be compared easily. The maximum loads and displacements upon failure are listed for the second test. Furthermore a short description of the failure mode is given. The temperature of the specimen is listed because the material properties of the Sentry Glass Plus (SGP) interlayer are highly dependent on this temperature. The E-modulus drastically decreases as the temperature rises.

	test 01				test 02			failure	
	spec.	temp.	w at load step 2	w at load step 6	max. H	max. V	max. w	load step nr.	description
		[°C]	[mm]	[mm]	[kN]	[kN]	[mm]	-	
all layers intact	1	20	2.40	2.36	154	129	8.38	22	breakage of all layers
	2	30	2.00	1.98	155	130	8.41	22	breakage of lower layer
	4a	22	1.98	2.00	156	116	7.22	21	breakage of lower layer
upper layer broken	3	32	1.65	1.67	133	109	7.85	19/20	breakage of all layers
	5	22	1.74	1.75	154	127	8.72	22	breakage of lower layer
lower layer broken	4b	22	8.37	8.68	154	81	19.83	14	breakage of all layers. delamination of lower layer

Table 3: Test results

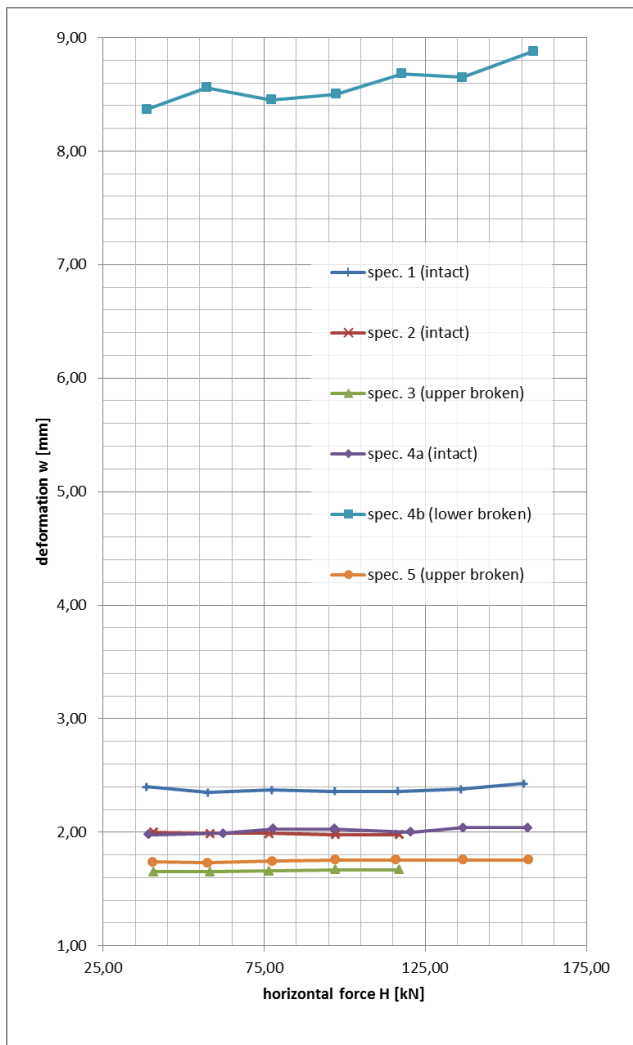


Figure 16: Force H vs. deformation all specimen, test 01

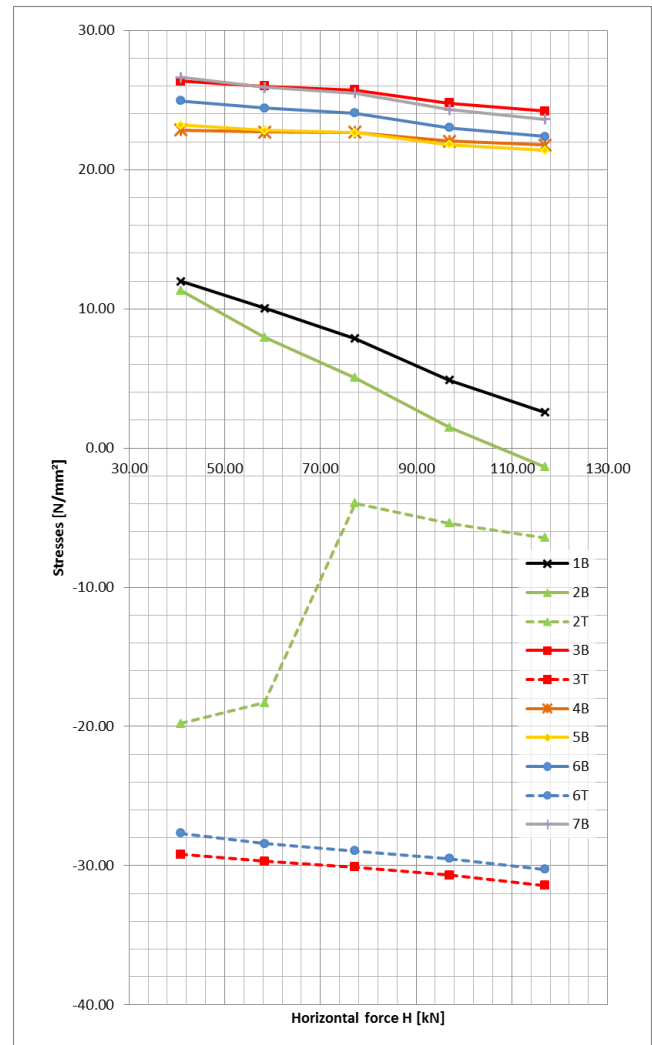


Figure 17: force H vs. stresses specimen 2, test 01

### *Global deformation of the glass panel*

Figure 16 shows the horizontal force  $H$  vs. the out-of-plane deformation  $w$  of test 01 of all specimen. The horizontal force does not seem to affect the deformation of the intact specimen and the specimen with a broken upper layer. The non-linear effect does not occur, the panel does not buckle at a higher compressive load. This is different to what was assumed in the handcalculations, equation 4. The deformation of the panel with a broken lower layer does increase a little when the horizontal force increases. This leads to the conclusion that the non-linear effect needs first to be taken into account at a deformation of approximately half the thickness of the panel.

The difference between specimen 1 and 2 and 4a is approximately 0.4 mm and can be explained by the fact that the measurement of the deflection for the first specimen was done only with one displacement transducer in the middle of the panel. In this measurement a bending of the frame will be accounted for as deflection of the panel. All the other panels were equipped with three displacement transducers, calculating the difference between the movement at the middle and at the sides as explained in section 5.4.

The panels with a broken upper layer failed at approximately the same loads as the intact panels. The upper layer is only loaded with compression and apparently the broken layer is still able to withstand these compressive stresses due to the stiff interlayer. At higher deflections some pieces of glass got pushed out of the upper layer, flying around the laboratory.

The volume of a broken glass ply is higher than the volume of an intact ply. Therefore the panel bent upwards when the upper layer was broken with a center punch. The deflection caused by the difference in volume was -0.87 mm for specimen 3 and -0.80 mm for specimen 5. This partly explains the difference in deflection between the intact panels and the panels with a broken upper layer.

The total deflection of specimen 3 at load step 6 is  $1.67 + 0.87 = 2.54$  mm, where the deflection of specimen 2 and 4a is  $\pm 2.0$  mm. This means that the panel with a broken upper layer is slightly less stiff.

### *Stress distribution in the glass panel*

Figure 17 shows the horizontal force  $H$  vs. the stresses measured with the ten strain gauges for test 01. The position of these strain gauges are given in figure 15.

The stresses at 3B are higher than at 6B, also the stresses at 1B is higher than at 2B and the stresses 3T slightly lower than at 6T. The transducers at the sides of the glass panel also show a slight difference at both sides. The horizontal force  $H$  was likely not applied completely symmetrically. Consequentially it is not possible to say that the maximum measured stress is the highest stress that occurred in the panel. However, the maximum stress does not automatically imply the location of the initial failure as this location is highly dependent on the surface quality. A small imperfection in the surface might cause the glass to fail at a lower stress than expected. The highest stress  $114 \text{ N/mm}^2$  was measured at strain gauge 7B at the side of the panel at step 22 of test 02.

The figure shows a big increase of the stress at 2T around  $H = 78 \text{ kN}$ . This increase is likely to be caused by a failure in the equipment. This increase does not occur at test 02. A short disconnection between the strain gauge and the computer might have set the measurement back to zero. Before the second test all measurements of the strain gauges started at zero again.

The vertical force  $V$  causes a bending of the panel and therefore all bottom side strain gauges show a tension stress. Even the gauges 1B and 2B near the supports measure a tension stress. This means that the panel is bent at these locations too, although this is less than at the middle of the panel. When the horizontal force increases all tension stresses decrease, because it causes an compressive stress in the panel.

### *Failure mode of the glass panel*

As stated in table 4 some panels failed with all layers broken and some with only the lower layer broken. When the load jack applying the vertical force was set to automatically maintain the required force it would instantly break all layers in case one layer failed, because the jack would maintain the same force on the panel. In the cases where only one layer broke the vertical force was regulated manually. Therefore we were able to reduce the force as soon as one ply failed, so the other plies remained intact.

Figure 18 shows specimen 2 after the tests. There are several things that can be concluded from this failure mode. Firstly, the circle named A can be indicated as the point where the failure was initiated, as all crack lines propagate from there. These cracks are mainly perpendicular to the applied horizontal force  $H$ , which indicates that the glass failed due to the bending of the panel.

The size of the glass pieces give an indication of the stresses that occurred at that location. The smaller the pieces, the higher the stresses have been. Near to where the horizontal load was applied, location B in the picture, the glass pieces are relatively large. Also the crack lines around the supports are perpendicular to the compressive force. Crack lines parallel to the

compressive force would be the result of splitting tension, these do not occur however. A special note needs to be made here of the outstanding edge quality of the glass panels. Normally the edges of glass are a point of concern as there are little cracks and discontinuities expected there due to the finishing. However, when the edges are polished well, the quality is as good as at the surface.

The locations for the initial failure of all specimen are slightly different. This is logical as the failure will occur at the location of the most severe surface flaw. However it is clear that all specimen failed due to the bending of the panel.



Figure 18: Failure mode

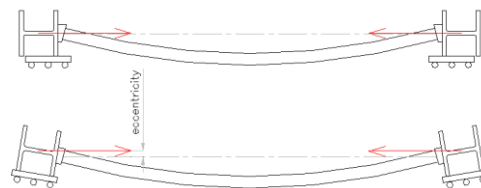


Figure 19: Bending of the frame

#### *Discussion of test results*

There are several things that might have caused inaccuracies during the tests. Firstly, the frame would bend a little due to the vertical force. This causes an eccentricity, because the horizontal force is not applied exactly in the middle of the glass, see figure 19. In order to reduce this bending as much as possible the wheels on which the frame stands were placed closer together. This way the weight of the metal frame would compensate the bending due to the vertical force. The tests were filmed with a normal camera and it is possible to see that the bending of the frame was reduced to a minimum by playing the video in slow-motion.

The vertical load was kept at its required value automatically by the force controlled jack. This was not exactly the same value all the time. A slight increase in the vertical force causes a deflection of the panel. Hence we had to wait some time at each load step to allow the vertical load jack to stabilize. Another reason to wait at each load step has to do with the crack growth in the surface of the glass panel. The small cracks in the surface will grow under tension stresses. This does take some time however. None of the intact specimen failed before load step 20, however if a specimen would have been loaded at load step 20 for a longer period it might have failed due to one crack that has grown severe in that time. In order to eliminate the effects of crack growth as much as possible, each load step was kept for the same period of time.

Another conclusion that can be drawn from the test results listed in table 4 is that the loads at which the specimen fail lie relatively close together. This is remarkable as the stress at which the specimen will fail is highly dependent on the surface flaws. The high quality of the glass finishing is probably the reason that the specimen did not show a big difference in the failure loads. Statistical testing should be done however in order to confirm this theory.

The temperature of the specimen varies between 20 and 32 °C, the E-modulus of the interlayer is respectively 567 Mpa to 324 Mpa for a load duration of 1 minute, DuPont (2008). Opposite to what was expected this did not seem to have a great influence on the test results. The deflection measured in test 01 of the panels with the higher temperature is less than the colder panels. Figure 16 shows that the deflection of specimen 2 and 3 is slightly less than the deflection of 4a and 5, even though specimen 2 and 3 were warmer. According to figure 4 the deflection of a specimen with a stiff interlayer should be less than with an interlayer of less stiffness. The failure of the specimen at test 02 seems independent of the temperature. This is also because the failure is highly dependent on the surface defects.

#### **5.6 Validation of calculations with test results**

The hand calculations and numerical models are validated by comparing its results with the results of experimental investigations.

### Deformation and stress distribution in the glass panel

The hand calculations as described in section 4.2 and the simple FE-model without the SGP interlayer and with shell elements (section 4.3) have been used. The same loadsteps 3 to 6 from test 01 have been calculated through in order to make a feasible comparison. One calculation of the more detailed FE-model under the design loads was also used for the comparison. The specimen did not have any initial deflection, so this had to be taken into account for the models and calculations as well.

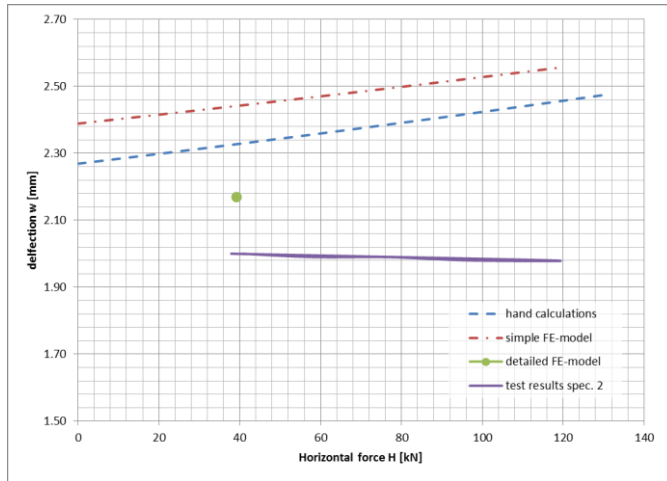


Figure 20: force H vs. deflection intact panel

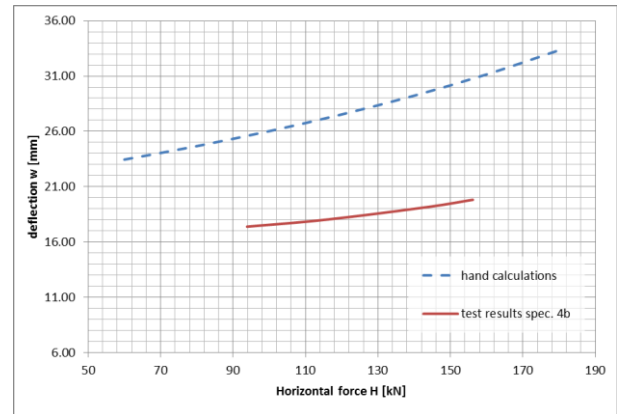


Figure 21: force H vs. deflection lower panel broken (at V=80.8)

Figure 20 shows the deformation at the design vertical load and an increased horizontal load. The measured deflections are less than the calculated deflections. As explained with figure 4 the deflection of a laminated panel would be more than that of a monolithic panel. This is in contradiction to the test results. The stiffness of the interlayer is very high and therefore the thickness of the interlayer should be added to the thickness of the monolithic panel. This would give similar deflections for the hand calculations. It is also possible that the vertical force applied to the specimen causes a different deflection because the force is applied on two lines instead of a distributed force over the complete area. This is a very common method to simulate a distributed load however.

From figure 20 it is clear that according to the calculations the deflection increases with an increasing horizontal force. The test results do not show the same pattern, the expected buckling does not occur. With a larger buckling length, or a smaller thickness this non-linear effect might be visible in the test results. In order to confirm this, the test results of specimen 4b, with the lower layer broken, and hand calculations of a panel with a thickness of 20 mm are compared in figure 21. The results of load steps 11 to 14 of test 02 are used and a vertical force of 82.5 kN is used in the hand calculation. This vertical force consists of the vertical load used in the test (80.8 kN) plus the dead load of the frame (1.7 kN). A higher vertical load than the design load is used because the non-linear effect is better visible at larger deformations. The deformations calculated by hand are larger than the measured values, the slope of both graphs however is similar.

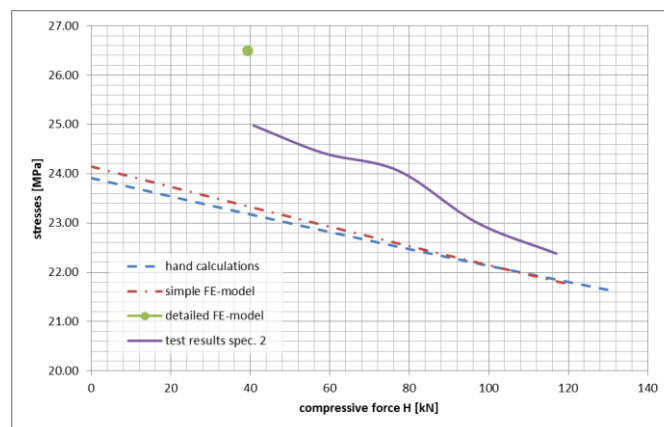


Figure 22: force H vs. stresses intact panel

Figure 22 shows the stresses in the glass panel. The stresses measured with strain gauge 6B are used. The stresses of all methods seem to reduce due to the increasing compressive force. The slight difference between the gradient of the measurements and the calculations has to do with how the stresses due to bending and due to compression relate, equation 5. In general the measured stresses are higher than the stresses determined with the hand calculation and FE-models, despite of the measured deflections being less. Hence, the stresses due to bending are more than expected. The stresses determined

with the detailed FE-model are higher than the measured stresses. However, the differences are approximately 10%, which is quite accurate considering the simplifications made in the calculations and FE-models.

### *Conclusion*

The calculations give larger deformations than measured. The calculated stresses are slightly less than the measured stresses. The values are close together, so the hand calculations can be used to give a first indication on the required glass thicknesses of a new design. It is advisable to use the calculation for an indication only, and choose all values conservative. The more detailed FE-model seems to give slightly more accurate values.

## **6. REGULATORY BODIES**

As the amount of glass used on yachts has been increasing the last several years, the use of glass has been a mayor point of interest of the regulatory bodies. Using glass as a load bearing material has not yet been done on board a yacht. There are no specific rules for glass as a structural material. (Verbaas, 2012)

### **6.1 Current regulations for glazing on yachts**

Vessels built for sport and pleasure, and not engaged in trade are excluded from the International Convention on Load Lines (ICLL). When a yacht is offered for charter however it need to have a load line assigned. Feadship normally designs its yachts to meet the regulations of the Flag States for having a Load Line assigned, because even if the owner does not intend to use the yacht for charter it improves the resale value in case he wants to sell the yacht later on.

It is not easy to apply the requirements in ICLL to yachts, as these are specifically made for commercial ships. For that reason some Flag States have National Equivalents adopted like the MCA Large Commercial Yacht Code (third version: LY3).

The Large Yacht Code stipulates that the weathertight integrity of portholes and windows should meet ‘an appropriate national or international standard’, so it does not give specific criteria. These criteria are given in for example the UK national standard BS MA 25 or in the international standards ISO.

All elements and sizes of the windows are fully prescribed in BS MA 25 and the ISO standards. This way the windows would be easy to replace and repair. On the modern yachts, however, windows with a predetermined size and a rectangular shape are not often what the designer has in mind. The standards give methods to determine the required thickness for of the glass of different sizes. As these standards were developed in the 1970’s these methods are not completely up to date with the current knowledge on glass. There are no methods given for the calculation of laminated glass panels, therefore these need to be tested to demonstrate sufficient strength of the glazing. A test result is only valid for the sizes of the tested panel. In order to cover all the windows on a yacht a lot of expensive testing needs therefore to be done.

A workgroup of yacht builders, glazing manufacturers, flag authorities and classification societies was formed to develop ISO 11336 under the International Standardization Organization. ISO 11336 is a up-to-date standard for yacht glazing consisting of three parts. Part 1 is finished and in use since 2012. This first part deals with pre-fabricated units and glazed openings that are fitted in frames. This part also defines the design pressures on the windows. The criteria are more dependent on the size of the vessel than the conventional criteria. For a given size of vessel, the design pressure is a function of the position along the ship and the height above the waterline, see also the calculation at section 3.3.

The first part also defines the test procedures for pressure testing. The previous standard did not have the test parameters specified, which made the criteria very open to interpretation. This caused a lot of debating and case-to-case decisions. The standard approaches glass as a structural material to support the application of glass in items other than windows and portholes (e.g. balustrades) but also the application of glass as a load bearing material. The used methods are well established in other industries.

The second and third part are being defined at the moment. Part 2 covers integral glazing and bonding of windows. The deflections of the supporting hull and deckhouse structure under thermal load and sea load will be taken into consideration. Furthermore, the required glass thickness will be determined with a modified method using a non-linear method to calculate the stress and deflection. This method is likely to be similar to the method used in section 4.2. Part 3 deals with quality control and inspection. Wherever possible this part will adopt procedures and standards from the glazing industry. Survey procedures will be described precisely and complete documentation will be provided on board the yachts to ensure that the right materials will be used for replacement.

### **6.2 Aspects that need to be considered when glass is used as a load bearing material**

There are no specific rules for the application of load bearing glass yet. However, in part 1 of ISO 11336 the glass is approached as a structural material, so the basics are known. During the project Frans Verbaas was contacted for

information and advice several times. Frans Verbaas is working for Lloyd's register and is in the workgroup ISO 11336. In his expert opinion it should be possible to use load bearing glass in the deckhouse, considering the following aspects.

*Maintain safety of navigation, communication and stability.*

In case the windows lose its weathertight integrity the vessel should not be in danger of flooding. There are two positions for openings defined in the international load line convention (ILLC). The complete deckhouse is located at position 2; upon exposed superstructure decks situated abaft a quarter of the ship's length from the forward perpendicular and at least one standard height of superstructure above the freeboard deck, ILLC (1966).

According to Lloyd's register part 3, Ch. 4, sec. 7.1.9 the doors are considered to be sufficient protection between windows and access below. However, when the wheelhouse exhibits an internal stairway opening this needs to be surrounded with a weathertight cover of at least 230 mm in height. In this case the wheelhouse needs to be fitted with adequate means of draining, Lloyd's Register pt.3, ch.4, sec. 7.12.8 (2010).

In the case that all windows would not be able to hold any load, for example because of a fire, the deflection of the deck above should reach a stable deflection. High temperatures will cause a significant decrease in the stiffness of the SGP interlayer, DuPont (2008). Hence the deflection of the three layers will be much bigger, causing higher stresses and likely failure of all layers. The deflection of the sundeck is approximated with a simple calculation based on the basic equation for a fixed-free beam with a distributed load, Roark's formulas (2002).

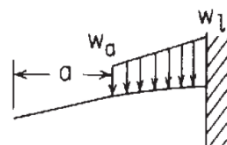


Figure 23: Deformation of fixed-free beam

$$y_a = \frac{-w_a}{24EI} (l - a)^3 (3l + a) - \frac{w_l - w_a}{120EI} (l - a)^3 (4l + a) \tag{7}$$

Where:

a	=	0	-	distance from free edge to load
w <sub>a</sub>	=	51.3	kN/m	distributed load at free edge
w <sub>l</sub>	=	70.4	kN/m	distributed load at fixed edge
E	=	69 x 10 <sup>-5</sup>	N/m <sup>2</sup>	E-modulus aluminum
I	=	4.84 x 10 <sup>-5</sup>	m <sup>4</sup>	total moment of inertia of sundeck
L	=	4.32	m	length of the deck

W<sub>a</sub> and w<sub>l</sub> are determined by multiplying the deckload (9.4 kN/m<sup>2</sup>) by the width of the sundeck at the free and fixed edge respectively (approximately 2.72 m and 3.74 m). The shape of the deck is hence simplified to a trapezoid. The total moment of inertia is determined using the construction of the deck in autocad. The maximum deflection of the deck is therefore 0.74 m, this is stable as the sundeck does not reach the deckhouse deck.

*Protective outer layer*

Surface areas likely to be touched need to be protected. Damage can occur from everyday actions like cleaning. A piece of sand in the sponge used to clean the windows, every day, will slowly grind in the surface of the glass. Hence a sacrificial outer layer may be added.

*Post breakage behavior*

A broken glass layer takes up more volume than an intact layer, this causes tension stresses in the adjacent layer due to the stiff interlayer. This volume difference also causes a deflection of the panel and the length reduces. Therefore it is likely that the surrounding windows will carry the load of the broken panel, especially in the deckhouse, where there are relatively much small windows. The load on the surrounding glass panels in case one is broken is 47.9 kN. As shown in figure 17. the stresses in the panel reduce when the compression force increases. In other applications however, the wish is to have as large windows as possible.

A three layered laminate is chosen, in order to increase the reliability of the system. The intact panel is designed so that the stresses stay below the design flexural strength (40 MPa for fully tempered glass, ISO (2012)). In the building industry the stresses in the panel when both the outside and the inside layers are broken need to be below the characteristic failure strength of the glass (160 Mpa for fully tempered glass, ISO (2012)). On a yacht however it is not uncommon to take special precautions or operational measures in case one layer breaks, the saloon could be closed for example to reduce the risk of breaking another layer.

Pillars could be placed in the wheelhouse to reduce the loads on the broken panel. Breakage of the outer layer seems the most likely breakage that can happen. From the test results it is concluded that the strength of the panel does not reduce much in this case.

#### *Durability of glass*

The strength of glass decreases over time, due to crack growth under loading and weathering. The dynamic loading of the ship in waves will cause subcritical crack growth which can lead to sudden breakages. The cyclic thermal loading that will occur in a sunny area can cause the glass to fail. The properties of glass under cyclic loading are still being investigated, Pankhardt (2010). The effects of the durability of glass on the load-bearing glass application is not being investigated in this project. This might have to be done however in order to get approval for the application by the regulatory bodies.

### **7. CHANGES THAT A STRUCTURAL GLASS APPLICATION BRINGS ABOUT**

This chapter determines the changes that will occur when glass is used in a structural manner. There will be changes in the construction, the building process and costs and the weight of the yacht.

#### **7.1 Construction load bearing vs. non load bearing glass**

There will be several changes in the construction when load bearing glass will be used instead of 'normal' glass.

Firstly, the mullions can be left out. As well as the insulation and interior around the mullions. This needs to be adopted in the construction plan of the F45.

A sealant is needed to prevent contact between the two glass panels, or between the glass panel and the metal structure of the yacht. As the windows will be placed under an angle relative to each other, a deflection of the panels will cause the gap between the windows to increase. The sealant needs to be able to withstand this and maintain its watertight integrity. On another Feadship yacht a similar sealant was applied because the deflection of the hull was significant and the sealant needed to prevent contact between the glass and the yacht.

#### **7.2 Building process and costs**

An important change in the production process will be that the windows will have to be installed at an earlier stage. The construction above the load bearing windows will be held in its place with pillars. These pillars need to be removed in order to install the interior. Therefore the windows will need to be installed. When the glass is applied in a nonstructural manner, placing the windows is done later to reduce the risk of damaging it. In order to replace the windows these studs need to be able to be placed even with the interior intact.

The building costs of the yacht will increase due to the extra man-hours and the more expensive glass panels. More man-hours will be needed because placing the windows has to be done with more precision and will be more laborious. At the same time, the glass panels need to be thicker and made out of the best quality which will inadvertently result in significantly higher costs. There will be a few savings, on the other hand, as the mullions can be left out as well as a part of the interior and insulation.

#### **7.3 Weight difference**

The difference between the weight of glass used in the original non load bearing manner and as a structural material is determined. The weight of the non-load bearing glass, mullions, isolation and interior can be subtracted and the weight of the load bearing windows can be added to the ships weight.

The total weight that can be subtracted is 554 kg. The total weight of the load bearing windows will be 790 kg. When the glass in the wheelhouse of the F45 would be used as structural material, the total weight of the yacht would increase approximately by 235 kg. This is an increase of the lightship weight of 0.1%.

### **8. CONCLUSIONS AND RECOMMENDATIONS**

The use of glass in yacht construction became increasingly popular during the last decades as glass enables yacht designers to provide more light and sight at the inside and from the outside it gives the yacht a modern impression. This design trend is likely to continue in the near future and therefore, the challenges of using glass as a load-bearing structure had to be addressed by naval architects.

In 2011 de Voogt naval architects conducted a research 'stiffness through glass' on the use of glass as a load bearing material on yachts in order to indicate the possibilities and effects of structural glass on yachts, Mendes de Léon (2011). This research showed that it could be possible to use glass to increase the stiffness of the vessel. However, at specific locations in the ship's structure, the glass panels have to become very thick in order to fulfill the strength criteria. This will most likely result in an increased ship's weight. Therefore in 2013, Feadship decided to conduct another research on a realistic, local, first application of load-bearing glass using toughened glass as a test material.



This paper describes the 2013 research and its conclusions. The main conclusion is that the application of load bearing windows in the wheelhouse of a 45-metre Feadship design is a realistic first application of glass as a load bearing structure on board yachts. The main research question, *'is it possible to use loadbearing glass realistically on board of a yacht?'*, can be summarized by answering on the following main research questions:

*What are the properties of glass?*

- The strength of glass is highly dependent on the defects in the surface, therefore glass can withstand a lot of compression but not so much tension stresses.
- Strengthening the glass is a way to improve the glass properties, this can be done thermally or chemically. Laminating the glass also improves these properties.

*Where on board can load bearing glass be used, and what are the loads acting at this location?*

- The wheelhouse windows of an existing 45-meter Feadship design are analyzed for structural use.
- The loads acting on this location are determined locally and consists of the deckload and normal load. There are nine windows in the wheelhouse, each of them is loaded with a compressive force of 29.3 kN due to the deckload. The normal design pressure on the wheelhouse windows is 30 kN/m<sup>2</sup>.

*What is the required glass thickness for structural glass on the chosen location?*

- As the properties of glass are better in compression than under tension loads, the windows are subject to a constant compression force. This way the glass is only loaded with tension due to bending of the panel.
- The buckling of the glass in combination with the normal load is analyzed with a simplified hand calculation and non-linear FE-models in order to determine the required glass thickness. This was determined to be a laminate of 3 x 10 mm fully tempered glass with a SetryGlass interlayer of 1.52 mm.
- The hand calculations and FE-models were validated with full-scale experimental investigations:
  - The full scale tests of the wheelhouse windows break when loaded with four times the design normal load and four times the design compression load.
  - When the exterior layer was broken before the test the results are similar to an intact panel, because the broken layer can still withstand compression due to the stiff interlayer.
  - A panel with an broken interior layer fails when loaded with three times the design normal load and three times the design compression load.
  - The calculations give larger deformations than measured. The calculated stresses are slightly less than the measured stresses. However, the differences are approximately 10%, which is quite accurate considering the simplifications made in the calculations and FE-models. The hand calculations can be used to give a first indication on the required glass thicknesses of a new design. It is advisable to use the calculation for an indication only, and choose all values conservative. The more detailed FE-model seems to give slightly more accurate values.

*How does the application of structural glass fit into classification rules?*

- A new set of international standards for yacht glazing is being worked on at the moment under the International Standardization Organisation. The standard ISO 11336 approaches glass as a structural material to support the application of glass in loadbearing applications in the future. The main object for the load bearing glass application to fit into the classification rules is that the safety of navigation, communication and stability should be maintained.
- The accommodation doors in the wheelhouse are sufficient to keep the water out in case a windows breaks.
- When none of the windows is capable to hold any load, for example because of fire, the deflection of the sundeck is 74 cm. This is a stable situation.
- In case one of the wheelhouse windows breaks, the remaining eight windows are capable to withstand the increased compressive load.

*What changes are needed in the construction and building process of the yacht when using load bearing glass instead of 'normal' glass?*

- By the application nine loadbearing wheelhouse windows the weight of the yacht will increase with 235 kg due to the thicker glass panels.
- The building costs will increase as more man-hours will be needed because of the complexity and bigger windows.
- The only changes in the building process will be that the windows have to be placed in an earlier stage. The sundeck will be built on studs first, but in order to finish the interior the windows will have to be placed.

The research shows that the application of loadbearing windows in the wheelhouse of the F45 is a realistic option. However, more research is needed before the first structural glass application on a different location in the yacht design can be considered.

- More research has to be done on the effects of mechanical vibrations on the load bearing application. It should be investigated how much ‘extra’ compression load is needed on the windows in order to reduce the vibrations.
- The panels that were tested in this research were made of toughened glass. When one layer fails the glass breaks into very small pieces, making it hard to look through the window. Heat strengthened glass has a lower design flexural strength, but has the advantage that it fails into large pieces. So it could be investigated if it is possible to use heat strengthened glass for the whole panel or only for the exterior layer.
- Also the static fatigue and stress-corrosion cracking of glasses could be interesting to investigate. Glass will experience static fatigue, a time-dependent failure of glass constantly loaded in an environment containing water. Stress corrosion occurs under cyclic loading, a crack in the surface grows every time the stress at the crack tip exceeds a critical value.
- The difference in coefficient of thermal expansion between the glass and aluminum of the yacht can cause a big difference in the deformations of both materials, especially in the plane of the glass panel. The sealant between the glass and metal should be able to maintain its watertight integrity during large deformations. The deformations could be quantified with a detailed model of the complete wheelhouse in order to define a suitable sealant.

## REFERENCES

- Mendes de Léon, E., “Stiffness through glass: Increasing the stiffness of the superstructure of a yacht, by integrating load bearing glass applications into the structure”, Thesis Feanship & TU Delft, 2011
- Schittich, C., *Glass construction manual*, Basel: Birkhäuser, 2007
- Pankhardt, K., *Load bearing glasses*, Doctoral thesis Budapest University, 2010
- Maniatis, I., *Numerical and experimental investigations on the stress distribution of bolted glass connections under in-plane loads*, dissertation, 2005
- Fröling, M., *Strength design methods for laminated glass*, Dissertation Lund University, 2011
- International Organization for Standardization, Large yachts – strength, weathertightness and watertightness of glazed openings - part 1: ISO 11336-1, Geneva: ISO, 2012
- Wurm, J., *Glass structures: design and construction of self-supporting skins*, Basel: Birkhäuser, 2007
- Wellershoff, F., *Nutzung de Verglasung zur Aussteifung von Gebäudehüllen*, Dissertation Technischen Hochschule Aachen, 2006
- Lloyd’s Register, Rules and regulations for the classification of special service craft, Londen: Lloyd’s Register, 2010
- Luiblé, A., *Stabilität von Tragelementen aus Glas*, Thesis École Polytechnique fédérale de Lausanne, 2004
- Blaauwendraad, J., Buckling of laminated columns, *Heron Vol. 52.*, 2007
- Shama, M., *Buckling of ship structures – Ch10: Columns and beam columns*, Springer verlag, 2013
- Cook, R., Concepts and applications of finite element analysis, USA: J. Wiley & Sons, 2001
- Mocibob, D., Glass panel under shear loading – use of glass envelopes in building stabilization, Thesis École Polytechnique fédérale de Lausanne, 2008
- DuPont – Glass Laminating Solutions, SentryGlas® Plus Elastic Properties, [www.dupont.com](http://www.dupont.com), 2008
- Verbaas, F., Use of glass and the regulations. 22<sup>nd</sup> Hiswa Symposium on Yacht Design and Yacht Construction proceedings, 2012
- International Convention on Load Lines, chapter I: Regulation 13 Position of hatchways, doorways and ventilators, 1966
- Warren Young and Richard Bunynas, *Roark’s formulas for stress and strain*, New York: McGraw Hill, 2002

# **ADHESION: LESSONS LEARNED ABOUT ADHESIVE BONDING IN SHIP STRUCTURES**

**K. Custers** MSc, Research Engineer, Damen Shipyards, The Netherlands

**Bernd-Jan Bekkers**, Welding Engineer, Damen Shipyards, The Netherlands

## **SUMMARY**

A joint research program called ADHESION, consisting of 13 different stakeholders, has led to a structured acquaintance of the Dutch shipbuilding industry with adhesive bonding. The project goal was to gain information and implement technology for certified adhesive joints in shipbuilding practice.

A large number of specimen tests were performed to test the applicability of various adhesives systems on (coated) shipbuilding materials. The test results showed that for high strength adhesives failure occurs in the coating/primer, which means the full capacity of the adhesive is not used. However, the test results did show that coatings are required to prevent corrosion of metals underneath the bondline.

Besides specimen testing, four case studies into typical ship structural components were carried out, which indicated bonding of ship structures is feasible. An important result that followed from the cases is that stress values attained in practice are a factor 2 lower compared to values attained in specimen tests. The biggest remaining challenge after this cooperative research project is to predict the service life of an adhesive joint. This challenge needs to be addressed before “standard” certified adhesive joints in shipbuilding will become common practice.

## **1. INTRODUCTION**

Traditionally the shipbuilding relies almost exclusively on welding to assemble metal structures and to install equipment. However, under the pressure to produce lightweight and cost effective structures, plate material of which ships are constructed becomes thinner, and composite materials are increasingly applied. This creates situations in which welding is no longer possible or has negative impact on aesthetics. Adhesive bonding could provide a cost effective solution for these joining problems, but questions exist about the long term durability and mechanical strength of adhesive joints.

To implement adhesive bonding technology in shipbuilding practice a research project ‘ADHESION’ was initiated within the Netherlands Maritime Innovation Program. Among the project participants were shipyards (Damen, classification societies, engineering firms, an adhesive supplier and knowledge institutes. The objectives of the projects were as follows:

- To develop and provide knowledge in the field of adhesive bonding that can be used by engineers to design maritime structures
- To determine the effect of the shipyard production environment on the quality of the adhesive bond
- To transfer know how of bonding procedures to shipyard and service employees
- To identify the technical and economic potential of large scale bonding applications in light weight maritime structures

This paper presents a brief overview of the results of the ADHESION project. Section 2 describes the challenges the maritime sector is facing in the field of bonding and those are related to bonding practices in other industries. The third section focuses on the mechanical aspects of bonded joints and presents the results of the case studies. Section 4 describes durability related issues of adhesive joints in a maritime environment. The road forward towards certified adhesive joints in shipbuilding practice is described in Section 5. The paper ends with the conclusion in section 6.

## **2. UNIQUE CHALLENGES OF BONDING IN THE SHIPBUILDING INDUSTRY**

With the exception of composite ship building, adhesive bonding is not yet widely applied in maritime engineering. Adhesive technology has found its way in furnishing of yachts and other specific applications such as window bonding. However, as of today bonding is not yet used in primary structural joints in metal ships. There have been research efforts in the field of adhesive bonding for maritime applications before of which BONDSHIP is the most noteworthy. One of the main achievements of BONDSHIP was the publications of a set of guidelines that can be used for designing adhesive bonds (Weitzenböck J. , 2010). The authors argued that the next step was to move from precompetitive research to product development. A critical mass of users of bonding technology in shipbuilding is required to make bonding a widely accepted technology.

Examples of industries where bonding technology is more widely accepted are the aerospace- and automotive industry. Adhesive bonding literature is full of references to the aerospace industry as an example of an industry where bonding is already widely applied (Kinloch, 1987; Kwakernaak, Hofstede, Poulis, & Benedictus, 2010; Weitzenböck J. , 2012). However, a critical review of the bonded applications in the aerospace industry indicates this is only partly true. Structural bonding in aircraft structures is limited mainly to secondary applications. Aerospace manufacturer Fokker from the Netherlands is one of the few exceptions in the aerospace industry who widely applies bonding. Fokker has been bonding stringers to metal wing skins for over 80 years now, leading to metal structures with excellent fatigue life (Kwakernaak, Hofstede, Poulis, & Benedictus, 2010).

The challenge for the shipbuilding industry is that the manufacturing standards from aerospace engineering are not easily transferred into the shipbuilding industry. For example, for bonding aluminum Fokker uses a chromic acid anodizing pretreatment and primes the surfaces with a heat curing epoxy primer. The anodizing process improves the strength of the adhesive joint and also creates a very stable oxide layer (Kinloch, 1987). Such extensive pretreatment requires significant investments in chemical pretreatment machinery and leads to high manufacturing costs, which makes these processes not suitable for the shipbuilding industry.

Another industry which is often referenced in bonding literature is the automotive industry (Habenicht, 2008). For example, adhesive bonding has been extensively used for over 30 years in the elastic bonding of windshields. Also truck trailers are increasingly assembled relying solely on adhesive bonding technology. Accelerated aging test are widely used by automotive manufacturers for assessing the durability of adhesive systems. All automotive manufacturers have their own test cycles, but usually they involve cycles of about 7-10 days with temperatures ranging between -30°C and +70°C, UV radiation and humidity levels up to 100% (Kinloch, 1987). Although these testing conditions are severe and seem to give reliable results for the automotive industry, their applicability to the maritime industry are questionable. Take for example the environmental conditions in Singapore, where temperatures of 30°C and higher are reached on a daily basis, in which surfaces can heat up to 80°C. In combination with high humidity levels and a saline environment, these conditions can form a much higher loading for the adhesive system than a common accelerated aging test. This means the shipbuilding industry has to develop its own standards for accelerated test that yield representative results for the service life of a bonded joint.

A final challenge that the maritime industry has to address before adhesive bonding can be readily applied is the influence of the production environment and the influence of the “bonder” making the adhesive joint. In theory a dirty production environment could negatively influence the quality of an adhesive joint. Oil and dust particles in the air can deposit on the substrate leading to a lower adhesive strength. The bonder is another contributing factor, because the quality of the joint is determined by how carefully the bonder follows the prescribed manufacturing procedure. The quality assessment is complicated because it is difficult to inspect adhesive bonds using non-destructive testing methods.

Both manufacturing aspects described above were briefly addressed during ADHESION. For this purpose a series of samples was made under different circumstances: clean laboratory conditions, “clean” shipyard conditions and “dirty” shipyard conditions. No trend followed from the destructive tests that were carried out on the samples (Bosman, 2012). A large spread was present in the data, which indicates the bonder seems to have a large influence on the quality of the joint. To get a better idea of the influence of the shipyard environment on the bonding process a more thorough test setup is required: eliminate the effect of the bonder, by letting 1 person make samples under the 3 different conditions.

An important lesson that can be learned from the effect of the production environment and the bonder on the quality of the joint is that one has to take these effects into account for the serviceability of adhesive joints. An adhesive joint does not only need to be achievable under shipyard conditions, but here should also be a solution to service the joint in the field by a service engineer.

### **3. MECHANICAL TESTING OF ADHESIVE BONDS**

During ADHESION 4 different cases were studied which represented typical ship structures. The goal of the case studies was to evaluate the suitability of adhesive joints for primary structural joints. Practical tests were performed on 2 different levels of the so called testing pyramid (Figure 1): at coupon level and at component level. The testing pyramid is commonly applied in aerospace engineering for describing the process through which a technology develops up to a point where it can be readily applied in the industry (Beumler, 2004). When a technology is still relatively new, tests are performed at a coupon level, because at this level testing is still relatively cheap. Afterwards the higher levels of the testing pyramid are filled by performing test at component and full scale level. The latter is not applied in shipbuilding because it would simply make the development process too costly. By testing at multiple levels knock down factors can be set that can be used during the design phase.

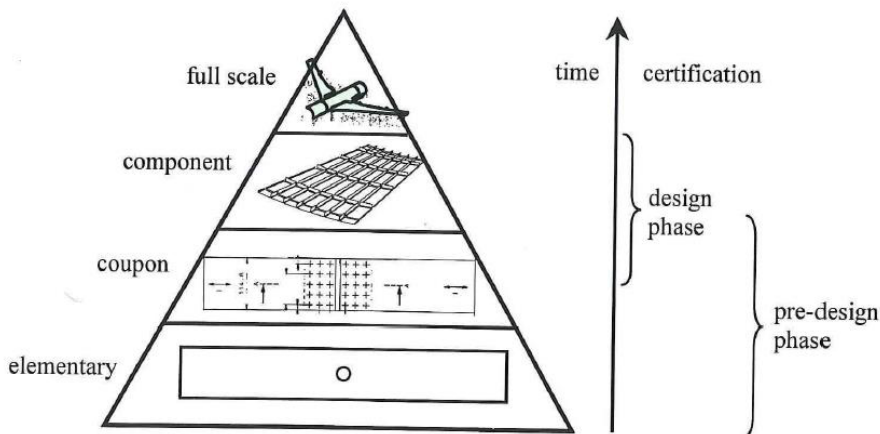


Figure 1: Testing pyramid during the development of an aircraft (Beumler, 2004)

During the ADHESION the following 4 cases were selected to be investigated, which are listed below (see Figure 2). In each case specific properties regarding the performance of the adhesive joint were required such as fatigue resistance, underwater bonding and different substrate material.

1. Mast-Superstructure connection
2. Stainless steel bow plate
3. Foundations for rotating machinery
4. Streamline fairing

The case studies performed during ADHESION did not result in certified adhesively bonded solutions for the structural elements that were under investigation (Bosman, 2012). For achieving this too many question marks remain, such as the durability of the joint and the way to inspect the joint by means of non destructive inspection. The main lesson learned was that the joint geometry has a large influence on the strength values that are achieved. The strength values that resulted from ASTM standards were roughly a factor 2 higher compared to the stress values that were obtained in the actual application. This implies two things: first of all, alternative testing standards compared to ASTM standard D1002 have to be used to produce engineering values that can be used during the design phase. Secondly, accurate FEA methods are required to calculate stresses in bondlines to avoid preliminary failure.



Figure 2: cases that were studied: left, stainless steel bow plate (source: Amels); right, composite streamline fairing bonded to steel or aluminum hull

#### 4. DURABILITY OF ADHESIVE BONDS

This chapter describes durability aspects of adhesive joints in maritime environments. Sub-section 4.1 describes adhesive forces on a molecule level and how these forces are affected by the maritime environment. Sub-section 4.2 presents the durability results that were obtained during the ADHESION project and what the results imply for design practices of adhesive bonds in shipbuilding practice.

##### 4.1 Physical and chemical principles at a molecule level

Substrates like metal, glass, wood and fiber reinforced composites all have a similar surface topology when it comes to bonding: they all have (at least some) hydroxyl groups and double bonded oxygen molecules at the surface. The precondition for a strong adhesive bond is that the adhesive molecules come in close contact with the substrate (Kinloch, 1987). Close molecular contact is only achieved when the adhesive wets out properly on the surface. Proper wetting is achieved when the attractive forces of the substrate on the liquid adhesive are higher than the attractive forces in the liquid itself.

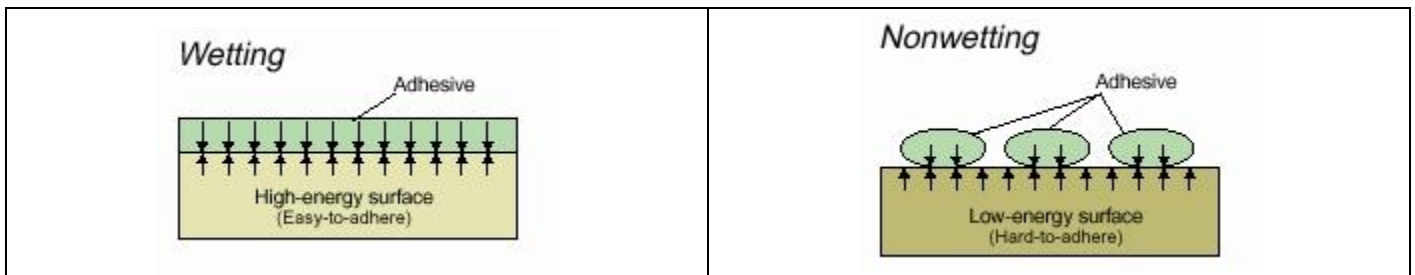


Figure 3: left, proper wetting in case of a clean and high energy surface; right, poor wetting in case of a low energy surface (source: machinedesign.com)

The same molecule structure that improves wetting characteristics of adhesives also makes them vulnerable to environmental attack: adhesives often have polar groups to improve wetting and adhesion characteristics, but as a result water also diffuses more easily into the bulk adhesive (Burchardt, 2010). Water and Oxygen diffuse into the adhesive and attack an adhesive joint on multiple places: in the cohesive zone, the adhesive zone and the substrate itself (Figure 4). However, the diffusion of moisture into the adhesive is not always an unwanted side effect; elastomers like MS polymers and 1 component PU adhesives, require moisture to cure.

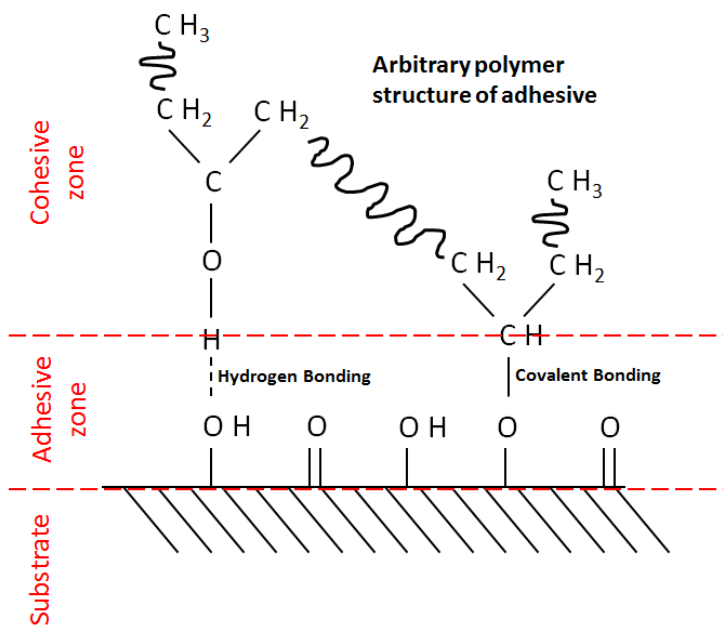


Figure 4: Different areas of an adhesive joint where the environment can attack

Below the mechanisms by which the maritime environment can attack an adhesive joint are listed. The list is limited to the contribution of water, oxygen, UV and heat, while other substances such as alkaline and acid solutions (gasoline, cleaning agents, etc.) can reduce the strength of an adhesive joint as well. However, the mechanisms by which this attack occurs are similar to the ones described below. It is important to understand the processes by which adhesive joints age in a marine environment, because failures that occur in practice can be recognized and appropriate countermeasures to increase joint durability can be taken.

1. Water, Oxygen, heat and UV attack the adhesive itself in the cohesive zone:
  - a. Moisture can plasticize adhesive (intercalation of water): water molecules that diffuses into the adhesive displace polymer chains, this increases the distance between the polymer chains and thereby they slide easier along each other plasticizing the adhesive.
  - b. Acid hydrolysis of adhesive: polymer chains are broken by water molecules (Figure 5)
  - c. Migration of molecules such as plasticizers, stabilizers or catalysts, which is caused by an intrinsic instability in the adhesive
  - d. Oxygen can scission polymer chains under the influence of UV light
  - e. Heat can break chemical bonds in the adhesive
2. Water, Oxygen, heat and UV attack the chemical and physical bonds between adhesive and substrate in the adhesive zone
  - a. moisture can displace adhesive (intercalation of water) at the adhesive substrate interface (see 1a)
  - b. Oxygen and/or water can scission chemical bonds between substrate and adhesive
  - c. Heat can break chemical bonds at the adhesive substrate interface
3. Water and Oxygen can attack the substrate:
  - a. Water and oxygen can attack metal oxide layers, creating a weak interface which easily breaks away. Salt water can considerably speed up this process
  - b. Fiber reinforced polymers can be weakened by moisture ingress, oxygen, UV and heat

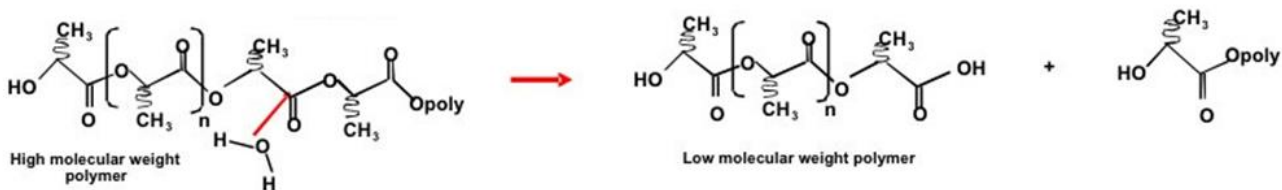


Figure 5: Hydrolysis and cleavage of the ester linkage in a polymer (source: <http://www.uweb.engr.washington.edu/>)

From the overview of failure modes it becomes obvious that if one would like to model or predict the long term durability of adhesives in a maritime environment, one needs to have a thorough understanding of the above described mechanisms. The overview of failure modes does not take the effect of cyclic loading into account, while it is known that adhesive joints are sensitive to fatigue (Kinloch, 1987). The fatigue life of a joint can be expressed by  $N \cdot S^m = C$ , in which N is the number of cycles, S the stress amplitude and C is a material constant. The variable m is a measure which indicates how sensitive the material is for the stress range. For welded details in metals a common value for m equals 3. During the fatigue tests that were performed as part of ADHESION, m-values in the range of 8-10 were found (Bosman, 2012). This indicates the stress amplitude affects the fatigue life of adhesive joints, but they perform better compared to welded or mechanically fastened joints. This essentially arises from a better stress distribution in the joint, since adhesive joints do not lead to stress concentrations (Kinloch, 1987).

Most of the progressive damage models for disbond growth in adhesive joints under the influence of cyclic loading that are currently available are based on empirical models (Pascoe, Alderliesten, & Benedictus, 2013). These empirical models work relatively well under well-defined laboratory conditions, but are of little use for predicting service life in practice. Therefore, models on a more physical and chemical basis are required to make accurate service life predictions for bonded joints.

#### 4.2 Increasing the durability of adhesive joints

To create a durable bond one has to create a stable interface between the adhesive and the adherent (Kinloch, 1987). The oxide layer of steel is known to be very unstable and easily breaks away. The oxide layer of aluminum is much more stable as the layer passivates by itself. However, under the influence of water molecules, the aluminum oxide can hydrate leading to a weak layer that can easily break away (Kinloch, 1987). During the ADHESION project the durability of uncoated steel and aluminum surfaces was tested. The result was that uncoated metals did indeed not result in durable bonds. Figure 6 shows two examples of

specimen after aging and destructive testing. In the left side of the figure is clearly visible that edge-corrosion occurs at the steel-adhesive interface. In the right side of the figure the white layer after aging indicates hydrolysis of the aluminum oxide layer, leading to a reduction in adhesive strength.





Steel samples bonded with Teroson MS-9380 adhesive, subjected to salt spray testing at 35°C		Aluminium samples bonded with Loctite UK1366B10/UK5452, subjected to deionized water	
	unaged		unaged
	6 weeks salt spray testing		10 weeks of deionized water

Figure 6: Left, uncoated steel samples subjected to salt spray testing; right, Aluminium samples subjected to deionized water

During the ADHESION project commonly applied ship building primer systems were investigated as an interface for bonding. These primer systems normally form the basis of a paint system that protects the metal surface from corroding. The results of the test performed during ADHESION are twofold (Bosman, 2012):

1. Shipbuilding primer systems make adhesive bonds durable in corrosive environments
2. When shipbuilding primers systems are used in combination with structural adhesives, failure occurs in the primer layer

Although the first result is promising the second result poses a major design challenge. The primer failure is a brittle failure and difficult to model during joint design. In a bonded joint one generally aims for a cohesive failure, because this yields a more predictable failure mode during the design process. Shipbuilding primers did turn out to be a suitable substrate for low strength elastic adhesives, such as MS polymers and 1 component PU adhesives. These adhesive have considerably lower strength and therefore fail before the primer layer fails.

For durable bonds which do use the full potential of the adhesive, leading to cohesive failure, a different primer system than the currently applied paint primers needs to be identified. Silane primers have been successfully applied in the past for creating durable adhesive bonds (Kinloch, 1987). To what extent these systems are applicable to ship building requires more testing. There is already experience with Silane primer in composite patching of metal ship structures (Karr, 2014). Alternatively the adhesive can be applied directly to the bare metal but then the joint needs to be protected from the corrosive environment by a coating or sealing on top of the bonded joint.

## 5. TOWARDS PRIMARY STRUCTURAL BONDING IN SHIP STRUCTURES

The ADHESION project did not lead to a large breakthrough in adhesive bonding of ship structures, but it did create the required knowledge base to increase the number of applications of adhesive bonding in the industry. At multiple shipyards that participated in the ADHESION project engineers continue to design bonded solutions to joining challenges. Due to the limited experience with the durability of adhesives, the applications should be limited to low risk applications for the moment. In case more critical components are bonded, one can opt for a hybrid solution, where mechanical fasteners are used in combination with the adhesive. This way trust can be built in this promising technology. Best bonding practices need to be secured in hand books and applications need to be monitored to gain knowledge about the long term performance of adhesives in a maritime environment. This way adhesive bonding can find its way in the industry as a cost effective alternative to welding and mechanically fastening.

## 6. CONCLUSIONS

This paper described the key results of the research project 'ADHESION' which focused on adhesive bonding in the maritime industry. The project goal was to gain information and implement technology for certified adhesive joints in shipbuilding



practice. The project resulted in a firm knowledge base about requirements that a bond needs to fulfill, to survive in a marine environment. The conditions at the shipyard proved to be suitable for bonding and employees from the yard were trained in bonding practices. A large number of specimen tests were performed, which showed metals need to be protected against corrosion prior to bonding. A corrosion resistant primer system that is strong enough to result in cohesive failure has not been identified yet. The biggest challenge that remains is to develop adhesive bonds that survive the marine environment and to make accurate predictions about the service life. To tackle this challenge it necessary to gain experience with bonding by means of low risk applications. This process has been started at some of the shipyards that participated in ADHESION.

## 7. ACKNOWLEDGEMENTS

The authors would like to thank the project participants: Airborne Composites, Amels B.V., Bureau Veritas, CMTI, Damen Schelde Naval Shipbuilding, Damen Shipyards Gorinchem, Henkel & Co Gmbh, MTI Holland BV, Netherlands Maritime Technology, Lightweight Structures BV, Lloyd's register EMEA, TU Delft (faculteit Luchtvaart- en Ruimtevaarttechniek/Hechtingsinstituut, Design and Production of composite Structures, faculteit 3ME)

## REFERENCES

- Beumler, T. (2004). *Flying Glare*. Delft: DUP Science.
- Bosman, T. (2012). *Adhesion Project, Technical Summary*. Delft: TU Delft.
- Burchardt, B. (2010). Advances in Polyurethane adhesives. In A. Dillard, *Advances in structural adhesive bonding* (pp. 35-65). Cambridge: Woodhead Publishing Limited.
- Habenicht, G. (2008). *Applied Adhesive Bonding: A Practical Guide for Flawless Results*. London: Wiley.
- Karr, D. (2014). Fatigue Testing of Composite Patches for Ship Steel Plating Fracture Repair. *Ship Structure Committee 2014 Conference proceedings* (pp. 1-17). Blatimore: Ship Structure Committee.
- Kinloch, A. (1987). *Adhesion and Adhesives*. London: Chapman and Hall.
- Kwakernaak, A., Hofstede, J., Poulis, J., & Benedictus, R. (2010). Improvements in bonding metals (steel, aluminium). In D. Dillard, *Advances in structural bonding* (pp. 185-236). Cambridge: Woodhead Publishing.
- Pascoe, J., Alderliesten, R., & Benedictus, R. (2013). Methods for the prediction of fatigue delamination growth in composites and adhesive bonds – A critical review. *Engineering Fracture Mechanics*, 72-96.
- Weitzenböck, J. (2010, 11 17). *The BONDSHIP project guidelines*. Retrieved 08 26, 2014, from BONDSHIP DNV research: <http://research.dnv.com/bondship/Guidelines.htm>
- Weitzenböck, J. (2012). *Adhesives in Marine Engineering*. Cambridge: Woodhead Publishing.

# MERITS OF FLAPPING ROLL STABILIZER FINS

R.P.Dallinga, MARIN, The Netherlands

S.Rapuc, MARIN, The Netherlands

## 1. SUMMARY

Since their introduction in the late 1990s, the use of fin stabilizers in the stabilization of rolling ships at zero forward speed has become quite common. This stabilization is generally achieved with more or less conventional low-aspect ratio fins with increased actuator power to realize a “kicking” motion. The limitations of this compromise and a wealth of literature on “flapping flight” led MARIN in 2008 to explore the merits of a flapping fin alternative by means of a set of experiments. The present work describes, after a general introduction, the results of these tests and a comparison with the conventional solution. In addition the results of very recent experiments with a commercial application of the principle are discussed.

## 2. INTRODUCTION

In the late 1990’s MARIN suggested using low-aspect ratio stabilizer fins in a “kicking” mode to stabilize the roll of a motor yacht at zero speed. After publication [Dallinga, 1999], the industry quickly recognized the potential and developed a range of products that make use of the principle; nowadays stabilizers with a “zero-speed” mode are quite common for this kind of ship.

To obtain reaction forces at zero speed the normal “zero-speed” fin is a more or less conventional stabilizer fin with a low aspect ratio and an eccentric shaft position. This geometry is a compromise with the optimum arrangement for transit conditions.

One point concerns the performance of a low aspect ratio fin in transit. The related low lift-slope leads to relatively large fin angles which in turn yield a relatively large root-gap, resulting in relatively low stabilizing performance and a relatively high drag. In addition the position of the fins in the bilge leads to considerable interaction with the bilge keels ahead of and behind the fins, interactions which downgrade the overall performance.

Another point is the efficiency of the kicking motion that is used at zero speed in generating a transverse force, limitations in the eccentricity of the fin shaft imply that only the aft part of the fin contributes to the desired reaction force.

Last but not least, the “solution” for these issues, a relatively large fin, yields a drag penalty in transit.

The above observations and developments in research on flapping flight [Licht, 2004, Soueid, 2005] led MARIN to investigate the merits of a high-aspect ratio “flapping” fin rotating along an axis parallel to the centre line of the ship. This investigation was conducted in 2008.

Although the interpretation of these exploratory measurements was hampered by limitations of digital servo engines of the day, the results were sufficient to inspire AntiRoll BV to develop a practical application of the principle. This system consists of a retractable high aspect ratio fin with a dual rotating mechanism. This innovation allows switching of the operation between a conventional rotation mode and a flapping mode. The hydrodynamic performance of the concept was the subject of a theoretical study in 2013 and detailed model testing in the spring of 2014.

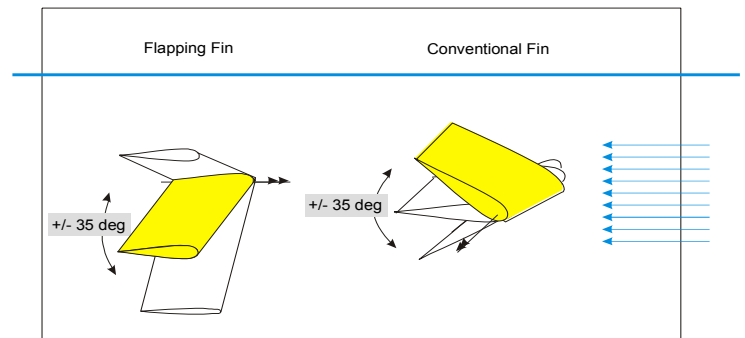


Figure 1 [Fin Operating Modes]



Figure 2 [AntiRoll fin design]

### 3. FIN REACTION FORCES, CONTROL AND ROLL DAMPING

#### 3.1 Fin reaction forces

##### 3.1 (a) Zero speed

As will be demonstrated, the forces at zero speed can be estimated to some extent by regarding them as the sum of an inertia and a drag component. The inertia component is the product of the “added mass” and the acceleration of the fin. The drag follows from the exposed area and the square of the fin velocity. Because the mechanical velocity and acceleration of the fin are relatively high, the roll and wave induced hydrodynamic water velocities and accelerations as well as memory in the generated flow can be neglected.

A practical implementation of the above principle evaluates the forces in a “strip”-wise manner, neglecting the interactions between the individual strips. For the conventional rotation mode, the integration is chord-wise; the estimate of the added mass assumes the proximity of the ship side shell. For the flapping mode the integration is span-wise.

##### 3.1 (b) Transit

Work in the MARIN Cooperative Research Ships (CRS) addressed the reaction forces of conventional high- and low-aspect ratio fin stabilizers in transit. The developed calculation method recognizes that the basic lift-drag characteristics, which are determined by the planform, aspect ratio, thickness and area (see Hoerner, 1965, van Oossanen, 1981), require a correction for the fact that the fin is operating on a curved surface, below a free surface and in the boundary layer of the ship.

In the above method a panel code is used in the evaluation of the actual angles of attack; the method accounts for the motion and wave induced local cross-flow velocities along the bilge. In this way the contribution of the fin stabilizers to the roll excitation (through the wave induced false angles of attack) is accounted for.

Last but not least, the calculated fin forces require a correction for a substantial frequency-dependent fin-to-hull interaction (see Dallinga, 1993).

The reaction forces of “flapping” fins at increasing forward speed change from inertia and drag driven forces at low speed to lift dominated reaction forces at high speed. The evaluation of the forces is complicated because the angles of attack at modest forward speed are extremely large. The physics resembles that of “dynamic stall” (Gaillard, G., 2003), a problem that complicates the definition of exact operational limits for conventional stabilizer fins.

#### 3.2 Fin control

##### 3.2 (a) Zero speed

As will be shown in the next section, a simple way to increase the effectivity of zero-speed operation is to generate a high reaction force at the moment the roll velocity is highest. This can be achieved with a “bang-bang” mode in which the fin is moving fast from one extreme position to the other. In this case the fin motion trajectory may be regarded as a sequence of an acceleration, a constant-speed transit and a deceleration.

A first objective of a zero-speed control strategy consists of maximizing the overall work of the reaction force in roll within the constraints of the actuator (torque, velocity). A second objective is to avoid exposing passengers to the unpleasant jerk associated with transient forces. Last but not least, it may be very economic to reduce fin activity if the roll amplitudes hardly contribute to passenger discomfort.

##### 3.2 (b) Transit

In transit stabilizer fins are often operated in a passive mode if the comfort requirements are met. In higher waves the fins become active with a mechanical reaction on the roll and roll velocity. The first reaction limits any low-frequency response of the ship due to, for instance, wind gusting and steering and wave induced excitation at low encounter frequencies. The reaction on the roll velocity suppresses the resonant roll response due to excitation at the natural frequency of roll.

Experience from model tests shows that a simple PD control yields a very satisfactory roll reduction. A common way to estimate the control gain is by assuming that the fins should work at their “limits” when the criterion of roll is reached. The limits can refer to the maximum mechanical angles or the effective angles of attack in relation to (an assumption on) stall.

In principle there is a wide range of secondary objectives which could be addressed. One can think of reducing the drag by avoiding “unnecessary” large fin reactions (if the roll angles are below a particular criterion), avoiding the wave induced roll excitation originating in the wave induced false angles of attack on the fins with a force feedback and avoiding the perils of loss of lift due to stall. For conventional and flapping fins alike, one can speculate on a control strategy which maximizes the forward thrust due to the wave and motion induced false angles of attack.

### 3.3 Roll damping

The key factor relating the fin reaction forces to the equivalent linear damping  $b_{EL}$  is the dissipated power  $P$  of the fin reaction moment  $M_x$  counteracting the roll velocity  $\dot{\phi}$ . It is given by:

$$b_{EL} = \frac{P}{\sigma_{\dot{\phi}}^2} \text{ in which } P = \frac{\int_0^T M_x \cdot \dot{\phi} \cdot dt}{T}$$

If the reaction moment  $M_x$  is proportional to the roll velocity (as in the case of the wave making damping), the dissipated power is proportional to the rms roll velocity  $\sigma_{\dot{\phi}}$  squared. This means that the roll damping is independent of the roll amplitude.

In the case where quadratic drag forces dominate the reaction forces (as for the drag from bilge keels), the work increases with the third power of the roll amplitude. In this case the equivalent linearized damping is proportional to the roll amplitude.

Because in the case of zero-speed operation the reaction forces are governed by the inertia and drag forces induced by local, relatively high velocities and accelerations of the fin, the reaction forces are virtually independent of the roll velocity. Consequently the work in roll is proportional to the roll amplitude and the equivalent linearized damping declines with the roll amplitude. This characteristic is also partly observed in case of stabilization by means of anti-roll tanks [Dallinga, 2002].

Because the lift slope of conventional stabilizer fins is quite linear, the reaction forces of passive fins at forward speed are proportional to the roll velocity as long as the angles of attack stay below the stall angle. If the mechanical reaction of the fin is also proportional to the roll velocity, the reaction forces due to the fin activity behave in the same way. In this case the effective damping is independent of the roll amplitude.

Once the fins start reaching their mechanical limits or if the (sum of the false and mechanical) angles of attack reach (the poorly defined) stall angle the effective linearized damping will reduce with increasing roll amplitude.

## 4. SIMPLE ESTIMATES OF ZERO-SPEED REACTION FORCES AND DAMPING FROM FLAPPING FINS

### 4.1 Fin reaction forces from a strip-wise analysis

#### 4.1 (a) Flapping fin

Assuming a fin with span  $s$  and chord  $c$ , rotating around the base and neglecting end-effects the added mass  $a_{\alpha\alpha}$  can be estimated from the 2D sectional added mass  $a'$ . Neglecting free-surface effects the 2D value equals  $\rho \cdot \pi \cdot (c/2)^2$ . The reaction force and the moment around the base become:

$$M_{xI} = \int_0^s \ddot{\alpha} \cdot x \cdot a' \cdot x \cdot dx = \ddot{\alpha} \frac{1}{3} a' s^3 = \ddot{\alpha} \frac{1}{12} \rho \pi c^2 s^3 \text{ and } F_{yI} = \int_0^c \ddot{\alpha} \cdot x \cdot a' \cdot dx = \ddot{\alpha} \frac{1}{2} a' s^2 = \ddot{\alpha} \frac{1}{8} \rho \pi c^2 s^2$$

The ratio of the moment and the reaction force (the arm of the reaction force) becomes two-thirds of the span  $s$ .

Assuming a quadratic local drag force, proportional to the chord, the moment and reaction force become:

$$M_{xD} = \int_0^s c_D \frac{1}{2} \rho (\dot{\alpha} \cdot x)^2 \cdot c \cdot x \cdot dx = \dot{\alpha}^2 \frac{1}{8} \rho c_D \cdot c \cdot s^4 \text{ and } F_{yD} = \int_0^s c_D \frac{1}{2} \rho \cdot (\dot{\alpha} \cdot x)^2 \cdot c \cdot dx = \dot{\alpha}^2 \cdot \frac{1}{6} \rho c_D \cdot c \cdot s^3$$

The arm of the drag component in the reaction force is three-quarters of the span.

#### 4.1 (b) Conventional fin

If the fin were mounted on a flat base plate, the expected sectional added mass increases to  $\rho \cdot \pi \cdot s^2/2$ . Reversing the chord and span and assuming a shaft position at a distance  $a$  from the “leading” edge the inertia components become:

$$M_{xI} = \int_{-a}^{c-a} \ddot{\alpha} \cdot x \cdot a' \cdot x \cdot dx = \ddot{\alpha} \frac{1}{6} \rho \pi s^2 [(c-a)^3 + a^3] \text{ and } F_{yI} = \int_{-a}^{c-a} \ddot{\alpha} \cdot x \cdot a' \cdot dx = \ddot{\alpha} \frac{1}{4} \rho \pi s^2 [(c-a)^2 - a^2]$$

The moment and force from the drag force become:

$$M_{xD} = \int_{-a}^{c-a} c_D \frac{1}{2} \rho (\dot{\alpha} \cdot x)^2 \cdot s \cdot x \cdot dx = \dot{\alpha}^2 \frac{1}{8} \rho c_D \cdot s \cdot [(c-a)^4 - a^4] \text{ and}$$

$$F_{yD} = \int_{-a}^{c-a} c_D \frac{1}{2} \rho (\dot{\alpha} \cdot x)^2 \cdot s \cdot dx = \dot{\alpha}^2 \frac{1}{6} \rho c_D s [(c-a)^3 + a^3]$$

#### 4.2 Work in roll and roll damping from a harmonic fin motion

If we assume a flapping fin going through a sinusoidal motion  $\alpha_a \cdot \sin(\omega \cdot t + \varepsilon)$  with amplitude  $\alpha_a$  with the same frequency  $\omega$  as the roll motion  $\varphi_a \cdot \sin(\omega \cdot t)$  (see Figure 3) the mean power dissipated by the reaction force F of a single fin performed in roll becomes:

$$P_F = \frac{\int_0^T \omega \cdot \varphi_a \cos(\omega t) \cdot (-\omega^2 \alpha_a \sin(\omega t + \varepsilon)) \frac{1}{8} \rho \pi c^2 s^2 + \omega \alpha_a \cos(\omega t + \varepsilon) \cdot |\omega \alpha_a \cos(\omega t + \varepsilon)| \cdot \frac{1}{6} \rho c_D c s^3}{T}$$

$$= \omega \cdot \varphi_a \cdot (\omega^2 \cdot \alpha_a \frac{1}{16} \rho \cdot \pi \cdot c^2 \cdot s^2 \cdot \sin(\varepsilon) - \omega^2 \alpha_a^2 \cdot \frac{4}{18\pi} \rho \cdot c_D \cdot c \cdot s^3 \cdot \cos(\varepsilon))$$

In the above  $\varepsilon$  denotes the phase lead of the fin angle with respect to the roll motion. The optimum value of the phasing of fin motion depends on the contribution of the drag.

The damping follows from the mean power of the moment of the above force around the ship CoG and the orientation of the fin with respect to the arm to the CoG. Assuming 2 fins with an arm  $r$  and assuming a mean fin orientation along the arm to the CoG the roll damping becomes:

$$b_\varphi = \frac{2 \cdot P_F \cdot r}{\frac{1}{2} \cdot (\omega \cdot \varphi_a)^2}$$

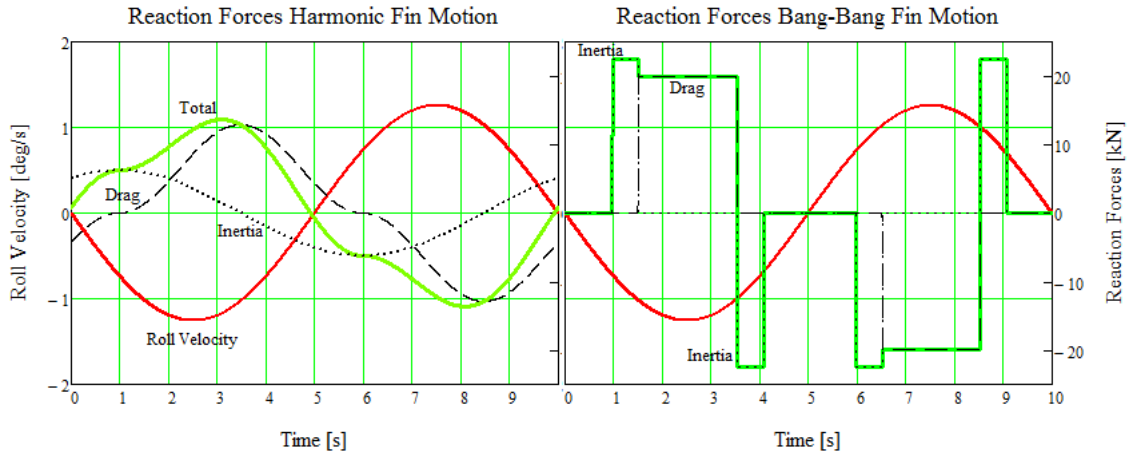


Figure 3 [Reaction forces from a harmonic and a bang-bang fin motion]

#### 4.3 Work in roll and roll damping from a bang-bang fin motion

Because the roll period of many ships is fairly long and because the angular range of the fins is limited, the acceleration and velocity and related inertia and drag forces become relatively small. In this case, concentrating higher reaction forces around the maximum roll velocity is a way to enhance the damping.

As a practical case, we considered the application of a constant torque over the initial acceleration and the constant-velocity transit stage. In this case, the initial acceleration follows roughly from the added inertia and the transit-velocity from the drag moment per unit angular velocity squared. Neglecting the increasing velocity, the duration of the initial acceleration is simply

the ratio of transit velocity and the acceleration; the duration of the transit stage follows from the fin angle range and the velocity.

If we assume active deceleration (by means of the actuator) its magnitude equals that of the acceleration, in which case the contributions to the impulse cancel each other if they occur more or less symmetrically with respect to the peak in the roll velocity. In this case the magnitude of the work tends towards the product of the drag force, roll velocity and the duration of the constant-speed transit stage with increasing available constant actuator moment  $M^*$ . In this case the reaction force  $F_{yDc}$ , the dissipated power  $P_{Fc}$  and roll damping  $b_{\phi c}$  simply become:

$$F_{yDc} = \frac{8}{6} \cdot \frac{M^*}{s} \text{ so } P_{Fc} = \omega \cdot \varphi_a \cdot F_{yc} = \omega \cdot \varphi_a \cdot \frac{8}{6} \cdot \frac{M^*}{s} \text{ and } b_{\phi c} = \frac{16}{3} \cdot \frac{M^*}{s \cdot \omega \cdot \varphi_a}$$

To illustrate the effect of available actuator torque and the difference between a harmonic and a shorter transient motion the work sample calculations were made for a fin with span  $s=4\text{m}$ , chord  $c=2\text{m}$  moving over a  $2 \times 35\text{deg}$  range. The assumed drag coefficient was  $c_D=4$ ; the sample roll amplitude and period were  $2\text{deg}$  and  $10\text{s}$ . Figure 4 below compares the dissipated power in roll of a single fin from a sinusoidal and a constant-moment approach. It is clear that the harmonic fin motion is relatively ineffective. The combined effect of the higher reaction force and a shorter duration of the constant-velocity stage yields a dissipated power in roll which is proportional to the square root of the available fin torque.

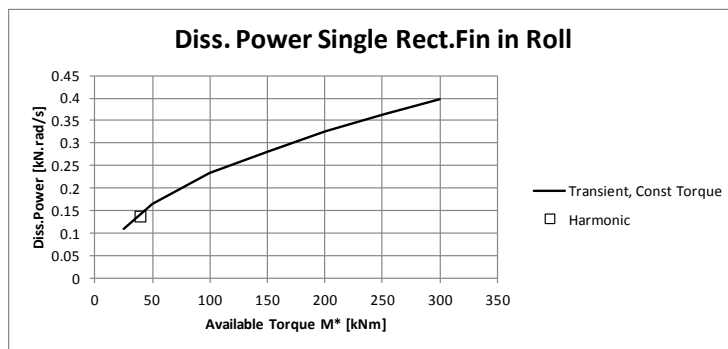


Figure 4 [*Damping power of a flapping fin as a function of the available actuator torque*]

## 5. 2008 EXPERIMENTS

The objective of the 2008 experiments was to explore the nature of the reaction forces and the related roll damping of flapping fins and to compare these with the conventional fin solution.

### 5.1 (a) Fin models

During the tests the fins (see Figure 5) were mounted on a flat plate. A digitally controlled servo engine on the back facilitated oscillations in a conventional rotation mode or a flapping mode.



Figure 5 [*Fin models*]

A rectangular fin with NACA0015 profile and a span of 175mm and a chord of 90mm was oscillated in a flapping mode; the set-up allowed an angular range up to 70deg. A limitation of the set-up was a rotation around a point 79mm below the base of the fin and a substantial gap between the base of the fin and the supporting plate.

The results were compared with measurements on a conventional NACA0015 fin with a span of 90mm and a mean chord of 175mm. The root gap of this fin was very small.

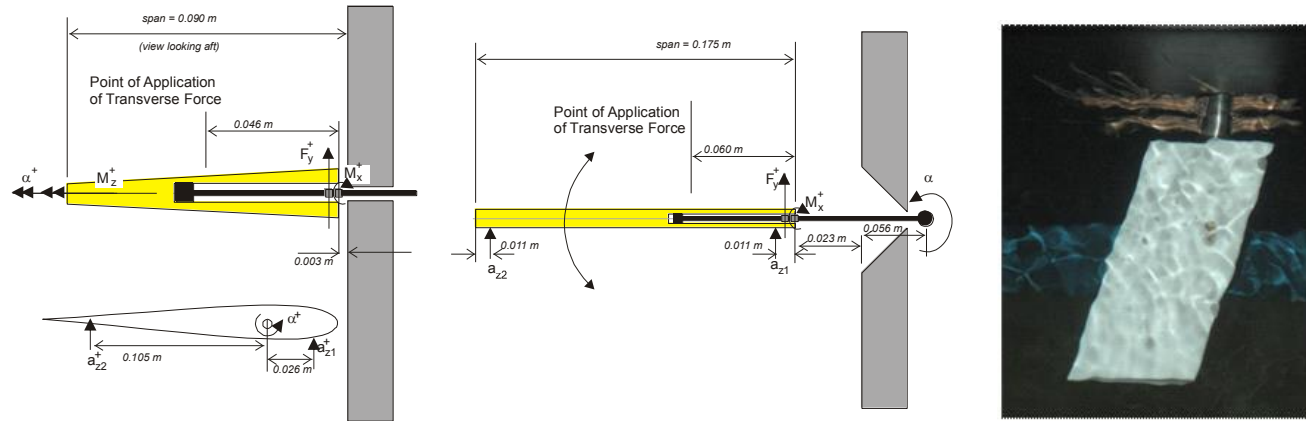


Figure 6 [Fin test set-up]

#### 5.1 (b) Measurements

The measurements comprised 5 components of the reaction forces at the base of the fin body, linear accelerations at two points (to enable derivation of the angular acceleration) and the output angle of the servo unit.

#### 5.1 (c) Fin actuator

At the time of the tests the kicking acceleration of the fin was regarded as a key parameter in the reaction forces. For this reason “hard kicking motions” were tested. This rather “aggressive” mode made us aware of the importance of a stiffness and the (the absence of) back-lash in the connections; vibrations of the fin on the transducer interfered with the hardware control loop inside the fin actuator servo. These vibrations made it hard to establish a clear relation between the fin motion and reaction forces. As shown by the most recent test results (see Section 6), new generations of servo units yield a better control over the actual maximum acceleration of the fin.

#### 5.1 (d) Test programme

For the conventional fin the test programme comprised tests in a harmonic and “bang-bang” mode at zero and two non-zero speeds. In addition, the static lift and drag at forward speed were determined.

For the flapping fin, tests were performed in a bang-bang mode at zero and two non-zero forward speeds. The harmonic oscillation was only performed at non-zero speed.

For both types of fins the cycle time (corresponding to half the roll period of the ship to be stabilized), which equals the sum of the fin acceleration, the constant velocity and the deceleration and a “resting” period, was varied to obtain information about fluid-memory effects.

#### 5.1 (e) Analysis

The measurements on the linear accelerations were used to derive the angular acceleration. The measured forces were corrected for the structural weight and inertia, which were derived from oscillation tests in air. The lift and drag, which were measured inside the rotating shaft, were corrected to obtain values in an earth-bound system of coordinates. These forces were correlated with the fin angular acceleration and velocity.

In addition to an analysis of the forces, the dissipated power of the reaction force in a virtual (1rad/s roll velocity) roll motion was evaluated. This quantity is the time averaged work performed by the linear reaction force in roll in Nrad/s. Derivation of the work of a pair of fins in roll requires multiplication by a factor of 2 (to account for a pair of fins) and the effective arm of the reaction force to the centre of gravity of the ship.

## 5.2 Results obtained for the flapping fin

### 5.2 (a) Nature of the reaction forces

Figure 7 illustrates the character of the signal measured on the flapping fin at zero speed (basic flapping fin, 2s cycle time, 70deg fin angle range, 150deg/s velocity). As indicated in the foregoing it shows that the acceleration and deceleration phases of the “kicking” motion vary quite erratically. Despite this behaviour the measured transverse force follows the measured acceleration quite well in these stages. In the intermediate stage, at constant velocity, the measurements suggest a more or less constant drag force.

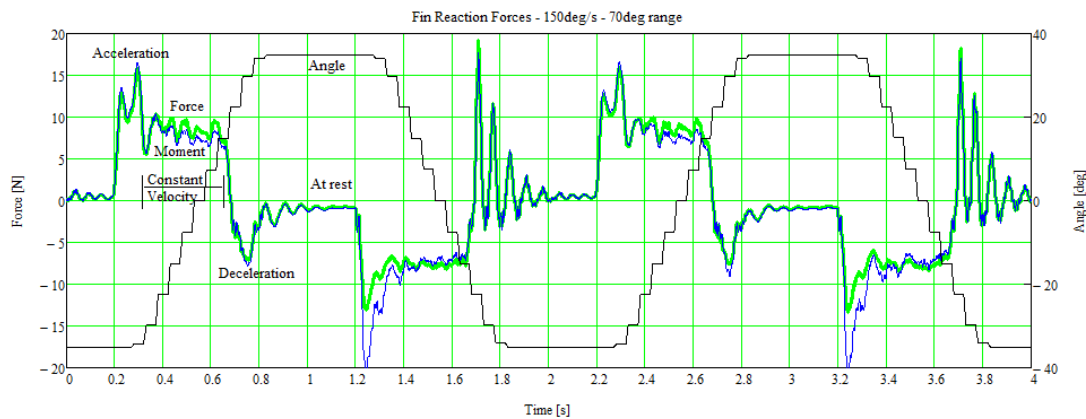


Figure 7 [Reaction forces of flapping fin]

The magnitude of the drag force is around 8.5N. The corresponding drag per unit velocity squared is  $8.5/2.62^2=1.24\text{N}/(\text{rad}/\text{s}^2)$ . Using the expression from Section 4.1, correcting for the fact that the rotation point is not at the base one obtains a force per unit angular velocity squared equal to  $1/6 \cdot \rho \cdot c_D \cdot c \cdot (S_{\text{tip}}^3 - S_{\text{base}}^3) = 0.245 \cdot c_D$ . This suggests an effective drag coefficient of around 5 (which is typical for this kind of instationary flow; see also Section 6).

Calculating the point of application of the reaction force in the same way yields a point at 0.11m above the fin base; this is considerably larger than the value suggested by the fin force and moment measurements, which suggest an arm of 0.06m. It is concluded that the simple expression presented in Section 4.1 highly exaggerates the moment acting on the fin.

### 5.2 (b) Effect of forward speed, range, cycle time

Figure 8 summarizes the power dissipated by a single fin against a 1rad/s roll velocity. The results are given for the basic rectangular flapping fin in the bang-bang mode, for zero and two forward speeds and two fin angular velocities as a function of the angular minimum-maximum range.

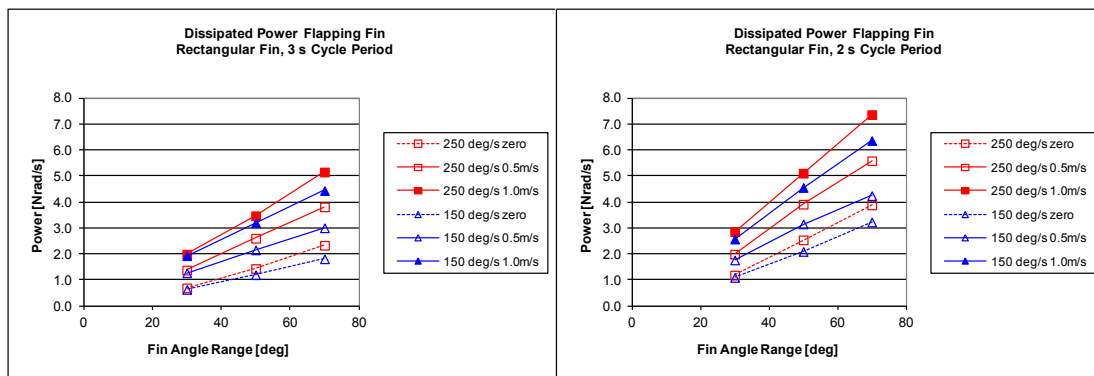


Figure 8 [Effect of angular range on power dissipated in roll]



The results can be understood by considering the nature of the reaction force discussed in the previous section. If we assume that the impulse contributions from the acceleration and deceleration stage largely cancel, the effective impulse of the reaction force follows from the force in the “stationary velocity” stage and the force, yielding  $8.5 \times 0.35 = 3\text{Ns}$ . If the pulse is sufficiently short, the corresponding dissipated power<sup>1</sup> of two “kicks” over a full 2cycle roll period (per 1rad/s roll velocity) becomes  $2 \times \frac{3}{2} = 3\text{Nrad/s}$ . This value agrees well with the result of the analysis of the test results which considers the evolution of the roll velocity over the duration of the fin motion.

### Effect of fin angle range

With an increasing fin angle range the reaction force does not always act in the ideal direction. In addition, the longer constant speed transit time decreases the work in roll. Despite these anticipated trends, the results in all conditions show that the work of the fin is proportional to the fin angle range.

### Cycle time

A longer roll period associated with a longer cycle time reduces (also through an increase of the waiting time between “kicks”) the work of the fin reaction force. It was expected that the cycle time would also affect the reaction forces through memory effects in the water. In practice these effects are limited.

### Forward speed

At the lower fin velocity (150deg/s) the vertical velocity at the fin tip is about  $2.62 \times 0.254 = 0.66\text{m/s}$ . At 0.5m/s this implies a local angle of attack of over 50deg; at 1m/s forward speed this reduces to about 33deg. Despite the expected changes in the nature in the fin reaction forces (from “quadratic drag” to “linear lift”) the magnitude increases very smoothly with increasing speed.

Figure 9 summarizes the foregoing trends with a plot of the product of the dissipated power and cycle time divided by the double-amplitude fin range and the square root of the fin velocity as a function of forward speed. These trends describe the overall test results quite well. At 1m/s (a speed which correspond with some 8knots full scale for the present fin size) the fin reaction forces are roughly twice the values at zero speed.

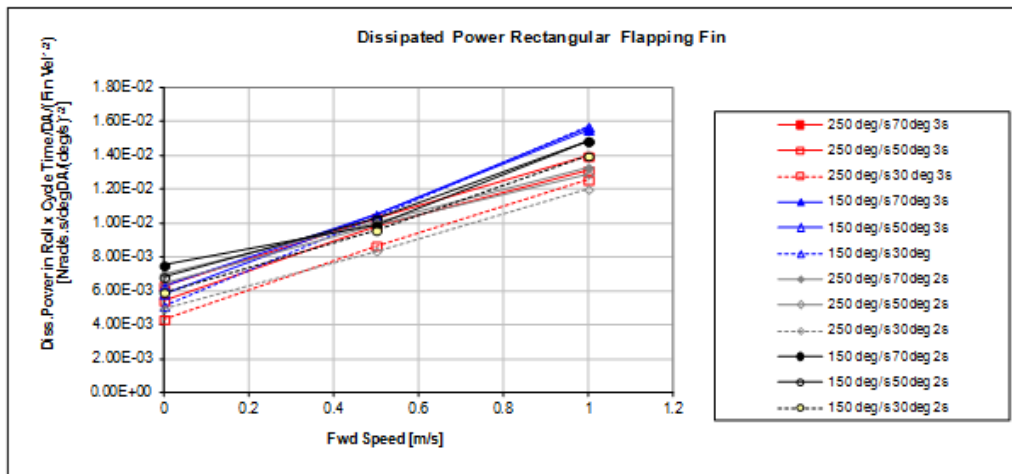


Figure 9 [Dissipated power in roll x cycle time per deg fin angle range square root of the fin velocity]

<sup>1</sup> Note that multiplication by the number of fins (often 2) and the arm to the CoG of the ship and an assumption on the roll amplitude are required to obtain the roll damping. See sections 2.3 and 3.2.

### 5.3 Results obtained for the conventional fin

#### 5.3 (a) Nature of the reaction forces

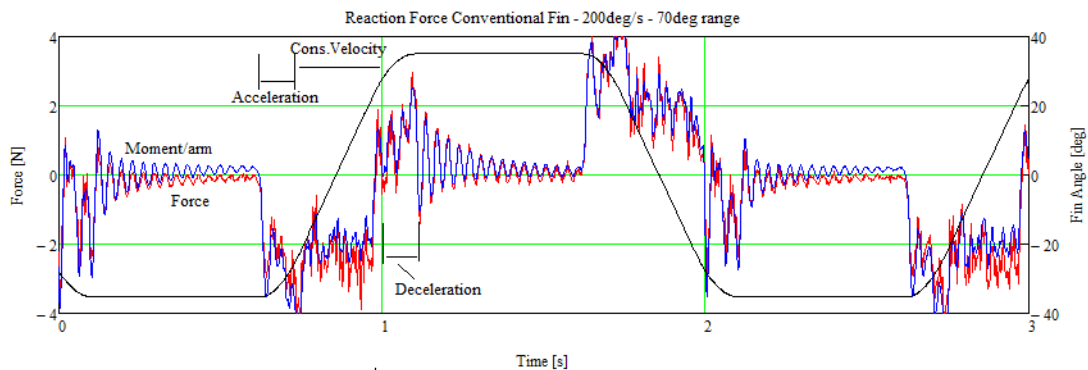


Figure 10: [Reaction forces of conventional fin]

The above figure shows a sample of the reaction force from a conventional fin at zero speed. As in the case of the flapping fin, the signals show considerable noise.

Despite the clear vibrations, the drag of the fin in the “constant velocity” stage can be recognized. The drag force, acting over a period of about 0.25s, amounts to about 2.5N, yielding an impulse of 0.625Ns. The related damping estimate amounts to  $2 \times 0.625 \times 1 \text{ rad/s} / 2\text{s} = 0.625 \text{ Nrad/s}$ .

The drag force amounts to  $2.5 / 3.5^2 = 0.2 \text{ N}/(\text{rad/s})^2$ . The estimate from Section 4.1 yields  $1/6 \cdot \rho \cdot \pi \cdot c_D \cdot ((c-a)^3 - a^3)$ , which amounts (with  $s=0.09$ ,  $c=0.16$  and  $a=0.033\text{m}$ ) to  $0.031 \cdot c_D$ . This suggests an effective drag coefficient of 6.

The measured moment and force suggests a point of application at 0.075m aft of the shaft, a value which is somewhat smaller than that from the estimates on the moment and force from Section 4.1 (which yields 0.1m).

#### 5.3 (b) Effect of forward speed, range and cycle time

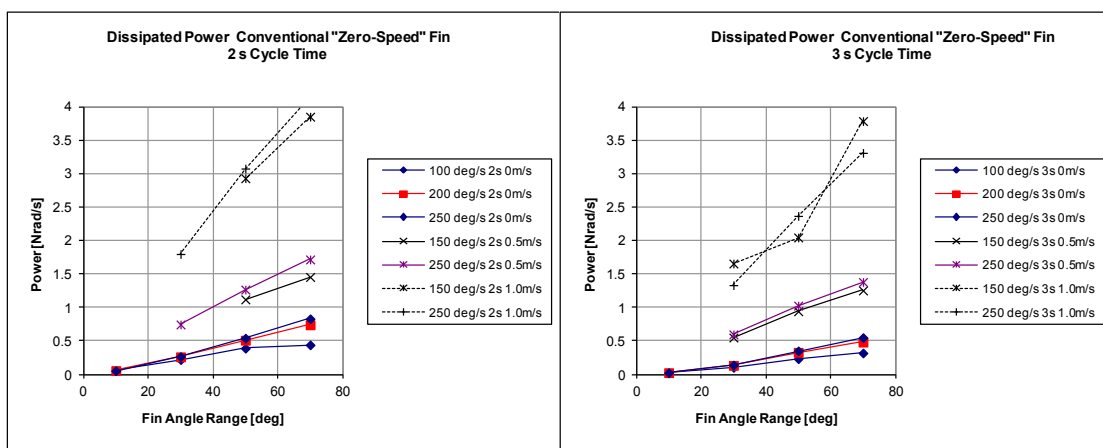


Figure 11: [Dissipated power in roll of conventional fin]

The figures above summarize the power dissipated by the conventional fin. The nature of the reaction force, being proportional to the fin angle range and decreasing with the cycle time, seems similar to the flapping fin; however the increase of the damping with forward speed seems much stronger.

### 5.3 (c) Comparison of a flapping and a conventional fin

The figure 12 shows results of a comparison of the work from both conventional and flapping fin systems at equal fin motions, velocities and accelerations.

Comparing the dissipated power in roll of both fins shows that the difference in performance is much larger than the small difference in fin area (the flapping fin was 9% larger than the conventional fin).

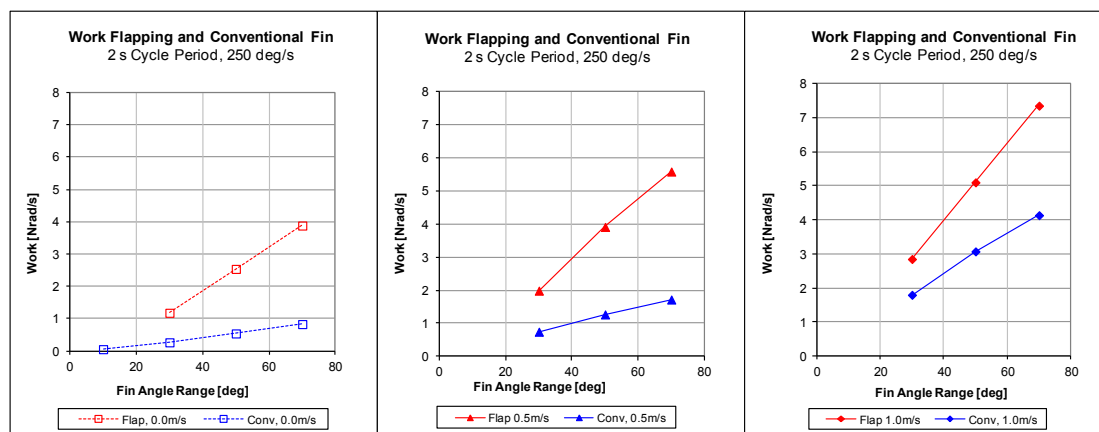


Figure 12: [Comparison of dissipated work in roll of conventional and flapping fins]

It is noted that, to achieve the same fin motions, velocities and accelerations, a flapping fin requires significantly more actuator power than a conventional fin. The comparison presented in Section 7 provided more information on this.

## 6. 2014 EXPERIMENTS

Perceiving advantages of flapping fins, AntiRoll BV developed an articulation which allows reduction of roll motion at both zero and forward speed. At zero speed, the fin is acting in a “flapping” mode while at forward speed it is acting in a conventional “rotating” mode. In addition, and if no active roll stabilisation is required, the AntiRoll fins can be retracted onto the hull.

Following extensive theoretical studies, and facing concrete applications, AntiRoll BV requested MARIN to perform an extensive test campaign which could be used as validation of the design tool. This was achieved through a two weeks test campaign in the MARIN Concept Basin (CB) in April 2014.

### 6.1 General information

#### 6.1 (a) Test setup

Contrary to the 2008 tests, the fin was mounted on a body of revolution, ensuring a minimal root-gap in the flapping mode. The set-up allowed activation of the fin in both flapping mode (used at zero and low forward speed) and rotative mode (used at forward speed).

Based on the experience gained with the test from 2008, a particular effort was made beforehand to ensure that the set-up was sufficiently rigid and the servo-control sufficiently fast to suppress vibrations.

#### 6.1 (b) Fin models

Because the concept “parks” the fin along the hull when not in use, four different fin curvatures were tested. All 1:8 scale fins had an aspect ratio of 2, and a full scale area of 2 m<sup>2</sup>. Each fin was fabricated out of injected PVC.

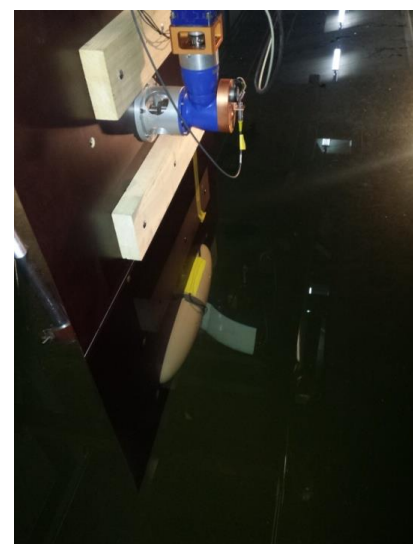


Figure 13 [2014 test setup]

### 6.1 (c) Fin actuator

A powerful modern servo motor available at MARIN was used for this test. It was placed above the water level. The servo position and velocity were controlled via a feedback system.

### 6.1 (d) Test programme

For each fin the tests comprised:

- Four different flapping acceleration profiles at zero speed
- One harmonic flapping acceleration profile at several forward speeds
- Two harmonic rotating acceleration profiles at several forward speeds

### 6.1 (e) Analysis

Linear accelerometers were placed on the fin models and on the servo shaft to derive the angular acceleration. The measured forces were corrected for the structural weight and inertia, which were derived from oscillation tests in air. The lift and drag, which were measured inside the rotating shaft, were corrected to obtain values in an earth-bound system of coordinates. These forces were correlated with the fin angular acceleration and velocity.

In addition to the analysis of the forces, the power dissipated in a virtual roll motion by the fin reaction force was evaluated.

## 6.2 Results obtained for flapping fins at zero speed

The following results were obtained from a test with the straight fin model.

Figure 14 gives an impression of the quality of the set-up and measurements for a case with acceleration and deceleration transient phases of  $120\text{deg/s}^2$  and a maximum velocity of  $65\text{deg/s}$ . The first three plots present the fin angle, angular velocity and angular acceleration. In these plots, the blue line represents the test measurement, while the red one represents the target values. From these figures, one may see that the target fin angle and the fin angular velocity were very well reproduced. Even the fin acceleration, which was harder to realize with the same accuracy, is rather well in line with the target value.

The lowest plot presents a comparison of the measured fin normal force and the estimated one. For the estimation of the force, a  $C_D$  of 5 was used. This comparison shows that the maximum peaks are not very well mimicked – possibly due to some residual variations in the test set-up – but the drag force and the global force shape are well estimated by the rather crude theoretical model detailed in Section 4.1 (a).

The present test campaign showed that the total required fin power and the realized damping in roll were estimated quite well by the theoretical model. Only the spanwise integration was truncated to allow for 3D “end effects”.

From the measured force and moment, the averaged point of application of the fin force is measured to be at 58% of the fin span. This result is rather well in line with the equations presented in Section 4, when taking into consideration the distance between the fin root and the fin pivot point.

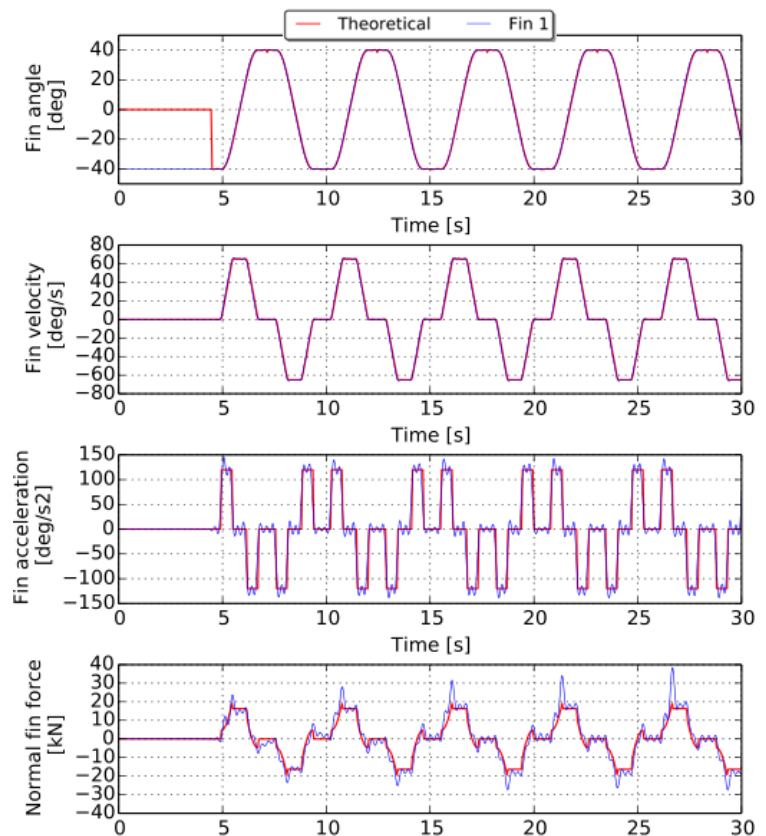


Figure 14 [Measured and target fin angular motion, velocity, acceleration and normal force. The calculated normal force was obtained with a drag coefficient of 5]

### 6.3 Comparison of the rotating and flapping mode at forward speed

#### Fin damping

Tests at forward speed were performed with the fin in the flapping and rotating mode. Figure 15 compares the derived roll damping for harmonic fin motions for:

- A flapping mode with an angular range of +/- 40 degrees
- A rotating mode with an angular range of +/- 15 degrees

From this figure, it is seen that as expected, the fin damping obtained from rotating fins increases quadratically as a function of the forward speed while the damping obtained from flapping fins increases linearly above the zero-speed value. Up to rather high speeds – about 12kn – the flapping mode generates more damping than the rotating mode.

Of course, the power required to activate the flapping motions is much higher than that to activate the rotating motions.

#### Drag

The above tests showed (just as in 2008) that the false angles of attack in the flapping mode produce forward thrust at non-zero speed. In the conventional mode the fin yields an “induced” drag (see Hoerner, 1965) which is largely governed by the aspect ratio.

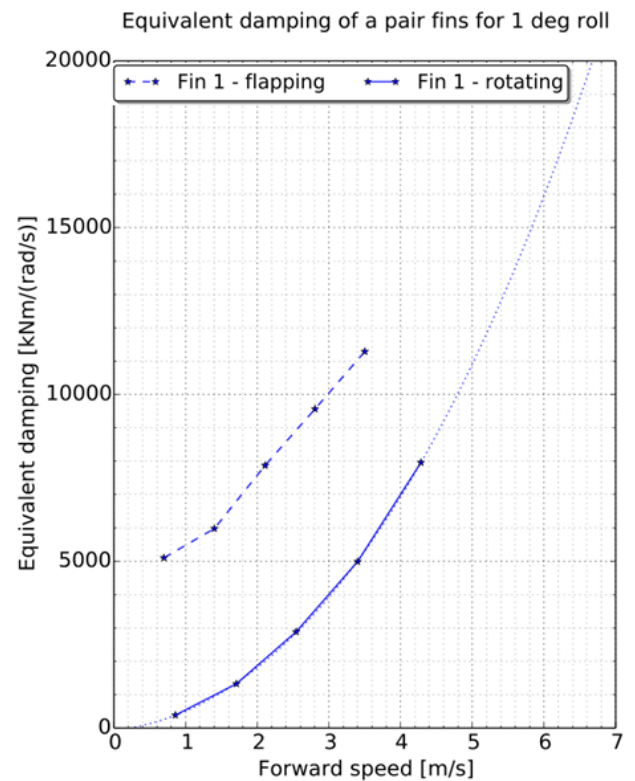


Figure 15 [Roll damping from conventional rotating and flapping mode]

## 7. MERITS OF FLAPPING FINS

Comparing flapping and conventional fins proved less straightforward than anticipated because the results depend on the details of the actuator limits and aspects of the fin arrangement. In the end we decided to make an assessment for a constant available actuator torque and a constant available instantaneous actuator power.

### 7.1 Basic fin forces

The assessment of the impulse and absorbed power of the fin reaction force builds on the expressions from Section 4.1 (truncating the integration to allow for end effects). Table 1 shows a comparison of a conventional fin and two flapping fins – one considering that the fin root is on the pivot point and one assuming that the fin root is at about 45% of the pivot point. This comparison assumes:

- Identical fin area
- The angular velocity and acceleration are only limited by the torque or the instantaneously absorbed actuator power
- The drag component dominates the impulse which yields the roll damping; the impulses from the initial acceleration and the deceleration are assumed to cancel each other

Regarding the results at constant torque the calculation shows that, while the reaction forces of the flapping fin are smaller than those of the conventional fin, the longer duration of the impulse yields a higher overall impulse. The increase over the conventional solution is at least some 20% (with the shaft at the fin base) and probably higher (the practicalities dictate a somewhat inboard location of the shaft).

At constant torque, as the travelled distance is the identical for all fins, the overall dissipated energy is the same. However, the flapping fin requires a lower instantaneous power.

Making the comparison at constant instantaneous power reduces the angular velocity of the conventional fin, leading to a substantial drop in the drag force. The resulting overall impulse of the flapping fin is at least some 40% higher. The total absorbed energy of the conventional fin is 25% lower.

	Designation		Conventional fin	Flapping fin	Flapping fin	units
	Conventional fin	Flapping fin	shaft at 20% of the chord	Fin root at the shaft	Fin root at 45% of the span from shaft	
Fin descriptions	Chord leading edge wrt shaft	Span root wrt shaft	-0.03	0.00	0.08	m
	Chord trailing edge wrt shaft	Span tip wrt shaft	0.14	0.18	0.25	m
	Span	Chord	0.09	0.09	0.09	m
	Aspect ratio		0.51	1.94	1.94	-
	Drag coefficient		5.00	5.00	5.00	-
	Drag force / $\alpha_v^2$		0.22	0.41	1.22	N/(rad/s <sup>2</sup> )
	Drag moment / $\alpha_v^2$		0.02	0.05	0.24	Nm/(rad/s) <sup>2</sup>
	Angular range		60.00	60.00	60.00	deg
Given an actuator torque	<b>Actuator torque</b>		<b>1.00</b>	<b>1.00</b>	<b>1.00</b>	<b>Nm</b>
	Resulting angular velocity		374.76	246.39	117.51	deg/s
	Duration of constant speed phase ( $\Delta t$ )		0.16	0.24	0.51	s
	Drag force		9.54	7.62	5.14	N
	Impulse: Drag Force . $\Delta t$		1.53	1.86	2.62	N.s
	Instantaneous actuator power		6.54	4.30	2.05	W
	Absorbed actuator energy		1.05	1.05	1.05	Ws
Given an actuator power	Actuator torque		0.72	0.95	1.56	Nm
	Resulting angular velocity		318.10	240.52	146.82	deg/s
	Duration of constant speed phase ( $\Delta t$ )		0.19	0.25	0.41	s
	Drag force		6.87	7.26	8.02	N
	Impulse: Drag Force . $\Delta t$		1.30	1.81	3.28	N.s
	<b>Actuator power</b>		<b>4.00</b>	<b>4.00</b>	<b>4.00</b>	<b>W</b>
	Absorbed actuator energy		0.75	1.00	1.63	Ws

Table 1 [Comparison of a conventional and a flapping fin]

## 7.2 Additional considerations

An additional aspect of the comparison is the fact that the point of application of the reaction force of a flapping fin is at a larger distance from the CoG. For a typical configuration we expect an increase of some 10% on top of the foregoing.

In addition to the above there are differences which are harder to quantify. We imagine the following:

- Flapping fins are not necessarily in line with bilge keels, allowing longer and higher bilge keels without negative interaction effects
- The limited chord at the root and the smaller angular motions of a high-aspect ratio fins limit the loss of lift in the rotating mode due to the root gap and significantly reduce the fin lift-induced drag (up to 75%).
- Conventional fins are less susceptible to a sudden loss of performance due to stall
- In case the perceived advantages materialize in smaller dimensions, flapping fins may yield a lower overall drag penalty.

## 8. CONCLUSIONS

Considering the results of the 2008 and 2014 test campaigns and the results of the simplified calculation method, it seems justified to conclude that:

- The modelling and measuring of transient motions of flapping fins is not entirely straightforward. The results of the 2014 campaign showed a much clearer relation between the fin motions and reaction forces.
- With some adaptations the theoretical model developed for zero speed stabiliser fins reproduces the test results fairly well.
- The damping from zero speed fins is largely governed by the angular velocity, the angular range, the cycle time and forward speed.
- Depending on the details of the actuator and the fin arrangement, a flapping fin seems to offer clear advantages in the lower speed range.

### Follow-up

Recognizing the complexity of the flow around flapping and stalling fins, MARIN has initiated a 2-year post-doc investigation to obtain an understanding of the physics of dynamic stall by means of CFD.

## 9. ACKNOWLEDGEMENTS

The authors gratefully acknowledge the permission of AntiRoll BV for using part of results from the 2014 test campaign.

## 10. REFERENCES

- Dallinga, R.P., "Roll stabilization of motor yachts: Use of fin stabilizers in anchored conditions", *Project 1999 Symposium*, Amsterdam, 1999
- Dallinga, R.P., "Hydromechanic aspects of the design of fin stabilizers", *RINA Spring Meeting*, London, 1993
- Dallinga, R.P., "Roll stabilization at anchor: Hydrodynamic aspects of the comparison of anti-roll tanks and fins", *Project 2002 Symposium*, Amsterdam 2002
- Gaillarde, G., "Dynamic stall and cavitation of stabilizer fins and their influence on the ship behaviour", *FAST*, Naples, 2003
- Hoerner, S.F., "Fluid – dynamic drag, theoretical, experimental and statistical information", 1965
- Licht, S., Hover, F. and Triantfyllou, M.S., "Design of a flapping foil underwater vehicle", *Int. Symp. on Underwater Technology*, 2004.
- Oossanen, P.van, "A method for the calculation of resistance and sail force of sailing yachts", *RINA Conf. on Calculator and computer aided design for small craft – The way ahead*, Southampton, 1981
- Soueid, H., Propulsion by mobile wings: Aerodynamic and applications to micro air vehicles, *DIAM, University di Genova, Internal Report 02*, 2005

## DESIGN OPTIMIZATION

A. Markov, Vripack, The Netherlands

A. Abma, Vripack, The Netherlands

### SUMMARY

This paper explains how a significant optimization step in the yacht design can be achieved. Within the yachting industry it is typical that a designer (read stylist) starts with the design and having a Naval Architect stepping in at a later stage. By approaching yacht design as a co-creation between the designer supported by a Naval Architect, the outcome will in many aspects be significantly better; more purposeful designed for the Owner's full intend. Looking back in time there is a clear trend that designs are getting more and more volume in a limited LOA. This trend is voting for getting a Naval Architect involved from day one.

### 1. INTRODUCTION

Over the last 5-8 years we clearly see a strong trend of Client requirements on efficiency, fuel consumption and comfort becoming more demanding. As a result the optimization process in yacht design has increased and improved significantly. The development of optimization tools like Computer Fluid Dynamics, viscous flow analysis, Wake field optimization studies, FEM Vibration analysis etc. have contributed largely to this.

While all of these tools are rather sophisticated nowadays and can provide remarkable results because of the required detailed input, they are usually being applied in the detailed design and engineering phase of the design process. While these optimization tools can significantly contribute to the efficiency gain and/or comfort increase, the biggest gain in optimizing the yacht can be found in the first stage of the design process, the concept design process.

### 2. HISTORICAL PERSPECTIVE

Figure 1 shows "Skipper" Herreshoff in his workshop on the third floor of the Castle. The nickname "Skipper Herreshoff" was given to him by the locals. During a period of 25 years Herreshoff designed a huge amount of classically beautiful yachts such as Ticonderoga, a sleek 72 foot clipper-bowed ketch that broke all kinds of records for her speed and agility, and larger Cup racing designs including J and M boats. A famous publisher of those days describes L. Francis Herreshoff's design style as follows, "His designs are marked by clean, sweeping lines and simplicity of hull and rig that show they have been drawn by a true artist." (Sensible Cruising Designs, McGraw Hill, Inc.) This statement is certainly clear to anyone who has seen Ticonderoga ("Big Ti" as many call her). Ticonderoga is a masterpiece of artwork, never mind speed. It is symmetry at anchor and symmetry in motion. No reverse-transom modern stern, no plastic hull and no aluminum mast.

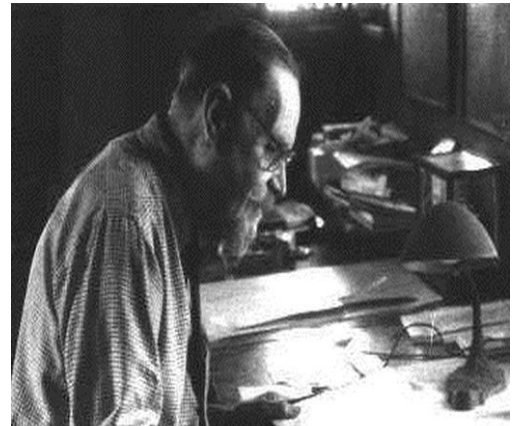


Figure 1 [Skipper Herreshoff]

This short biography nicely shows that back in the early days of yacht design, form and function were automatically integrated in the design because the designer and naval architecture profession simply were gathered in one and the same person. Any owner in need of a new yacht would hire a naval architect and commission him to design a new boat. The naval architect would then start with putting the main hull particulars along with calculating the weight of the boat. These main parameters would accommodate the weight and provide seagoing comfort, safety and efficiency. Based on the main particulars, the linesplan of the hull together with the general arrangement plan would be drawn. With the design of the main particulars and general arrangement, the naval architect basically determined the styling of the yacht as well. However, at that time, the form was more following the function.



Since the 1970's, designers like Jon Bannenberg Sr. introduced styling in the yacht design business as a dedicated profession. From that moment the naval architect and the stylist would work side by side on yacht design projects, each bringing their own skills and expertise. The stylist would work on the looks of the yacht above the waterline, while the focus of the naval architect would be more below the waterline. The functional design more and more followed the styling.

Today, the design process usually starts with a stylist; the naval architect being typically not yet involved in the conceptual design phase. It is the designer who determines the main particulars for the general arrangement. Obviously with this, the designer also determines the seakeeping behaviour, safety and performance of the design.

### 3. THE PROCESS

Since the early days it is the essence of yacht design to combine form and function into one and the same design. The final result should above all match the Owner's requests. Lots of decisions in the yacht design process have something to gain and something to lose. As we all know examples of such decisions are the main dimensions, building material, location of the engine room, propulsion concept, shape of the hull, internal volume versus the length etc. All these design considerations have impact on the behaviour, functionality and cost price of the yacht. While these considerations often are beneficial for one design consideration at the same time they might have a negative effect on other aspects of the yacht. This means in the conceptual design phase the proper balance between these design considerations is to be found. It is the main task of the designer and naval architect to match them corresponding to the intended use and preferences of the Owner.

In the concept design phase the main dimensions, characteristics and general arrangement plan are determined and often more or less fixed. Due to this fixation, the behaviour and functionality of the yacht are fixed for a great deal as well. Turning this around, this means that the yacht can be best optimized to match the intended use, the operational profile and preferences of the Owner in the conceptual design phase. In other words; the first weeks of the design process are crucial for the behaviour and functionality of the yacht over its full life time.

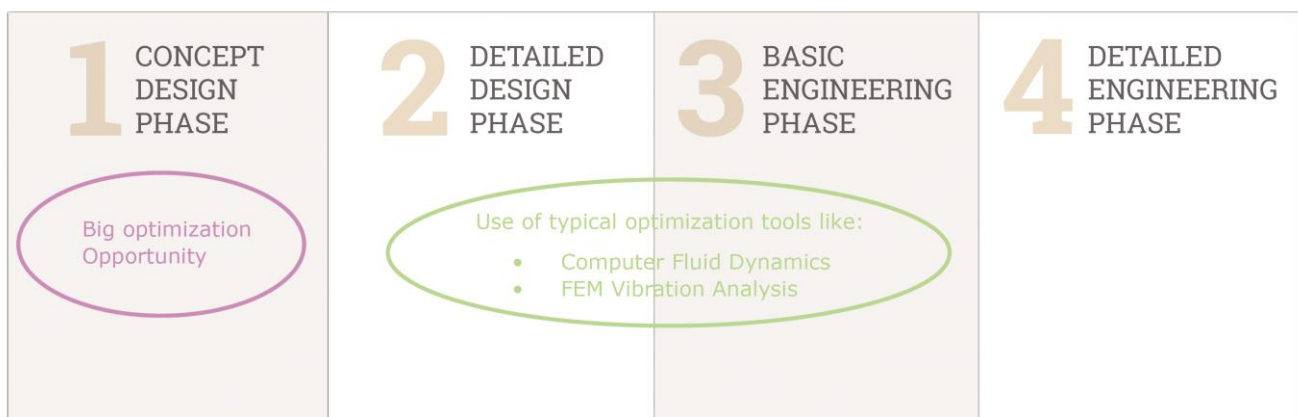


Figure 2 [Typical phases in design & engineering process]

While these design considerations usually affect the styling, the general arrangement, the naval architecture, structural arrangement, and mechanical engineering at the same time, as indicated in Figure 2, the biggest gain in this optimization process can be achieved if the various disciplines involved in yacht design and engineering are included in the concept design phase from day one. In other words, when applying a holistic design approach.

### 4. THE DESIGN PROCESS

The linguistic explanation of 'Holistic' is indicated in Figure 3. In line with this explanation, the holistic design approach takes all aspects into account at the same time. This result can only be achieved when the stylist and naval architect work closely together from day one of the project. Each of them putting their own

**Ho • lis • tic** - from Holism, Greek ὅλος - holos  
 Emphasizing the importance of the whole and the interdependence of its part.

Figure 3 [Holistic definition]

specialized experience and expertise in the concept design phase. When both specialized experts co-create in the right design process, the result will be more than the sum of each individual part.

#### 4.1. Naval Architecture Workflow

As indicated, in order to achieve the proper result it becomes crucial that a proper design process is followed. For Naval Architects, the basic of such a process is indicated in Figure 4. As can be seen in this diagram, the contribution of the naval architects in this stage of the project consists of two main tasks:

1. Naval Architecture work;
2. Ship Design work.

The main difference between these two tasks can be found in the same diagram as well.

The Naval Architecture work is commonly known and includes mathematical calculations, algorithms, equations etc. All being executed in order to obtain the performance from the drawings and main particulars. This work includes resistance calculations, stability calculations, weight calculations etc., the real number crunching work. It will be obvious that this part of the Naval Architect's work requires a crucial in-depth knowledge of the true story behind various equations and algorithms. Only with this knowledge there is true value in the results of the mathematics.

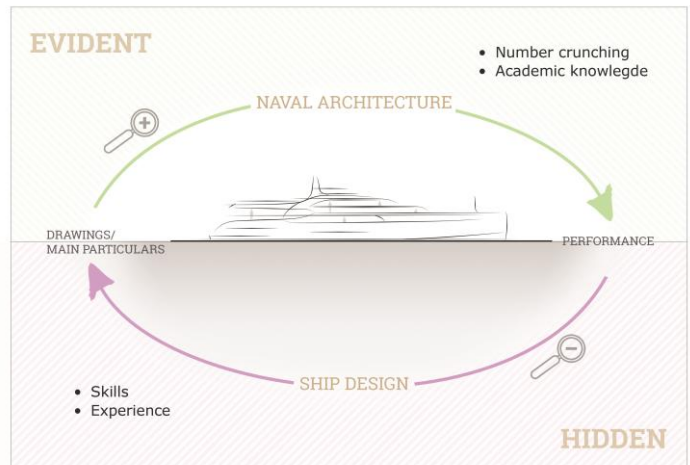


Figure 4 [Naval Architecture workflow]

The second part of the Naval Architecture job is the ship design task. This might be the less common, say the more unknown part of the Naval Architect's expertise. The design task is way apart from the 'comfortable' number crunching, it is the helicopter view on the total design, the zoomed out perspective. This is the part of thinking along with the designer, to support him or her in giving valuable information to the design process.

So when we combine these two tasks we get a very valuable tool in the development of the optimum design.

#### 4.2. The Smarter Design Process

We all are familiar with the design spiral as commonly known, see Figure 5. This spiral is a flow from outside towards the center representing that the Naval Architect's work is getting more and more detailed as time passes.

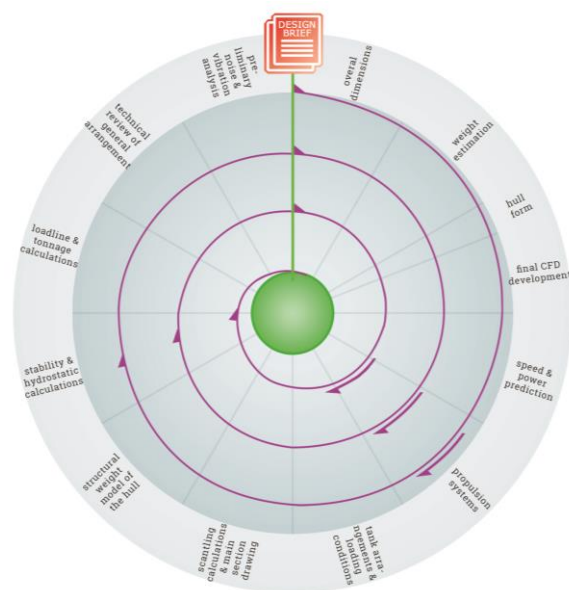


Figure 5 [Classical design spiral]

We believe that is not a correct representation of the happening in the co-creation of a design between the designer and the Naval Architect. If we take the distance between each axes for the effort the Naval Architect gives in his or her work, the process should start in the center of the spiral and working the way out towards the end of the spiral. In the conventional spiral there is a clear end of the spiral. You could even debate this. Is there an end towards the work of a Naval Architect. Is it not the case that his or her expertise is also valuable during the build and commissioning?

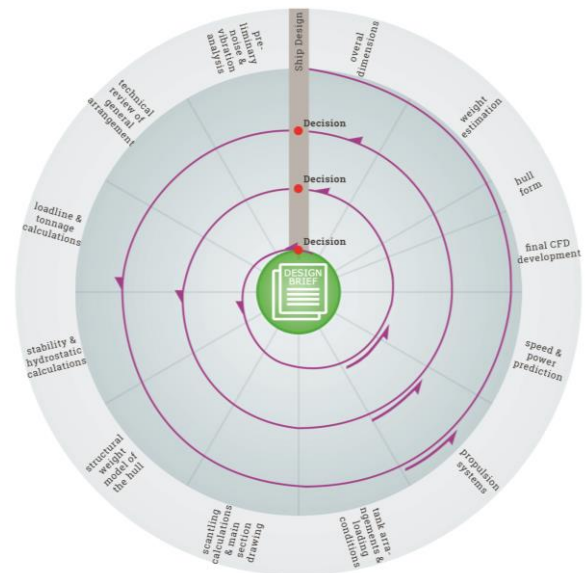


Figure 6 [*Smarter design spiral*]

The figure of the smarter design spiral shows clearly that:

- The first iterations are finished much quicker than the last iterations. The sequence of the iterations is high, the time between each of them is short;
- The further the progress, the more time each iteration takes and their sequence is getting longer. The further the progress the more time it takes to execute each iteration;
- The level of work and detail is increasing per iteration;
- Most likely the amount of people working per iteration will increase as well. Ideally the spiral starts with a very limited amount of naval architects (preferably one!) were gradually more people can be added to the team;
- The impact of the alterations to the design should decrease per iteration. With every new iteration, the impact of the changes should be reduced. As a result of that, the decisions which have big impact on the design should be taken at the beginning of the design process, while gradually the impact of the decisions is reduced;

The smarter design spiral starts with the Owners requests and intended use of the yacht. Summarized in the design brief. For this design brief, based on reference yachts (read: experience!) the first main dimensions are determined along with a first hull form. For these main particulars the essential performance is checked (the hard core naval architecture) based on which the main particulars can be adjusted again.

Having a closer look at this figure, we can add one important conclusion as well: The right decisions need to be taken at the right moment. When decisions are delayed in the process, they will pop up later and force you to go back to the part of the process where this decision needed to be taken in the first place. This will result in redoing part of the process. The impact of a set-back is large and getting larger as we move on. The further in the process, the more effect this rework will have in terms of money and capacity.

The main conclusion here: the duration of a proper yacht design process cannot be decreased by skipping some elements (deliberately reducing the amount of iterations) trying to save time. Not even by adding more resources in the beginning of the process. In this respect, the proper design process follows the general rule:

***‘What 1 woman can do in 9 months, 9 women cannot do in 1 month’***

This leads to the question; how to effectively reduce the duration of the yacht design process. The answer is easy: aim at first time right, focus on the center of the spiral in the co-creation process. Put an experienced Naval Architect with access to a proper reference database beside the designer this will lead to a reduction of the number of required iterations and hence reduce the duration of the design process while keeping the quality of the design AND performance.

## 5. DESIGN RATIOS

### 5.1. Main Particulars

As indicated and very commonly known main particulars affect the performance of any yacht. Some of these main particulars are directly related to the profile and layouts and are therefore usually determined in the very early beginning of the design process.

One of the most important design particulars is the amount of volume for a certain amount of length, or the amount of gross tonnage per length:  $\frac{GT}{L_{oa}}$ . This ratio is influenced by the amount of superstructure which is put on the hull. While the amount of Gross Tonnage usually represents a certain amount of weight, this figure has a rather significant effect on the performance of the yacht.

In addition to the Gross Tonnage per length ratio, in general, the influencing parameters can be distinguished for seakeeping and wavemaking behaviour.

#### 5.1.1. Wavemaking resistance

The design ratios which significantly affect the wavemaking resistance are: the weight per length ratio, the length over beam ratio, the prismatic coefficient and the longitudinal location of the centre of buoyancy.

For motor yachts, the most dominant factor for the performance is the ratio between the waterline length and the weight of the yacht, often indicated as the slenderness ratio:  $\frac{L}{\sqrt[3]{\nabla}}$  (Gaillarde, Toxopeus, Verwoest, & Hooijmans, 2006). This ratio actually gives an indication on how much weight is 'carried' per length. While the internal volume of the yacht directly affects the weight, this figure is significantly influenced by the GT per length ratio. A higher slenderness ratio implicates a relative longer waterline length, which means a relative lower Froude number. The Froude number is an important factor in the wave making resistance. This means the higher slenderness ratio will decrease resistance. Longer and light boats have relatively less resistance.

The second coefficient which affects the resistance is the prismatic coefficient,  $C_p$ . The ideal prismatic coefficient is dependent on the Froude number, however, for hull speeds, the optimum  $C_p$  is approx. 0.59 to 0.60. For displacement yachts, a higher  $C_p$  will increase the calm water resistance.

The longitudinal location of the centre of gravity in relation to the waterline length is important for the wavemaking resistance as well. The optimum LCB location is related to the Froude number. At the same time, the location of LCB should match the longitudinal location of the centre of gravity. While LCG is mainly the result of the general arrangement, the general arrangement directly affects the location of LCB as well.

In addition to these design ratios, a bulbous bow can significantly reduce the wavemaking resistance. In-house calculations, proven in sea trials, show that a CFD optimized bulbous bow can improve the performance with 10% to 15%.

#### 5.1.2. Seakeeping

While the slenderness ratio has a significant effect on resistance, it also affects the seakeeping behaviour. In addition, the B/T ratio and the shape of the bow are examples of main particulars which affect the seakeeping capabilities of a yacht.

Where a higher slenderness ratio reduces the resistance, in general, a higher slenderness ratio reduces the motions in the vertical plane (heave and pitch) and therefore reduces the vertical accelerations as well, (Gaillarde, Toxopeus, Verwoest, & Hooijmans, 2006). This increases the comfort level at sea.

As described by Dallinga (Dallinga & Kanerva, 1993) and Gaillarde et al. (Gaillarde, Toxopeus, Verwoest, & Hooijmans, 2006), the beam over draft ratio significantly influences the seakeeping behaviour as well. Like the slenderness ratio,

increasing the B/T ratio decreases the motions in the vertical plane and the vertical accelerations. This results in increased comfort in seagoing conditions.

The effect of the bow on the seakeeping capabilities can be found in the damping effect of the bow on the pitch motions. The amount and way of damping is related to the centreline longitudinal section as well as the transverse sections in the bow area. The stem line; a negative bow and bow flare, they all influence the seakeeping behaviour.

In addition to these ratios the general arrangement itself strongly affects the comfort level on board as well. The vertical accelerations vary over the length of the yacht. In general, obviously, the highest accelerations can be expected near the bow and stern of the yacht, while the area of lowest accelerations will be approximately at  $\frac{1}{3}$  from the aft. This means that in accommodation spaces which are located at the ends of the yacht, the comfort level will be less compared to the accommodation spaces located at  $\frac{1}{3}$  from the aft.

## 5.2. Underwater trends

Knowing the main particulars which affect the performance, it is interesting to see the trends of these particulars over the last years.

As described here above, an important design ratio is the slenderness ratio. The trend of this ratio from the year 2000 to today is given in Figure 7. This graph clearly shows that the weight per length is significantly increased over the last years.

As a result of this, the trend lines of the block coefficient and prismatic coefficient have increased as well over the last years, see Figure 8 and Figure 9.

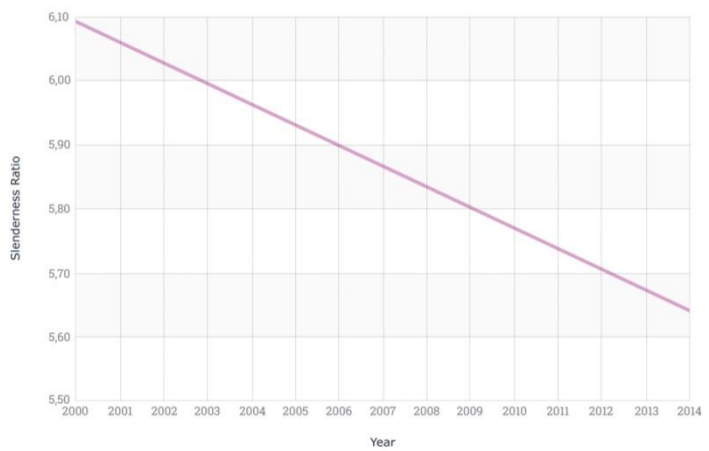


Figure 7 [Trend line average Slenderness Ratio. Source: MARIN]

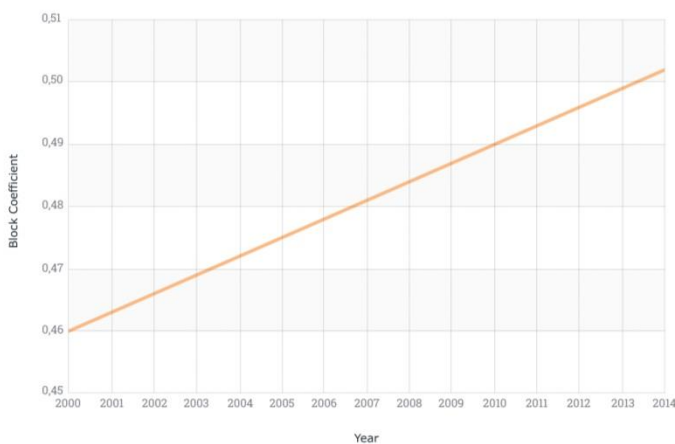


Figure 8 [Trend line  $C_B$ . Source: MARIN]

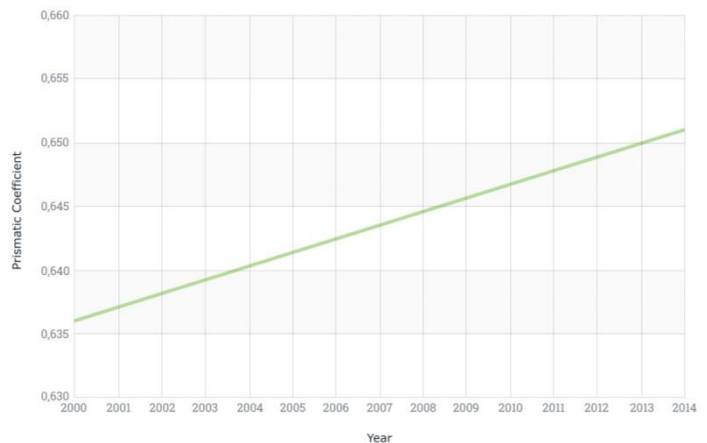


Figure 9 [Trend line  $C_p$ . Source: MARIN]

With the description of these design ratios as indicated in the graphs above, the effect of these trends on the performance is evident. While today's Naval Architects are trying hard to compensate the unfortunate effects of these trends by means of optimization of the details and appendages, it would of course be much more effective to get these design ratios right in the first place.

## 6. TO THE OWNERS BENEFIT

The main aim for the world wide yachting industry is to serve the yachting Owners with the development of the right products. Here comes the question: what is a right product? Is a yacht with a truly splendid exterior and interior design but being uncomfortable a right product? For any yacht which is made for sailing, even short distances, performance is somehow somewhere important. With performance we mean speed-power balance, stability, motions, but also functionality and safety. The Owners who spend money (some even lots of it) to develop a product deserve to receive value for money, not only in the design! Besides the fact that no matter how beautiful a yacht design is, when you get seasick on board or have an annoying AC system, you will tend to like the yacht just a bit less. A pity and for sure not deserved.

The yachting industry's common understanding of holistic is combining exterior and interior design. We strongly believe that this is just half way. Adding naval architecture and engineering to the yacht design process results in the True Holistic Approach.

Taking the smarter spiral (see Figure 6) and add a (system) engineer to the process, have him or her take a look at the design, giving input and support will lead to an even better design. In the end we all know that HVAC space requirements will happen, so why not better take this into account from day one. Obviously this again requires a hands-on approach from all the team members. Typically an engineer is easily distracted by details. In this phase it is all about the main concept along with respect for all the elements involved. Does this make the stylist's life harder? Does it border her or his creativity? Yes it might..... on the other hand; wouldn't it make the stylist life more valuable and interesting? In the end, all the systems and functionality will be there anyhow. So better have the stylist take this into account, up to a certain level for sure. Stylist; you are there to serve the Owners of this world so better do it properly. Join forces with a Naval Architect and an engineer and put the stakes high(-er). You will be surprised on how much experience you will gain yourself in this process!

## 7. CONCLUSION

As we all see a growing trend that yachts are getting more and more complex along with demands to get deliveries sooner. This really calls for a true holistic approach working in a smarter design spiral to ensure the Right Product First Time Right: Better Boats in Less Time!

## ACKNOWLEDGMENTS

The authors would like to thank MARIN and the Superyacht Group for their input in this paper.

## REFERENCES

- Dallinga, R., & Kanerva, M. (1993). *Recent changes in ferry hull from design and their impact on seakeeping*. London: Cruise & Ferry conference.
- Gaillarde, G., Toxopeus, S., Verwoest, T., & Hooijmans, P. (2006). *Hydrodynamics of Large Motor Yachts*. Wageningen: MARIN.